INVESTIGATING MOLECULE-SEMICONDUCTOR INTERFACES WITH NONLINEAR SPECTROSCOPIES

Paul George Giokas

A dissertation submitted to the faculty at the University of North Carolina at Chapel Hill in partial fulfillment of the requirements for the degree of Doctor of Philosophy in the Department of Chemistry.

Chapel Hill
2016

Approved by:

Wei You

Yosuke Kanai

Joanna M. Atkin

M. Kyle Brennaman

Andrew M. Moran

ABSTRACT

Paul George Giokas: Investigating Molecule-Semiconductor Interfaces
With Nonlinear Spectroscopies
(Under the direction of Andrew M. Moran)

Knowledge of electronic structures and transport mechanisms at molecule-semiconductor interfaces is motivated by their ubiquity in photoelectrochemical cells. In this dissertation, optical spectroscopies are used uncover the influence of electronic coupling, coherent vibrational motion, and molecular geometry, and other factors on dynamics initiated by light absorption at such interfaces. These are explored for a family of ruthenium bipyridyl chromophores bound to TiO_2, varying in the number of phosphonate anchors and the presence (or absence) of a methylene bridge between the ligand and the TiO_2. Transient absorption measurements show molecular singlet state electron injection in 100 fs or less. Resonance Raman intensity analysis suggests the electronic excitations possess very little charge transfer character. The connections drawn in this work between molecular structure and photophysical behavior contribute to the general understanding of photoelectrochemical cells.

Knowledge of binding geometry in nanocrystalline films is challenged by heterogeneity of semiconductor surfaces. Polarized resonance Raman spectroscopy is used to characterize the ruthenium chromophore family on single crystal TiO_2. Chromophores display a broad distribution of molecular geometries at the interface, with increased variation in binding angle due to the presence of a methylene bridge, as well as additional phosphonate anchors. This result implies multiple binding configurations for chromophores which incorporate multiple

phosphonate ligands, and indicates the need for careful consideration when developing surface-assembled chromophore-catalyst cells.

Electron transfer transitions occurring on the 100 fs time scale challenge conventional second-order approximations made when modeling these reactions. A fourth-order perturbative model which includes the relationship between coincident electron transfer and nuclear relaxation processes is presented. Insights provided by the model are illustrated for a two-level donor molecule. The presented fourth-order rate formula constitutes a rigorous and intuitive framework for understanding sub-picosecond photoinduced electron transfer dynamics. Charge transfer systems fit by this model include catechol-sensitized TiO_2 nanoparticles and a closely-related molecular complex, $[Ti(cat)_3]^{2-}$. These systems exhibit vibrational coherence coincident with back-electron transfer in the first picosecond after excitation, which suggests that intramolecular nuclear motion strongly influences the electronic transfer process and plays an important role in the dynamics of interfacial systems following light absorption.

ACKNOWLEDGEMENTS

Neither this dissertation nor the work presented herein would have been possible without the support, advice, or encouragement provided by my research advisor, Andrew Moran. Thank you for always encouraging me to find solutions to the problems I've encountered, and always keeping the science at the forefront. I would like to express gratitude to past and current members of the Moran Group, whom it has been a pleasure to work alongside. The support of the UNC Solar Fuels EFRC and its director, Thomas Meyer, has been invaluable. I am also grateful to my colleagues and collaborators in the EFRC, especially Kyle Brennaman, Kenneth Hanson, Lesheng Li, and Katherine Michaux. Your knowledge, skills, and efforts are greatly appreciated. Finally, I owe the sincerest of thanks to my family and friends who provided me unwavering confidence while this work was being completed.

TABLE OF CONTENTS

LIST OF TABLES xv

LIST OF FIGURES xvi

LIST OF ABBREVIATIONS AND SYMBOLS xxi

CHAPTER 1: INTRODUCTION 1

1.1. A Broader Understanding of Electron Transfer at Molecule-Semiconductor Interfaces 1

1.2. Dye-Sensitized Solar Energy Technology 3

1.2.A. DSSC Architecture 3

1.2.B. Artificial Photosynthesis 5

1.3. Radiative and Non-Radiative Processes in the Photoelectrochemical Cell 6

1.4. Understanding Interfacial Dynamics with Ultrafast Spectroscopy 8

1.5. Structure of this Dissertation 10

1.6 References 12

CHAPTER 2: SPECTROSCOPY AND DYNAMICS IN CONDENSED PHASES 17

2.1. Introduction 17

2.2. Perturbation Theory with a Density Matrix 18

2.3. Cumulant Expansion for Fluctuations with Gaussian Statistics 23

2.4. Third-Order Nonlinearities 27

2.4.A. Transient Absorption Spectroscopy 27

2.4.B. Spontaneous Raman Scattering 30

2.4.C. Heller's Approach for Spontaneous Resonance Raman Scattering 37

2.5 Marcus Theory 40

2.6 Concluding Remarks 48

2.7 References 49

CHAPTER 3: NONLINEAR SPECTROSCOPY AND ULTRAFAST TECHNIQUES 51

3.1. Introduction 51

3.2. Raman Spectroscopy 52

3.2.A. Resonance Raman Spectroscopy 52

3.2.B. Polarized Raman Spectroscopy 53

3.3. Pump Pulse Generation 55

3.4. Transient Absorption Spectroscopy 58

3.4.A. Overview 58

3.4.B. Experiment Design 58

3.5. Transient Grating Spectroscopy 61

3.5.A. Overview 61

3.5.B. Experiment Design 62

3.6. Conclusion 68

3.7. References 70

CHAPTER 4: SPECTROSCOPY AND DYNAMICS OF PHOSPHONATE- DERIVITIZED RUTHENIUM COMPLEXES ON TiO_2 74

4.1. Introduction 74

4.2. Background on Spectral Fitting and Physical Interpretations of Parameters 77

4.2.A. Algorithm for Resonance Raman Intensity Analysis 78

4.2.B. Nature of Solvent Coordinates in Ruthenium Complexes 80

4.2.C. Correlated Line Broadening in Ruthenium Complexes 82

4.3. Experimental Methods 89

4.4. Results and Discussion 94

4.4.A. Analysis of Linear Absorption Line Shapes 94

4.4.B. Resonance Raman Measurements 93

4.4.C. Interfacial Electron Transfer Dynamics 100

4.5. Conclusions....110

4.6. References....114

CHAPTER 5: MOLECULE-SEMICONDUCTOR INTERFACIAL GEOMETRY WITH RAMAN SPECTROSCOPY....118

5.1. Introduction....118

5.2. Background on Polarized Resonance Raman Spectroscopy....120

5.2.A. Dipole Interaction Model....120

5.3. Experimental Methods....123

5.3.A. Sample Preparation....123

5.3.B. Resonance Raman Measurements....124

5.4. Results and Discussion....125

5.5. Conclusions....137

5.6. References....138

CHAPTER 6: MODELING TIME-COINCIDENT ULTRAFAST ELECTRON TRANSFER AND SOLVATION PROCESSES AT MOLECULE-SEMICONDUCTOR INTERFACES....140

6.1. Introduction....140

6.2. Modeling Ultrafast Electron Transfer Kinetics....142

6.2.A. Hamiltonian....143

6.2.B. Fourth-Order Rate Formula....145

6.2.C. Assumptions and Limitations of Model....151

6.3. Second and Fourth-Order Dynamics in a Three-Level System....152

6.4. Combining Fourth-Order Model with a First-Principles DOS for TiO_2....157

6.4.A. Theoretical Methods....157

6.4.B. Model Calculations....159

6.5. Correspondence Between Second and Fourth-Order Rate Formulas....163

6.6. Wavepacket Representation of Relaxation Processes....165

6.7. Concluding Remarks....167

6.8. References....169

CHAPTER 7: NONEQUILIBRIUM CHARGE TRANSFER ON SEMICONDUCTING NANOPARTICLES....172

7.1. Introduction....172

7.2. Background....173

7.2.A. Modeling Catechol Back Electron Transfer....173

7.3. Experimental Methods....176

7.3.A. TiO_2 Nanoparticle Synthesis....176

7.3.B. Spontaneous Raman Measurements....176

7.3.C. Transient Absorption Spectroscopy Measurements 178

7.3.D. Transient Grating Raman Spectroscopy Measurements 179

7.3.E. Six-Wave Mixing FSRS 181

7.4. Results and Discussion 184

7.4.A. Spontaneous Raman Spectroscopy 184

7.4.B. Transient Absorption Spectroscopy 185

7.4.C. Transient Grating Spectroscopy 191

7.4.D. Background-Free FSRS Measurements 194

7.5. Conclusions 197

7.6. References 199

CHAPTER 8: ULTRAFAST SPECTROSCOPIC SIGNATURES OF COHERENT ELECTRON TRANSFER MECHANISM IN A TRANSITION METAL COMPLEX 204

8.1. Introduction 204

8.2. Model for Spectroscopy and Dynamics 207

8.2.A. Hamiltonian 207

8.2.B. Model for Transient Absorption Signals 209

8.2.C. Spectral Fitting of Absorbance and Resonance Raman Cross Sections 214

8.3. Experimental Methods 217

8.3.A. Sample Preparation 217

8.3.B. Raman Spectroscopy 217

8.3.C. Transient Absorption Experiments 218

8.4. Experimental Methods 219

8.4.A. Resonance Raman Intensity Analysis and Spectral Fitting 220

8.4.B. Decomposition of Transient Absorption Signal Components 225

8.4.C. Initiation of Vibrational Coherence by Back-Electron Transfer 228

8.4.D. Analysis of the Back-Electron Transfer Mechanism 231

8.5. Broader Implications for Electron Transfer Reactions 240

8.6. Concluding Remarks 243

8.7. References 245

CHAPTER 9: CONCLUDING REMARKS 249

APPENDIX A: SUPPLEMENT TO "SPECTROSCOPY AND DYNAMICS OF PHOSPHONATE- DERIVITIZED RUTHENIUM COMPLEXES ON TIO_2 253

A.1. Spectral broadening of 400 nm laser pulses in a hollow-core fiber 253

A.2. Sample holder for dye-sensitized TiO 2 films 254

A.3. Solvent and pH dependence of Raman spectra 256

A.4. Fitting Linear Absorbance Spectra and Resonance Raman Cross Sections 257

A.5. Linear Absorbance Spectra 259

A.6. Fits to Raman Excitation Profiles 259

A.7. Fits to Linear Absorbance Spectrum 270

A.8. Effect of Fluence on TA Line Shapes 272

A.9. Fitting Transient Absorption Signals 273

A.10. Raman Fit Optimization 275

A.11. Oxidation Potentials 277

APPENDIX B: SUPPLEMENT TO "NONEQUILIBRIUM CHARGE TRANSFER ON SEMICONDUCTING NANOPARTICLES" 278

B.1. Linear Absorption of Sensitized Nanoparticles 278

B.2. Resonance Raman Intensity Analysis 279

APPENDIX C: SUPPLEMENT TO "ULTRAFAST SPECTROSCOPIC SIGNATURES OF COHERENT ELECTRON TRANSFER MECHANISMS IN A TRANSITION METAL COMPLEX" 280

C.1. Decomposition of Transient Absorption Signals 280

C.2. Analysis of Uncertainty in Spectral Fits 281

C.2.A. Fits Conducted with Homogeneous Width Fixed at 2150 cm^{-1} 282

C.2.B. Fits Conducted with Homogeneous Width Fixed at 3150 cm^{-1} 285

C.3. The Hot Ground State Signal Component Dominates the Coherent Raman Response of $[Ti(cat)_3]^{2-}$ 289

C.4. Density Functional Theory Analysis of the Most Appropriate Basis Set 290

C.5. Comparison of GSB, HGS, and BB Signal Components to Catechol on TiO_2 in Aqueous Solution.....291

C.6. References 295

LIST OF TABLES

Table 4.1: Resonance Raman fitting parameters for all complexes in methanol.....87

Table 4.2: Resonance Raman fitting parameters for all complexes on TiO_2 films.....88

Table 4.3: TA fitting Parameters for ruthenium complexes on TiO_2 106

Table 5.1: Polarization ratios (R_x,R_y) for the chromophores on TiO_2. 129

Table 6.1: Parameters used in Model Calculations.....166

Table 7.1: Raman peak assignments. 184

Table 7.2: Raman peak exponential fitting constants. 194

Table 8.1. Resonance Raman Fitting Parameters 224

Table 8.2. Organization of Quantum Numbers for Multi-Mode Basis Set.....239

Table A.1. Complete set of Resonance Raman fitting parameters in methanol. 257

Table A.2: Complete set of Resonance Raman fitting parameters on TiO_2 films. 258

Table A.3: Zero Crossing Fitting Parameters. 274

Table A.4: Fitting Parameters for Figure A.22. 274

Table B.1: Complete set of Resonance Raman fitting parameters for catechol on TiO_2.....279

Table C.1: Resonance Raman fitting for Homogeneous Width Fixed at 2150 cm^{-1}. 284

Table C.2: Resonance Raman Fitting Parameters.....288

LIST OF FIGURES

Figure 1.1: A rudimentary DSSC consisting of a chromophore and electrode. 4

Figure 1.2: Diagram of Interfacial Processes....7

Figure 1.3: Example Transient Absorption Spectroscopy Signal....9

Figure 1.4: Depiction of different binding modalities of RuP on a planar interface. 10

Figure 2.1- Feynman diagram for linear absorption of a two-level system....22

Figure 2.2: Feynman diagram for sum-frequency generation in a three-level system 23

Figure 2.3: Feynman diagrams for a three level system....29

Figure 2.4: Two-state example system for the investigation of spontaneous light emission 35

Figure 2.5: Spontaneous emission Feynman diagrams....36

Figure 2.6: Example wavepacket overlap....38

Figure 2.7: Free energy surfaces for a bimolecular donor-acceptor system....41

Figure 2.8: Free energy regimes for a bimolecular donor-acceptor system 45

Figure 2.9: Comparison between adiabatic and nonadiabatic potential surfaces 46

Figure 3.1: Diagram of the spontaneous Raman experimental setup 53

Figure 3.2: Experimental Raman Polarizations 54

Figure 3.3: Hollow Core Fiber Apparatus 56

Figure 3.4: Hollow Core Fiber Pulse Spectra 57

Figure 3.5: Experimental diagram for the TA measurements....59

Figure 3.6: Pulse sequence in a 3rd order TG spectroscopy experiment....62

Figure 3.7: Depiction of the Transient Grating....63

Figure 3.8: Experimental diagram for the TG Raman experiment....64

Figure 3.9: Interferometric Detection Example....66

Figure 3.10: The Sample Jet 68

Figure 4.1: Molecular structures of phosphonated ruthenium complexes 75

Figure 4.2: Diagram of Solvent Fluctuation Coordinates 78

Figure 4.3: Measured absorbance spectra of all molecules 90

Figure 4.4: Resonance Raman Spectra 94

Figure 4.5: Fits of experimental Raman excitation profiles for 2 on TiO_2 95

Figure 4.6: Vibrational Reorganization Energies for all molecules 96

Figure 4.7: Potential binding motifs for Ru complexes with multiple phosphonated ligands 97

Figure 4.8: Transient absorption spectra 101

Figure 4.9: Normalized transient absorption signals 103

Figure 4.10: Transient absorption time constants 105

Figure 4.11: Zero crossing wavenumbers 108

Figure 4.12: Relaxation scheme diagram 110

Figure 5.1: Chromophore molecular structures 119

Figure 5.2: Dipole projection diagram 121

Figure 5.3: Diagram of the polarized Raman experimental setup 124

Figure 5.4: Polarized Resonance Raman spectra 127

Figure 5.5: Average polarization ratios for RuP measured on each crystal face 130

Figure 5.6: Average polarization ratios for RuCP measured on each crystal face 131

Figure 5.7: Average polarization ratios for Ru2P measured on each crystal face 132

Figure 5.8: Geometry map for RuP 133

Figure 5.9: Geometry map for RuCP 134

Figure 5.10: Geometry map for Ru2P 135

Figure 5.11: Chromophore geometry distributions....136

Figure 6.1: Wavepacket relaxation diagram....141

Figure 6.2: Double-sided Feynman diagrams corresponding to the two rate kernels. 146

Figure 6.3: Wavepacket calculation plots....154

Figure 6.4: Second and fourth-order dynamics are simulated for a three-level system 157

Figure 6.5: Conduction Band DOS of TiO_2....158

Figure 6.6: Electron transfer dynamics computed with the first-principles DOS....161

Figure 6.7: Energy Distribution Diagram....162

Figure 7.1: Catechol-TiO_2 proposed relaxation diagram....175

Figure 7.2: Diagram of the spontaneous Raman experimental setup 177

Figure 7.3: Experimental diagram for the transient absorption measurements 179

Figure 7.4: Experimental diagram for the transient grating Raman experiment 181

Figure 7.5: Experimental diagram for the six-wave mixing FSRS experiment....183

Figure 7.6: Resonance Raman measurement of dye- sensitized nanoparticles 185

Figure 7.7: Transient absorption spectroscopy contour plots....187

Figure 7.8: Transient absorption spectroscopy component contour plots 188

Figure 7.9: Detailed fitting of the hot ground state band over the first 4 ps....189

Figure 7.10: Raman spectra for the spontaneous and stimulated Raman experiments....192

Figure 7.11: Stimulated Raman spectrogram from catechol-TiO_2 NP solution 193

Figure 7.12: Femtosecond Stimulated Raman peak amplitudes for the catechol loaded TiO_2....195

Figure 7.13: FSRS spectrogram from catechol-TiO_2 NP solution....196

Figure 8.1: Four potential $[Ti(cat)_3]^{2-}$ photoexcitation pathways. 205

Figure 8.2: Nonlinearities associated with the hot ground state....210

Figure 8.3: The measured absorption spectrum is fit with Equation (8.19). 220

Figure 8.4: Resonance Raman spectrum of $[Ti(cat)_3]^{2-}$. 221

Figure 8.5: Experimental Raman cross sections are fit using Equation (8.20). 223

Figure 8.6: The (a) experimental TA signal is (b) fit using Equation (8.23). 226

Figure 8.7: The magnitude of the HGS signal component. 228

Figure 8.8: Coherences in the TA HGS signal component. 230

Figure 8.9: Physical picture suggested by theoretical model. 232

Figure 8.10: Doorway functions computed with Equation (8.20). 234

Figure 8.11: Doorway functions computed with Equation (8.20). 235

Figure 8.12: TA signal calculated at 500 nm with Equation (8.18) 237

Figure 8.13: Diagram of population-to-coherence pathways 242

Figure A.1: Hollow-core fiber setup 253

Figure A.2: Spectra of 400 nm pulses 254

Figure A.3: Homemade cuvette used to contain dye-sensitized films 255

Figure A.4: Sample films are held in a homemade cuvette and oscillated 255

Figure A.5: Raman Spectra of chromophores 256

Figure A.6: The absorption spectra of the six $Ru(bpy)_3$ complexes 259

Figure A.7: The excitation profile of 1 in methanol solution overlaid with fitting curve 260

Figure A.8: The excitation profile of 1 on TiO_2 overlaid with fitting curve 260

Figure A.9: The excitation profile of 2 in methanol solution overlaid with fitting curve 261

Figure A.10: The excitation profile of 2 on TiO_2 overlaid with fitting curve 262

Figure A.11: The excitation profile of 3 in methanol solution overlaid with fitting curve 263

Figure A.12: The excitation profile of 3 on TiO_2 overlaid with fitting curve 264

Figure A.13: The excitation profile of 1C in methanol solution overlaid with fitting curve.....265

Figure A.14: The excitation profile of 1C on TiO_2 overlaid with fitting curve.....266

Figure A.15: The excitation profile of 2C in methanol solution overlaid with fitting curve.....267

Figure A.16: The excitation profile of 2C on TiO_2 overlaid with fitting curve.....268

Figure A.17: The excitation profile of 3C in methanol solution overlaid with fitting curve.....269

Figure A.18: The excitation profile of 3C on TiO_2 overlaid with fitting curve.....270

Figure A.19: Experimental absorption spectra overlaid with model fit.....271

Figure A.20: Experimental absorption spectra overlaid with model fit.....272

Figure A.21: Transient absorption spectra of 1C on TiO_2.....273

Figure A.22: Normalized TA signals and fits for all ruthenium complexes in solution.....275

Figure A.23: Sum of squares error of the fit of the absorbance spectrum.....276

Figure A.24: Comparison of energy levels for each of the ruthenium complexes and TiO_2.....277

Figure B.1: Catechol-TiO_2 charge transfer absorption spectrum.....278

Figure C.1: Parameters of a broadband signal component.....281

Figure C.2: Absorption spectrum fit with Equation (8.19) and the parameters in Table C.1.....282

Figure C.3: Raman cross sections fit using Equation (8.20) and the parameters in Table C.1. ..283

Figure C.4: Absorption spectrum fit with Equation (8.19) and the parameters in Table C.2.....286

Figure C.5: Raman cross sections fit using Equation (8.20) and the parameters in Table C.2 ...287

Figure C.6: The coherent response of the $[Ti(cat)_3]^{2-}$ analyzed for a range of wavelengths 289

Figure C.7: Linear absorbance spectra of $[Ti(cat)_3]^{2-}$ and catechol on a TiO_2 film. 292

Figure C.8: TA spectrogram for the chirp-corrected signal from catechol on TiO_2.....293

Figure C.9: Decomposition of TA signal components for catechol on TiO_2.....294

LIST OF ABBREVIATIONS AND SYMBOLS

A	acceptor molecule
A^-	reduced acceptor molecule
Å	angstrom
$A_A(\omega)$	acceptor molecule absorption spectrum
$\alpha(\omega)$	polarizability
α	rotation angle
BBO	β-barium borate
BET	back electron transfer
c	speed of light
CB	conduction band
CCD	charge coupled device
$c_n^{(1)}$	first order coefficient of state "b"
$C(T)$	correlation function
cm^{-1}	wavenumber
$\chi^{(n)}(\omega)$	susceptibility at n^{th} order
D	donor molecule
D^*	photoexcited dye or photoexcited donor molecule
D^+	oxidized dye or donor molecule
DFT	density functional theory
DSPEC	dye sensitized photoelectrosynthesis cell
DSSC	dye sensitized solar cell
δ	delta function or Kronecker delta

$\underset{\sim}{d}_{\alpha}^{A}$	specific vibrational nuclear coordinate
Δ	fluctuation in energy gap due to interactions with surroundings
DOS	density of states
E(t)	electric field
e^-	electron
e	excited state index
ESA	excited state absorption
ESE	excited state emission
ET	electron transfer
eV	electron volt
$\Delta E^{\dagger}$	energy activation barrier
ε	extinction coefficient
F	fluence
$f(s)$	oscillator strength
Φ	fraction of monomers photoexcited
FROG	frequency resolved optical gating
fs	femtosecond
FSRS	Femtosecond stimulated Raman spectroscopy
FT	Fourier Transform
FWHM	full width at half maximum
ΔG	free energy change
$G(s)$	Gaussian distribution
g	ground state index
$g(t)$	line broadening function

$G(t';w)$	Gaussian instrument response function
$\mathcal{G}(t_n)$	Green Function
GSB	ground state bleach
GVD	group velocity dispersion
Γ	damping constant
h	Planck's constant
$\hbar$	reduced Planck's constant ($=h/2\pi$)
H^{Coul}	coulombic coupling
H_{DA}	energy gap Hamiltonian ($=H_A-H_D$)
H^{el-ph}	electron-phonon coupling
HOMO	highest occupied molecular orbital
HGS	hot ground state
I	Intensity or auxillary function
ITO	indium tin oxide
η (%)	photovoltaic power conversion efficiency
J_{DA}	dipole-dipole coupling between donor and acceptor molecules
K	rate function
k_{bt}	Boltzmann's constant
k	rate constant
k_n	wavevector of pulse "n"
$L(\omega)$	absorption lineshape
LMCT	ligand to metal charge transfer
LO	local oscillator
LUMO	lowest unoccupied molecular orbital

Λ^{-1}	correlation time of solvent fluctuations
λ	reorganization energy or wavelength
MLCT	metal to ligand charge transfer
^{1}MLCT	singlet metal to ligand charge transfer
^{3}MLCT	triplet metal to ligand charge transfer
$M(t)$	solvation correlation function
μm	micrometer
N_{A}	Avogadro's constant
ND	neutral density
nm	nanometer
NOPA	noncollinear optical parametric amplifier
OHD	optical heterodyne signal detection
OPA	optical parametric amplifier
OPG	optical parametric generation
OPV	organic photovoltaic
ω	angular frequency
ω_0	carrier frequency
ω_{vib}	vibrational frequency
ϕ	phase or phase shift
$P_n(t)$	probability of residing in state "n" at time t.
$P_n(kT)$	thermal population of state "n"
$P^{(n)}$	polarization of nth order
ps	picosecond
q	collective nuclear coordinate

r_{DA}	intermolecular distance between donor and acceptor molecules
$r(T)$	polarization anisotropy
$\hat{\rho}(t)$	time dependent density operator
ρ	depolarization ratio
Q_C	fluorescence quantum yield
$R(t)$	response function term
$Ru(bpy)_3$	ruthenium(II)tris(bipyridine)
RuP	single-ligand phosphonated $Ru(bpy)_3$
RuCP	single-ligand phosphonated $Ru(bpy)_3$ with methylene spacers
Ru2P	double-ligand phosphonated $Ru(bpy)_3$
$S^{(n)}(t)$	response function of n^{th} order
SNR	signal-to-noise ratio
$\psi(t)$	wavefunction
σ	cross section or Gaussian width parameter
T	temperature (or time interval)
τ	time delay or interval
t	time interval
TA	transient absorption
TDPT	time dependent perturbation theory
TG	transient grating
$t_{group}(\omega)$	group velocity
TOD	third order dispersion
$\theta(t)$	Heaviside step function or temporal phase

$\theta(\omega)$	spectral phase
μ	transition dipole
$\hat{\mu}(t)$	dipole operator
$\hat{V}_I(t)$	time dependent interactive pertubation
V_{ba}	coupling between states “a” and “b”
V	volume, potential, or coupling
ν	frequency
v_A	number of valence electrons
W	rate kernel
X	Beam polarization axis
Y	Beam polarization axis
$\xi(t)$	Gaussian envelope function
z	charge

CHAPTER 1: INTRODUCTION

1.1. A Broader Understanding of Electron Transfer at Molecule-Semiconductor Interfaces

Energy is an important global resource. Population increases and industrial advancements have only increased the demand for energy in recent history. Current power requirements (as well as predicted future consumption) [1] make it necessary to develop efficient and sustainable energy conversion technologies. While several sources of renewable energy exist, most are infeasible to meet global energy demand due to excessive cost, lack of physical resources, or geographic incompatibility.[2-4] Solar radiation is the most abundant power source available on the planet, delivering more energy to the Earth's surface in one hour than was used during the entire year of 2002.[5,6] The abundance of solar energy across the globe as well as the potential for cleaner, low-cost alternatives to fossil fuels has made efficient solar energy conversion an important technological goal in recent decades.[5,7-23] Many approaches to harvesting solar energy have been developed, from semiconductor junction photovoltaic devices (including most commercially available solar panels) to solar power concentrators. [8,12,13,22,24-26]

The dye-sensitized solar cell (DSSC) is a device which utilizes a light-harvesting molecule (chromophore) attached to an electrode, often a metal-oxide semiconductor. DSSCs will be discussed in greater detail in Section 2. Rather than using solar energy to charge a battery or directly power other devices, DSSCs can store solar energy by performing chemical reactions patterned after photosynthesis, often water-splitting.[11,27-33] While there are several components to a DSSC, this dissertation is specifically concerned with the interface between the semiconductor

and the molecular chromophore, where the radiation energy absorbed by the chromophore transfers to the electrode in order to be used by the cell (see Section 3). The physical and chemical properties of both the chromophore and the semiconductor influence the dynamics of electron transfer processes. As a result, wide arrays of chromophore and semiconductor pairings have been investigated in the field. [14,32,34,35]

The work presented in this dissertation has thoroughly investigated the nature of electron transfer at molecule-semiconductor interfaces. Specifically, the studies presented here are concerned with uncovering the impact of molecular structure and nuclear geometry on the electron dynamics in these systems. Furthermore, the work presented here[36] demonstrates that conventional second-order electron transfer models (Marcus theory)[37] are insufficient to correctly model systems in which electron transfer occurs from nonequilibrium nuclear geometries and explores experimental techniques[38,39] to uncover the origins of such behavior. Primarily, the work presented here:

- Systematically compares electron injection rates and vibrational spectra across a series of closely related chromophores.
- Presents a detailed study of the binding geometry of phosphonated bipyridyl ruthenium chromophores to TiO_2 crystals with resonance Raman spectroscopy, concluding that a broad distribution of molecular orientations exists.
- Establishes a new fourth-order theoretical picture of the effect of nonequilibrium processes on ultrafast electron transfer reactions in condensed phases.
- Applies the developed nonequilibrium approach to a model system exhibiting time-coincident ultrafast electron transfer and relaxation using multiple spectroscopic techniques to characterize the nonequilibrium dynamics.

The accomplishments presented in this dissertation all further the understanding of the molecule semiconductor interface. Such understanding is necessary for progress toward the common goal of improving the quantum efficiency of DSSC devices.

1.2. Dye-Sensitized Solar Energy Technology

1.2.A. DSSC Architecture

DSSCs utilize a light-harvesting molecule (chromophore) attached to an electrode, often a metal-oxide semiconductor. Simply, the device operates when the chromophore absorbs solar radiation, which promotes an electron into an excited state. This excited electron then transfers to the electrode, where its energy can be used to do work. [11,14,20,40] Figure 1.1a shows a basic diagram of a DSSC.

In 1991, O'Regan and Grätzel achieved significant improvement in the design of DSSCs by incorporating nanocrystalline semiconductor films[18] in order to increase quantum efficiency by greatly increasing the surface area of the electrode (see Figure 1.1b). In other words, the devices were able to produce more useable current per absorbed photon. Despite significant advances in solar energy science over the past 30 years, sensitized nanocrystalline substrates remain an important feature of DSSCs. TiO_2 is widely used in DSSCs for its relative abundance, low cost, and favorable band gap energy.[41-44]

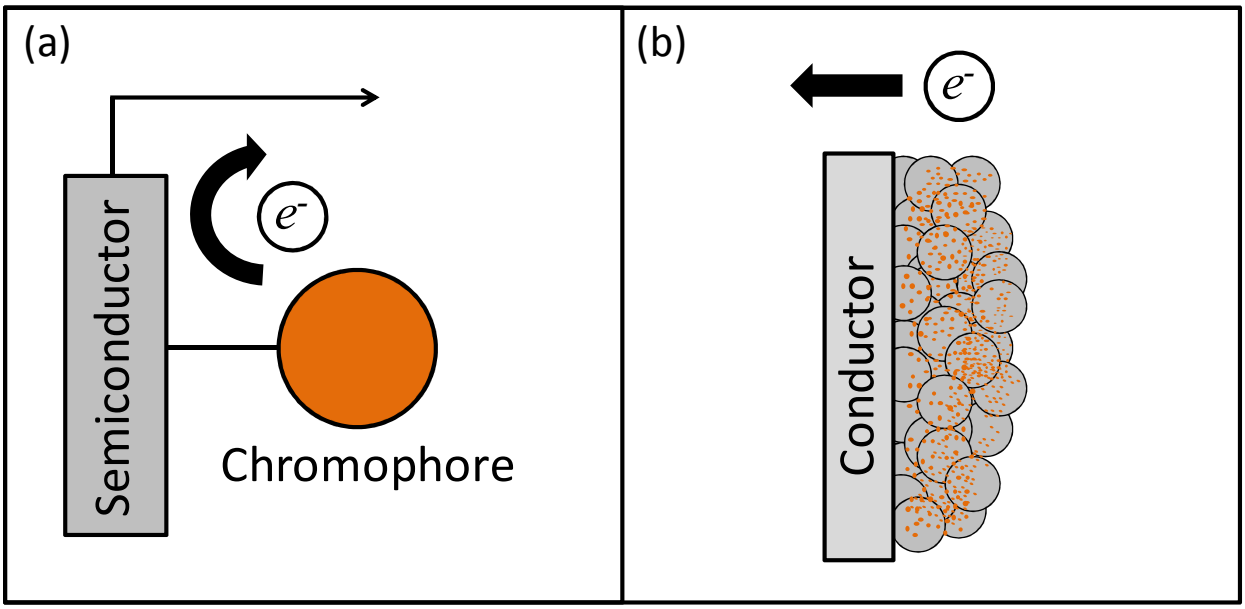

Figure 1.1: (a) A rudimentary DSSC consisting of a chromophore and electrode. The chromophore molecule is attached to the semiconductor electrode such that electrons transfer from the molecule into the semiconductor, and are then drawn into the wire to their destination. **(b)** While still consisting of the same basic components, this DSSC utilizes nanoparticles to increase the surface area of the electrode. The orange dots represent many chromophore molecules like those in panel a. In this DSSC, the nanoparticles form a film on a conductive glass which serves the same purpose as the wire.

The light-harvesting chromophore is another main focus of improving DSSC technology. This is not surprising, as the chromophore is responsible for capturing the solar radiation and quickly and efficiently transferring it to the semiconductor, which is integral to device function. One of the largest advantages of DSSCs over bare metal-oxide nanoparticles devices is the absorption of light across the visible spectrum, rather than a relatively narrow region near the ultraviolet.[18,20,32,44,45] By absorbing more of the solar spectrum, the chromophore is able to collect more energy per hour of daylight, which equates to increased power. The drastic increase

in efficiency justifies the expense of the molecular chromophore compared to the metal-oxide electrode. Among the most popular chromophores for use in DSSCs are functionalized transition metals, particularly ruthenium-centered inorganic molecules such as, $[Ru(bpy)_3]^{2+}$, formally tris(bypyridine)ruthenium(II). [35,40,46-52] $[Ru(bpy)_3]^{2+}$ possesses a broad visible absorption band corresponding to a metal-to-ligand charge transfer (MLCT) transition which allows it to harvest a great deal of solar energy. The processes which occur between the chromophore and the semiconductor will be discussed in the next section.

1.2.B. Artificial Photosynthesis

Another key challenge undertaken by researchers designing solar cell technology in recent years is energy storage. Energy storage is a necessary concern for solar energy harvesting because any given area of the Earth's surface does not receive constant amounts of solar radiation, for example, at night. One solution to the problem of energy storage is the generation of solar fuels. In other words, chemical products are made using the energy collected by the solar cell which can be stored and used as chemical fuel analogous to the natural photosynthesis performed by plant life. Electrolysis of water separates it into oxygen and hydrogen gases, both of which are well-known fuels. Additionally, carbon dioxide can be converted into methane or related carbohydrates, which serve equally well as fuel.[53] DSSCs which aim to generate solar fuels by such artificial photosynthetic means have been termed dye-sensitized photoelectrosynthesis cells, or DSPECs.[11,28-33] Electrochemical water oxidation requires more charge than provided by a single electron- in fact, four electrons are required to split water. For this reason, the chromophore must be able to transfer electrons to the semiconductor very rapidly and efficiently. In order to develop DSPECs which can oxidize water effectively, it is necessary to understand intimately the processes which occur at the molecule-semiconductor interface.

This understanding includes knowledge of the physical properties (including vibrational motion and relaxation) of the chromophore and nanoparticles which impact the dynamics of these processes.

1.3. Radiative and Non-Radiative Processes in the Photoelectrochemical Cell

The work presented in this dissertation explores the ultrafast electron transfer between a semiconductor and covalently bound chromophore. TiO_2 serves as the primary semiconductor surface, and in each of the following studies it is bound to one of several chromophores. The first of these chromophores is catechol. Catechol exhibits strong binding to TiO_2 and sensitization is the result of the formation of a broad ligand-to-metal charge transfer (LMCT) band in the visible region. The other chromophores are all closely related to $[Ru(bpy)_3]^{2+}$ as discussed in the previous section. Specifically, the ruthenium chromophores have been functionalized with phosphonic acid groups which allow covalent attachment to the semiconductor surface.[34,54] This attachment is critical to the electron transfer event, as will be shown. One such ruthenium chromophore is shown bound to TiO_2 in Figure 1.2.

A number of radiative (processes involving a photon) and nonradiative processes occur at the interface of the chromophore and semiconductor.[55] Light-absorption occurs when a resonant photon promotes an electron from the ruthenium metal to a bipyridine ligand, and completes within a few femtoseconds. The light-absorption causes vibrational excitation in the chromophore, which relaxes over 10s of picoseconds.[50] Due to spin-orbit coupling, electrons promoted to the ligand by absorption rapidly undergo intersystem crossing to a more stable triplet state which is longer lived than the higher energy singlet.[50,56-60] The relatively long-lived

triplet state makes ruthenium complexes attractive for increasing the quantum efficiency of electron transfer reactions. In addition, because the rate of intersystem crossing is faster than fluorescence which occurs on the μs timescale, very little of the absorbed energy is lost by radiative emission from the singlet state.

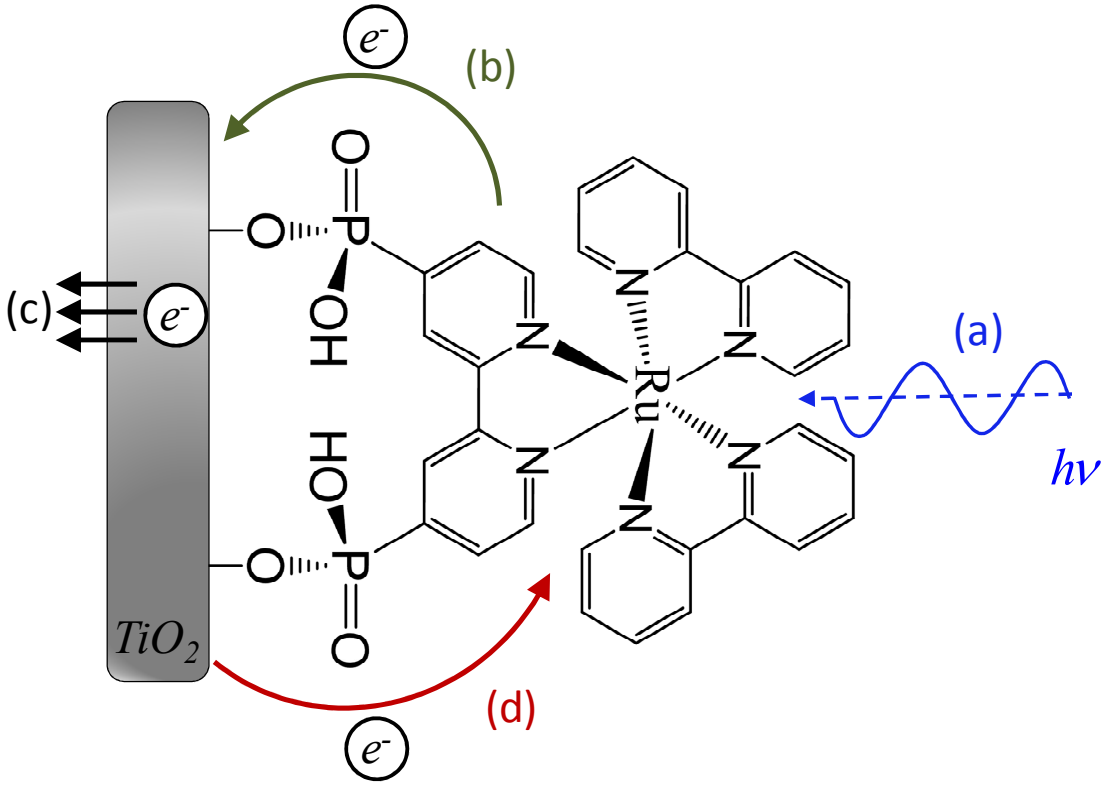

Figure 1.2: A depiction of some of the key processes which occur at the molecule-semiconductor interface. **(a)** Light-absorption occurs when a resonant photon promotes an electron from the ruthenium metal to a bipyridine ligand. This process occurs on the femtosecond timescale. **(b)** The excited electron transfers (injects) into the semiconductor surface in the 10s of femtoseconds to picoseconds after absorption. **(c)** The electron moves from the surface of the semiconductor into the bulk electrode. From there, it can be used by the rest of the cell to do useful work. **(d)** Alternatively, the electron may return to the molecule (back-electron transfer or BET) from the surface of the semiconductor. This process is not useful for harvesting solar energy.

The excited electron transfers (injects) into the semiconductor surface in the 10s of femtoseconds to picoseconds after absorption. This process outcompetes radiative emission processes such as phosphorescence which occurs on the timescale of microseconds.[50,56,57,60] After transferring to the semiconductor surface, the electron moves into the bulk states of the electrode. From there, it can be used by the rest of the cell to do useful work. If the electron becomes trapped in the states of the semiconductor, it may return to the molecule (back-electron transfer or BET). Like fluorescence and phosphorescence, BET is not a desired process for a DSPEC as the electron's energy is lost before it can be converted to useable fuel.[61,62]

1.4. Understanding Interfacial Dynamics with Ultrafast Spectroscopy

The study of ultrafast processes at interfaces requires techniques which can precisely measure the dynamics in these molecule-semiconductor systems. Transient absorption spectroscopy is a valuable technique for determining the kinetics of electron transfer reactions[63-69] by measuring the growth and decay of populations simultaneously. It is a "pump-probe" experiment in which the system is excited ("pumped") by one laser pulse and then the system is measured ("probed") by another pulse at a controlled delay. The probe pulse essentially collects an absorption spectrum of the species. By comparing the absorption spectrum measured at a known delay between the two pulses, the change in absorption spectrum can be calculated. Since the intensity of a spectral feature is proportional to its concentration, transient absorption signals give information about the rate of formation and disappearance of short-lived species as a function of pulse delay. Figure 1.3 shows how these features can be used to extract interfacial dynamics.

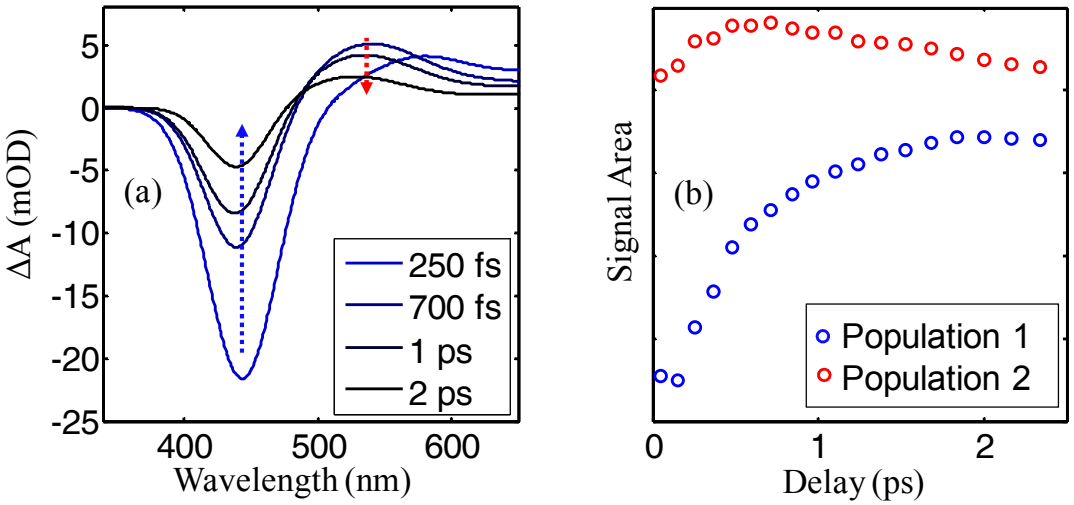

Figure 1.3: Transient absorption spectroscopy signals provide information about the dynamics of short-lived species. **(a)** Transient absorption spectra of catechol on TiO_2 nanoparticles at several delay times show a large negative feature which decays (blue arrow) while another feature grows in before decaying as well (red arrow). The negative feature corresponds to the BET process, while the positive feature reveals nuclear relaxation in the ground state. **(b)** The growth and decay of the associated populations as a function of delay time provides the dynamics of both interfacial processes.

A more a complete picture of the molecular interface requires the use of several specialized experimental techniques providing complementary information. In addition to the dynamics measured with transient absorption spectroscopy, the systems investigated in this dissertation have also been characterized with Resonance Raman spectroscopy. Raman spectroscopy measures the vibrational motion of a molecule, which provides information about nuclear geometry and structure important for modeling ultrafast processes.[70-72] The binding geometry of the ruthenium chromophores to TiO_2 is investigated with polarized Raman spectroscopy in Chapter 5. Figure 1.4 shows various binding geometries for the doubly-

phosphonated ruthenium chromophore. The binding mode of the ruthenium chromophores to the TiO_2 surface is not trivial. The molecule-semiconductor attachment has the potential for wide variation, which affects the dynamics of electron transfer processes. Resonance Raman spectroscopy provides structural information to gain a clearer picture of the interface. The fundamental relationships between the resonance Raman spectrum and the absorption spectrum[73-75] will be used to construct Raman excitation profiles to calculate vibrational reorganization energy of the ruthenium complexes[76] in Chapter 4, and provide important parameters for the electron transfer model developed in Chapter 6.[36]

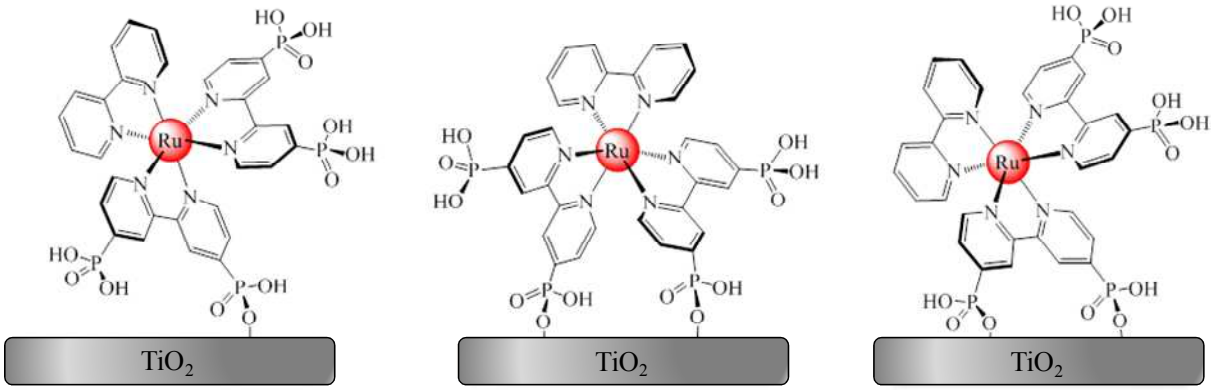

Figure 1.4: Depiction of different binding modalities of RuP on a planar interface.

1.5. Structure of this Dissertation

This chapter has presented the ideas central to the work of this dissertation which utilizes steady-state and ultrafast spectroscopies to elucidate electron transfer processes at the molecule-semiconductor interface by determining and incorporating interfacial structure into an ultrafast electron transfer model. Chapter 2 will explore past and current models used to discuss the

underlying physical and chemical processes in these systems, as well as the foundations of the spectroscopic techniques used to investigate them. The technical aspects of the experiments used in the work are discussed in Chapter 3, which details ultrafast spectroscopy techniques and their application to studying nanoparticle films and solutions.

The first of the experimental studies is found in Chapter 4. Transient absorption spectroscopy is used to measure the electron transfer timescale from the MLCT states of a series of ruthenium chromophores, demonstrating the effect of increasing distance between the molecule and semiconductor on the electronic coupling.[76] Raman spectroscopy is also used to investigate the correlation between vibrational reorganization energy and these injection times. Chapter 5 contains a subsequent study performed to answer questions raised by the investigation in Chapter 4. Specifically, the orientation of the ruthenium chromophore on a TiO_2 crystal is measured using polarized Raman spectroscopy in order to determine the role heterogeneity at the surface may play in the wide range of electron transfer timescales observed.

In Chapter 6, a theoretical model[36] is introduced in order to describe electron injection events which occur before the chromophore has relaxed to its equilibrium geometry, which is outside the realm of the conventional Marcus theory of electron transfer. Such a model is important especially for systems which exhibit the ultrafast electron transfer dynamics desired in a DSPEC. Illustrating the need for such a model, Chapter 7 contains a study of catechol sensitized TiO_2 nanoparticles, which is a strongly coupled system. This charge transfer complex undergoes BET on the picosecond timescale and has been demonstrated to inject into TiO_2 well before nuclear relaxation can occur.[77] Chapter 8 builds on Chapters 6 and 7 with an investigation of a molecular charge transfer system, $[Ti(cat)_3]^{2-}$, which allows for a more detailed approach to the relaxation pathways present in such systems.

1.6. REFERENCES

(1) Hostick, D.; Belzer, D. B.; Hadley, S. W.; Markel, T.; Marnay, C.; Kinter-Meyer, M. "End-Use Electricity Demand," NREL, 2012.

(2) Bragg-Sitton, S. M.; Boardman, R.; Zinaman, O.; Ruth, M.; Forsberg, C. "Rethinking the Future Grid: Integrated Nuclear Renewable Energy Systems," NREL, 2014.

(3) Ladanai, S.; Vinterback, J. "Global Potential of Sustainable Biomass for Energy," Swedish University of Agricultural Sciences, 2009.

(4) Zayas, J.; Derby, M.; Gilman, P.; Anathan, S.; Cotrell, J.; Lantz, E.; Beck, F.; Tusing, R. "Enabling Wind Power Nationwide," U.S. Department of Energy, 2015.

(5) Morton, O. *Nature* **2006**, *443*, 19.

(6) Moore, G. F.; Brudvig, G. W. *Annu. Rev. Condes. Matter Phys.* **2011**, *2*, 303.

(7) Chen, H.-Y.; Hou, J.; Zhang, S.; Liang, Y.; Yang, G.; Yang, Y.; Yu, L.; Wu, Y.; Li, G. *Nat Photon* **2009**, *3*, 649.

(8) Clarke, T. M.; Durrant, J. R. *Chem. Rev.* **2010**, *110*, 6736.

(9) Dennler, G.; Scharber, M. C.; Brabec, C. J. *Adv. Mater.* **2009**, *21*, 1323.

(10) Fujishima, A.; Honda, K. *Nature* **1972**, *238*, 37.

(11) Grätzel, M. *Nature* **2001**, *414*, 338.

(12) Green, M. A. *Sol. Energy* **2004**, *76*, 3.

(13) Green, M. A.; Emery, K.; Hishikawa, Y.; Warta, W.; Dunlop, E. D. *Prog. Photo. Res. Appl.* **2012**, *20*, 12.

(14) Hagfeldt, A.; Boschloo, G.; Sun, L.; Kloo, L.; Pettersson, H. *Chem. Rev.* **2010**, *110*, 6595.

(15) Liang, Y.; Xu, Z.; Xia, J.; Tsai, S.-T.; Wu, Y.; Li, G.; Ray, C.; Yu, L. *Advanced Materials* **2010**, *22*, E135.

(16) Liang, Y.; Yu, L. *Accounts of Chemical Research* **2010**, DOI:10.1021/ar1000296.

(17) Nelson, J. *Curr. Opin. Solid State Mat. Sci.* **2002**, *6*, 87.

(18) O'Regan, B.; Grätzel, M. *Nature* **1991**, *353*, 737.

(19) Park, S. H.; Roy, A.; Beaupre, S.; Cho, S.; Coates, N.; Moon, J. S.; Moses, D.; Leclerc, M.; Lee, K.; Heeger, A. J. *Nature Photonics* **2009**, *3*, 297.

(20) Peter, L. M. *J. Phys. Chem. Lett.* **2011**, *2*, 1861.

(21) Service, R. F. *Science* **2011**, *332*, 293.

(22) Yu, J.; Zheng, Y.; Huang, J. *Polymers* **2014**, *6*, 2473.

(23) Zhou, H.; Yang, L.; Stuart, A. C.; Price, S. C.; Liu, S.; You, W. *Angew. Chemie* **2011**, *50*, 2995.

(24) NREL. Concentrating Solar Power Projects, 2012.

(25) Reiβ, W.; Karg, S.; Dyakonov, V.; Meier, M.; Schwoerer, M. *Lumin.* **1994**, *60-61*, 906.

(26) Tang, C. W. *Appl. Phys. Lett.* **1985**, *48*, 183.

(27) Alstrum-Acevedo, J. H.; Brennaman, M. K.; Meyer, T. J. *Inorg. Chem* **2005**, *44*, 6802.

(28) House, R. L.; Iha, N. Y. M.; Coppo, R. L.; Alibabaei, L.; Sherman, B. D.; Kang, P.; Brennaman, M. K.; Hoertz, P. G.; Meyer, T. J. *J. Photochem. Photobiol. C: Photochem. Rev* **2015**, *25*, 32.

(29) Concepcion, J. J.; Jurss, J. W.; Brennaman, M. K.; Hoertz, P. G.; Patrocinio, A. O. T.; Iha, N. Y. M.; Templeton, J. L.; Meyer, T. J. *Acc. Chem Res.* **2009**, *42*, 1954.

(30) Dismukes, G. C.; Brimblecombe, R.; Felton, G. A. N.; Pryadun, R. S.; Sheats, J. E.; Spiccia, L.; Swiegers, G. F. *Acc. Chem Res.* **2009**, *38*, 25.

(31) McEvoy, J.; Brudvig, G. *Chem. Rev.* **2006**, *106*, 4455.

(32) Swierk, J. R.; Mallouk, T. E. *Chem. Soc. Rev.* **2013**, *42*, 2357.

(33) Youngblood, W. J.; Lee, S.-H. A.; Maeda, K.; Mallouk, T. E. *Acc. Chem Res.* **2009**, *42*, 1966.

(34) Hanson, K.; Brennaman, M. K.; Luo, H.; Glasson, C. R. K.; Concepcion, J. J.; Song, W.; Meyer, T. J. *Appl. Mater. Interfaces* **2012**, *4*, 1462.

(35) Ardo, S.; Meyer, G. J. *Chem. Soc. Rev.* **2009**, *38*, 115.

(36) Li, L.; Giokas, P.; Kanai, Y.; Moran, A. M. *J. Chem. Phys.* **2013**, *140*.

(37) Marcus, R. A. *J. Chem. Phys.* **1965**, *24*, 966.

(38) Molesky, B. P.; Giokas, P. G.; Guo, Z.; Moran, A. M. *J. Chem. Phys.* **2014**, *141*.

(39) Molesky, B. P.; Guo, Z.; Moran, A. M. *J. Chem. Phys.* **2015**, *142*.

(40) Grätzel, M. *J. Photochem. Photobiol. C: Photochem. Rev* **2003**, *4*, 145.

(41) Desilvestro, J.; Gratzel, M. *J. Am. Chem. Soc.* **1985**, *107*, 2990.

(42) Diebold, U. *Surf. Sci. Rep.* **2003**, *48*, 53.

(43) Kung, H. H.; Jarrett, H. S.; Sleight, A. W.; Ferretti, A. *J. Appl. Phys.* **1977**, *48*, 2463.

(44) Xu, Y.; Schoonen, A. A. *American Minerologist* **2000**, *85*, 543.

(45) Serpone, N. *J. Phys. Chem. B* **2006**, *110*, 24287.

(46) Alibabaei, L.; Luo, H.; House, R. L.; Hoertz, P. G.; Lopez, R.; Meyer, T. J. *J. Mater. Chem.* **2013**, *1*, 4133.

(47) Kalyanasundaram, K. *Coord. Chem. Rev* **1982**, *46*, 159.

(48) Balzani, V.; Credi, A.; Venturi, M. *Coord. Chem. Rev* **1998**, *171*.

(49) Robertson, N. *Angew. Chem. Int. Ed* **2006**, *45*, 2338.

(50) Roundhill, D. M. *Photochemistry and Photophysics of Metal Complexes*; Plenum: New York, 1994.

(51) Thompson, D. W.; Ito, A.; Meyer, T. J. *Pure Appl. Chem.* **2013**, *85*, 1257.

(52) Vleck Jr., A.; Busby, M. *Coord. Chem. Rev* **2006**, *250*.

(53) Morris, A. J.; Meyer, G. J.; Fujita, E. *Acc. Chem Res.* **2009**, *42*.

(54) Norris, M. R.; Concepcion, J. J.; Glasson, C. R.; Fang, Z.; Lapides, A. M.; Ashford, D. L.; Templeton, J. L.; Meyer, T. J. *Inorg. Chem* **2013**, *52*, 12492.

(55) Duncan, W.; Prezhdo, O. V. *Annu. Rev. Phys. Chem.* **2007**, *58*, 143.

(56) Bock, C. R.; Meyer, T. J.; Whitten, D. G. *J. Am. Chem. Soc.* **1974**, *96*, 4710.

(57) Demas, J. N.; Harris, E. W.; McBride, R. P. *J. Am. Chem. Soc.* **1977**, *99*, 3547.

(58) Lee, J.-J.; Rahman, M. M.; Sarker, S.; Nath, N. C. D.; Ahammad, A. J. S.; Lee, J. K. **2011**.

(59) Mulazzani, Q. G.; Hoffman, M. Z.; Ford, W. E.; Rodgers, M. A. *J. Phys. Chem.* **1994**, *98*, 1145.

(60) Young, R. C.; Meyer, T. J.; Whitten, D. G. *J. Am. Chem. Soc.* **1976**, *98*, 286.

(61) Knauf, R.; Kalanyan, B.; Parsons, G. N.; Dempsey, J. *J. Phys. Chem. C* **2015**, *119*, 28353.

(62) Wee, K.-R.; Sherman, B. D.; Brennaman, M. K.; Sheridan, M. V.; Nayak, A.; Alibabaei, L.; Meyer, T. J. *J. Mater. Chem. A* **2015**, *4*, 2969.

(63) Berera, R.; van Grondelle, R.; Kennis, J. T. *Photosynth. Res.* **2009**, *101*, 105.

(64) Damrauer, N. H.; Cerullo, G.; Yeh, A.; Boussie, T. R.; Shank, C. V.; McCusker, J. K. *Science* **1997**, *275*, 54.

(65) Ghosh, H. N.; Asbury, J. B.; Lian, T. *J. Phys. Chem. B* **1998**, *102*, 6482.

(66) Henry, W.; Coates, C. G.; Brady, C.; Ronayne, K. L.; Matousek, P.; Towrie, M.; Botchway, S. W.; Parker, A. W.; Vos, J. G.; Browne, W. R.; McGarvey, J. J. *J. Phys. Chem. A* **2008**, 4357.

(67) Iorio, Y. D.; Rodriguez, H. B.; San Roman, E.; Grela, M. A. *J. Phys. Chem. C* **2010**, *113*, 11515.

(68) Kuciauskas, D.; Monat, J. E.; Villahermosa, R.; Gray, H. B.; Lewis, N. S.; McCusker, J. K. *J. Phys. Chem. B* **2002**, *106*, 9347.

(69) Wallin, S.; Davidsson, J.; Modin, J.; Hammarstrom, L. *J. Phys. Chem. A* **2005**, *109*, 4697.

(70) Ambrosio, F.; Martsinovich, N.; Troisi, A. *J. Phys. Chem. C* **2012**, *116*, 2622.

(71) Long, D. A. *The Raman Effect: A Unified Treatment of the Theory of Raman Scattering by Molecules*; Wiley: Chinchester, England, 2002.

(72) Mallick, P. K.; Danzer, G. D.; Strommen, D. P.; Kincaid, J. R. *J. Phys. Chem.* **1988**, *92*, 5628.

(73) Heller, E. *J. Chem. Phys.* **1975**, *62*, 1544.

(74) Myers, A. *Chem. Rev.* **1996**, *96*, 911.

(75) Myers Kelley, A. *J. Phys. Chem. A* **1999**, *103*, 6891.

(76) Giokas, P. G.; Miller, S. A.; Hanson, K.; Norris, M. R.; Glasson, C. R. K.; Concepcion, J. J.; Bettis, S. E.; Meyer, T. J.; Moran, A. M. *J. Phys. Chem. C* **2013**, *117*.

(77) Miller, S. A.; West, B. A.; Curtis, A. C.; Papanikolas, J. M.; Moran, A. M. *J. Chem. Phys.* **2011**, *135*, 081101.

CHAPTER 2: SPECTROSCOPY AND DYNAMICS IN CONDENSED PHASES

2.1. Introduction

Descriptions of condensed phase systems are much more complicated than their gas phase counterparts due to the effect of thermal fluctuations inherent to the relatively dense solvent environment. In other words, a large number of degrees of freedom make the explicit treatment of all coordinates impractical or impossible. As a result, it is often necessary to treat the system and surrounding solvent using reduced descriptions which leverage statistical information about the ensemble (such as line widths) to gain insight into the mechanisms of microscopic processes. [1-3]

In the following sections, theoretical models for condensed phase systems will be introduced in order to provide a context which will be referenced extensively in the subsequent chapters. Specifically, Section 2.2 discusses perturbation theory from the perspective of the density matrix. It will be shown how double-sided Feynman diagrams can be used to communicate information about spectroscopies. In Section 2.3, cumulant expansions and line broadening functions are utilized to describe the effect of fluctuations on spectroscopic observables. Section 2.4 explores the topics of third-order nonlinear spectroscopies such as transient grating and transient absorption before continuing into the nature of spontaneous light emission. That topic is especially relevant to Raman spectroscopy, as well as the next, which is a description of Resonance Raman derived by Eric Heller in the 1970s.[4] Finally, Section 2.5

explores the Marcus picture of electron transfer in donor acceptor systems, which is fundamental to discussion of nearly all of the work which follows.

2.2. Perturbation Theory with a Density Matrix

Nonlinear spectroscopies are most naturally described by following the dynamics in the density operator instead of the wavefunction, because the time-ordering of field-matter interactions is most transparent with this approach. This also applies to any non-radiative process that is higher-order in the sense that the coupling between initial and final states exceeds the regime in which traditional second-order formulas are appropriate.

The density operator is written as the outer-product in the state vector, $\left|\psi(t)\right\rangle$, whose dynamics may be described with the Schrodinger equation. The equation that described the time-evolution of the density operator is found by taking the time-derivative of the outer-product,

$$\frac{\partial\left|\psi(t)\right\rangle\left\langle\psi(t)\right|}{\partial t}=\left|\frac{\partial\psi(t)}{\partial t}\right\rangle\left\langle\psi(t)\right|+\left|\psi(t)\right\rangle\left\langle\frac{\partial\psi(t)}{\partial t}\right| . \tag{2.1}$$

Schrodinger's equation can be used to rewrite this formula as,

$$\frac{\partial\left|\psi(t)\right\rangle\left\langle\psi(t)\right|}{\partial t}=\left(\frac{-iH}{\hbar}\right)\left|\psi(t)\right\rangle\left\langle\psi(t)\right|+\left|\psi(t)\right\rangle\left\langle\psi(t)\right|\left(\frac{iH}{\hbar}\right) , \tag{2.2}$$

or as

$$i\hbar\frac{\partial\rho}{\partial t}=\left[H,\rho\right] , \tag{2.3}$$

using the definition of the commutator and denoting the density operator as ρ. Equation (2.3) is known as the quantum Liouville equation.

We next consider a situation in which a weak external perturbation interacts with the system (e.g., external electric field). The Hamiltonian is partitioned as

$$H = H^{(0)} + \lambda H'(t) \ , \tag{2.4}$$

where $H^{(0)}$ is the zeroeth-order Hamiltonian and $H'(t)$ is a weak perturbation. For convenience, we write the density operator in a basis set, where it becomes a matrix,

$$\rho_{mk}(t) = \langle m|\psi(t)\rangle\langle\psi(t)|k\rangle \ . \tag{2.5}$$

The density matrix is also expanded is orders of the perturbation,

$$\rho_{mk}(t) = \rho_{mk}^{(0)}(t) + \lambda\rho_{mk}^{(1)}(t) + \lambda^2\rho_{mk}^{(2)}(t) + \cdots \tag{2.6}$$

where the order of the density matrix represents the number of times that the system has interacted with the perturbation. Substitution of Equations (2.4) and (2.6) into the quantum Liouville equation yields

$$\rho_{mk}^{(N)}(t) = -\frac{i}{\hbar}\int_0^\infty \langle m|\left[H'(t-t_N), \rho^{(N-1)}(t-t_N)\right]|k\rangle \exp(-i\omega_{mk}t_N)\,dt_N \tag{2.7}$$

Here, N is the order of the perturbation and t_N represents the time-interval between interactions N and N-1. Notably, Equation (2.7) contains N nested commutators (only the highest order commutator is shown explicitly). Observables can be computed in a straightforward way once

the N^{th}-order density operator is in hand. For example, the lowest three orders of the polarization induced by light are given by

$$\begin{aligned} P^{(1)}(t) &= \mathrm{Tr}\left[\mu\rho^{(1)}(\mathrm{t})\right] \\ P^{(2)}(t) &= \mathrm{Tr}\left[\mu\rho^{(2)}(\mathrm{t})\right] . \\ P^{(3)}(t) &= \mathrm{Tr}\left[\mu\rho^{(3)}(\mathrm{t})\right] \end{aligned} \qquad \textbf{(2.8)}$$

The same approach is taken without regard to the order of the polarization. In contrast, the same orders of the polarization are written using the wavefunction as

$$\begin{aligned} P^{(1)}(t) &= \left\langle \psi^{(1)}(t)\middle|\mu\middle|\psi^{(0)}(t)\right\rangle + \left\langle \psi^{(0)}(t)\middle|\mu\middle|\psi^{(1)}(t)\right\rangle \\ P^{(2)}(t) &= \left\langle \psi^{(2)}(t)\middle|\mu\middle|\psi^{(0)}(t)\right\rangle + \left\langle \psi^{(1)}(t)\middle|\mu\middle|\psi^{(1)}(t)\right\rangle + \left\langle \psi^{(0)}(t)\middle|\mu\middle|\psi^{(2)}(t)\right\rangle \\ P^{(3)}(t) &= \left\langle \psi^{(3)}(t)\middle|\mu\middle|\psi^{(0)}(t)\right\rangle + \left\langle \psi^{(2)}(t)\middle|\mu\middle|\psi^{(1)}(t)\right\rangle + \left\langle \psi^{(1)}(t)\middle|\mu\middle|\psi^{(2)}(t)\right\rangle + \left\langle \psi^{(0)}(t)\middle|\mu\middle|\psi^{(3)}(t)\right\rangle \end{aligned} \qquad \textbf{. (2.9)}$$

The simplicity of Equation (2.8) motivates use of the density operator approach instead of the wavefunction when describing nonlinear spectroscopic techniques.

There will always be N classes of terms in $\rho_{mk}^{(N)}(t)$ when the commutators in Equation (2.7) are expanded. For a specific system, this number is multiplied by S^N, where S is the number of states in the system. Fortunately, it is necessary to consider only a small fraction of dominant terms. Negligible terms correspond to off-resonant conditions in a nonlinear spectroscopy. These dominant terms are identified using double-side Feynman diagrams. The following set of rules can be used to quickly write the relevant terms in a nonlinear spectroscopy:

1) The density matrix must begin and end in a population (i.e., a diagonal element).
2) N+1 transition dipole matrix elements must be written. N interactions occurs with the applied field, and 1 interaction corresponds to emission of the signal by the sample.

3) A propagation function must be written for each of the N intervals between field matter interactions (these are damped waves). For example, the simplest propagation function is written as $I_{eg}(t_N) = \theta(t_N)\exp(-i\omega_{eg}t_N - \Gamma_{eg}t_N)$, where $\theta(t_N)$ is a Heaviside step function the enforces causality, ω_{eg} is the frequency association with the energy gap between levels g and e, and Γ_{eg} is damping caused by interaction with an environment.
4) Incoming arrows change the state index such that the energy of the state increases.
5) Outgoing arrows change the state index such that the energy of the state decreases (the last interaction is ALWAYS written outgoing on the left in this thesis).
6) Arrow pointing to right (left) correspond to positive (negative) wavevectors.
7) The sum of the incident wavevectors with appropriate signs yields the wavevector of the signal field.
8) The sign of the term is positive (negative) if we have an even (odd) number of interactions with the bra (i.e. on the right).

We next consider two examples in which the above rules are applied. First, linear absorption by a two-level system with ground state (g) and excited state (e). The Feynman diagram for this linear process is shown in Figure 2.1.

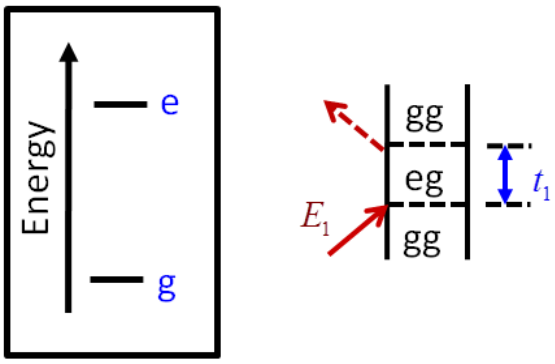

Figure 2.1: Feynman diagram for linear absorption of a two-level system. The electric field E_1 is generally treated as a classical field governed by an envelope function, $E_n(r,t) = \xi_n(t)\left[\exp i(k_n r - \omega_n t) + c.c\right]$ where k_n is the wavevector of field n (see rules 6 and 7 for dealing with Feynman diagrams).

Application of the rules yields the following response function:

$$R(t_1) = \left|\mu_{eg}\right|^2 \theta(t_1) \exp(-i\omega_{eg} t_1 - \Gamma_{eg} t_1) \ . \tag{2.10}$$

The Lorentzian line shape is found by Fourier transformation,

$$\int_0^\infty R(t_1) \exp(i\omega t_1)\, dt_1 = \left|\mu_{eg}\right|^2 \frac{\left(\omega - \omega_{eg} + i\Gamma_{eg}\right)}{\left(\omega - \omega_{eg}\right)^2 + \Gamma_{eg}^2} \ , \tag{2.11}$$

where the real and imaginary parts represent dispersion and absorption. Figure 2.2 presents the example of second-harmonic generation. Again, the rules are applied to produce the response function, $R(t_1, t_2) = \mu_{ba}\mu_{cb}\mu_{ac} \exp\left(-i\omega_{ba} t_1 + i\Gamma_{ba} t_1\right) \exp\left(-i\omega_{ca} t_2 + i\Gamma_{ca} t_2\right)$. It should be noted that

detection of the signal in the direction, $k_s = k_1 + k_2$, defines the resonance condition.[5,6] Fourier transformation yields the hyperpolarizability,

$$\int_0^\infty \int_0^\infty R(t_1, t_2) \exp\left[i\omega_1 t_1 + i(\omega_1 + \omega_2) t_2 \right] dt_1 dt_2 \propto \frac{\mu_{ba}\mu_{cb}\mu_{ac}}{(\omega_1 - \omega_{ba} + i\Gamma_{ba})(\omega_1 + \omega_2 - \omega_{ca} + i\Gamma_{ca})} \quad \textbf{(2.12)}$$

We now see that the signal will only be large when fields 1 and 2 are tuned into the energy gaps between states a and b and c and b, respectively. Other second-order processes such as difference frequency mixing possess alternate response functions.

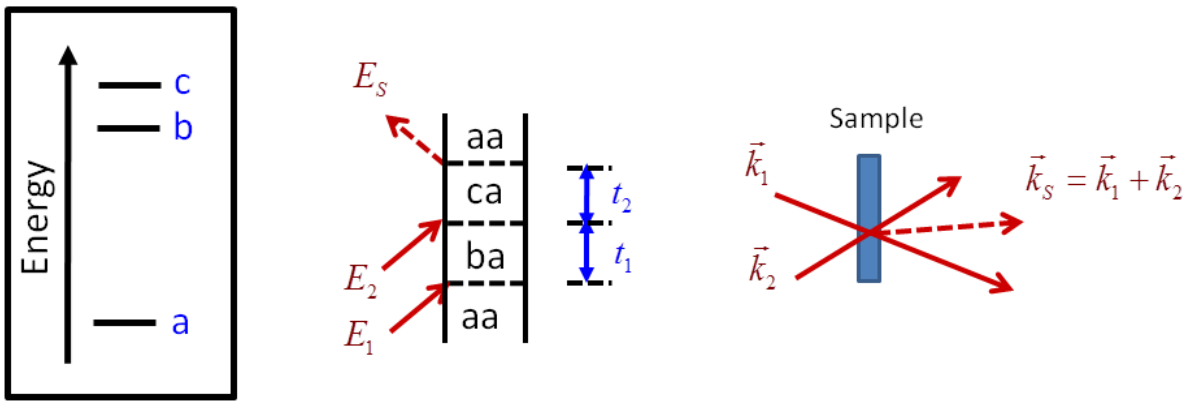

Figure 2.2: Feynman diagram for sum-frequency generation in a three-level system. The experimental beam geometry is shown on the right.

2.3. Cumulant Expansion for Fluctuations with Gaussian Statistics

The condensed-phase systems investigated in this thesis are far too complex to explicitly account for all degrees of freedom. Instead we pick only a handful of degrees of freedom that the

spectroscopic observables are most sensitive to. The explicit degrees of freedom define the system, whereas the remainder of the sample is relegated to a bath.[1-3] In this reduced description, fluctuation of the system's degrees of freedom is the price we pay for partitioning the Hamiltonian. This type of problem is ordinarily handled by letting the system couple to a bath of an extremely large number of harmonic oscillators. Variables governed by a large number of random degrees of freedom are expected to exhibit Gaussian statistics by the central limit theorem. It will be shown in this section how the central limit theorem greatly simplifies the treatment of condensed phases.

Consider a matrix element in the perturbative part of the Hamiltonian for an isolated system which does not undergo fluctuations,

$$\begin{aligned}\langle b|\hat{H}'(t)|a\rangle &= \langle b|\exp(iH_0 t)\,\hat{H}'\exp(-iH_0 t)|a\rangle \\ &= \hat{H}'_{ba}\exp(-i\omega_{ab}t)\end{aligned}, \qquad \textbf{(2.13)}$$

where it is assumed that we have expanded in a basis of eigentstatates of H_0 (i.e., the most natural choice). The matrix element then is the solution to the following equation of motion,

$$\frac{d}{dt}\langle b|\hat{H}'(t)|a\rangle = -i\omega_{ab}\langle b|\hat{H}'(t)|a\rangle. \qquad \textbf{(2.14)}$$

For a two-level system in a condensed phase, we let the frequency undergo thermal fluctuations and rewrite the equation of motion as

$$\frac{d}{dt}\langle b|\hat{H}'(t)|a\rangle = -i\omega_{ab}(t)\langle b|\hat{H}'(t)|a\rangle, \qquad \textbf{(2.15)}$$

where $\omega_{ab}(t)$ represents the sum of the average frequency, $\bar{\omega}_{ab}$, and the stochastic fluctuation, $\delta\omega_{ab}(t)$. Equation (2.15) is solved by integration,

$$\langle b|\hat{H}'(t)|a\rangle = \hat{H}'_{ba}\exp(-i\bar{\omega}_{ab}t)\exp\left[-i\int_0^t dt'\delta\omega_{ab}(t')\right]. \quad \textbf{(2.16)}$$

We next turn our attention towards an ensemble average for the equilibrium system. Integration of the stochastic part of the equation is achieved by conducting a cumulant expansion on the *integrand* and evaluating the averages (this is different that a Taylor expansion of the overall integral). The equilibrium correlation function for the perturbative part of the Hamiltonian is given by

$$\left\langle \hat{H}'_{ba}(t)\hat{H}'_{ba}(0)\right\rangle = \exp(-i\bar{\omega}_{ab}t)\exp\left[-i\int_0^t d\tau_1\left\langle\delta\omega_{ab}(\tau_1)\right\rangle - \frac{1}{2}\int_0^t d\tau_1\int_0^t d\tau_2\left\langle\delta\omega_{ab}(\tau_2)\delta\omega_{ab}(\tau_1)\right\rangle + \cdots\right]. \quad \textbf{(2.17)}$$

The first term is zero when fluctuations are symmetric about the mean (e.g., Gaussian fluctuations). The second term provides information about the time scales and magnitudes of fluctuations. All higher-order terms are zero if the fluctuations have Gaussian statistics.

Practical applications of Equation (2.17) requires choosing a form for the time-correlation function. Kubo's function is most often used for this purpose,

$$\left\langle\delta\omega_{ab}(t)\delta\omega_{ab}(0)\right\rangle = \Delta_{ab}^2\exp(-\Lambda_{ab}t). \quad \textbf{(2.18)}$$

Here, Δ_{ab}^2 is the variance in the fluctuation magnitude and Λ_{ab} is the rate at which a fluctuation relaxes to equilibrium. With this form of the correlation function, the correlation function is rewritten as

$$\left\langle \hat{H}'_{ba}(t)\hat{H}'_{ba}(0)\right\rangle = \left|\hat{H}'_{ba}\right|^2 \exp\left[-i\bar{\omega}_{ab}t - g_{ab}(t)\right], \tag{2.19}$$

where

$$g_{ab}(t) = \frac{\Delta_{ab}^2}{\Lambda_{ab}^2}\left[\exp\left(-\Lambda_{ab}t\right) + \Lambda_{ab}t - 1\right]. \tag{2.20}$$

The standard deviation, Δ_{ab} is usually much larger than Λ_{ab} for electronic energy gaps in solution. In this realistic limit, the absorption line shape of Equation (2.11) becomes Gaussian,

.

$$\left\langle \hat{H}'_{ba}(t)\hat{H}'_{ba}(0)\right\rangle \approx \left|\hat{H}'_{ba}\right|^2 \exp\left[-i\bar{\omega}_{ab}t - \frac{\Delta_{ab}^2}{2}t^2\right], \qquad \Delta_{ab} >> \Lambda_{ab}\,. \tag{2.21}$$

Equation (2.21) can be used to obtain traditional rate formulas for electron and energy transfer in addition to absorption and fluorescence line shapes. These formulas differ in the definition of the perturbative part of the Hamiltonian.

Let's now reconsider absorption of the two-level system in Figure 2.1 when the levels are coupled to a harmonic bath. For radiative processes, the perturbative part of the Hamiltonian is given by $H' = -\vec{\mu}\cdot\vec{E}$. The normalized absorptive line shape becomes

$$\begin{aligned}\sigma_A(\omega) &\propto \mu_{eg}^2 \int_0^\infty \exp\left[-i\bar{\omega}_{eg}t - \frac{\Delta_{eg}^2}{2}t_1^2\right]\exp\left(i\omega t_1\right)dt_1 \\ &\propto \frac{\mu_{eg}^2}{\sqrt{2\pi\Delta_{eg}^2}}\exp\left[-\frac{\left(\omega-\bar{\omega}_{eg}\right)^2}{2\Delta_{eg}^2}\right]\end{aligned}\,. \tag{2.22}$$

The fluctuation-dissipation theorem states that fluctuations at equilibrium are indistinguishable from energy dissipation following a weak perturbation. Invoking this theorem, the fluorescence line shape then is a replica of the absorptive line shape red-shifted (decreased in frequency) by an amount of 2 times the reorganization energy, λ_{eg}. The fluorescence lineshape is given by

$$\sigma_F(\omega) = \frac{\mu_{eg}^2}{\sqrt{2\pi\Delta_{eg}^2}} \exp\left[-\frac{\left(\omega - \bar{\omega}_{eg} - 2\lambda_{eg}\right)^2}{2\Delta_{eg}^2} \right], \tag{2.23}$$

where

$$\lambda_{eg} = \frac{\Delta_{eg}^2}{2k_B T}. \tag{2.24}$$

This stochastic approach yields an interesting and perhaps non-intuitive insight. Namely, absorbance and fluorescence line shapes are fully determined by thermal fluctuations which take place without the applied field present.

2.4. Third-Order Nonlinearities

2.4.A. Transient Absorption Spectroscopy

As the progression is made from 1st to 3rd order in perturbation theory, the advantage of the diagrammatic approach become more apparent. Let us consider the three-level system (e.g., Figure 2.2). Of the 216 combinations from the action of 3 applied electric fields, only 6 remain after accounting for phase matching and a defined order in which the fields arrive at the sample (the pump interacts before the probe). These 6 terms in the time domain[7] can be represented in

the frequency domain as well which is intuitive especially when dispersed detection is employed, which effectively Fourier transforms the signal. The signal components in a third-order nonlinearity are described by

$$
\begin{aligned}
S_{ESE}\left(\omega_{pu},\omega_{pr}\right) &= \left|\vec{\mu}_{ba}\right|^4 \operatorname{Im}\left\{\frac{i}{\hbar^3} I_{ba}\left(\omega_{pr}\right)\left[I_{ba}\left(-\omega_{pu}\right)+I_{ba}\left(\omega_{pu}\right)\right]\right\} \\
S_{GSB}\left(\omega_{pu},\omega_{pr}\right) &= \left|\vec{\mu}_{ba}\right|^4 \operatorname{Im}\left\{\frac{i}{\hbar^3} I_{ba}\left(\omega_{pr}\right)\left[I_{ba}\left(-\omega_{pu}\right)+I_{ab}\left(\omega_{pu}\right)\right]\right\} \\
S_{ESA}\left(\omega_{pu},\omega_{pr}\right) &= \left|\vec{\mu}_{ba}\right|^2\left|\vec{\mu}_{cb}\right|^2 \operatorname{Im}\left\{\frac{i}{\hbar^3} I_{cb}\left(\omega_{pr}\right)\left[I_{ba}\left(-\omega_{pu}\right)+I_{ba}\left(\omega_{pu}\right)\right]\right\}
\end{aligned}
\quad , \qquad \textbf{(2.25)}
$$

where $\vec{\mu}_{ba}$ is the dipole for a transition from a to b, Γ_{ab} is the line width, ω_{pu} (ω_{pr}) is the frequency of the pump (probe), and the line shape functions are given by

$$
I_{ab}\left(\omega\right) = -i\int_0^\infty I_{ab}\left(t\right)\exp\left(i\omega t\right)dt = \left(\frac{1}{\omega-\omega_{ab}+i\Gamma_{ab}}\right) . \qquad \textbf{(2.26)}
$$

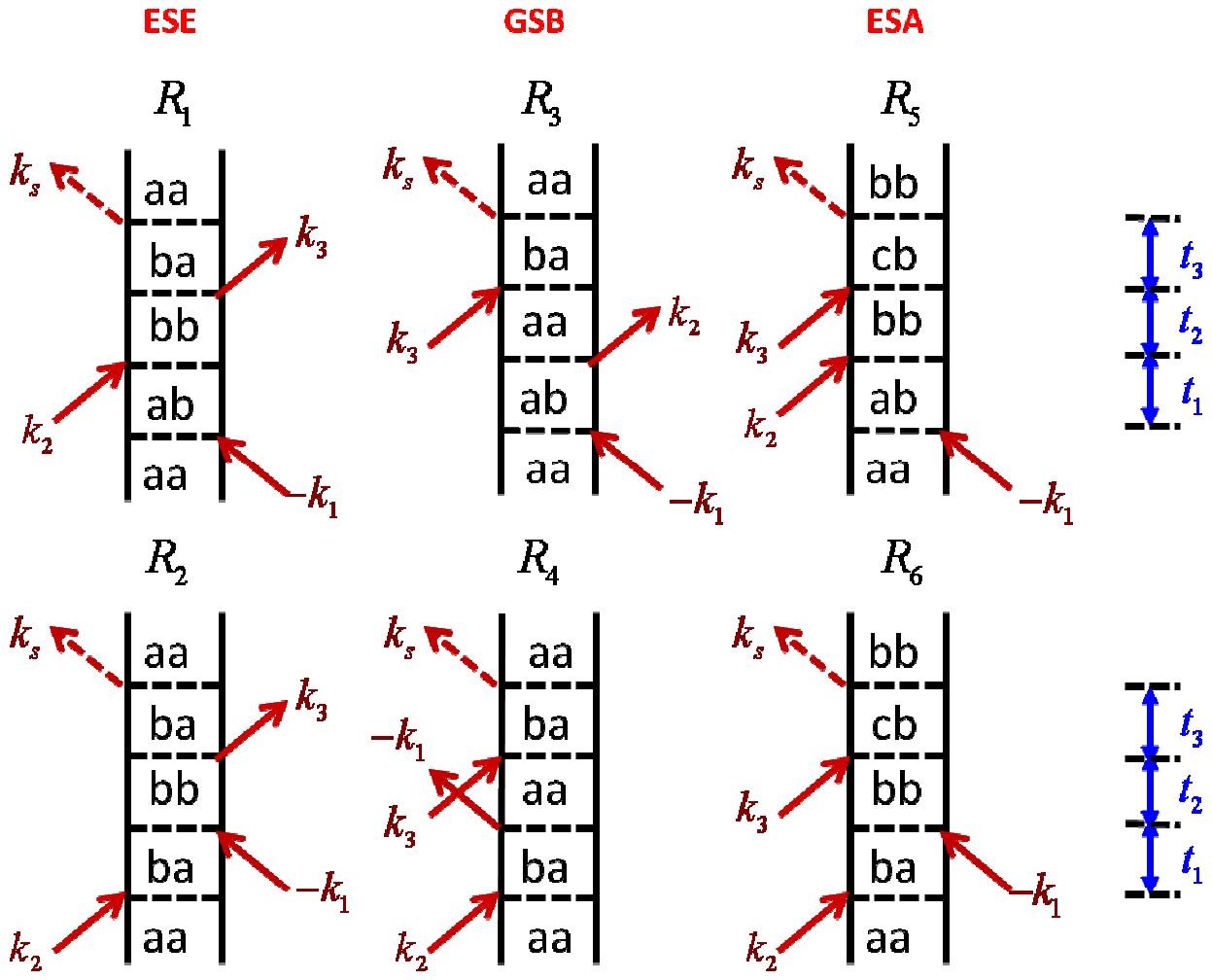

Figure 2.3: Feynman diagrams for a three level system where $E_a < E_b < E_c$. Time intervals t_1, t_2, and t_3 represent the time between interactions with the electric fields. The response function can be generated from each diagram and these can be summed and used to compute the polarization in the sample. GSB, ESE, and ESA notation relates to signals generated in third order spectroscopic experiments discussed in Chapter 3.

The auxillary functions which depend on ω_{t_3} are related to the probe interaction, and each of the terms depending on ω_{pu} depend on the pump. While even these terms can become tedious, the same information is communicated clearly with 6 double-sided Feynman diagrams, shown in Figure 2.3. Each component of S shown in Equation (2.25) corresponds to two of the diagrams shown. The Feynman diagrams depicted in Figure 2.3 are relevant to both Transient Absorption and Transient Grating spectroscopies, which are discussed in Chapter 3. Transient grating techniques probe exactly the same terms in the response function but are sensitive to both absorptive and dispersive signal components.

2.4.B. Spontaneous Raman Scattering

Raman scattering encompasses a number of related phenomena more specifically categorized as either spontaneous or stimulated, and resonant or non-resonant. Resonance Raman scattering will be addressed in Section 2.4.C, in this section the focus will primarily be on spontaneous, non-resonant Raman scattering. The process can be described in several ways depending on the physical behavior of interest. It is necessary to begin by discussing spontaneous emission. Unlike previously discussed situations where the applied field is strong and is therefore treated classically, when the field is weak it is treated quantum mechanically.[8,9] In this approach, the radiation field is considered to be confined to a three dimensional box of volume V. This leads to a quantized, monochromatic field of frequency ω_s,

$$E(t) = E_s \exp(-i\omega_s t) + E_s^* \exp(i\omega_s t) \text{ ,} \qquad \textbf{(2.27)}$$

where $E_s = i\left(2\pi\hbar\omega_s / V\right)^{1/2} a_s$, $E_S^* = -i\left(2\pi\hbar\omega_s / V\right)^{1/2} a_s^\dagger$, and $a_s^\dagger$ (a_s) is a creation (annihilation) operator for photons. The use of creation and annihilation operators follows from the form of the radiation field as a set of independent oscillators. More specifically, the state $\left|n_{k\alpha} m_{k'\alpha'}\right\rangle$ is defined as having n (m) photons with wavevector k (k') and polarization α (α') such that the creation annihilation and operator acts on the state to give $a_{k\alpha}^\dagger \left|n_{k\alpha}\right\rangle = \sqrt{n_{k\alpha}+1}\left|\left(n+1\right)_{k\alpha}\right\rangle$ and $a_{k\alpha}\left|n_{k\alpha}\right\rangle = \sqrt{n_{k\alpha}}\left|\left(n-1\right)_{k\alpha}\right\rangle$, respectively. Additionally, these operators can be used in tandem to form the population operator, $N_{k\alpha}\left|n_{k\alpha} n_{k'\alpha'}\cdots\right\rangle = a_{k\alpha}^\dagger a_{k\alpha}\left|n_{k\alpha} n_{k'\alpha'}\cdots\right\rangle = n_{k\alpha}\left|n_{k\alpha} n_{k'\alpha'}\cdots\right\rangle$, which acts to give the number of photons in a particular mode. The initial density operator for the material and field is given by

$$\rho_{total}\left(-\infty\right) = \left|g\right\rangle\left\langle g\right|\left|n_s\right\rangle\left\langle n_s\right| = \left|n_s\right\rangle\left\langle n_s\right|\left|g\right\rangle\left\langle g\right| . \qquad \textbf{(2.28)}$$

In order to obtain the steady-state rate of change in the number of photons, we must solve an equation similar to the quantum Liouville equation for the density operator,

$$\mathbb{N}_s = \frac{d}{dt} a_s^\dagger a_s = \frac{i}{\hbar}\left[H^{(1)}\left(t\right), a_s^\dagger a_s\right] , \qquad \textbf{(2.29)}$$

where $H^{(1)}\left(t\right) = \vec{V}\cdot\vec{E}\left(t\right)$. Evaluation of the commutator in Equation 2.29 results[10] in

$$\mathbb{N}_s = a_s^\dagger a_s E_S^* \vec{V} \exp\left(i\omega_S t\right) . \qquad \textbf{(2.30)}$$

In order to determine a response function for the light emission process, it is important to remember the rules outlined in Section 2.2. Specifically, since the field must begin and end in a population and not a coherence, only terms which contain one interaction each with E_s and its conjugate are valid for the linear process. Also, by convention, only terms with the final

interaction on the bra side are considered. The response term of interest therefore is the same double-sided Feynman diagram depicted in Figure 2.1, which corresponds to the response function term,

$$R_1(t_1) = \sum_g P(g)\mu_{eg}\mu_{ge}\exp(-i\omega_{eg}t_1) \ , \tag{2.31}$$

which is proportional to the polarization,

$$\begin{aligned}
&P^{(1)}(t) = \mathrm{Tr}\left[\mathbb{N}_s \rho_{total}^{(1)}(t)\right] \\
&\propto \int_0^\infty dt_1 \mathrm{Tr}\left[a_s^\dagger a_s E_s^* V_{ge}\exp\left(\frac{-i}{\hbar}H^{(0)}t_1\right)E_s V_{eg}\rho_{gg}^{(0)}(-\infty)\rho_s(-\infty)\exp(-i\omega_s t_1)\exp\left(\frac{i}{\hbar}H^{(0)}t_1\right)\right] \\
&\propto \int_0^\infty dt_1 \mathrm{Tr}\left[a_s^\dagger a_s E_s^* E_s \rho_s(-\infty) V_{ge}\exp\left(\frac{-i}{\hbar}H^{(0)}t_1\right)V_{eg}\rho_{gg}^{(0)}(-\infty)\exp(-i\omega_s t_1)\exp\left(\frac{i}{\hbar}H^{(0)}t_1\right)\right] \\
&\propto \int_0^\infty dt_1 \mathrm{Tr}\left[\frac{2\pi\hbar\omega_s}{V} a_s^\dagger a_s a_s^\dagger a_s \rho_s(-\infty) V_{ge}\exp\left(\frac{-i}{\hbar}H^{(0)}t_1\right)V_{eg}\rho_{gg}^{(0)}(-\infty)\exp(-i\omega_s t_1)\exp\left(\frac{i}{\hbar}H^{(0)}t_1\right)\right] \\
&\propto \int_0^\infty dt_1 \mathrm{Tr}\left[a_s^\dagger a_s a_s^\dagger a_s |n_s\rangle\langle n_s| V_{ge}\exp\left(\frac{-i}{\hbar}H^{(0)}t_1\right)V_{eg}\rho_{gg}^{(0)}(-\infty)\exp(-i\omega_s t_1)\exp\left(\frac{i}{\hbar}H^{(0)}t_1\right)\right] \\
&\propto \int_0^\infty dt_1 \mathrm{Tr}\left[a_s^\dagger a_s a_s^\dagger |(n-1)_s\rangle\langle n_s| V_{ge}\exp\left(\frac{-i}{\hbar}H^{(0)}t_1\right)V_{eg}\rho_{gg}^{(0)}(-\infty)\exp(-i\omega_s t_1)\exp\left(\frac{i}{\hbar}H^{(0)}t_1\right)\right] \\
&\propto \int_0^\infty dt_1 \mathrm{Tr}\left[a_s^\dagger |(n-1)_s\rangle\langle n_s| V_{ge}\exp\left(\frac{-i}{\hbar}H^{(0)}t_1\right)V_{eg}\rho_{gg}^{(0)}(-\infty)\exp(-i\omega_s t_1)\exp\left(\frac{i}{\hbar}H^{(0)}t_1\right)\right] \\
&\propto \int_0^\infty dt_1 \mathrm{Tr}\left[|n_s\rangle\langle n_s| V_{ge}\exp\left(\frac{-i}{\hbar}H^{(0)}t_1\right)V_{eg}\rho_{gg}^{(0)}(-\infty)\exp(-i\omega_s t_1)\exp\left(\frac{i}{\hbar}H^{(0)}t_1\right)\right]
\end{aligned} \tag{2.32}$$

Note that Equation (2.32) has been obtained by taking advantage of the fact that material and field operators commute and constants pertaining to the dimensions of the three-dimensional box have been excluded. Also, note that at negative infinity,

$$a_s^\dagger a_s a_s^\dagger a_s \rho_s(-\infty) = a_s^\dagger a_s a_s^\dagger a_s |n_s\rangle\langle n_s| \propto a_s^\dagger a_s a_s^\dagger |(n-1)_s\rangle\langle n_s| \propto a_s^\dagger |(n-1)_s\rangle\langle n_s| = |n_s\rangle\langle n_s| , \tag{2.33}$$

which has also been used in Equation (2.32) above. Tracing over the states of the radiation field then shows that

$$
\begin{aligned}
&P^{(1)}(t) \propto \int_0^\infty dt_1 \sum_j \langle n_j | n_s \rangle \langle n_s | n_j \rangle \cdot \\
&\mathrm{Tr}_{\text{material}} \left[V_{ge} \exp\left(\frac{-i}{\hbar} H^{(0)} t_1 \right) V_{eg} \rho_{gg}^{(0)}(-\infty) \exp(-i\omega_s t_1) \exp\left(\frac{-i}{\hbar} H^{(0)} t_1 \right) \right] \\
&\propto \int_0^\infty dt_1 \sum_j \delta_{js} \delta_{sj} \mathrm{Tr}_{\text{material}} \left[V_{ge} \exp\left(\frac{-i}{\hbar} H^{(0)} t_1 \right) V_{eg} \rho_{gg}^{(0)}(-\infty) \exp(-i\omega_j t_1) \exp\left(\frac{-i}{\hbar} H^{(0)} t_1 \right) \right] \\
&\propto \int_0^\infty dt_1 \mathrm{Tr}_{\text{material}} \left[V_{ge} \exp\left(\frac{-i}{\hbar} H^{(0)} t_1 \right) V_{eg} \rho_{gg}^{(0)}(-\infty) \exp(-i\omega_j t_1) \exp\left(\frac{-i}{\hbar} H^{(0)} t_1 \right) \right] \\
&\propto \int_0^\infty dt_1 \mathrm{Tr}_{\text{material}} \left[\mu_{ge} |g\rangle\langle e| \exp\left(\frac{-i}{\hbar} H^{(0)} t_1 \right) \mu_{\text{eg}} |e\rangle\langle g| |g\rangle\langle g| \exp(-i\omega_j t_1) \exp\left(\frac{-i}{\hbar} H^{(0)} t_1 \right) \right] \\
&\propto |\mu_{\text{eg}}|^2 \int_0^\infty dt_1 \mathrm{Tr}_{\text{material}} \left[|g\rangle\langle e| \exp\left(\frac{-i}{\hbar} H^{(0)} t_1 \right) |e\rangle\langle g| \exp(-i\omega_j t_1) \exp\left(\frac{-i}{\hbar} H^{(0)} t_1 \right) \right] \\
&\propto |\mu_{\text{eg}}|^2 \int_0^\infty dt_1 \mathrm{Tr}_{\text{material}} \left[|g\rangle\langle g| \exp\left(\frac{-i}{\cancel{\hbar}} \omega_{eg} t_1 \right) \exp(-i\omega_j t_1) \exp\left(\frac{-i}{\hbar} H^{(0)} t_1 \right) \right] \\
&\propto |\mu_{\text{eg}}|^2 \int_0^\infty dt_1 \exp\left(-i\omega_j t_1 - i\omega_{eg} t_1 - \Gamma_{eg} t_1 \right)
\end{aligned}
\qquad \textbf{.(2.34)}
$$

Moving from the linear (first order) to third order nonlinear case of light emission relevant to Raman scattering requires the presence of an incident radiation field. If the total electric field is taken to be the sum of incident and spontaneous fields, following the form of Equation (2.27) gives

$$E(t) = \left[E_L(t) \exp(-i\omega_L t) + E_L^*(t) \exp(i\omega_L t) \right] + \left[E_S \exp(-i\omega_S t) + E_S^* \exp(i\omega_S t) \right]. \quad \textbf{(2.35)}$$

Due to the strength of E_L as compared to E_S, the former can be treated classically, while the latter matches its earlier form. It is also important to note that initially (t = -∞) the density of the

quantum field is zero for the frequency of interest (i.e. it has no photons). Using a similar strategy as shown in Equations (2.29) and (2.30), the trace of the operator in third order is

$$\begin{aligned}\mathrm{Tr}\left[\mathbb{N}_s\rho_{total}^{(3)}(t)\right]=\frac{1}{\hbar^4}\int_0^\infty dt_3\int_0^\infty dt_2\int_0^\infty dt_1\mathrm{Tr}\left[a_s^\dagger a_s\mathcal{L}_{int}(t)\mathcal{G}(t_3)\mathcal{L}_{int}(t-t_3)\right.\\ \left.\mathcal{G}(t_2)\mathcal{L}_{int}(t-t_3-t_2)\mathcal{G}(t_1)\mathcal{L}_{int}(t-t_3-t_2-t_1)\rho_{total}^{(0)}(-\infty)\right]\end{aligned}, \quad \textbf{(2.36)}$$

where the density operator has been expanded to third order. In Equation (2.36), the Greens function, $\mathcal{G}(t)A=\theta(t)\exp\left(\frac{-i}{\hbar}H^{(0)}t\right)A\exp\left(\frac{i}{\hbar}H^{(0)}t\right)=A(t)$, has been included. $\mathcal{G}(t)$ is known as a superoperator because rather than operating on a wavefunction, it operates on other operators, which is useful as the response functions increase in number and complexity. $\theta(t)$ is merely a step function which imposes causality by being 0 if $t<0$ or 1 otherwise. In addition to the Green's function, $\mathcal{L}_{int}(t)A=\left[H^{(1)}(t),A\right]$ has also been included. While the operation is challenging, it is helpful at this point to define a set of selection rules based on what has been assumed up to this point. Specifically:

1) Since the system must end in a population, two (and only two) of the four interactions must occur with E_L.
2) Of the two interactions with E_L, one must act on the left side, and one must act on the right. The same is true for E_S.
3) Since E_L is the only field with photons of ω_s initially, it must have the first interaction with the material.
4) Since the desired emission signal is in E_S, the radiated field (the last interaction) also must be with E_S.

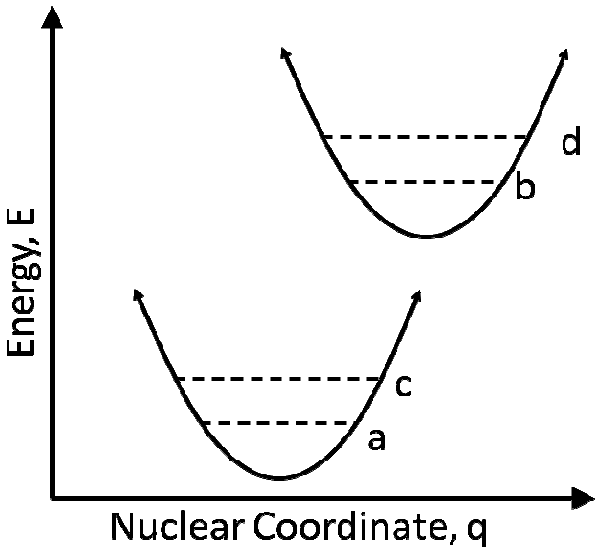

Figure 2.4: Two-state example system for the investigation of spontaneous light emission. Each of the two potential energy surfaces has two indexed vibrational states (a,c and b,d, respectively). The quadratic surfaces exist in a quantized space of nuclear coordinates.

In Figure 2.4, the system is defined as possessing two electronic states, where two-vibrational levels have been designated with dummy indices for reference. Utilizing the double-sided Feynman diagrams outlined earlier, there are 8 terms in the response function which are possible. However, only 4 of the terms are shown as the other 4 represent simple complex conjugates of these 4. After generating the terms (see Figure 2.5a), application of the selection rules defined previously excludes the R_4 term (it violates rule 2). Assignment of the interactions to specific electric fields is accomplished by applying the other 3 selection rules (see Figure 2.5b). Specifically, by rule 1, the first (lowest) interaction must always be with E_L. Likewise, by rule 4 the final (highest) interaction must be with E_S. Rule 3 dictates that the first interaction with E_S must be radiative (since we have defined no initial density in the field which could add energy to the system) and rule 2 allows assignment of the remaining interaction.

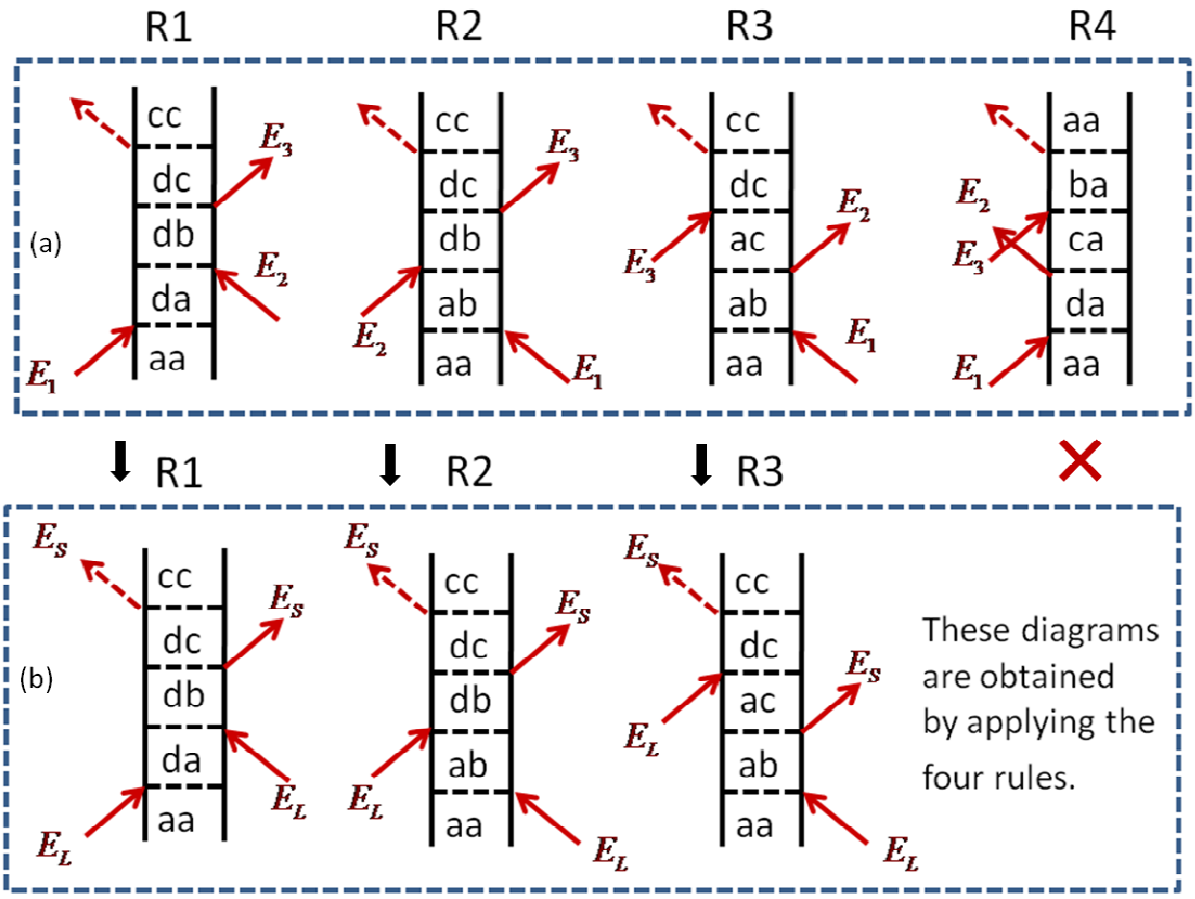

Figure 2.5: Spontaneous emission Feynman diagrams. a) Feynman diagrams for spontaneous emission in the presence of an applied field for the system (shown in Figure 2.4). The complex conjugates of the 4 pictured terms are not shown. **b)** Applying the selection rules in Section 2.4.B results in the exclusion of the rightmost term in **(a)** and allows assignment of the particular electric fields interacting at each time.

Mukamel has shown that two types of terms emerge when the response functions are Fourier transformed,[1]

$$
\begin{aligned}
&S_{SLE}\left(\omega_L,\omega_s,t\right)=S_{Fl}\left(\omega_L,\omega_s,t\right)+S_{Raman}\left(\omega_L,\omega_s,t\right)\\
&=2\,\mathrm{Re}\sum_{a,c}P(a)\mu_{ab}\mu_{bc}\mu_{cd}\mu_{da}\left\{I_{ab}\left(-\omega_{\mathrm{L}}\right)I_{da}\left(\omega_{\mathrm{L}}\right)\left[I_{cb}\left(-\omega_{\mathrm{s}}\right)+I_{dc}\left(\omega_{\mathrm{s}}\right)\right]\frac{2i\hat{\Gamma}}{\omega_{bd}+i\gamma}\right\}, \qquad \textbf{(2.37)}\\
&-4\pi i\,\mathrm{Re}\sum_{a,c}P(a)\mu_{ab}\mu_{bc}\mu_{cd}\mu_{da}\delta\left(\omega_{ca}+\omega_s-\omega_L\right)I_{ab}\left(-\omega_{\mathrm{L}}\right)I_{da}\left(\omega_{\mathrm{L}}\right)
\end{aligned}
$$

where the line shape functions are given by,

$$
I_{ab}\left(\omega\right)=\frac{1}{\omega-\omega_{ab}+i\Gamma_{ab}}\ , \qquad \textbf{(2.38)}
$$

The first two terms on the right side of the equation yield broad emission spectra and correspond to fluorescence. The third term possess narrow lines (i.e., vibrational resonances) and is associated with the spontaneous resonance Raman response.

2.4.C. Heller's Approach for Spontaneous Resonance Raman Scattering

In Chapter 4, we employ a well-established model for analyzing resonance Raman intensities.[11,12] The principal motivation for this approach is that the Franck-Condon progressions associated with intramolecular modes of a chromophore are hidden by broad absorbance line widths in solution.[1] Resonance Raman measurements provide information about the forces exerted on particular intramolecular modes following photoexcitation despite such broad line widths. Iterative fitting of both the linear absorbance spectrum and the Raman cross sections is leveraged in the model to obtain the displacement for each intramolecular mode, the electronic origin of the transition (0-0 transition), the solvent reorganization energy, and the relative contributions of homogeneous and inhomogeneous line broadening mechanisms.

The linear absorbance line shape is simulated using

$$\sigma_A(\omega) = \frac{4\pi\omega\mu_0^2}{3\hbar c}\sum_{m=1} P_m \,\mathrm{Re}\int_{-\infty}^{\infty} d\delta G(\delta)\int_0^{\infty} dt \langle m|m(t)\rangle \exp\left[i(\omega-\omega_0-\delta+\omega_m)t-g(t)\right], \quad \textbf{(2.39)}$$

where m is an index for a nuclear mode, P_m is the Boltzmann population of the initial state, μ_0 is the electronic transition dipole, ω_m is the mode frequency, ω_0 is the purely electronic transition frequency, and $\langle m|m(t)\rangle$ is a dynamic overlap integral between nuclear wavefunctions (whose Fourier transform is a Franck-Condon progression).[13]

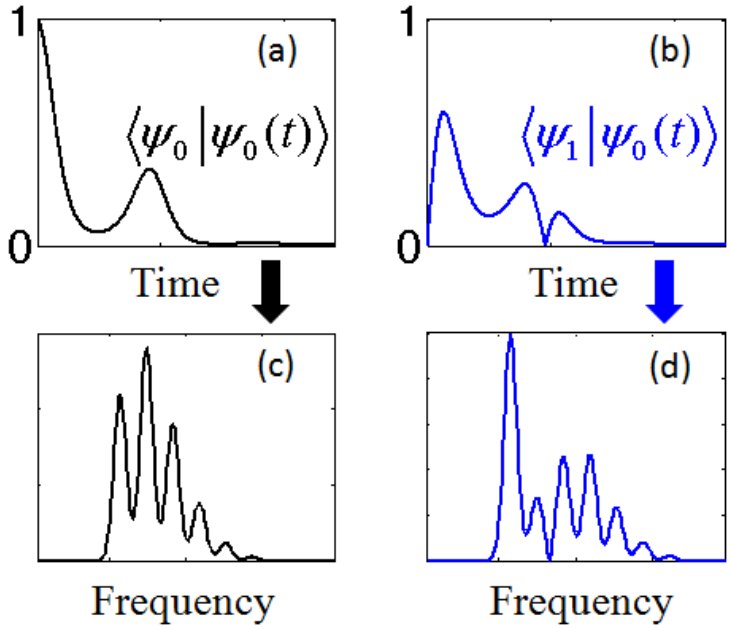

Figure 2.6: Example wavepacket overlap. The overlap of the wave packet electronically excited to vibrational index 0 with the ground state vibrational indices 0 **(a)** and 1 **(b)** for an example system. The Fourier transform of **(a)** gives **(c)**, the absorption spectrum, while the square of the half-Fourier transform of **(b)** gives **(d)**, the Raman profile. In other words, the Raman profile and absorption spectrum are closely related, as can be seen by inspection of Equations (2.39) and (2.42).

The key parameters governing $\langle m|m(t)\rangle$ are the dimensionless displacements between the ground and excited state (harmonic) potentials, d_m; the displacements are converted to intramolecular mode-specific reorganization energies using $\lambda_m = \hbar\omega_m d_m^2/2$. Fluctuations in the resonance frequency induced by thermal motion in the solvent are partitioned into fast (homogeneous) and slow (inhomogeneous) components. Inhomogeneous line broadening is incorporated by integrating over the static Gaussian distribution, $G(\delta)$. The homogeneous line shape is simulated with the line broadening function

$$g(t) = \left(\frac{2\lambda k_B T}{\Lambda^2} - i\frac{\lambda}{\Lambda}\right)\left[\exp(-\Lambda t) + \Lambda t - 1\right], \tag{2.40}$$

where λ is the reorganization energy for the homogeneous bath coordinate and Λ^{-1} is the characteristic time scale for thermal motion. The resonance Raman response depends on the same parameters governing $\sigma_A(\omega)$. The differential resonance Raman cross section is written as

$$\sigma_{R,mn}(\omega) = \frac{4\omega_S^3\omega_L}{15c^4}\sum_{mn} P_m \int d\omega_S \int_{-\infty}^{\infty} d\delta G(\delta) L_{mn}(\omega_L - \omega_S)\left|\alpha_{mn}(\omega_L,\delta)\right|^2, \tag{2.41}$$

where m (n) is an index for the initial (final) vibrational state, ω_L (ω_S) is the incident (scattered) light frequency, and $L_{mn}(\omega_L - \omega_S)$ is the normalized line shape of the $m \to n$ ground state vibrational transition. The integral with respect to ω_S extends over the full Raman emission band. The Raman polarizability is given by

$$\alpha_{mn}(\omega_L,\delta) = \frac{\mu_0^2}{\hbar}\int_0^{\infty} dt \langle n|m(t)\rangle \exp\left[i(\omega_L - \omega_0 - \delta + \omega_m)t - g(t)\right]. \tag{2.42}$$

The resemblance between $\alpha_{mn}(\omega_L, \delta)$ and $\sigma_A(\omega)$ makes clear the origin of the resonance enhancement. The cancellation between the laser frequency, ω_L, and the electronic (vibronic) resonance frequency, $\omega_0 + \delta - \omega_m$, enhances the magnitude of $\alpha_{mn}(\omega_L, \delta)$ by keeping the sign of the integrand from oscillating.

2.5. Marcus Theory

Rudolph Marcus's theory of electron transfer has been critical to the study of electron transfer reactions in condensed phases over the last several decades. [14] It is of course therefore central to an understanding of the work presented here. A simple system described by Marcus theory can be formulated as a bimolecular system containing and electron donor, D, and an electron acceptor, A, such that the electron transfer reaction is written as

$$D + A \rightarrow D^+ + A^- \ , \tag{2.43}$$

where D has transferred an electron to A, resulting in an oxidized donor and a reduced acceptor species. Since this theory relates to condensed phase systems, D and A are not necessarily isolated. That is, self-exchange reactions can also occur such as

$$D + D^+ \rightarrow D^+ + D, A^- + A \rightarrow A + A^- \ , \tag{2.44}$$

which is isoergonic with respect to the molecules themselves.[15] The reaction between the donor and acceptor takes place along a single *collective* nuclear coordinate, *q*. The nuclear coordinate is defined such that it contains all degrees of freedom with respect to nuclear motion, including both "inner-sphere" (i.e intramolecular vibrations of covalently bound ligands) and "outer-sphere" (i.e. unbound solvent molecules) contributions.[14,16] The central limit theorem can be

applied in this reduced description, where we are assuming that the energy levels are modulated by a large number of random degrees of freedom (this is also why the surfaces are parabolas).[2,17] The states belonging to the donor and acceptor molecules can therefore be described within the parameter space of the collective nuclear coordinate. Specifically, the states lie on parabolic free energy surfaces in this so-called "*q*-space." It is important to note that in the formulation of these surfaces the Born-Oppenheimer approximation is made (nuclear motion is ignored with respect to electronic motion). Because the surfaces denote the free energy of the system, areas of overlap between surfaces allow for population transfer between those surfaces, since at those coordinates the donor and acceptor are degenerate (see Figure 2.7).

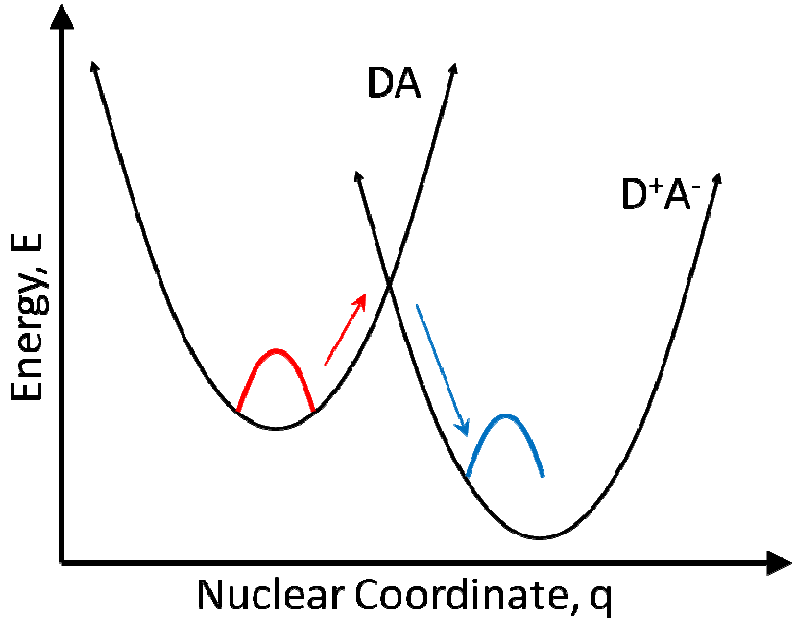

Figure 2.7: Free energy surfaces for a bimolecular donor-acceptor system. If the population initially at equilibrium in the minimum of the DA surface is excited (red) to the intersection, the electron transfers from the donor to the acceptor surface, which subsequently relaxes (blue) along the surface to the most stable nuclear configuration of the oxidized donor (D^+) and reduced acceptor (A^-) state.

The potential energy diagram shown in Figure 1 contains important information about the system. First and foremost, the distance between the potential energy minima in q relates to the reorganization energy of the system. The reorganization energy, λ, has two main contributors similar to the nuclear coordinate, namely the intramolecular reorganization energy (λ_{in}) and the solvent reorganization energy (λ_{out}).[15] These energies are cumulative such that

$$\lambda_{total} = \lambda_{in} + \lambda_{out} \ . \tag{2.45}$$

Specifically, Marcus has treated the inner reorganization energy by considering the first solvation shell as a harmonic oscillator[15] and obtaining

$$\lambda_{in} = \sum_j \frac{f_j^r f_j^p}{f_j^r + f_j^p}(q_j^r - q_j^p)^2 \ , \tag{2.46}$$

where f is the j^{th} ion-solvent bond, q is the equilibrium nuclear coordinate, and r and p correspond to the reactant and product states, respectively. The intramolecular reorganization energy therefore arises from motion in the inner ligand bonds relative to the equilibrium positions. In contrast, the solvent reorganization energy arises from the polarization of solvent molecules in response to the electron transfer. Marcus and Levich[14,18] have derived the solvent reorganization in detail by treating the solvent molecules as a continuum. The polarization is separated into a fast and slow component with an energy associated with each. Because electron transfer is concerned primarily with the energy of the slow reorganization of solvent molecules, for a spherical molecules[18,19] the resulting energy is derived to be

$$\lambda_{out} = \frac{(\Delta e)^2}{4\pi\varepsilon_0}\left[\frac{1}{2r_D} + \frac{1}{2r_A} - \frac{1}{2r_{DA}}\right]\left(\frac{1}{n^2} - \frac{1}{\varepsilon_s}\right) \ , \tag{2.47}$$

where r is the radii of the donor (D), acceptor (A), and between them (DA) and ε_0 is the permittivity of free space. The relation between the free energy change of electron transfer and the reorganization energy significantly effects the electron transfer diagram (see Figure 2.8).

Assuming that population is initially localized in the DA state, at equilibrium it will exist in the minimum of the potential energy surface. Perturbations such as those from solvent fluctuations result in rearrangement of nuclei, expressed as movement along the coordinate q. As DA oscillates in the nuclear coordinate, it progresses along the potential energy surface. Should the fluctuations $k_b T$ exceed the energy required to reach the intersection with surface D^+A^-, electronic population can transfer to the other surface. The rate of this transfer is given by

$$k_{ET} = \frac{2\pi |J|^2}{\hbar\sqrt{4\pi\lambda kT}} \exp\left(\frac{-(\Delta G + \lambda)^2}{4\lambda kT}\right), \qquad \textbf{(2.48)}$$

where ΔG is the free energy change of electron transfer (energy difference between the minima), J is the matrix element corresponding to donor-acceptor coupling, and λ is the reorganization energy of the surrounding nuclei following electron transfer.[14,20,21] It is important here to note that for a given donor-acceptor system, the rate is directly affected by the free energy difference in the minima if all other parameters are held constant. That is, the relationship between ΔG and λ can be used to classify the electron transfer process into a subset of regimes. Namely, these are the normal ($-\Delta G < \lambda$), activationless ($-\Delta G = \lambda$), and inverted ($-\Delta G > \lambda$) regimes.[14] Surfaces depicting the different cases are shown in Figure 2.8.

Remembering that the free energy surfaces are drawn with the Born-Oppenheimer approximation in mind, they can be written as product states of nuclear configurations and

electronic configurations. For example, the donor state can be expressed as $|D\rangle = |d,n\rangle$. By the Condon approximation to ignore the nuclear portion, the donor-acceptor coupling, *V*, can then be defined to be

$$V = J\left[|d\rangle\langle a| + |a\rangle\langle d|\right], \tag{2.49}$$

such that *d* refers to the donor, and *a* refers to the acceptor configuration. While often difficult to measure the electronic coupling directly, it has been shown[22] that it can be approximated as

$$V = \frac{0.0206}{r_{DA}}\sqrt{\varepsilon \cdot \omega_{\max} \cdot \delta\omega_{fwhm}}, \tag{2.50}$$

where ε is the molar extinction coefficient, $\omega_{\max}$ is the peak of the absorbance spectrum, $\delta\omega_{fwhm}$ is the full width at half maximum of the lineshape (both in cm^{-1}), and r_{DA} is the distance between the donor and acceptor. Knowledge of the magnitude of the coupling is critical to modeling the system in relation to its other parameters, as the relative scale of the electronic coupling can significantly alter the electron transfer rate. Treating the donor-acceptor system as a 2x2 matrix, the zeroeth order Hamiltonian can be written as

$$H^{(0)} = \begin{pmatrix} E_g & H_{ge} \\ H_{eg} & E_e \end{pmatrix}, \tag{2.51}$$

where E_g and E_e are energies of the ground and excited state, respectively. The electronic coupling has been renamed from Equations (2.48) and (2.49) for clarity, that is $H_{ge} = H_{eg} = J$. In the limit where the coupling is small compared to the reorganization energy λ as has been assumed to this point, it can be ignored. That is, the two potential energy surfaces do not

significantly interact in the electron transfer transition, so there is a nearly instantaneous (discontinuous) change in free energy. In the opposing limit where the coupling is large compared to λ , additional considerations must be made.

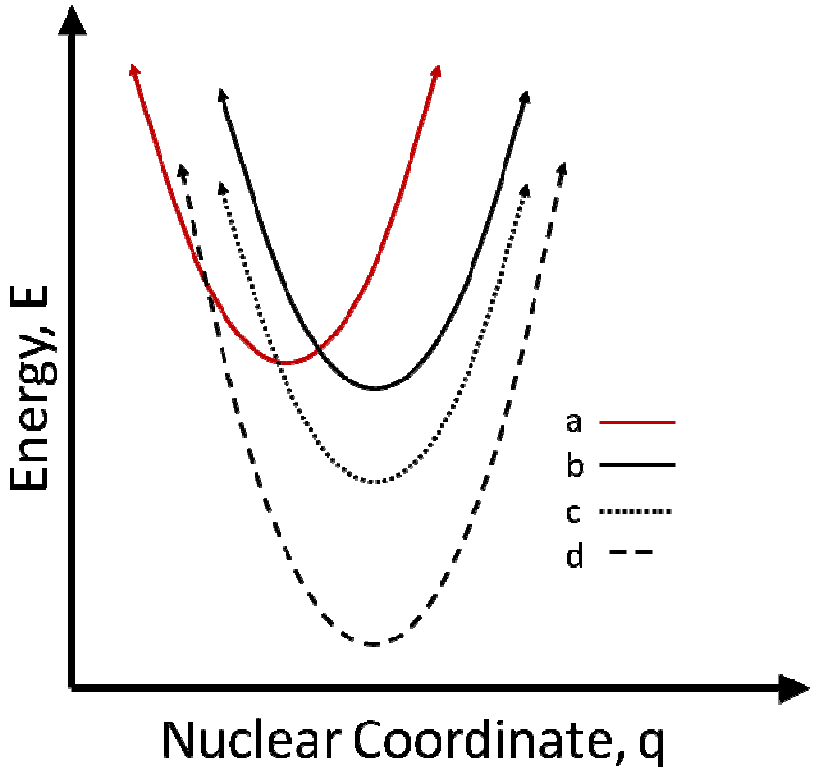

Figure 2.8: Free energy regimes for a bimolecular donor-acceptor system. Specifically, the surfaces represent the DA surface (a), and three corresponding D^+A^- surfaces for systems in the normal (b), activationless (c), and inverted (d) regimes. Note that λ and the width of the surface are constant for b,c, and d, and the d. The only difference between the surfaces is the energy relative to a.

When the Hamiltonian is diagonalized, splitting is observed such that the energies are

$$E_{\pm} = \frac{1}{2}\left(E_g + E_e\right) \pm \frac{1}{2}\sqrt{\left(E_g - E_e\right)^2 + 4\left|H_{eg}\right|^2} \quad . \tag{2.52}$$

Unlike the case where $\lambda >> H_{eg}$ and $E_{\pm} = E_g, E_e$ respectively, the case where the coupling is large results in a gap at the point of degeneracy equal to $2H_{eg}$, shown in Figure 2.9.

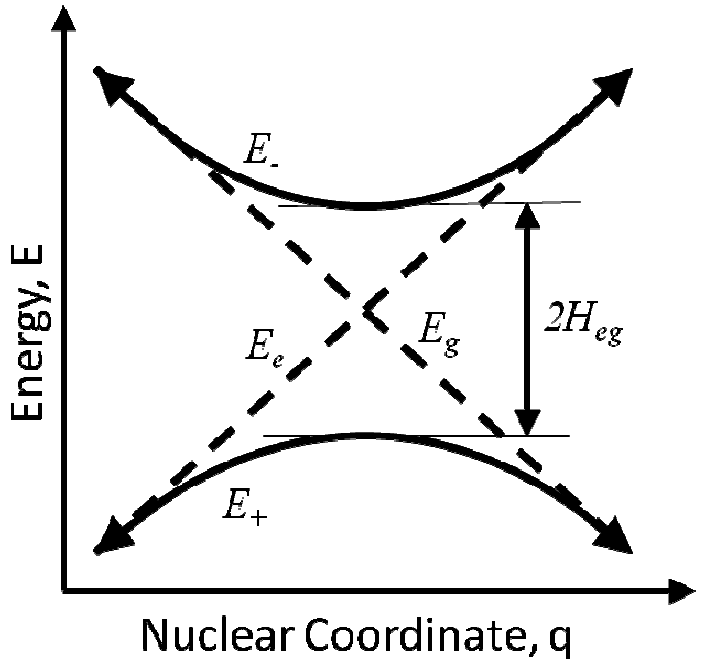

Figure 2.9: Comparison between adiabatic and nonadiabatic potential surfaces in the crossing region. In the nonadiabatic limit, the DA surface (E_e) and the D^+A^- surface (E_g) are degenerate at the intersection. In the adiabatic limit, the free energy surfaces are continuous at the intersection and exhibit a minimum energy gap of $2H_{eg}$.

It is important to consider systems in which neither the adiabatic nor nonadiabatic models are satisfied (e.g, when neither $\lambda >> H_{eg}$ or $\lambda << H_{eg}$ applies). Furthermore, is it also necessary to be able to quantify whether or to what degree the assumptions of either limit are applicable.

An expression has been derived[17] which interpolates between the two coupling regimes utilized by performing a resummation of terms of multiple orders of perturbation theory. In other words, considering the rate of electron transfer as an infinite series of terms

$$k_{ET} = H_{eg}^2 C_2 + H_{eg}^4 C_4 + H_{eg}^6 C_6 \ldots \ , \tag{2.53}$$

where C_n is a correlation function of order n, the Marcus equation (Equation 2.48) is equivalent to the truncation of the series after the first term. The derivation of Mukamel and Sparpaglione[17] is merely mentioned here, however the resulting equations provide an interesting context relevant to discussion of the work found in Chapter 7. Their resulting interpolation between the adiabatic and nonadiabatic regimes is expressed as

$$k_{ad} = \frac{\left\{ 2\pi \frac{\left|H_{eg}\right|^2}{\hbar \left(4\pi\lambda k_B T\right)^{1/2}} \exp\left[\frac{-\left(\Delta G + \lambda\right)^2}{4\lambda k_B T} \right] \right\}}{1 + \nu_{ad}} \ , \tag{2.54}$$

where the numerator is the Marcus equation and the so-called adiabaticity parameter, ν_{ad}, is defined as

$$\nu_{ad} = \frac{2\tau}{\hbar} \sqrt{\frac{\pi H_{eg}^4}{\lambda k_B T}} \ . \tag{2.55}$$

The adiabaticity parameter is governed by a relation between the donor-acceptor coupling and the reorganization energy as expected, as well as the time scale, τ ,

$$\tau = \exp\left(\frac{-q}{2} \right) \int_0^\infty dt \left\{ \frac{1}{\sqrt{1 - \exp\left(-2\Lambda t\right)}} \exp\left(\frac{q^2 \exp\left(-\Lambda t\right)}{1 + \exp\left(-\Lambda t\right)} \right) - 1 \right\} \ . \tag{2.56}$$

The benefit of Equation 2.54 is immediately obvious, as when the coupling can be ignored, $\nu_{ad} = 0$ and the rate is described by the Marcus equation (the system is completely nonadiabatic). When the adiabaticity parameter is between 0 and 1, the system is moderately well modeled by the Marcus equation. As ν_{ad} grows larger than 1, however, the assumptions inherent to the nonadiabatic formalism will no longer be sufficient. While none of the systems studied in this thesis are treated adiabatically, the nature of the distinction between regimes will be especially important to the discussion of Chapters 4 and 7.

2.6. Concluding Remarks

In this chapter, the underlying concepts of condensed phase spectroscopy relevant to this thesis have been discussed. In addition to the complexity inherent to studying any condensed system, the specific systems of interest to this work (namely molecule-semiconductor interfaces) exhibit further complications. Specifically, following photoexcitation of the DA system electron transfer is experimentally observed on timescales faster than reasonable for nuclear relaxation to have completed (100 fs).[23,24] The kinetic models (Marcus theory) presented in Section 2.5 deal mainly with nonadiabatic conditions where the electron population initially resides in the equilibrium position of the DA energy surface (see Figure 2.7). The result is the inability of second-order models to account for electron transfer occurring from nonequilibrium nuclear geometries. A model utilizing fourth-order perturbation theory will be described with the goal of modeling electron transfer occurring simultaneously with nuclear relaxation processes in the context of photoexcited donor-acceptor systems.[25] This model will be discussed in detail in Chapter 6, where it is the primary focus.

2.7. REFERENCES

(1) Mukamel, S. *Principles of Nonlinear Optical Spectroscopy*; Oxford University Press: New York, 1995.

(2) Nitzan, A. *Chemical Dynamics in Condensed Phases*; Oxford University Press: New York, 2006.

(3) Valkunas, L.; Abramavicius, D.; Mančal, T. *Molecular Excitation Dynamics and Relaxation: Quantum Theory and Spectroscopy* Wiley-VCH: Weinheim, 2013.

(4) Heller, E. *J. Chem. Phys.* **1975**, *62*, 1544.

(5) Gallagher, S. M.; Albrecht, A. W.; Hybl, J. D.; Landin, B. L.; Rajaram, B.; Jonas, D. M. *J. Opt. Soc. Am. B* **1998**, *15*, 2338.

(6) Lepetit, L.; Chériaux, G.; Joffre, M. *J. Opt. Soc. Am. B* **1995**, *12*, 2467.

(7) Abramavicius, D.; Mukamel, S. *Chem. Rev.* **2004**, *104*, 2073.

(8) Craig, D. P.; Thirrunamachandran, T. *Molecular Quantum Electrodynamics*; Academic Press, Inc: Orlando, 1984.

(9) Heitler, W. *The Quantum Theory of Radiation*, Third Edition ed.; Oxford: Clarendon Press: New York, 1954.

(10) Marx, C.; Harbola, U.; Mukamel, S. *Phys. Rev. A.* **2008**, *77*.

(11) Myers, A. B.; Mathies, R. A. Resonance Raman intensities: a probe of excited state structures and dynamics. In *Biological Applications of Raman Spectroscopy*; Spiro, T. G., Ed.; Wiley: New York, 1987; Vol. 2; pp 1.

(12) Kelley, A. M. *J. Phys. Chem. A* **1999**, *103*, 6891.

(13) Heller, E. J. *Acc. Chem. Res.* **1981**, *14*, 368.

(14) Marcus, R. A. *J. Chem. Phys.* **1965**, *24*, 966.

(15) Memming, R. *Semiconductor Electrochemistry*, 1 ed.; Wiley-VCH, 2001.

(16) Barbara, P. F.; Meyer, T. J.; Ratner, M. A. *J. Phys. Chem.* **1996**, *100*, 13148.

(17) Sparpaglione, M.; Mukamel, S. *J. Chem. Phys.* **1988**, *88*.

(18) Levich, V. *Adv. Electrochem. Electrochem. Eng.* **1966**, *4*.

(19) Jortner, J. *J. Chem. Phys.* **1976**, *64*, 4860.

(20) Englman, R.; Jortner, J. *Mol. Phys.* **1970**, *18*.

(21) Kubo, R.; Toyozawa, Y. *Prog. Theor. Phys.* **1955**, *13*.

(22) Hush, S. N. *Prog. Inorg. Chem* **1967**, *8*.

(23) Anderson, N. A.; Lian, T. *Annu. Rev. Phys. Chem.* **2005**, *56*, 491.

(24) Akimov, A. V.; Neukirch, A. J.; Prezhdo, O. V. *Chem. Rev.* **2013**, *113*, 4496.

(25) Li, L.; Giokas, P.; Kanai, Y.; Moran, A. M. *J. Chem. Phys.* **2013**, *140*.

CHAPTER 3: NONLINEAR SPECTROSCOPY AND ULTRAFAST TECHNIQUES

3.1. Introduction

The study of ultrafast processes in condensed phases requires design and implementation of sophisticated spectroscopic techniques to properly measure molecular observables.[1-25] The experiments must maintain a high degree of temporal resolution in order to obtain useful information about physical processes occurring on these timescales. For the work presented in this thesis, a more a complete picture of the molecular interface often requires the use of several specialized experimental techniques in concert, each providing complementary information.[3,26-32]

In this chapter, the details of the primary experimental techniques employed in this thesis will be discussed. In Section 3.2, resonance Raman spectroscopy will be discussed. Raman scattering is a topic relevant to the work in each of the later chapters, but is most fundamental to Chapter 4. There, it will be used to construct Raman excitation profiles to calculate vibrational reorganization energy of the ruthenium chromophore systems. In addition, polarized Raman spectroscopy will be the primary tool for investigating the geometry of these chromophores on a semiconductor crystal surface in Chapter 5. Section 3.3 outlines the fiber system used to achieve ultra short visible pump pulses for use in pump-probe experiments. Section 3.4 deals with transient absorption spectroscopy, which is central to Chapters 4, 7, and 8 as a tool for measuring both the identity and the kinetics of short-lived electronic species at the molecule-semiconductor interface.[1,2,14,19,33] Section 3.5 extends the discussion of transient absorption to the related technique of transient grating spectroscopy, which is utilized in Chapter 7. While similar from a

theoretical standpoint, the technical implementation of transient grating spectroscopy differs in several ways which set it apart from transient absorption.

3.2. Raman Spectroscopy

3.2.A. Resonance Raman Spectroscopy

Resonance Raman spectroscopy is a technique which measures important sample properties[34-36] while remaining relatively simple in execution. The laser used for the resonance Raman spectra measured here is a Spectra Physics Stabilite 2017 continuous source with visible lines at 457.9 nm, 488 nm, and 514.5 nm. Spectra were collected with a Renishaw inVia- Leica DM2500 M microscope setup. The objective is interchangeable between a Leica N PLAN EPI 50x/0.75 objective lens or an alternate 20x/0.4 lens (also from Leica) depending on the sample type. The sample itself is mounted to a computer-controlled XYZ translation stage (where the laser propagates in the Z direction of the laboratory frame.) Nanocrystalline films are measured either under ambient conditions (dry) or soaked with a solvent and covered with a glass slide (wet). Additionally, nanoparticle or chromophores solutions are measured in a 1 mm path length quartz cuvette purchased from Starna cells.

The apparatus uses a 180º backscattering geometry (see Figure 3.1) such that the scattered light is collected via the same objective used to focus the incident field onto the sample. Because of the backscattering results in the Rayleigh (elastically) and Raman (inelastically) scattered signals to be collinear, the undesired photons are attenuated by a long pass filter. This is necessary due to the relative intensity of Rayleigh scattering to Raman scattering.[35] After passing through the filter, a grating (2400 l/mm) disperses the signal onto the CCD.

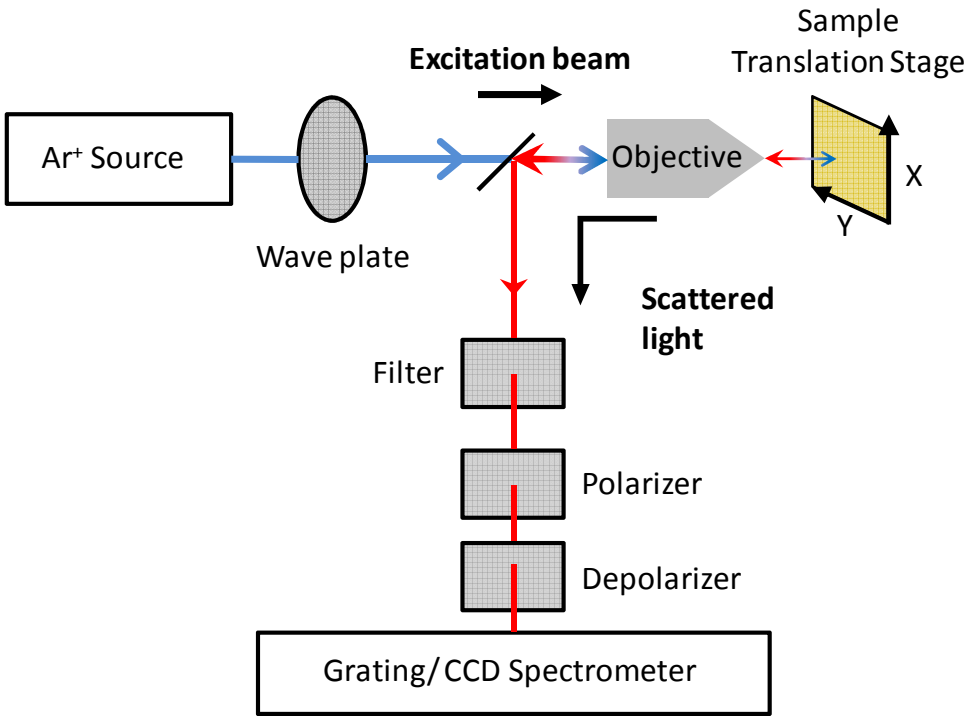

Figure 3.1: Diagram of the spontaneous Raman experimental setup. The incident beam (blue arrow) is focused through an objective onto the sample, which is housed on a translation stage. The Raman signal (red arrow) is scattered at 180° through the same objective and dispersed onto the CCD via a grating. The filter attenuates elastically scattered light. Additional optics shown are included in the setup for more quantitative or selective measurement as is required for the polarized experiments. The excitation beam then first passes through a $\lambda/2$ wave plate before arriving at the sample. The scattered signal is collected after passing through a polarizer and a scrambler or depolarizer.

3.2.B. Polarized Raman Spectroscopy

Polarized Raman scattering experiments utilize the same apparatus as the other resonance Raman experiments while incorporating additional optics to select only the desired signals (see Figure 3.1). The laboratory frame is defined as the incident beam propagating in the negative Z

direction. The scattered light propagates in the positive Z direction after collection by the objective. The experiments required to obtain all necessary information about the scattering polarization are then defined by the polarization of the incident and scattered fields. Employing the notation of Porto[37] and others, the specific experiments relevant to the signals in Chapter 5 are: –Z(XX)Z, -Z(XY)Z, -Z(YX)Z, and -Z(YY)Z.

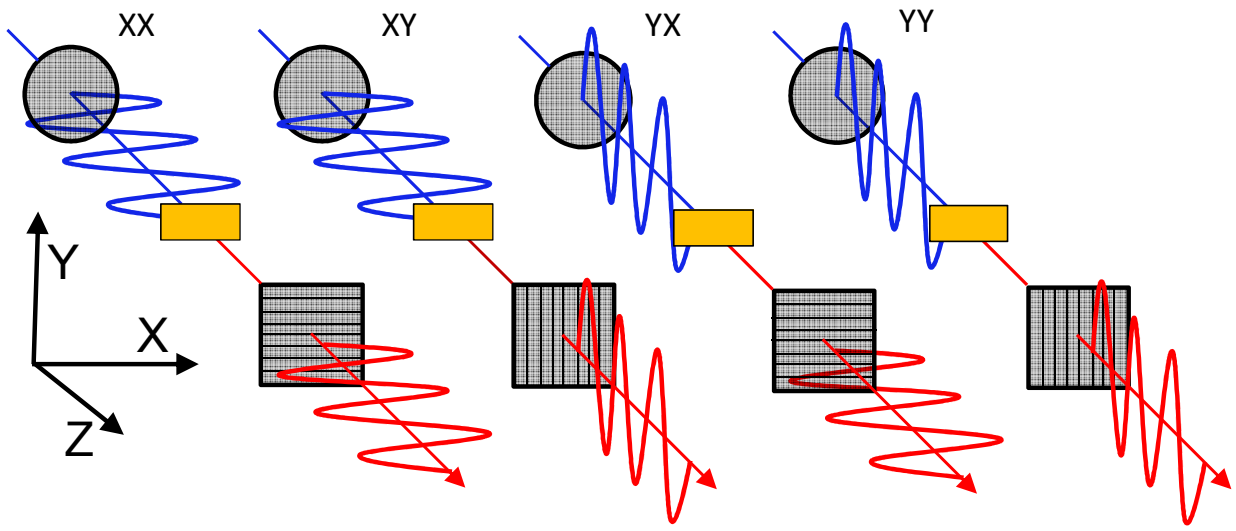

Figure 3.2: Experimental Raman Polarizations. The four polarized Raman experiments are defined by the relation of the polarizations of the incident and scattered radiation to the laboratory frame. The incident beam (blue arrow) travels through a $\lambda/2$ wave plate (gray circle) and the microscope objective (not pictured) to the sample (orange box). The Raman signal (red arrow) is backscattered at 180° through the objective. Before proceeding to the detector, the scattered light passes through a polarizer (gray box) which selects only the signal with the desired polarization.

Figure 3.2 shows the polarization orientations relative to the propagation. Excitation beam polarization control is established by installation of a half wave plate before the sample. Likewise, a wire grid polarizer is placed in the path of the scattered light to select the measured

polarization. All measurements utilize a depolarizer after the polarizer in order to remove any bias in the grating.

Using the translation stage, data is collected at a series of sample locations in a grid pattern with points separated by 10 μm in the X and Y dimensions on the substrate. Scanning the stage is also for proving that the results are independent of location on the crystal surface, as well as preventing photobleaching of the samples. At each location, the signal is integrated for 60 seconds.

3.3. Pump Pulse Generation

The ultrafast experiments reported in this dissertation require pump pulses with durations short enough (~20 fs) to resolve the molecular dynamics. Such pulse durations are achieved for the transient absorption and transient grating spectroscopies described in the following sections using a hollow-core fiber filled with argon, a noble gas. Propagation of the pulse through the fiber results in spectral broadening[38-40] which is necessary to reduce pulse length. The design of the fiber mount and housing is derived from previous fiber system built in the Moran group[23,41,42] which was in turn based on an apparatus utilized by Durfee and coworkers.[43,44] The fiber system used here is shown in Figure 3.3.

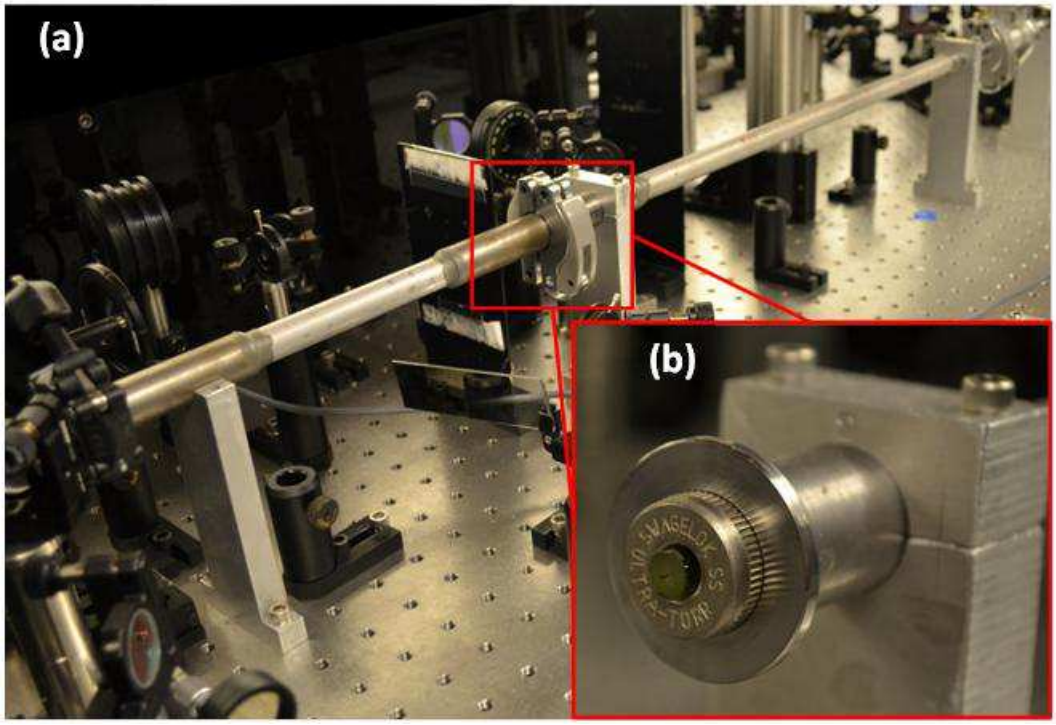

Figure 3.3: Hollow Core Fiber Apparatus. a) A photograph of the custom-built fiber mount and sealed housing. The three sections of tubing are joined at flanges with o-rings and secured with clamps. On each end, a fused silica window is held by another clamp. The mount ensures the housing is aligned to the beam path at multiple points. The gas inlet valve, near the top-right of the image, is connected to a vacuum pump and argon gas tank (located beneath the optical table) via polyethylene tubing. **b)** The middle section of the housing contains the hollow-core fiber itself, which is seated inside a glass rod to maintain its shape and position within the housing. Ordinarily the fiber is completely contained within the housing for pressurization, however in panel (b) it is shown with the clamp and end section removed.

Before entering the fiber, the laser is frequency-doubled in a β-BaB_2O_4 (BBO) crystal to produce a 400 nm pulse. This pulse is focused using a 10” focal length lens into the entrance of a 23” long, 100 μm inner diameter fiber (Polymicro Technologies TSP100375VS). The fiber is seated inside a glass tube to maintain its shape and position (see Figure 3.3b). The fiber is housed

within a steel tube capped on each end with another segment of tube terminated by a fused silica window. The housing is airtight, allowing the pressure and composition of the fiber's atmosphere to be controlled by means of a vacuum pump and pressurized argon tank. The laser pulse induces a change in the refractive index of the gas which results in spectral broadening.

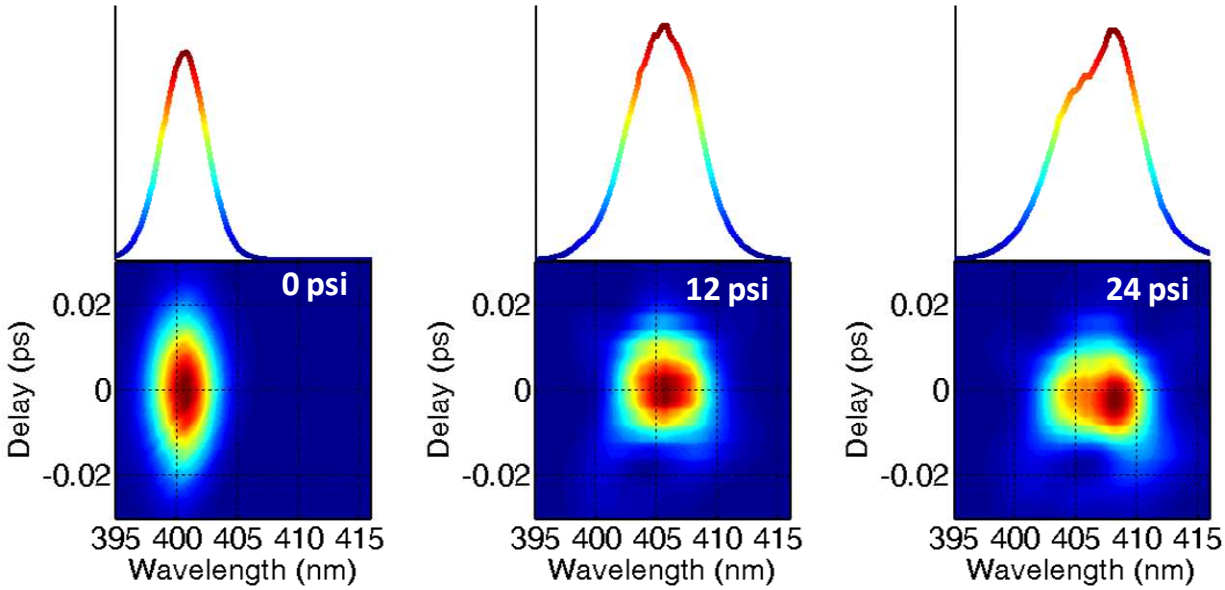

Figure 3.4: Hollow Core Fiber Pulse Spectra. Pulse spectrum (top) and auto-spectrogram (bottom) for three fiber pressures. At 0 psi there is no argon medium, resulting in no spectral broadening within the fiber. At 12 psi Ar, the spectrum is nearly twice as wide and has a significantly reduced duration as well. By 24 psi, the spectrum has broadened further to the point at which dispersion prevents adequate prism compression (notice the bowed shape compared to the circular shape at 12 psi).

The degree of broadening is dependent on the pressure of the medium (see Figure 3.4). By increasing the bandwidth of the pulse, its minimum duration is significantly reduced. However, if the pulse spectrum is too wide, higher order dispersion cannot be avoided with conventional prism-compression. Therefore, there is an optimum pressure of argon (empirically determined as

12 psi argon for the current fiber configuration) at which the spectrum is broad enough to achieve sufficiently short time duration, yet narrow enough to be effectively compressed to near its bandwidth limit. Pulses broadened in the fiber system have a duration of approximately 20 fs.

3.4. Transient Absorption Spectroscopy

3.4.A. Overview

The most common nonlinear spectroscopy employed in electron transfer research is transient absorption (TA.) TA may be performed in many spectral regions including the infrared and ultraviolet. The work presented here exclusively presents TA experiments performed at visible wavelengths, and therefore the discussion is concerned mainly with that spectral region.[45,46] TA spectroscopy is a superficially simple technique, possessing many similarities to conventional steady-state absorption spectroscopy. However, unlike linear absorption spectroscopy, TA measures the absorption of transient species in the sample in a "pump-probe" configuration. As discussed in Chapter 2, TA is a third-order perturbative measurement.

3.4.B. Experiment Design

The probe pulse utilized in the experiments presented here is a white light continuum ranging from 350 nm- 750 nm and generated in a CaF_2 window, or alternately from 450 nm- 950 nm when generated in sapphire. The 800 nm pulse used to generate the continuum is obtained by splitting 2% of the Ti:Sapphire kHz pulse beam power using a beam splitter. The window is translated in a circular pattern by a motorized arm with a period of 0.3 sec, which allows the optic to move by a distance of approximately 270 μm (greater than the spot size) between pulses.

Striking a different region of the window with each shot results in minimal damage and maintains consistent spectral generation. The pump pulse is the second harmonic generated in a BBO crystal from the rest of the 800 nm pulse. The pump pulse delay is controlled using a computerized translation stage. After passing through a chopper wheel, the pump and probe are overlapped at a small (5°) crossing angle at the sample position (see Figure 3.5, below.) Probe light is collected through an optical fiber and dispersed by in a spectrometer. Hundreds of difference spectra are collected at each delay point in the scan, and the scan is repeated 10-30 times for averaging during each measurement.

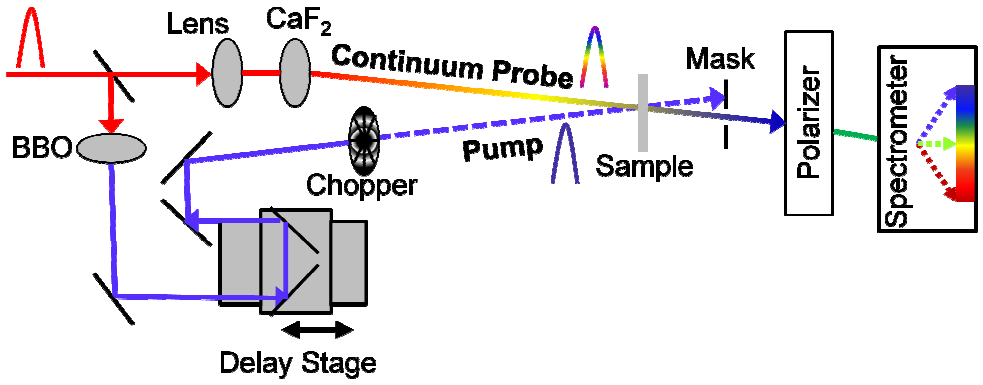

Figure 3.5: Experimental diagram for the TA measurements. The 800 nm pulse is split into two paths. The first travels through a translating CaF_2 (as depicted, or sapphire) window to become the continuum probe pulse, while the other is frequency doubled in a BBO crystal to serve as the 400 nm pump pulse. As the computer controlled delay stage is moved to the left, delay time *t* increases as the pump pulse takes relatively less time to reach the sample. (Likewise, moving to the right decreases delay time.) After the sample position, residual pump light is attenuated with a polarizer. The probe signal is finally dispersed and detected by a spectrometer. Probe spectra are collected from shots with pump both blocked and unblocked by the chopper in order to measure both A_{pumped} and $A_{unpumped}$.

In the experiment, a system is excited by an electronically resonant "pump" pulse. While the "pump" is traditionally a single pulse, two field-matter interactions occur between the system and the "pump" (such that the desired third-order signal will be radiated collinearly with the "probe.").[17,47] The intensity of the pump pulse is tuned such that less than 10% of the system is electronically excited; that is, the laser intensity is tuned such that interactions with the pump pulse are perturbative in nature.[2] While the system is still in a non-equilibrium state, a "probe" pulse interacts with the system; this portion of the experiment is similar to steady-state absorption in that the delayed probe is partially absorbed by the system. The transmitted light is dispersed and collected by a spectrometer.

At each delay time, the probe pulse is measured after passing through the excited sample and is compared to the probe pulse collected from the equilibrium system. In this way, the change in absorbance (ΔA) induced by the interactions with the pump pulse is experimentally determined. By varying the delay time, t , the growth and decay of spectral features can be measured. Coupled with dispersed detection, the resulting information is a function of both frequency and delay time, $\Delta A(\omega,t)$. The TA signal can be written as,

$$\Delta A(\omega,t) = A_{pumped}(\omega,t) - A_{unpumped}(\omega,t) \ . \qquad \textbf{(3.1)}$$

TA spectra are simple to interpret as they can contain contributions from only a few classes of signals. However, similar to linear absorption spectra, TA spectra can contain multiple overlapped features which can complicate interpretation. TA features are classified into three basic types: ground state bleach (GSB), excited state absorption (ESA), and excited state emission (ESE). When measuring a GSB signal, more of the "probe" reaches the detector relative to the equilibrium measurement, and a negative sign feature is recorded which

corresponds to a decrease in the absorbance of the sample ($A_{unpumped} > A_{pumped}$). This is the result of decreased population at frequencies corresponding to a region of the probe spectrum after excitation by the pump pulse. Likewise, ESE signals (from emission stimulated by the probe) have a negative sign. These features are distinguishable from bleach signals because they are emitted at lower detection frequencies. That is, as the wave packet relaxes the energy gap with the ground state decreases, and ESE features will exhibit Stokes shift, while GSB signals will not.[14,48] Conversely, for ESA the excited sample shows an increased absorbance of light and therefore a positive signal (less intensity on the detector, $A_{pumped} > A_{unpumped}$) which is the result of increased excited state population.

3.5. Transient Grating spectroscopy

3.5.A. Overview

Transient grating (TG) spectroscopy, like TA spectroscopy is a third-order spectroscopic technique. Also like TA, TG is a "pump-probe" technique which corresponds to the third-order response function described in Chapter 2. The interference of these pulses within the sample medium generates the holographic "transient grating" for which the technique is named.[49-52] The remaining "probe" pulse scatters off of the grating produced by the pump pulses in such a way that carries information about the system.[51,53,54] TG spectroscopy differs from TA in that the two pump interactions arise from separate laser fields. A consequence, TG is sensitive to both transient dispersion and absorption.[17,51,55-59]

3.5.B. Experiment Design

As discussed in Chapter 2, experimental TG signals consist of the field radiated after three light-matter interactions induce a nonlinear polarization in the sample;[17,47] two interactions occur with the grating forming "pump" pulses and a third interaction with the "probe" pulse. A schematic of the sequence of pulses is shown in Figure 3.6, which describes the order of events during an experiment. Two identical pulses first arrive at the sample simultaneously (i.e., $\tau = 0$) and excite an electronic transition in the sample- these are the "pump" pulses. Following the first two interactions, the excited system relaxes during an experimentally controlled delay time, T. After T has elapsed, a final laser pulse arrives and interacts as the "probe" which stimulates the radiation of the signal field from the sample after delay t.

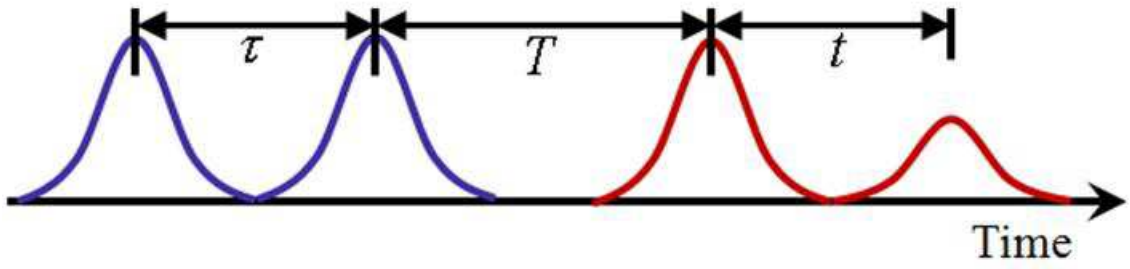

Figure 3.6: Pulse sequence in a 3rd order TG spectroscopy experiment. The pump pulses are colored blue while the probe and signal pulses are colored red. The delays between pulses are defined as τ, T, and t, respectively, which represent the time between the arrival of the intensity maxima at the sample. For all of the experiments described in this thesis, $\tau = 0$.

TG spectroscopy is named for the action of the pump pulses on the sample. Specifically, the two "pump" pulses which are matched in both frequency and time are coincident on the sample with a defined angle of separation, θ. The interference and electronic absorption of these

two pulses results in a "population" grating within the sample.[51] For example, within the ~200 μm laser spot, there are alternating areas of excited state and ground state systems. After the experimentally controlled delay time, T, the probe pulse incident on this grating is diffracted. The angle of diffraction dictates the vector of the signal, which is emitted in a direction free of background radiation from the three incident pulses. The grating is depicted in Figure 3.7.

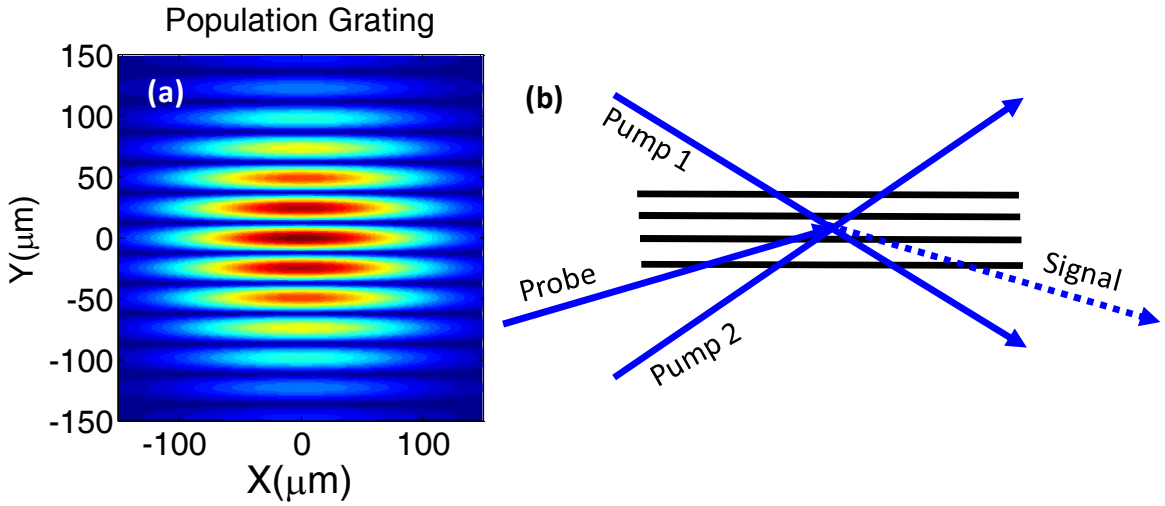

Figure 3.7: Depiction of the Transient Grating. **a)** The population grating formed by the 410 nm pump pulses at their focus in the molecular sample, where X and Y are dimensions in the laboratory frame. The parameers used in this calculation correspond to experimental conditions used in Chapter 7. **b)** A static population grating represented by the solid black lines is produced in the sample by the pumps during a TG spectroscopy experiment. Later, the probe diffracts off of this grating, which causes the signal field to radiate in a direction independent of the three preceding pulses, which allows background radiation to be spatially filtered.

The TG spectroscopy measurements described in this thesis consist of three incident 20 fs, 410 nm pulses in a boxcar geometry.[8] A schematic of the experimental setup is shown in Figure 3.8. Two beams are each split in a diffractive optic and directed onto the sample by the

same 20-cm focal length concave mirror. The spatial separation of the pump pulses allows for independent polarization tuning of each beam. The signal is radiated in the phase-matched direction, $k_s = -k_1 + k_2 + k_3$. In the preceding equation, k_1 and k_2 represent the wave vectors of the two pump fields and k_3 is the wave vector of the probe pulse. A fourth reference beam propagates in the same direction as the signal. After a fixed delay, the reference pulse interferes with the signal field to produce a frequency resolved interferogram on the CCD detector.

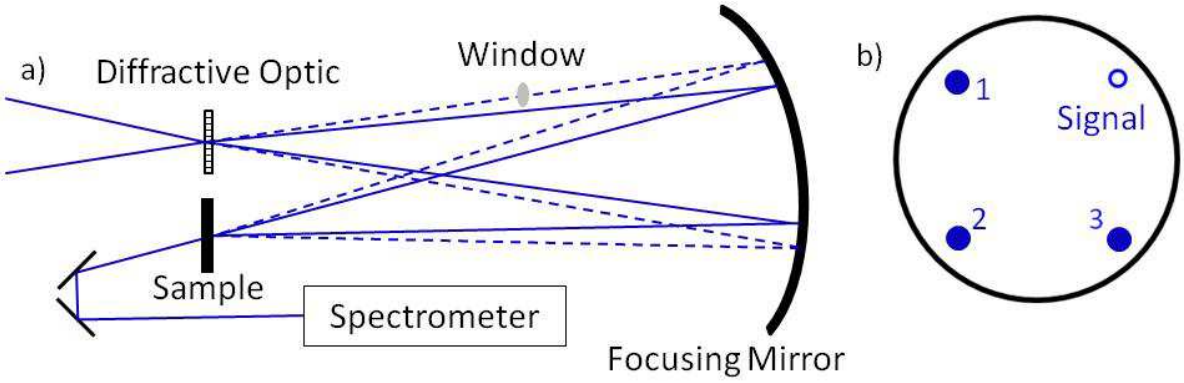

Figure 3.8: a) **Experimental diagram for the TG Raman experiment**. Four beams are split at a diffractive optic and relayed onto the sample with a 20-cm focal length concave mirror. The beam geometry on the focusing mirror is shown in (b). Unlike TA spectroscopy, this TG experiment results in the signal propagating noncolinearly with the probe which eliminates the need for spectral differencing. Additionally, the separation of the pump pulses allows for polarization tuning of each pump beam independently.

Use of a diffractive optic to split the pulses is convenient, because it simplifies the inclusion of interferometric (heterodyne) detection using spectral interferometry in Chapter 7.[60-

[62] Specifically, passive phase stabilization of the interferometer is one of the most important benefits of the use of the diffractive optics .[56] As is shown in Equation 3.2, the measured signal depends on the relative phase between the reference field and the signal,

$$\Delta\phi = \frac{\pi}{2} + \phi_{\chi} + (\phi_{P1} - \phi_{P2}) - (\phi_{LO} - \phi_{PR}) \ , \tag{3.2}$$

where ϕ_{Pn} and ϕ_{PR} refer to the "pump" and "probe" phases, respectively. The term ϕ_{χ} is the phase shift due to the complex nonlinear susceptibility, and the $\frac{\pi}{2}$ term corresponds to the phase shift between the induced 3rd order polarization and the radiated field.[53,63] Air currents, temperature, and vibrations in optics can all affect the phases of the pulses. While the relative phase can be controlled or monitored as the experiment progresses[64-66], the process is tedious for experiments which can take hours to complete. Utilizing a diffractive optic such that the pump, probe, and reference fields all originate from the same pulse ensures that they are subject to the same phase fluctuations for much of the experiment, and their relatively small angle separation (~5°) allows use of common optics which stabilizes the phase without the need for a complex apparatus.[53,54,63,67-69]

The measured interference pattern possesses a significantly increased signal-to-noise ratio (SNR) than a conventionally detected signal, because the signal scales linearly in the signal field intensity (instead of quadratically). The interferogram measured on the detector is governed by

$$I = \left|E_{LO}\right|^2 + \left|E_S(t)\right|^2 + 2\left|E_{LO}E_S(t)\right|\cos(\phi_{LO} - \phi_S) \ , \tag{3.3}$$

where the subscripts *S* and *LO* denote the signal and local oscillator fields, respectively.[53,63] When $|E_{LO}|^2 \gg |E_S(t)|^2$, the second term in Equation 3.3 can be ignored. Additionally, $|E_{LO}|^2$ is easily measured and separated from the interferogram, which leaves only the term linearly dependent on the signal field, $I \approx 2|E_{LO}E_S(t)|\cos(\phi_{LO} - \phi_S)$. Comparing the heterodyne signal to the directly measured (homodyne) intensity, $|E_S(t)|^2$, the interferometrically detected signal is larger by a factor of $2|E_{LO} / E_S(t)|$.

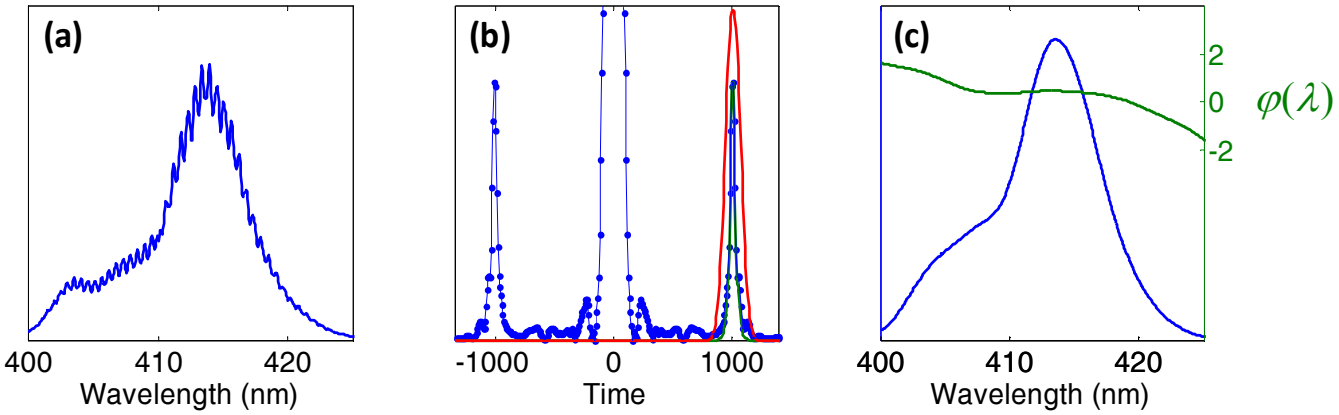

Figure 3.9: Interferometric Detection Example. a) An example interferogram measured using heterodyne detection in a TG spectroscopy experiment. The small peaks over the broad local oscillator spectrum are fringes caused by the interference of the local oscillator and signal fields. Although a similar interferogram is measured at each delay time, only one interferogram is shown here. **b)** The signal from panel (a) is shown Fourier transformed to the time domain. The red line is an apodization function applied to the transformed signal to filter out all but the relevant TG response signal. **c)** After filtering, the signal is inverse transformed back to the frequency domain to give a measured signal spectrum (blue line) and spectral phase (green line).

As shown in Figure 3.9, the directly detected interferogram is Fourier transformed to the time domain, where the component, $E_{LO}E_S(t)$, can be filtered using an apodization function before inverse Fourier transformation. The amplitude and phase of the signal field is obtained at each delay time between pump and probe pulses. The real and imaginary components of the signal field correspond to transient absorption and dispersion, respectively. The absorptive part of the transient grating signal field gives the same information as a traditional transient absorption experiment. The dispersive signal component may be sensitive to the solvent response as well as the thermal grating induced by fast ground state recovery.

TG spectroscopy is engineered to detect small signals as described, however the specific samples of interest to this work undermine some of the means by which such sensitivity is achieved. Molecule-sensitized semiconductor films possess rough, highly scattering surfaces which defeat the benefit of background-free signal detection. Therefore, film scattering can be reduced by replacing solid films with suspensions of nanoparticles. Solutions are contained in a homemade sample jet described in detail elsewhere[70] to simultaneously prevent photodegradation and minimize pulse duration (see Figure 3.10) . Briefly, 50 mL drains through a narrow (3 mm diameter) tube with a loop of ~0.5 mm tungsten wire at its end. As the solution flows a film forms between the sides of the wire loop due to the surface tension of the solvent. At its center the film is approximately 220-μm thick. A peristaltic pump returns the solution to the top of the tube to recycle the sample volume. The key benefits of using a sample jet over a flow cell is elimination of both the need to compensate for the dispersion ordinarily caused by cuvette windows as well as the scattering inherent to the additional interfaces.

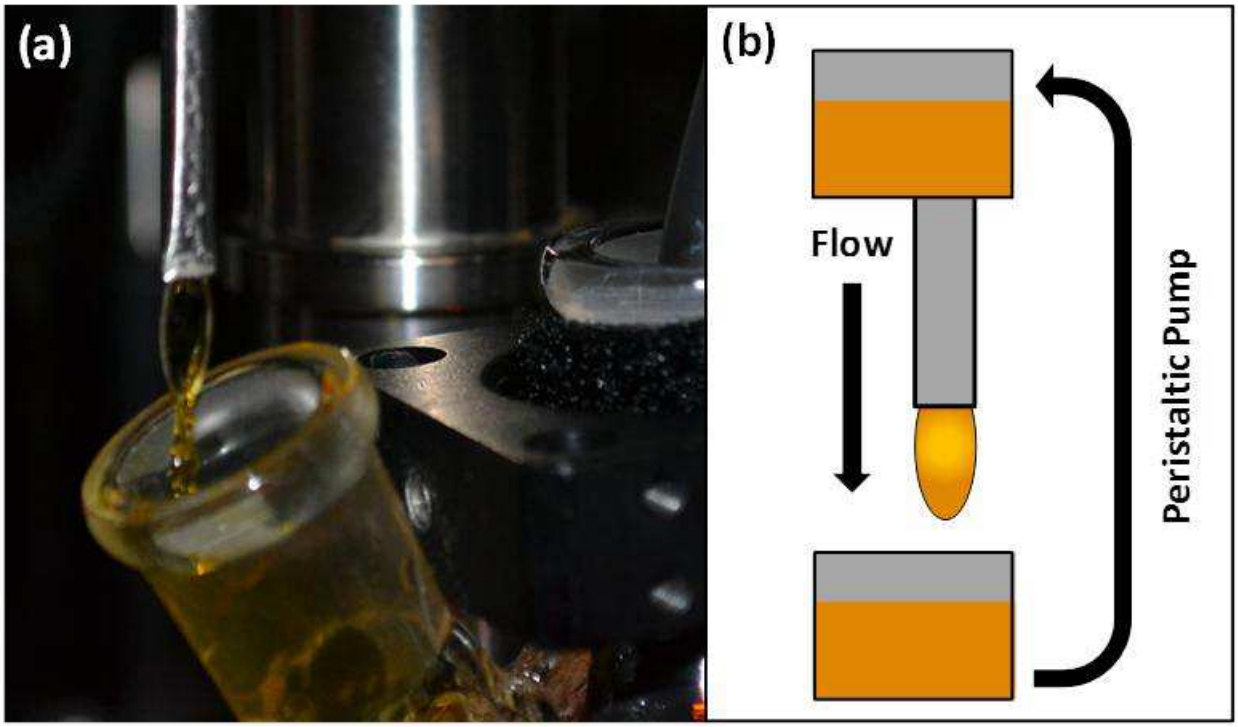

Figure 3.10: The Sample Jet. a) A photograph of catechol-sensitized nanoparticle solution flowing through the jet into the lower reservoir. **b)** A diagram of the sample jet shown in panel (a). The solution flows from the upper reservoir through a 3 mm diameter tube which ends with a loop of approximately 0.5 mm tungsten wire. As the solution flows past the wire, a 220-μm thick film forms inside the bend. As the solution drains into the lower reservoir, a peristaltic pump is used to return the solution to the top of the apparatus allowing for a total sample volume of only 50 mL.

3.6. Conclusion

Molecule-semiconductor interfaces are the systems of interest to the work presented here. This chapter has explored key spectroscopic and mechanical techniques which serve as tools to investigate their nuclear and electronic behavior upon photoexcitation. In addition to sophisticated nonlinear spectroscopies, thorough investigation of condensed systems also

requires solutions to practical problems such as sample preparation and delivery, which have also been presented. Each experiment is useful to the studies presented in the remainder of this dissertation. Resonance Raman spectroscopy in particular is central to each subsequent experimental chapter. TA spectroscopy and TG spectroscopy are likewise leveraged to provide information about photoinduced dynamics.

3.7. REFERENCES

(1) Asbury, J. B.; Hao, E.; Wang, Y.; Ghosh, H. N.; Lian, T. *J. Phys. Chem. B* **2001**, *105*, 4545.

(2) Berera, R.; van Grondelle, R.; Kennis, J. T. *Photosynth. Res.* **2009**, *101*, 105.

(3) Berg, M.; Vanden Bout, D. A. *Acc. Chem. Res.* **1997**, *30*, 65.

(4) Bixner, O.; Lukes, V.; Mancal, T.; Hauer, J.; Milota, F.; Fischer, M.; Pugliesi, I.; Bradler, M.; Schmid, W.; Riedle, E.; Kauffmann, H. F.; Christensson, N. *J. Chem. Phys.* **2012**, *136*, 204503/1.

(5) Boyd, R. W. *Nonlinear Optics*, 3rd. ed.; Elsevier: Burlington, MA, 2008.

(6) Bucksbaum, P. H. *Science* **2007**, *317*, 766.

(7) Diels, J.-C.; Rudolph, W. *Ultrashort Laser Pulse Phenomena: Fundamentals, Techniques, and Applications on a Femtosecond Time Scale*; Academic Press: San Diego, 1996.

(8) Druet, S. A. J.; Taran, J.-P. E. *Prog. Quant. Electr.* **1981**, *7*, 1.

(9) Engel, G. S.; Calhoun, T. R.; Read, E. L.; Ahn, T. K.; Mancal, T.; Cheng, Y. C.; Blankenship, R. E.; Fleming, G. R. *Nature* **2007**, *446*, 782.

(10) Fleming, G. R. *Chemical Applications of Ultrafast Spectroscopy*; Oxford University Press: New York, 1986.

(11) Gallagher, S. M.; Albrecht, A. W.; Hybl, J. D.; Landin, B. L.; Rajaram, B.; Jonas, D. M. *J. Opt. Soc. Am. B* **1998**, *15*, 2338.

(12) Ghosh, H. N.; Asbury, J. B.; Lian, T. *J. Phys. Chem. B* **1998**, *102*, 6482.

(13) Kosma, K.; Trushin, S. A.; Fuß, W.; Schmid, W. E. *Phys. Chem. Chem. Phys.* **2009**, *11*, 172.

(14) Kovalenko, S. A.; Ruthmann, J.; Ernsting, N. P. *Chem. Phys. Lett.* **1997**, *271*, 40.

(15) Kuthirummal, N.; Rudakov, F. M.; Evans, C. L.; Weber, P. M. *J. Chem. Phys.* **2006**, *125*, 133307.

(16) Miller, S. A.; West, B. A.; Curtis, A. C.; Papanikolas, J. M.; Moran, A. M. *J. Chem. Phys.* **2011**, *135*, 081101.

(17) Mukamel, S. *Principles of Nonlinear Optical Spectroscopy*; Oxford University Press: New York, 1995.

(18) Nitzan, A. *Chemical Dynamics in Condensed Phases*; Oxford University Press: Oxford, 2006.

(19) Pullen, S. H.; Walker, L. A.; Donovan, B.; Sension, R. J. *Chem. Phys. Lett.* **1995**, *242*, 415.

(20) Richards, G. H.; Wilk, K. E.; Curmi, P. M. G.; Quiney, H. M.; Davis, J. A. *J. Phys. Chem. Lett.* **2012**, *3*, 272.

(21) Towrie, M.; Doorley, G. W.; George, M. W.; Parker, A. W.; Quinn, S. J.; Kelly, J. M. *Analyst* **2009**, *134*, 1265.

(22) Wegener, M. *Extreme Nonlinear Optics: An Introduction*; Springer: Berlin, 2005.

(23) West, B. A.; Womick, J. M.; Moran, A. M. *J. Phys. Chem. A* **2011**, *115*, 8630.

(24) Wirth, M. J. *Anal. Chem.* **1990**, *62*, 270.

(25) Womick, J. M.; Moran, A. M. *J. Phys. Chem. B* **2009**, *113*, 15771.

(26) Kaufman, L. J.; Heo, J.; Ziegler, L. D.; Fleming, G. R. *Phys. Rev. Lett.* **2002**, *88*, 207402:1.

(27) Kubarych, K. J.; Milne, C. J.; Lin, S.; Astinov, V.; Miller, R. J. D. *J. Chem. Phys.* **2002**, *116*, 2016.

(28) Kukura, P.; McCamant, D. W.; Mathies, R. A. *Annu. Rev. Phys. Chem.* **2007**, *58*, 461.

(29) Moran, A. M.; Nome, R. A.; Scherer, N. F. *J. Chem. Phys.* **2007**, *127*, 184505:1.

(30) Rhinehart, J. M.; Challa, J. R.; McCamant, D. W. *J. Phys. Chem. B* **2012**, *116*, 10522.

(31) Tanimura, Y.; Mukamel, S. *J. Chem. Phys.* **1993**, *99*, 9496.

(32) Underwood, D. F.; Blank, D. A. *J. Phys. Chem. A* **2005**, *109*, 3295.

(33) Wang, Y.; Hang, K.; Anderson, N. A.; Lian, T. *J. Phys. Chem. B* **2003**, *107*.

(34) Heller, E. *J. Chem. Phys.* **1975**, *62*, 1544.

(35) Long, D. A. *The Raman Effect: A Unified Treatment of the Theory of Raman Scattering by Molecules*; Wiley: Chinchester, England, 2002.

(36) Myers Kelley, A. *J. Phys. Chem. A* **2008**, *112*, 11975.

(37) Damen, T. C.; Porto, S. P. S.; Tell, B. *Phys. Rev.* **1966**, *142*.

(38) Kolevatova, O. A.; Naumov, A. N.; Zheltikov, A. M. *Opt. Commun.* **2003**, *217*, 169.

(39) Nisoli, M.; Silvestri, S. D.; Svelto, O. *Appl. Phys. Lett.* **1996**, *68*, 2793.

(40) Nisoli, M.; Stagira, S.; Svelto, O.; Sartania, S.; Cheng, Z.; Lenzner, M.; Spielmann, C.; Krausz, F. *Appl. Phys. B.* **1997**, *65*, 189.

(41) West, B. A.; Moran, A. M. *J. Phys. Chem. Lett.* **2012**, *3*, 2575.

(42) West, B. A.; Womick, J. M.; Moran, A. M. *J. Chem. Phys.* **2011**, *135*, 114505.

(43) Jailaubekov, A. E.; Bradforth, S. E. *Appl. Phys. Lett.* **2005**, *87*, 021107:1.

(44) Durfee, C. G.; Misoguti, L.; Backus, S.; Kapteyn, H. C.; Murnane, M. M. *J. Opt. Soc. Am. B* **2002**, *19*, 822.

(45) Herbst, J.; Heyne, K.; Diller, R. *Science* **2002**, *297*, 822.

(46) Schenkl, S.; van Mourik, F.; van der Zwan, G.; Haacke, S.; Chergui, M. *Science* **2005**, *309*, 917.

(47) Brixner, T.; Mančal, T.; Stiopkin, I. V.; Fleming, G. R. *J. Chem. Phys.* **2004**, *121*, 4221.

(48) Vos, M. H.; Jones, M. R.; Hunter, C. N.; Breton, J.; Lambry, J.-C.; Martin, J.-L. *Biochemistry* **1994**, *33*, 6750.

(49) Brown, E.; Zhang, Q.; Dantus, M. *J. Chem. Phys* **1999**, *110*.

(50) Fayer, M. D. *Ann. Rev. Phys. Chem.* **1982**, *33*, 63.

(51) Nelson, K. A.; Caselegno, R.; Miller, R. J. D.; Fayer, M. D. *J. Chem. Phys.* **1982**, *77*, 1144.

(52) Knoester, J.; Mukamel, S. *Physics Reports* **1991**, *205*.

(53) Goodno, G. D.; Dadusc, G.; Miller, R. J. D. *J. Opt. Soc. Am. B* **1998**, *15*, 1791.

(54) Maznev, A. A.; Nelson, K. A.; Rogers, J. A. *Opt. Lett.* **1998**, *23*, 1319.

(55) Hara, T.; Nirota, N.; Terazima, M. *J. Phys. Chem.* **1996**, *100*, 10194.

(56) Goodno, G.; Dadusc, G.; Miller, R. J. D. *J. Opt. Soc. Am. B* **1998**, *15*.

(57) Terazima, M.; Hara, T.; Hirota, N. *Chem. Phys. Lett.* **1995**, *246*, 577.

(58) Vöhringer, P.; Scherer, N. F. *J. Phys. Chem.* **1995**, *99*, 2684.

(59) Jonas, D. M. *Ann. Rev. Phys. Chem.* **2003**, *54*, 425.

(60) Hybl, J. D.; Albrecht, A. W.; Gallagher Faeder, S. M.; Jonas, D. M. *Chem. Phys. Lett.* **1998**, *297*, 307.

(61) Lepetit, L.; Chériaux, G.; Joffre, M. *J. Opt. Soc. Am. B* **1995**, *12*, 2467.

(62) Moran, A. M.; Nome, R. A.; Scherer, N. F. *J. Chem. Phys.* **2006**, *125*.

(63) Brixner, T.; Mancal, T.; Stiopkin, I. V.; Fleming, G. R. *J. Chem. Phys.* **2004**, *121*, 4221.

(64) Pohl, D. W. *IBM J. Res. Dev.* **1979**, *23*, 604.

(65) Matsuo, S.; Tahara, T. *Chem. Phys. Lett.* **1997**, *264*, 636.

(66) Strauss, J.; Hundhausen, M.; Ley, L. *Appl. Phys. Lett.* **1996**, *69*, 875.

(67) Gundogdu, K.; Stone, K. W.; Turner, D. B.; Nelson, K. A. *Chem. Phys.* **2007**, *341*, 89.

(68) Kim, J.; Wong, C. Y.; Nair, P. S.; Fritz, K. P.; Kumar, S.; Scholes, G. D. *J. Phys. Chem. B* **2006**, *110*, 25371.

(69) Moran, A. M.; Maddox, J. B.; Hong, J. W.; Kim, J.; Nome, R. A.; Bazan, G. C.; Scherer, N. F. *J. Chem. Phys.* **2006**, *124*, 194904:1.

(70) Tauber, M. J.; Mathies, R. A.; Chen, X.; Bradforth, S. E. *Rev. Sci. Instrum.* **2003**, *74*.

CHAPTER 4: SPECTROSCOPY AND DYNAMICS OF PHOSPHONATE-DERIVITIZED RUTHENIUM COMPLEXES ON TiO_2[1]

4.1. Introduction

Chromophores covalently bound to nanocrystalline TiO_2 are ubiquitous in dye-sensitized solar cells and dye-sensitized photoelectrochemical cells.[1-9] One vital area of research aims to uncover the elementary dynamics initiated by light absorption at such molecule-semiconductor interfaces.[10-17] Although the subsequent processes (back electron transfer, charge recombination, etc.) are clearly of great consequence, it is the rate/efficiency of photoinduced electron transfer from the dye molecule to the semiconductor that underpins the availability of free charges, and thus the overall device performance. Electron injection rates depend not only on the energy levels of the chromophore and semiconductor of choice, but also on the (fluctuating) geometry of the dye molecule and its mode of binding to the surface.[17,18] An improved understanding of the relationship between surface binding motifs and electron transfer mechanisms will guide the design of new chromophores for use in high efficiency devices.[12]

The photophysical and electrochemical properties of the six phosphonated ruthenium complexes shown in Figure 4.1 were recently investigated in solution and on ZrO_2 and TiO_2 surfaces.[19] Emission lifetimes, electron injection yields, back electron transfer rates, and other properties were compared. The electron injection yields were found to decrease with an increase in the number of phosphonate ligands, whereas all complexes exhibited similar back electron

[1] This article previously appeared as an article in the Journal of Physical Chemistry C. The original citation is as follows: Giokas, P.G., Miller, S.A., Hanson, K., Norris, M.R., Glasson, C.R.K., Concepcion, J.J., Bettis, S.E., Meyer, T.J., Moran, A.M. *J. Phys. Chem. C.* **2013**, *117*, 812-824.

transfer efficiencies. These results suggested a competition between electron diffusion from the surface into the particle interior and Coulombic attraction to the photo-oxidized dye molecule. Overall, molecules **1** and **2** possessed the best combination of photostabilities and electron injection efficiencies. These earlier measurements were limited to time scales greater than 10 ns. Sub-picosecond electron transfer processes are largely unexplored in this family of ruthenium complexes.

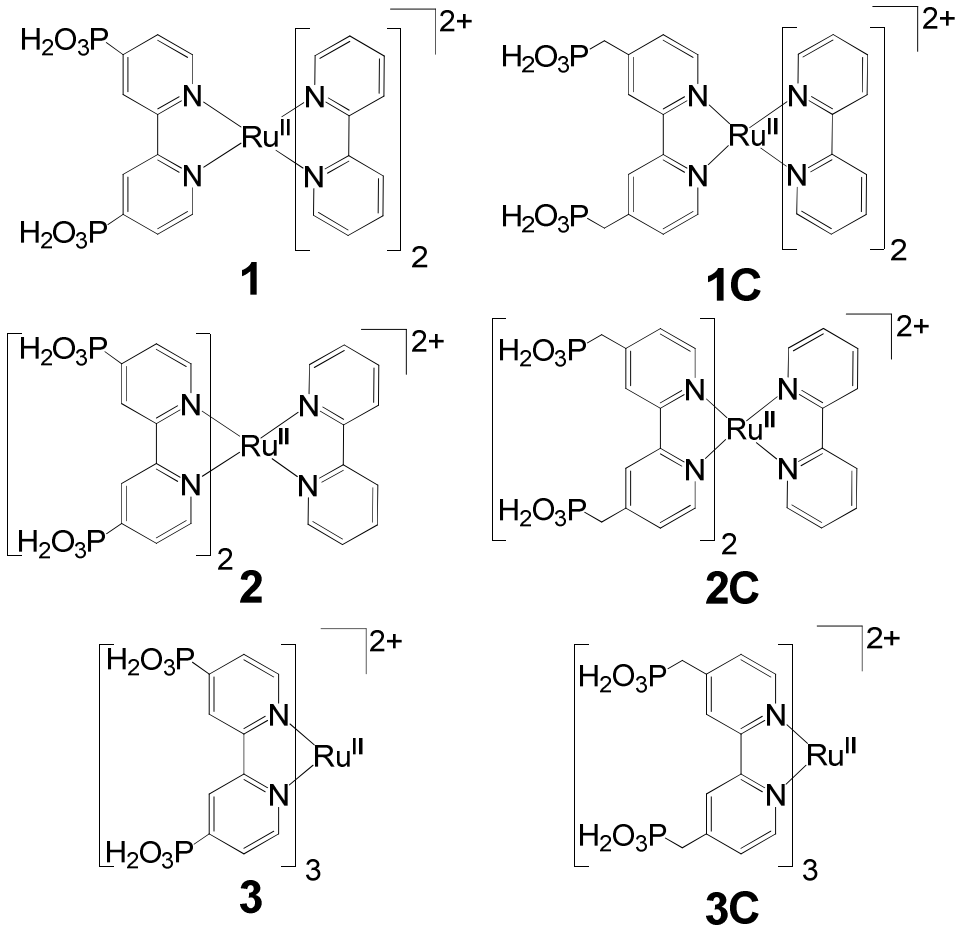

Figure 4.1: Molecular structures of phosphonated ruthenium complexes.

In this report, we expand upon earlier measurements of **1**-**3** and **1C**-**3C** on nanocrystalline TiO_2 with two primary areas of focus: (1) the vibronic couplings associated with the singlet metal-to-ligand charge-transfer transitions (^{1}MLCT); (2) the photoinduced electron transfer

dynamics of the chromophores on TiO_2. A resonance Raman intensity analysis is first applied to the ^{1}MLCT transitions of the six complexes.[20] We determine the reorganization energies for the solvent and all Franck-Condon active intramolecular vibrational modes. Vibrational signatures of the surface binding motifs are also examined. The molecular geometry has a readily interpreted impact on the electron injection dynamics, whereas conclusions regarding the implications of the Franck-Condon couplings must be more carefully drawn. It is suggested that correlated thermal fluctuations of the ligands, which are a natural consequence of their close proximity, may reduce the fluctuation amplitudes governing both spectroscopic line broadening and non-radiative transitions between excited electronic states. One transition of particular importance is internal conversion between MLCT states on different ligands (hereafter termed MLCT interconversion or dipole transfer).[21] This process influences the molecule-TiO_2 electron injection rate by moving the electron excitation between ligands that are either bound or unbound to the TiO_2 surface. Time-resolved transient absorption experiments are also used to probe the electron injection dynamics for all six molecules adsorbed on TiO_2. Injection is found to occur from both the ^{1}MLCT and ^{3}MLCT states of the chromophores. The rates of electron injection, which depend sensitively on the relative molecule-TiO_2 coupling strengths, are discussed in the context of the resonance Raman intensity analysis.

Much of the basic photophysics uncovered in TiO_2 films derivatized with other ruthenium complexes translates to the present systems.[13,22] In all systems, light absorption by the ruthenium complex initiates a series of processes. The molecules considered here possess low-lying ^{1}MLCT transitions based on each of the three polypyridyl ligands, so the photoexcitation is not necessarily (initially) located on the ligand that is directly bonded to the TiO_2 film. In cases where the bonded ligand absorbs light, electron injection into TiO_2 occurs in two phases. First,

the ^{1}MLCT state transfers an electron into TiO_2 in less than 100fs. Alternatively, the process slows down by 1-2 orders of magnitude when intersystem crossing in the molecule precedes electron transfer, because the reduction potential for the ^{3}MLCT state as an electron donor is near the bottom of the conduction band of TiO_2 where the density of states is relatively low. By contrast, when a non-bonded ligand absorbs light, it undergoes a sub-ps intersystem crossing transition before MLCT interconversion transfers the excitation onto the ligand(s) bonded to TiO_2. Interconversion between low-lying MLCT states by dipole reorientation is one of the rate limiting steps in the injection process for the present systems. Inter ligand electron transfer (ILET), which involves transfer of the electron but not the vacant orbital, is slower than dipole reorientation because it interconverts higher energy MLCT states.[21] The transient absorption methods employed here, which probe the systems in the visible wavelength range, are primarily sensitive to processes in which the ligand directly bonded to TiO_2 is photoexcited. Dipole reorientation is best probed in the near UV spectral range, where the bipyridine radical absorbs.[23,24]

4.2. Background on Spectral Fitting and Physical Interpretations of Parameters

In this Section, we summarize the spectral fitting algorithm and examine the physical insights provided by its parameters. The physics are first discussed from a semi-quantitative (geometric) perspective. We then address the underlying dynamics in a more quantitative way with a time correlation function approach. The goal here is to define a basis for thinking about the information provided by the spectroscopic measurements presented in Section 4.4. The properties under investigation hold implications for electron injection, dipole reorientation, and other processes relevant to device performance.

4.2.A. Algorithm for Resonance Raman Intensity Analysis

Below, we employ a well-established model for analyzing resonance Raman intensities.[20,25] The principal motivation for this approach is that the Franck-Condon progressions associated with intramolecular modes of a chromophore are hidden by broad absorbance line widths in solution.[26] Resonance Raman measurements provide information about the forces exerted on particular intramolecular modes following photoexcitation despite such broad line widths.

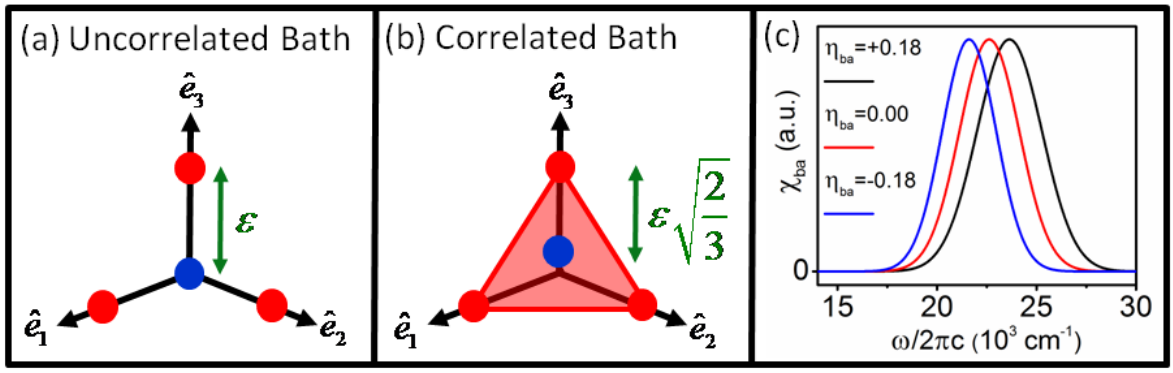

Figure 4.2: Diagram of Solvent Fluctuation Coordinates. (a) Each ^{1}MLCT transition is coupled to an independent solvent coordinate when fluctuations are uncorrelated. The blue and red points represent free energy minima associated with the ground and excited electronic states, respectively. All energy gaps are linear in the displacements between free energy minima when the surfaces possess the same curvatures. Here the gap changes by ε between the ground and excited state energy minima (i.e., the reorganization energy is $\varepsilon / 2$). (b) One experimentally tested representation projects the ground state surface onto a plane connecting the three ^{1}MLCT minima (see Reference [24]). Correlated ground and excited state energy level fluctuations reduce the sizes of the displacements to $\varepsilon\sqrt{2/3}$ and the reorganization energies to $\varepsilon\sqrt{1/6}$. (c) Absorbance line shapes computed using Equation (4.12) with different correlation parameters; ΔG_{ba}^{0} =17000cm^{-1} and $\Delta_{aa} = \Delta_{bb}$ =750cm^{-1} in all calculations.

Iterative fitting of both the linear absorbance spectrum and the Raman cross sections is leveraged in the model to obtain the Franck-Condon factor for each intramolecular mode, the electronic origin of the transition (0-0 transition), the solvent reorganization energy, and the relative contributions of homogeneous and inhomogeneous line broadening mechanisms. The linear absorbance line shape is simulated using

$$\sigma_A(\omega) = \frac{4\pi\omega\mu_0^2}{3\hbar c}\sum_{m=1} P_m \,\mathrm{Re}\int_{-\infty}^{\infty} d\delta G(\delta)\int_0^{\infty} dt \left\langle m \middle| m(t) \right\rangle \exp\left[i\left(\omega - \omega_0 - \delta + \omega_m\right)t - g(t)\right]. \quad \textbf{(0.1)}$$

where m is an index for a nuclear mode, P_m is the Boltzmann population of the initial state, μ_0 is the electronic transition dipole, ω_m is the mode frequency, ω_0 is the purely electronic transition frequency, and $\left\langle m \middle| m(t) \right\rangle$ is a dynamic overlap integral between nuclear wavefunctions (whose Fourier transform is a Franck-Condon progression).[27] The key parameters governing $\left\langle m \middle| m(t) \right\rangle$ are the dimensionless displacements between the ground and excited state (harmonic) potentials, d_m; the displacements are converted to intramolecular mode-specific reorganization energies using $\lambda_m = \hbar\omega_m d_m^2/2$. Fluctuations in the resonance frequency induced by thermal motion in the solvent are partitioned into fast (homogeneous) and slow (inhomogeneous) components. Inhomogeneous line broadening is incorporated by integrating over the static Gaussian distribution, $G(\delta)$. The homogeneous line shape is simulated with the line broadening function

$$g(t) = \left(\frac{2\lambda k_B T}{\Lambda^2} - i\frac{\lambda}{\Lambda}\right)\left[\exp(-\Lambda t) + \Lambda t - 1\right], \quad \textbf{(0.2)}$$

where λ is the reorganization energy for the homogeneous bath coordinate and Λ^{-1} is the characteristic time scale for thermal motion.

The resonance Raman response depends on the same parameters governing $\sigma_A(\omega)$. The differential resonance Raman cross section is written as

$$\sigma_{R,mn}(\omega) = \frac{4\omega_S^3\omega_L}{15c^4}\sum_{mn} P_m \int d\omega_S \int_{-\infty}^{\infty} d\delta G(\delta) L_{mn}\left(\omega_L - \omega_S\right)\left|\alpha_{mn}\left(\omega_L,\delta\right)\right|^2 , \qquad \textbf{(0.3)}$$

where m (n) is an index for the initial (final) vibrational state, ω_L (ω_S) is the incident (scattered) light frequency, and $L_{mn}\left(\omega_L - \omega_S\right)$ is the normalized line shape of the $m \to n$ ground state vibrational transition. The integral with respect to ω_S extends over the full Raman emission band. The Raman polarizability is given by

$$\alpha_{mn}(\omega_L,\delta) = \frac{\mu_0^2}{\hbar}\int_0^{\infty} dt \left\langle n\middle|m(t)\right\rangle \exp\left[i\left(\omega_L - \omega_0 - \delta + \omega_m\right)t - g(t)\right] . \qquad \textbf{(0.4)}$$

The resemblance between $\alpha_{mn}(\omega_L,\delta)$ and $\sigma_A(\omega)$ makes clear the origin of the resonance enhancement. The cancellation between the laser frequency, ω_L, and the electronic (vibronic) resonance frequency, $\omega_0 + \delta - \omega_m$, enhances the magnitude of $\alpha_{mn}(\omega_L,\delta)$ by keeping the sign of the integrand from oscillating.

4.2.B. Nature of Solvent Coordinates in Ruthenium Complexes

The optical transitions investigated in this work are primarily localized on the ruthenium complexes, which all possess ^{1}MLCT transitions near 22000cm^{-1} (455nm). The three bipyridine

ligands couple to common solvent motions because they are in close proximity. Correlated thermal fluctuations in the three ^{1}MLCT resonance frequencies may naturally arise, and impact the nature of the solvent coordinates that govern the optical line shapes. Here we consider the physical meaning of the solvent coordinates and associated fitting parameters in the model outlined above. The discussion takes inspiration from earlier work in which a two-dimensional representation of the free energy surfaces of the closely related molecule, $[Os^{II}(bpy)_3]^{2+}$, was proposed and shown to correctly describe linear and nonlinear spectroscopic measurements.[23,24] It is shown below from a different perspective why the collective nature of the solvent motion holds important implications for both radiative and non-radiative processes.

The spectrum of thermal fluctuations for a molecule in solution at ambient conditions is generally continuous and peaks at an energy less than k_BT.[26,28] Because the spectrum is (quasi-)continuous, it is often sufficient to describe the thermal fluctuations with a single solvent coordinate. Different phenomenological forms for the spectral density of solvent-induced fluctuations can be used (e.g., Brownian oscillator, Ohmic), but they all support essentially the same insights. Brownian oscillator spectral densities are used in the present model. The static limit has been assumed for the inhomogeneous coordinate, whereas the damping function for the homogeneous coordinate, $g(t)$, interpolates between the static ($\lambda >> \Lambda$) and motionally narrowed ($\lambda << \Lambda$) limits.

The two-dimensional representation of the solvent coordinates previously applied to $[Os^{II}(bpy)_3]^{2+}$ suggests that, while the transitions are localized on individual ligands, light absorption on one ligand induces relaxation in the solvent molecules surrounding the neighboring ligands. It follows that the spatial extent of a thermal fluctuation in the solvent encompasses all three ligands. These physics enter the present model by way of temporal

correlations in the electronic resonance frequencies. Such correlation effects have been treated from various perspectives.[29-32] Ultimately, the physics can be qualitatively understood in terms of the apparent amount of thermal noise "felt" by a particular ^{1}MLCT resonance. For a bath with Gaussian statistics, such noise reduction translates into smaller displacements in the free energy surfaces associated with the ground and excited states.[26] As shown in Figure 4.2, correlation effects reduce the reorganization energy for the ^{1}MLCT transition if the three ligands are indistinguishable, where the comparison is made to a limiting case in which each of the three ^{1}MLCT resonances couple to completely independent solvent motions. These correlation effects are reminiscent of exchange narrowing process in molecular crystals and photosynthetic complexes.[33,34] However, in the ruthenium complexes, the key difference is (apparently) that line narrowing originates in suppressed fluctuations of the (local) ^{1}MLCT resonance frequencies and not from the delocalization of excited states.

4.2.C. Correlated Line Broadening in Ruthenium Complexes

The geometric interpretation of solvation in the ruthenium complexes presented above is translated into the language of correlation functions in this Section. At first order in perturbation theory, the linear absorbance line shape can be written as a time correlation function in the transition dipole, $\hat{\mu}_0$, between the ground and excited electronic states

$$\chi(\omega) = \frac{1}{\hbar^2} \mathrm{Re} \int_{-\infty}^{\infty} dt \left\langle \hat{\mu}_0(t) \hat{\mu}_0(0) \right\rangle \exp(i\omega t) \ . \qquad \textbf{(0.5)}$$

The spectrum can then be expanded in a basis of electronic states[35]

$$\chi_{ba}(\omega)=\frac{1}{\hbar^2}\mathrm{Re}\int_{-\infty}^{\infty}dt\langle a|\exp\left(i\hat{H}t/\hbar\right)\hat{\mu}|b\rangle\langle b|\exp\left(-i\hat{H}t/\hbar\right)\hat{\mu}(0)|a\rangle\exp(i\omega t)\ , \qquad \textbf{(0.6)}$$

where the indices a and b respectively correspond to initial and final states, and contributions from thermal excitations are assumed to be negligible. Matrix elements involving the perturbative operator can be taken outside the ensemble average when $\hat{\mu}_0$ depends weakly on nuclear motion (i.e., the Condon approximation). The line shape can then be written as[26,35]

$$\chi_{ba}(\omega)=\frac{1}{\hbar^2}|\mu_{ba}|^2\,\mathrm{Re}\int_{-\infty}^{\infty}dt\exp\left[i\omega t-i\left(E_b-E_a\right)t/\hbar\right]\left\langle\exp_+\left[-i\int_0^t dt'\left(Q_a(t')-Q_b(t')\right)\right]\right\rangle, \textbf{(0.7)}$$

where $Q_a(t)$ and $Q_b(t)$ are primary Brownian oscillator coordinates coupled to energy levels a and b. Under the assumption of Gaussian statistics, a cumulant expansion yields[26,35]

$$\chi_{ba}(\omega)=\frac{1}{\hbar^2}|\mu_{ba}|^2\,\mathrm{Re}\int_{-\infty}^{\infty}dt\exp\left[i\omega t-i\Delta G_{ba}^0 t/\hbar-i\lambda_{ba}t/\hbar-g_{aa}(t)-g_{bb}(t)+2g_{ab}(t)\right]\ , \textbf{(0.8)}$$

where λ_{ba} is the reorganization energy, ΔG_{ba}^0 is the free energy gap between states b and a, $g_{aa}(t)$ ($g_{bb}(t)$) is a damping function that describes the fluctuation statistics for level a (b), and $g_{ab}(t)$ encodes correlations between levels a and b.

The underlying physics are made clear by assuming: (i) that the motion in the primary Brownian oscillator coordinates, $Q_a(t)$ and $Q_b(t)$, are overdamped; (ii) the standard deviations in the energy level fluctuations, Δ_{aa} and Δ_{bb}, are large compared to their relaxation rates. The damping functions can then be written as

$$g_{aa}(t) = \frac{1}{2\hbar^2}\Delta_{aa}^2 t^2 \ , \tag{0.9}$$

$$g_{bb}(t) = \frac{1}{2\hbar^2}\Delta_{bb}^2 t^2 \ , \tag{0.10}$$

$$g_{ab}(t) = \frac{1}{2\hbar^2}\eta_{ba}\Delta_{bb}\Delta_{aa} t^2 \ , \tag{0.11}$$

where the parameter, η_{ba}, interpolates between the limits of fully correlated, η_{ba}=1, and fully anti-correlated, η_{ba}=-1, fluctuations.[29] By combining Equations (8)-(11) and evaluating the time integral, we obtain

$$\chi_{ba}(\omega) = \frac{\sqrt{\pi}}{\hbar}\frac{|\mu_{ba}|^2}{\sqrt{\lambda_{ba}k_B T}}\exp\left[\frac{-\left(\hbar\omega - \Delta G_{ba}^0 + \lambda_{ba}\right)^2}{4\lambda_{ba}k_B T}\right] , \tag{0.12}$$

where the reorganization energy associated with light absorption is

$$\lambda_{ba} = \frac{\Delta_{bb}^2 + \Delta_{aa}^2 - 2\eta_{ba}\Delta_{bb}\Delta_{aa}}{2k_B T} \ . \tag{0.13}$$

Equation (4.13) provides a basis for quantifying the amount of correlation implied by the two-dimensional representation of the solvent coordinates. The geometric argument presented in Figure 4.2 suggests that correlations reduce the amount of reorganization energy by a factor of

$\sqrt{2/3}$. Under the approximation that $\Delta_{bb} \approx \Delta_{aa}$, the fluctuation statistics are then consistent with a correlation parameter of $\eta_{ba} \approx 0.18$. The calculated absorbance line shapes shown in Figure 4.2 suggest that even this modest amount of correlation has a significant impact on the absorbance spectrum.

It is also interesting to consider the implications of correlated fluctuations on the non-radiative transitions that occur subsequent to photoexcitation. A rate formula for electron transfer can be derived by the exactly same steps used to obtain Equation (12) if we start with a correlation[36,37] function in the electron donor-acceptor coupling, V_{DA}. The electron transfer rate is then given by a Marcus-like equation

$$K_{DA}^{ILET} = \frac{\sqrt{\pi}}{\hbar} \frac{|V_{DA}|^2}{\sqrt{\lambda_{DA} k_B T}} \exp\left[\frac{-\left(\Delta G_{DA}^0 + \lambda_{DA}\right)^2}{4\lambda_{DA} k_B T} \right], \qquad \textbf{(0.14)}$$

where D and A are the initial and final states involved in the ILET. Correlation effects influence the ILET rate by increasing or decreasing the magnitude of the reorganization energy, λ_{DA}. For example, Equation (14) indicates that an activationless transition is found under the condition

$$\eta_{DA} = \frac{\Delta_{AA}^2 + \Delta_{DD}^2 + 2k_B T \Delta G_{DA}^0}{2\Delta_{AA}\Delta_{DD}} \ . \qquad \textbf{(0.15)}$$

While spectroscopic measurements do not directly probe the correlation effects that control ILET, it is reasonable to assume that such correlations similarly influence both radiative and non-radiative processes.

As discussed above, MLCT interconversion is a second class of non-radiative processes initiated by light absorption.[21] The initial (i) and final (f) states in the MLCT interconversion processes are coupled by the nuclear kinetic energy operator. The rate formula for such internal conversion transitions generally sums over relaxation channels defined by particular "promoting modes". Still, the present time correlation function framework is readily adapted.[36,37] Equation (8) can be rewritten as

$$K_{fi}^{IC} = \frac{1}{\hbar^2} V_{fi} \,\mathrm{Re} \int_{-\infty}^{\infty} dt\, \Phi_{fi}(t) \exp\left[i\omega t - i\Delta G_{fi}^{0} t/\hbar - i\lambda_{fi} t/\hbar - g_{fi}(t) - g_{fi}(t) + 2g_{fi}(t) \right]. \quad \textbf{(0.16)}$$

The correlation function for the promoting mode is[36,37]

$$\Phi_{fi}^{p}(t) \approx \frac{\omega_p}{2\hbar} \exp\left(-i\omega_p t\right) , \quad \textbf{(0.17)}$$

where ω_p is the harmonic mode frequency and n is the quantum number. The electronic coupling between the initial and final states is given by

$$\left|V_{fi}\right|^2 = \hbar^2 \left| \left\langle \psi_f \right| \frac{\partial}{\partial Q_p} \left| \psi_i \right\rangle \right|^2 . \quad \textbf{(0.18)}$$

Use of $\Phi_{fi}^{p}(t)$ makes two key assumptions: (i) the frequency of the promoting mode is taken to be larger than $k_B T$ (this is the reason for the $\approx$ sign); (ii) the displacement in the promoting mode is small enough to neglect, which is a fair approximation for the present systems (cf., Tables 4.1 and 4.2). Under the same approximations that lead to Equation (12), we have

$$K_{fi}^{IC} = \frac{\omega_p \sqrt{\pi}}{2\hbar^2} \frac{\left|V_{fi}\right|^2}{\sqrt{\lambda_{fi} k_B T}} \exp\left[\frac{-\left(\Delta G_{fi}^{0} + \hbar\omega_p + \lambda_{fi}\right)^2}{4\lambda_{fi} k_B T} \right] . \quad \textbf{(0.19)}$$

Table 4.1. Resonance Raman fitting parameters for all complexes in methanol.

[a]Parameter	1	2	3	1C	2C	3C	
ω_0 (cm^{-1})	21800	21690	21400	20930	21790	21040	
δ (cm^{-1})	1180	1200	1370	1220	1525	1600	
λ (cm^{-1})	870	935	923	1000	940	970	
[b] $\lambda + \delta^2 / 2k_BT$ (cm^{-1})	4190	4360	5390	4540	6480	7065	
μ_0 (D)	4.90	6.72	6.90	6.24	6.87	6.48	
Raman Shift(cm^{-1})	**λ(cm^{-1})**						**[c]Assignment**
667	2.4	1.2	0.8	8.9	1.5		Bend
724	1.2	2.3	2.0				PO_3H_2 bend
1030	1.7	0.5	1.2				bpy ring breathing
1172	3.7	1.2	9.9	8.7	2.0		CCH bend
1248	4.0	5.0	2.3				bpy inter-ring str.
1274	9.6	7.1	19.1	4.0	5.8	16.1	bpy inter ring str.
1316	15.7	11.7		20.6	10.0	18.8	bpy inter ring str.
1404	0.2	1.08	2.5				unbound P-bpy str.
1485		15.7		59.9	10.9	26.5	bpy ring str.
1529	26.2	25.4	51.7				bpy ring str.
1554	13.4	6.0		40.8	27.3	65.4	bpy ring str.
1608	11.6	6.5	10.5	11.4	7.9	23.0	bpy ring str.

[a] Uncertainties for all parameters range from 20-30% (cf., Supporting Information).

[b] Estimate of total solvent reorganization energy.

[c] Parameters and assignments for additional modes are given in the Supporting Information.

For the present systems, Equation (4.19) makes clear that a correlated bath either enhances or suppresses the MLCT interconversion rate in a way that is similar to ILET. The MLCT interconversion rate maximizes when

$$\eta_{fi} = \frac{\Delta_{ff}^2 + \Delta_{ii}^2 + 2k_BT\left(\Delta G_{fi}^0 + \hbar\omega_p\right)}{2\Delta_{ff}\Delta_{ii}} \quad . \qquad \textbf{(0.20)}$$

Table 4.2. Resonance Raman fitting parameters for all complexes on TiO_2 films

	1	2	3	1C	2C	3C	
ω_0 (cm^{-1})	21800	22170	21835	22050	21850	21090	
δ (cm^{-1})	2390	2070	2050	1700	1580	2150	
λ (cm^{-1})	640	400	430	270	600	410	
[b] $\lambda + \delta^2 / 2k_BT$ (cm^{-1})	14240	10600	10440	7150	6540	11420	
μ_0 (D)	4.66	6.20	6.20	5.86	6.02	5.35	
Raman Shift(cm^{-1})	**λ(cm^{-1})**						**[c]Assignment**
726	2.1	1.3	2.8				PO_3H_2 bend
1028	7.7	5.6	6.7	14.3	3.7	8.8	bpy ring breathing
1248	11.4	5.1	14.0		1.4		bpy inter ring str.
1274	15.1	8.9	12.1	19.9	6.0	9.7	bpy inter ring str.
1318	23.8	12.4	22.6	31.9	9.8	21.4	bpy inter ring str.
1410		0.9	4.4				unbound P-bpy str.
1474	80.8	18.9	51.4				bpy ring str.
1487		18.2		93.6	30.6	66.9	bpy ring str.
1530	78.3	43.0	81.3				bpy ring str.
1554	25.2	12.9		92.7	31.7	84.6	bpy ring str.
1609	35.5	17.2	29.7	42.6	13.5	23.9	bpy ring str.

[a] Uncertainties for all parameters range from 20-30% (cf., Supporting Information).

[b] Total solvent reorganization energy cannot be estimated because inhomogeneous line width is dominated by geometric heterogeneity at interface.

[c] Parameters and assignments for additional modes are given in the Supporting Information.

The dependence of the rate on the correlation parameter, η_{fi}, differs from K_{DA}^{ILET} in that MLCT interconversion must involve a change in the number of vibrational quanta of the promoting mode. That is, intramolecular modes can be explicitly added to K_{DA}^{ILET}, but it is nonetheless possible for the coordinates to possess the same numbers of vibrational quanta in the

initial and final states.[38] Such relaxation channels may even dominate in systems with relatively small displacements, because they correspond to the largest Franck Condon factors.

4.3. Experimental Methods

Ruthenium complexes and TiO_2 films are prepared according to previously published procedures.[19,39] The 7 μm thick films are composed of anatase TiO_2 nanoparticles (~20 nm diameter) coated on fluorine-doped SnO_2 glass slides. The TiO_2 films are dye-derivatized by soaking them in an aqueous solution that is 100 μM in the ruthenium complex and 0.1 M in $HClO_4$ for approximately 2 hours. The films are then rinsed thoroughly with aqueous 0.1 M $HClO_4$ to remove excess, non-adsorbed dye. Prior to data collection, the films are stored in the dark under nitrogen to prevent degradation. During the experiments, the films are contained in a homemade cuvette with the samples immersed in a 60 μM triethanolamine aqueous solution (pH = 6.7) to quench long lived photoexcitations. Both the dye-sensitized films and solutions are moved continuously during the TA experiments using both a rotary motor and linear actuator. Absorbance spectra are measured before and after data collection to rule out contributions from sample degradation. Further details on the cuvette and sample mount are given in the Supporting Information (SI).

Linear absorption spectra of dye-sensitized films and the solutions are measured with a Hewlett Packard 8453 UV-Vis-NIR spectrometer. Raman spectra are collected with a Renishaw Via- Leica DM2500 M microscope. Raman excitation is accomplished using the 21840, 20490, and 19440 cm^{-1} laser lines of an Argon ion laser (Spectra Physics Stabilite 2017). In the Raman measurements, approximately 20 μW laser beams are focused onto the sample with a Leica N PLAN EPI 50x/0.75 objective lens, which is also used to collect the scattered Raman emission in

a confocal geometry. Immediately before data collection, the films are wetted with methanol and a 0.2 mm thick borosilicate microscope coverslip is placed over the film to suppress evaporation of the methanol solvent. During data collection, the films are continuously oscillated at approximately 2 μm s^{-1} to prevent photobleaching.

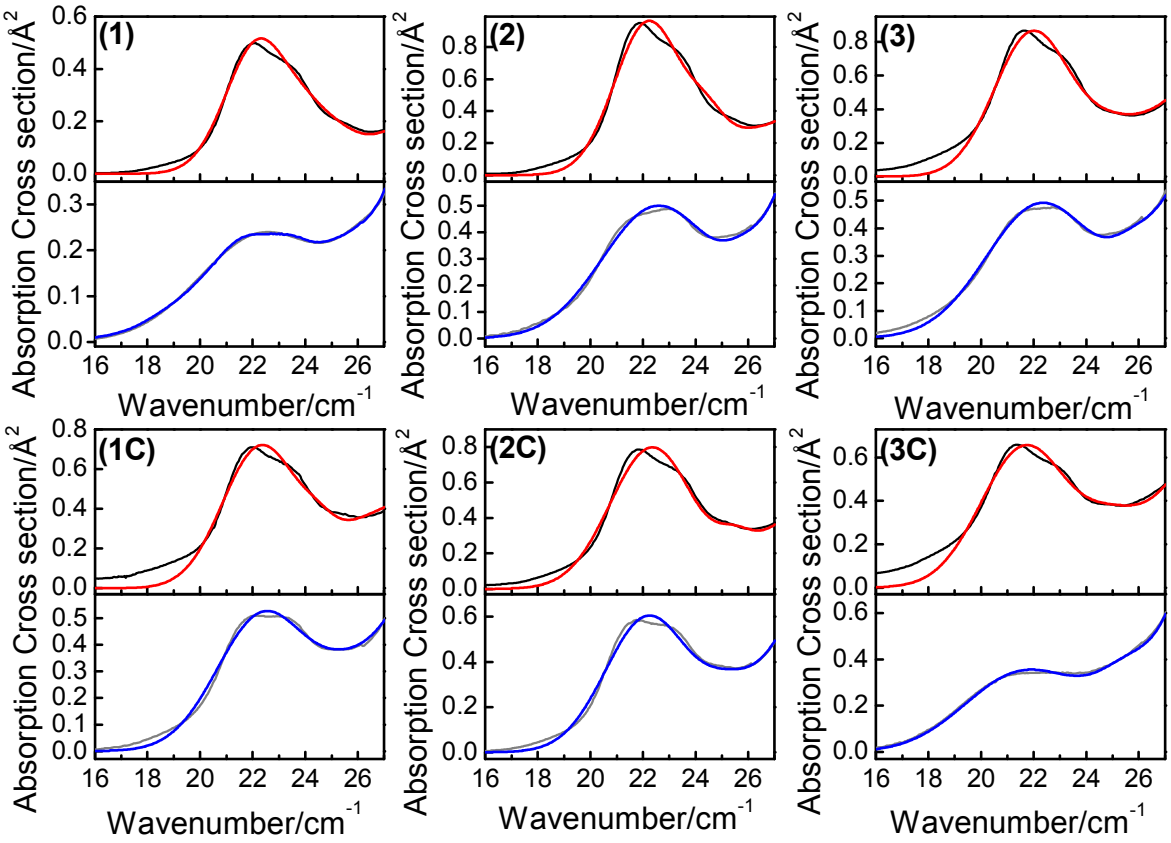

Figure 4.3: Measured absorbance spectra of all molecules in methanol (black lines) and adsorbed on nanocrystalline TiO_2 films (gray lines). Fits of the spectra (red = in methanol, blue = on TiO_2) are generated with Equation (1). The molecular sensitizers are indicated in each pair of panels.

For Raman measurements of the solutions (not films), the sample concentrations are approximately 400 μM. Approximately 2 mW laser beams are focused into the solutions, which were held in 2mm thick cuvettes and Raman scattering was collected using a Leica N PLAN EPI

5x/0.12 objective lens in a backscattering geometry. Reabsorption of the Raman emission is corrected using an established procedure.[40]

In the transient absorption (TA) experiments, the ^{1}MLCT transitions of all samples are excited with 45 fs, 400 nm, 1.5 μJ pump pulses. Relaxation processes are then monitored with 470-950nm continuum probe pulses, which are polarized at the magic angle with respect to the 400nm pump pulses. All laser beams are derived from a Ti:Sapphire laser system operating at a 1kHz repetition rate. The pump pulses are focused to a FWHM spot size of 500μm at the sample position. The laser fluence of 1.5×10^{15} photons/cm^2 excites approximately 10% of the molecules in the focal volume. Increasing or decreasing the laser fluence by a factor of 3 does not produce a measurable effect on the TA signals. The continuum probe pulses are focused to a spot size of 300 μm at the sample position. Dispersion in the probe pulses is corrected for numerically following data collection. Signals are collected with a ThorLabs CCS200 spectrometer that is synchronized to an optical chopper wheel at 83Hz (alternating 6 shots with "pump-on" and 6 shots with "pump-off"). Approximately 100 differences are collected at each time point in a single scan of the pump-probe delay line. The scans are repeated 15-30 times and averaged.

4.4. Results and Discussion

4.4.A. Analysis of Linear Absorption Line Shapes

Absorbance spectra of the six ruthenium complexes in solution and on nancrystallineTiO_2 films are shown in Figure 4.3. All spectra exhibit continuous absorption from 20000-25000cm^{-1} arising from overlapping ^{1}MLCT transitions.[19,41] Contributions from nominally spin-forbidden triplet metal-to-ligand charge transfer transitions (^{3}MLCT) are observed below 20,000 cm^{-1}.[42-44] Higher frequency absorption bands, which represent bipyridine-localized π-π^* transitions,

contribute above 26000cm^{-1}, but are masked by absorption and light scattering on the TiO_2 films.[19,41] The ^{1}MLCT absorption bands reveal (weakly modulated) vibronic progressions with periods of roughly 1570cm^{-1}, indicating the presence of moderate coupling between the electronic transition and C=C/C=N bond stretching mode(s) in the bipyridine ligands.[45-48] Notably, the progressions differ between the dye-sensitized films and the methanol solutions. These observations are consistent with studies of related systems, where molecule-TiO_2 interactions were shown to significantly alter intramolecular vibronic coupling strengths.[49-51]

Overlaid with the experimental absorption spectra in Figure 4.3 are fits conducted with Equation (1). Constraints on the parameters are applied by simultaneous fitting of the resonance Raman data discussed in the following section. The lower-frequency portions of the absorbance line shapes near 18000cm^{-1} possess contributions from ^{3}MLCT transitions, which leads to discrepancies between the measurements and calculations in this spectral region.[19,41-44,51] Gaussian line shapes are added in the 24000-32500cm^{-1} range to estimate the contributions of higher frequency resonances to the blue sides of the ^{1}MLCT bands (cf., Figures S19-S20 in the SI). The absorbance line shapes are primarily sensitive to the electronic origins, ω_0, and the solvation parameters, λ and δ. The differences in the electronic origins of the various complexes cannot be distinguished within experimental error (cf., Tables 4.1 and 4.2). It is also difficult to establish experimentally significant trends in λ and δ because of the challenge in partitioning the homogeneous and inhomogeneous contributions to the absorbance line widths. However, by summing λ and $\delta^2 / 2k_BT$, the total solvent reorganization energy in solution can be estimated without invoking such a separation in time scales, thereby yielding clear trends for both the **1**-**3** and **1C**-**3C** series of molecules. The total solvent reorganization energy increases steeply with the number of phosphonated ligands, and the effect is most pronounced in the **1C**-

3C molecules. It stands to reason that the phosphonate groups mediate strong solute-solvent interactions because they form relatively strong hydrogen bonds with methanol. In contrast with the solutions, the dye-sensitized films do not exhibit an experimentally significant pattern because the inhomogeneous part of the line shape is dominated by heterogeneity in the molecular geometries at the interface rather that solute-solvent interactions.

4.4.B. Resonance Raman Measurements

Qualitatively, resonance Raman spectra provide information on the part of the molecule that is most responsive to the applied radiation. The transition density represents the spatial distribution of the charge oscillations driven by light absorption. Thus, vibrational modes with the largest Franck-Condon factors are generally found in regions of space where the transition density is most concentrated. In this Section, we interpret resonance Raman data with these general ideas in mind. The systems under investigation possess numerous Franck-Condon active vibrations. We focus on the modes that yield the most direct insights into the nature of the electronic structure at the interface. A key consideration for us is whether or not the photoexcitations possess molecule-to-TiO_2 charge transfer character.[51] Light absorption and electron transfer are one in the same process when such wave function delocalization takes hold.[10,51] A sequential mechanism in which light absorption precedes electron transfer is operative in the opposite (non-adiabatic) limit of localized states.

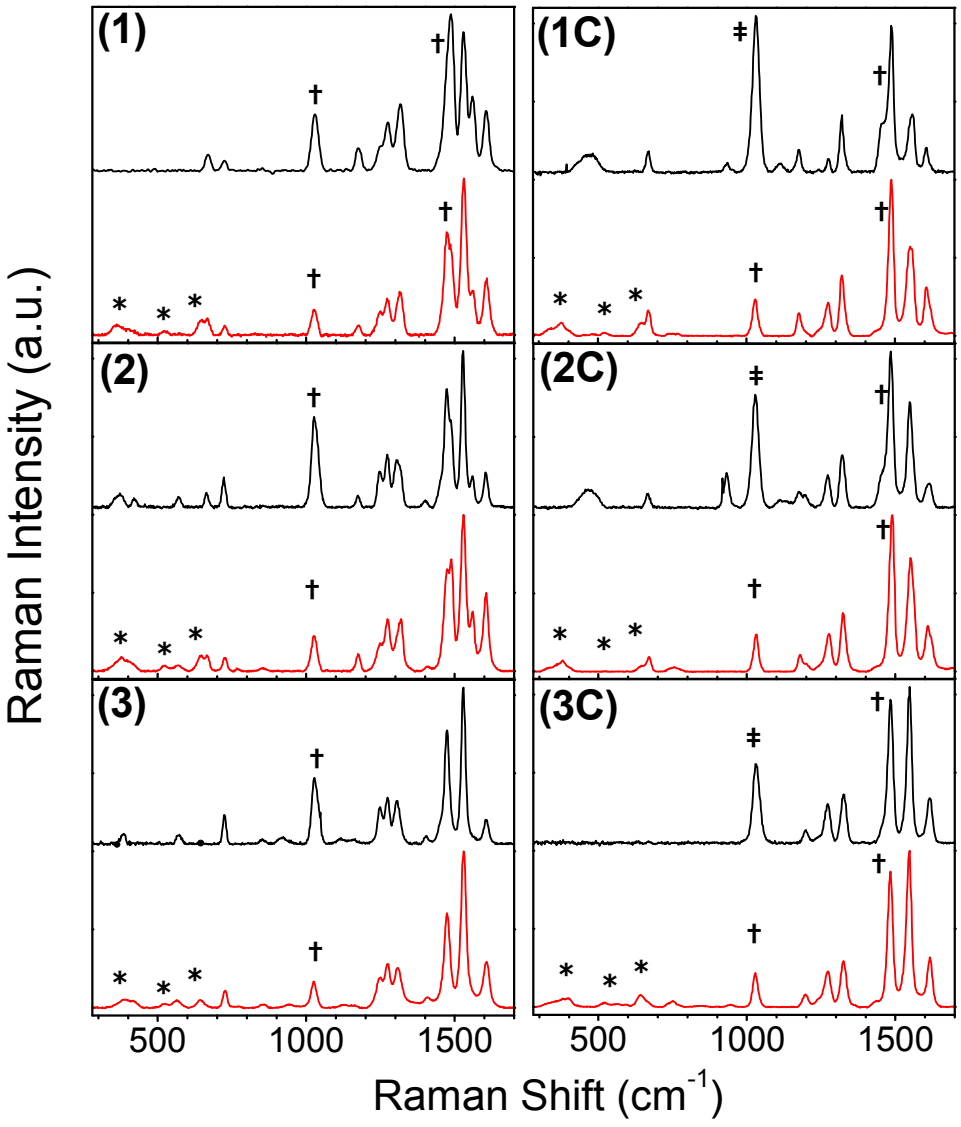

Figure 4.4: Resonance Raman spectra for **1-3** (left) and **1C-3C** (right) measured in methanol solutions (black) and on TiO_2 films wetted with methanol (red). Vibrational resonances of TiO_2 and methanol marked with an asterisks and daggers, respectively.

Raman spectra of all molecules in methanol and adsorbed on TiO_2 are shown in Figure 4.4. The vibrational mode assignments given in Tables 4.1 and 4.2 are based primarily on earlier studies of related ruthenium bipyridyl complexes.[42,45-47,49,52] All Raman spectra are dominated

by C=C/C=N stretching modes on the bipyridine ligands near 1550cm^{-1}. Additional Franck-Condon active vibrations include bipyridine inter-ring stretching modes in the 1250-1320cm^{-1} range and ring-breathing modes near 1030 cm^{-1} (these consist mostly of bending motions).

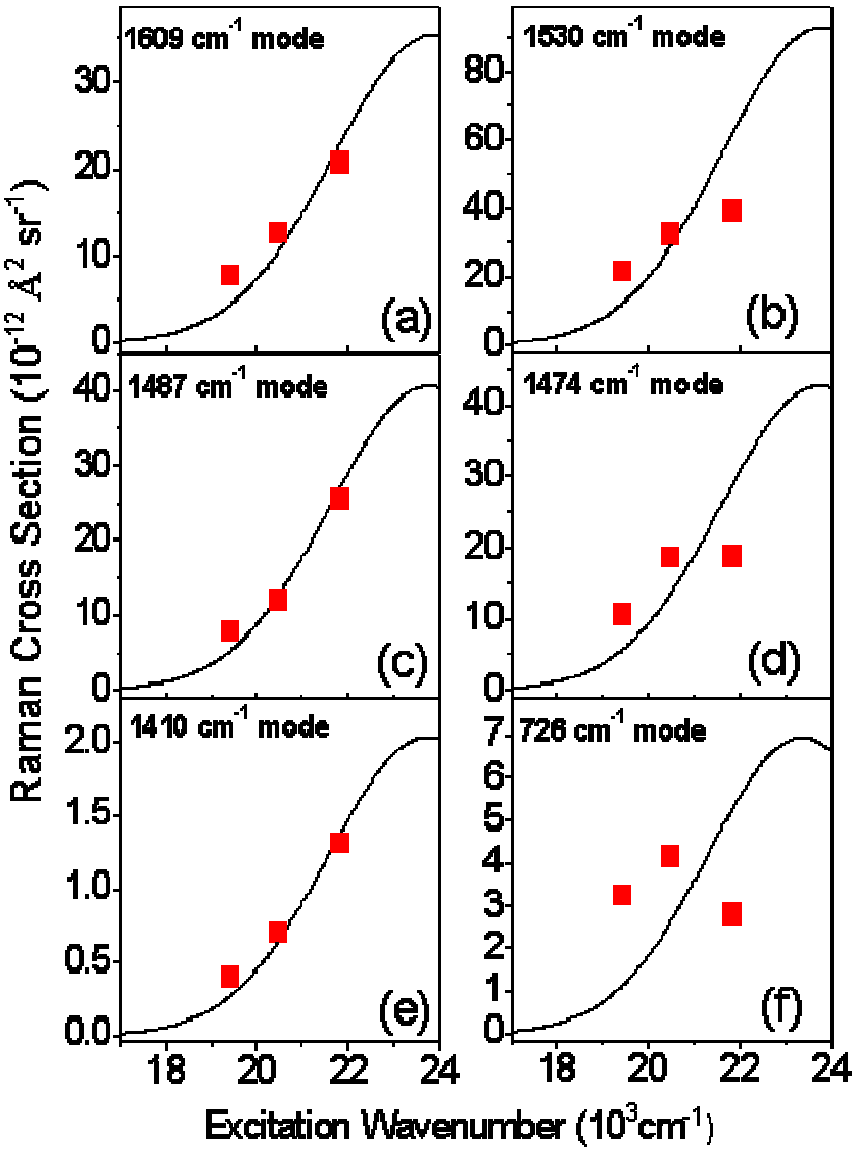

Figure 4.5: Fits (black) of experimental Raman excitation profiles (red) for **2** on TiO_2 carried out using Equation 4 with constraints imposed by the fits of the absorption spectra in Figure 4.3. These vibrations represent (a)-(d) bipyridine ring stretching modes, (e) the phosphorous-carbon bond stretching vibration of unbound phosphonates, and (f) a bending mode localized on the phosphonate group.

With the exception of the phosphorous-bipyridine stretching resonance at 1410cm^{-1}, the frequencies and line widths of the Raman peaks above 1000cm^{-1} are essentially independent of the identity of the molecule. In contrast, the vibrational spectra of different complexes bear little resemblance below 1000cm^{-1}; this is particularly true for molecules adsorbed on TiO_2. We interpret this as a signature that the lower frequency modes are most sensitive to the molecular geometries because they are relatively delocalized within the molecular structure. Moreover, the differences in the Raman spectra for the dye-sensitized systems also reflect the particular manner in which the phosphonated bipyridine ligands are anchored to the TiO_2 surfaces (e.g., monodentate, bidentate).

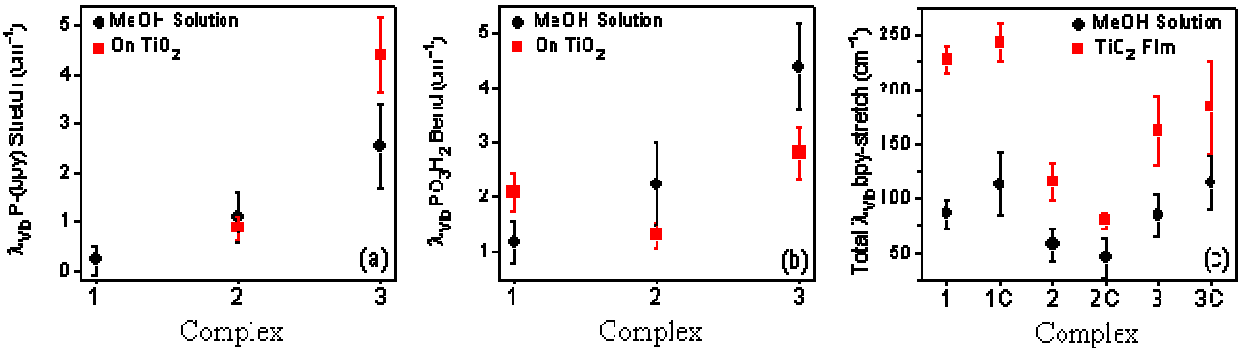

Figure 4.6: Vibrational Reorganization Energies for all molecules. Vibrational reorganization energies determined using the resonance Raman intensity analysis outlined in Section 4.2.A. **(a)** 1410cm^{-1} phosphorous-bipyridine stretching modes of *unbound* ligands. Molecule **1** does not exhibit a resonance because its phosphonates are both bound to TiO_2. **(b)** 725cm^{-1} bending motion localized to the phosphonate moieties in **1-3** (this mode is not observed in **1C-3C**). **(c)** Total reorganization energies associated with the 4 vibrational modes spanning 1485-1610cm^{-1} range (see Tables 4.1 and 4.2).

The vibronic coupling strengths for each mode can be quantitatively assessed by determining their reorganization energies. For molecule **2** on TiO_2, fits of the Raman excitation profiles for the four most intense bipyridine ring-stretching modes and two phosphonate-localized modes are presented in Figure 4.5. Fits conducted on the other systems are included in the SI. Raman cross sections for the dye-sensitized films were obtained only at three excitation frequencies because a limited number of laser lines was available, and photoluminescence dominates below 17000cm^{-1}.[19] Such steady state emission is almost entirely quenched for complexes adsorbed on TiO_2 due to efficient forward electron injection. Still, the amount of luminescence in these systems far outweighs Raman emission below 17000 cm^{-1}.[53-59]

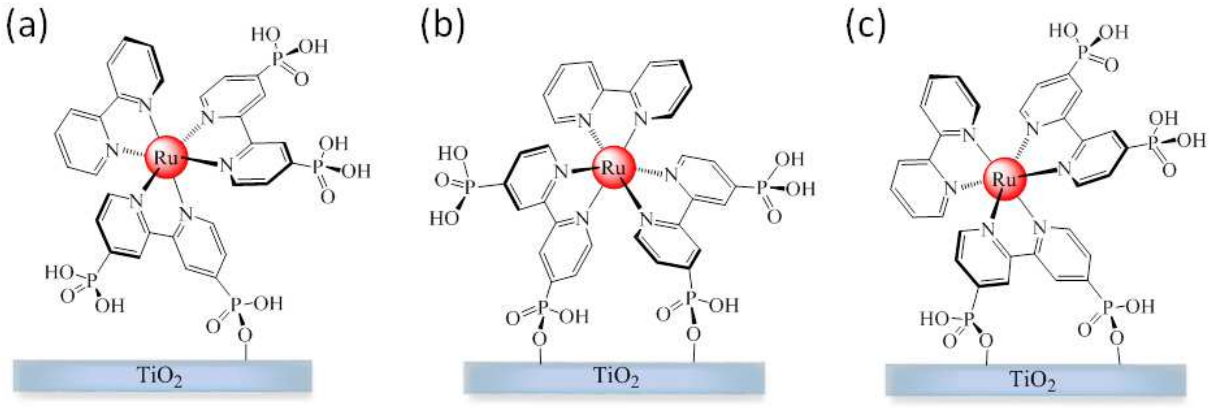

Figure 4.7: Potential binding motifs for Ru complexes with multiple phosphonated ligands (**2**, **2C**, **3**, **3C**). (a) Monodentate adsorption (b) Bidentate adsorption involving two ligands (c) Bidentate adsorption involving a single ligand. Our resonance Raman data rule out (a), but leave open the possibility of (b) and (c). In molecule **1**, the vibrational spectra make clear that the binding occurs by way of geometry (c).

Although the experimental Raman excitation profiles contain a limited number of data points, simultaneous fitting of the experimental absorption spectra shown in Figure 4.2 imposes

powerful constraints. We estimate the uncertainties in the parameters range from 20-30% (cf., Figure A.23 in Appendix A).

Reorganization energies for the 1410cm^{-1} phosphorous-bipyridine stretching modes (for unbound ligands) are presented in Figure 4.6a for **1**-**3**. This resonance is not observed in **1C**-**3C** because phosphorous-bipyridine bonds are absent. In methanol, the vibrational reorganization energy of this mode increases (almost linearly) with the number of phosphonate groups on the molecule. We believe that this trend reflects the "concentration" of phosphorous-bipyridine bonds in the system rather than the Franck-Condon activity of the vibration, which should change little between complexes with similar ^{1}MLCT character. *In other words, the reorganization energy for the (Franck-Condon active) phosphorous-bipyridine stretching mode on the excited ligand is so small that contributions from the (Franck-Condon inactive) unexcited ligands are observed in the Raman spectra.* On TiO_2, the vibrational reorganization energies similarly grow as the number of phosphonate moieties in the complex increases from **2** to **3**. Again, we interpret this as a reflection of the phosphorous-bipyridine mode "concentration" rather than Franck-Condon activity because the reorganization energies scale linearly with the number of unbound ligands.

We consider the information these data provide about molecular geometries in the context of the binding motifs depicted in Figure 4.7. The absence of the phosphorous-bipyridine stretching resonance for molecule **1** on TiO_2 suggests that both of the phosphonate groups on the ligand are bound to the surface. That is, a vibrational resonance would still be observed in **1** if a single phosphonate group is unbound. It follows that the other 5 molecules are unlikely to bind through only a single phosphonate group. Still, the near-linear trend in the reorganization energies shown in Figure 4.6a suggests that the molecules with more than one phosphonated

ligand bind through only two phosphonate groups. This leaves open the possibilities that molecule-TiO_2 adsorption involves either one of the geometries indicated in Figures 7b or 7c. Unfortunately, the present data do not distinguish these two binding motifs for **2** and **3**. Knowledge of the particular motif is important and should be addressed in future work, because it is likely to affect the molecule-TiO_2 coupling and associated processes (e.g., electron transfer).

Vibrational reorganization energies for the 725cm^{-1} bending modes on the phosphonate groups of **1**-**3** are given in Figure 4.6b. The reorganization energies determined in solution scale linearly with the number of phosphonated ligands, whereas a clear pattern is not observed in the dye-derivatized films. The small reorganization energies determined for this mode (and the 1410cm^{-1} phosphorous-bipyridine stretching mode) suggest that the ^{1}MLCT transition density extends very little into the region of the molecule near the TiO_2 interface. Such localized transition densities indicate that, in the vast majority of the ensemble, the excited state dynamics are well-described by a sequential process in which the molecule is photoexcited *before* it injects an electron into the semiconductor. The present evidence for the sequential process is consistent with the relatively weak molecule-TiO_2 couplings generally thought to be afforded by the phosphonate linker.[51,57] As to the absence of the 725cm^{-1} bending mode in Raman spectra of **1C**-**3C**, one possibility is that these resonances are below the detection thresholds because the -CH_2- groups suppress the amplitudes of the transition densities on the phosphonate groups. Alternatively, it may simply be that the presence of the -CH_2- groups prevents the formation of an analogous normal mode.

Figure 4.6c shows that the intramolecular reorganization energies of these systems are mainly concentrated in the double bond stretching modes of the bipyridine ligands. The data do not reveal a systematic pattern among the various complexes. However, the comparable

magnitudes of reorganization energies found in solution and on TiO_2 suggest that the electronic excitations in the dye-sensitized films are similar in nature to those in the solutions. This similarity provides further support for the interpretation that fairly weak molecule-TiO_2 couplings impart little charge transfer character to the electronic resonances in these systems.[51] Overall, the main contribution of the Raman measurements is evidence for weak molecule-TiO_2 interactions. Because the electronic excitations lack molecule-TiO_2 charge transfer character, the electron transfer dynamics measured in the following section can be viewed in the non-adiabatic framework previously applied to related ruthenium complexes.[13,22,51,60]

4.4.C. Interfacial Electron Transfer Dynamics

In this section, we probe photoinduced electron injection dynamics for all systems on TiO_2 using femtosecond TA experiments. These measurements excite the ^{1}MLCT absorbance bands of the ruthenium complexes at 25000cm^{-1} (400nm) and detect transmission of a 10250-21050cm^{-1} (475-975nm) probe pulse. TA spectra for molecules **2** and **2C** in aqueous solution and on TiO_2 are shown in Figure 4.8 for illustration. The TA signals of all systems exhibit an intense bleach above 19200cm^{-1} corresponding to the depleted ground state. The (positive) excited state absorption (ESA) response observed at lower frequencies has contributions from resonances localized on the bipyridine ligands in addition to ligand-to-metal charge transfer (LMCT) transitions.[61,62] Processes including nuclear relaxation, intersystem crossing, and electron transfer from the molecule to TiO_2 occur in the sub-5ps delay range that we are primarily interested in (cf., Scheme 1 in Reference [22]).[60,63-66] It should be noted that the TA signals for all systems investigated in this work are relatively insensitive to slower dipole reorientation processes, which occur with time constants of approximately 20ps. Such inter-

MLCT dynamics are best detected by probing the bipyridine radical at the peak of its resonance near 380nm.[23,24,61] Contributions from interfering ESA nonlinearities (e.g., LMCT transitions) and intramolecular relaxation processes (e.g., vibrational cooling, intersystem crossing) challenge the detection of inter-MLCT, dipole reorientation dynamics in the visible spectral range.

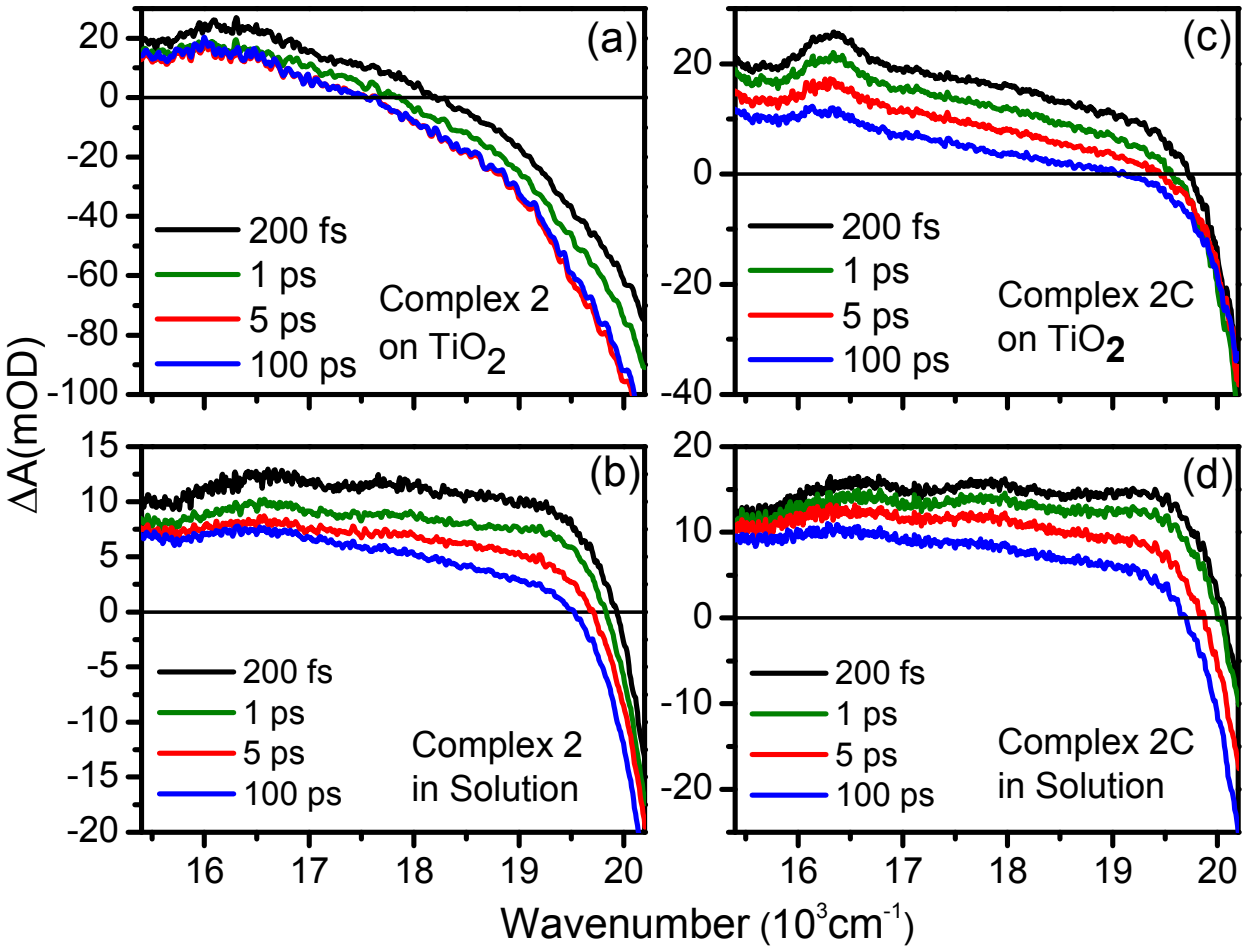

Figure 4.8: Transient absorption spectra following excitation at 25000cm^{-1} (400 nm) for: (a) **2** on TiO_2 and (b) **2** in solution; (c) **2C** on TiO_2; (c) **2C** in solution (d).

Markedly different TA signals are measured for **2** in solution and on the TiO_2 film. At all delay times, the 16770-20830cm^{-1} (480-600nm) spectral range in which the signal changes sign (i.e., where ΔA crosses zero) is red-shifted in the dye-sensitized film compared to the solution.

This spectral shift is attributed, in part, to the larger linear absorbance cross sections of the films found below 19000cm^{-1} (cf., Figure 4.3). The key idea is that ground state bleach (GSB) signal components, which correspond to negative ΔA, in TA spectra possess line shapes similar to the linear absorbance spectra.[26] GSB dominates the TA response in the 18200-19100cm^{-1} range for **2** on TiO_2, thereby shifting the sign change in ΔA to lower frequencies. Evolution in the overall signal amplitude is also evident. The sub-5ps dynamics of the TA signal amplitudes for **2** in solution represent both intersystem crossing and vibrational cooling in the lower energy ^{3}MLCT state. For **2** on TiO_2, the TA signals reflect electron injection dynamics in addition to the two intramolecular relaxation processes.

In contrast to **2**, the spectral ranges in which ΔA changes sign vary little for **2C** between the solution and TiO_2 film. This similarity can be rationalized by the strong resemblance between the linear absorbance spectra of **2C** in solution and on TiO_2. The observation of similar absorbance line shapes is a signature that the electronic resonance possesses little molecule-to-TiO_2 charge transfer character.[51] Given the weaker molecule-TiO_2 coupling afforded by the methylene spacer, we suggest that intersystem crossing and vibrational cooling outcompete electron injection from the ^{1}MLCT state in **2C**. Thus, the fastest dynamics in the TA signals of **2C** probably correspond to these intramolecular relaxation processes. The quantitative analysis of TA kinetics presented below is consistent with this interpretation. We remark that the data shown in Figure 4.8 for **2/2C** exhibit trends that are quite similar to those observed in **1/1C** and **3/3C**. The preceding discussion can therefore be extended to these complexes.

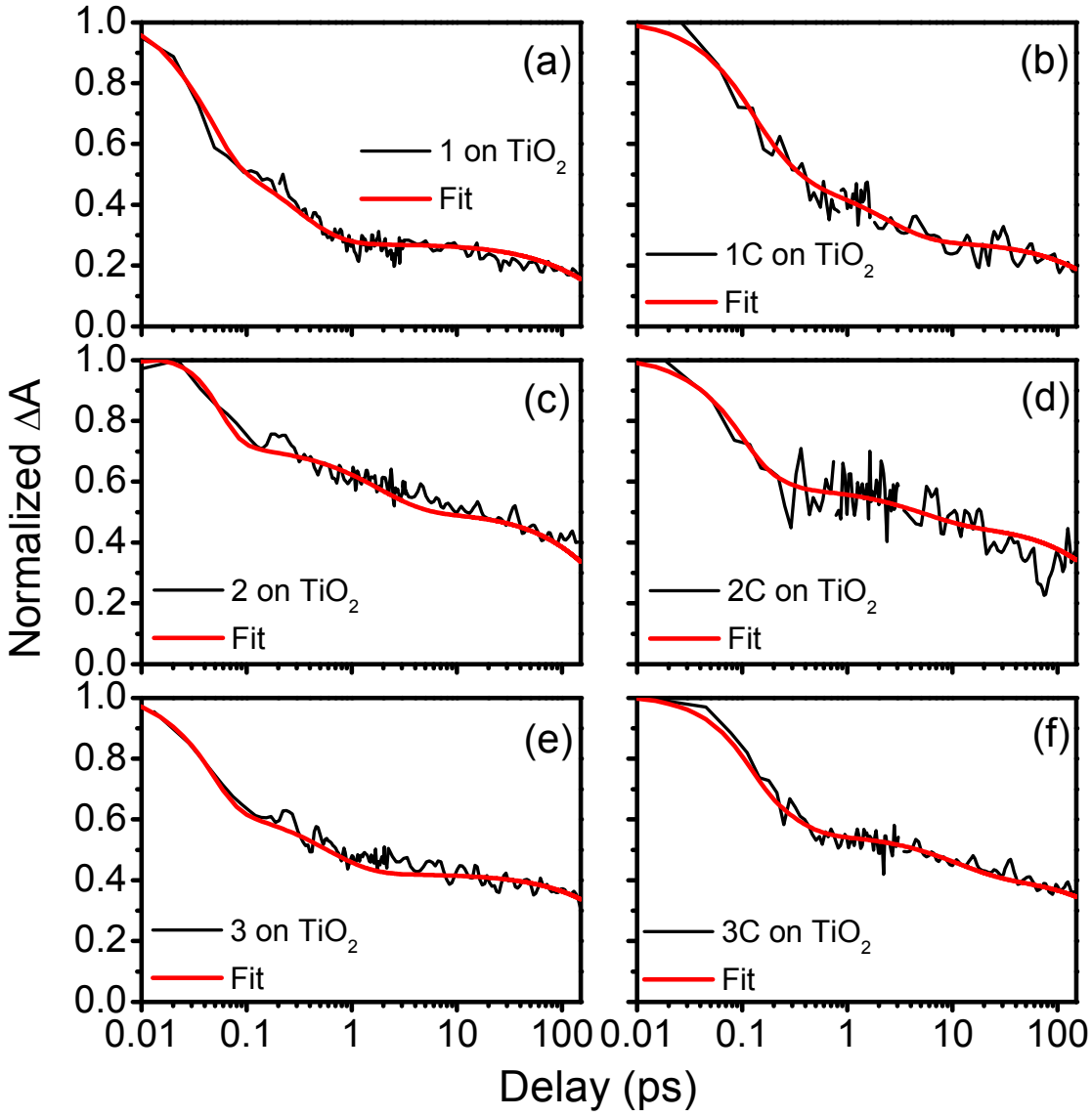

Figure 4.9: Normalized transient absorption signals probed at 15300 cm^{-1} (655 nm) following excitation at 25000 cm^{-1} (400 nm) for all ruthenium complexes.

In Figure 4.9, TA signals are fit at a probe wavenumber of 15270cm^{-1} in order to distinguish time constants associated with particular electron injection mechanisms. The signals are fit using the phenomenological equation,

$$S(T) = A_0 G(T) + \theta(T) \sum_{i=1}^{3} A_i \int_{-\infty}^{\infty} dt G(t) \exp\left[\frac{-(t+T)}{\tau_i} \right], \quad \textbf{(0.21)}$$

where $\theta(T)$ is a Heaviside step function, T is the pump-probe delay time, and the instrument response function is given by

$$G(T) = \exp\left[-4\ln(2) \left(\frac{T}{\delta} \right)^2 \right]. \quad \textbf{(0.22)}$$

The time constant, τ_1, is assigned to electron injection from the ^{1}MLCT state based on studies of related systems and the absence of such ultrafast dynamics for the molecules in solution (cf., Figures A.22 in Appendix A).[22] As summarized in Figure 4.10, the injection processes are most rapid for the molecules without the methylene linkers in all three pairs of systems (i.e., **1** and **1C**, **2** and **2C**, **3** and **3C**). Of course, this is expected based on the smaller molecule-TiO_2 coupling strengths associated with the methylene linkers. These data do not make clear how the number of phosphonate groups on the ruthenium complex affects the dynamics.

Relative rate constants cannot be rationalized based solely on the reduction potentials determined in Reference [19] (and summarized in Figure A.24 of Appendix A). The Ru(III)/Ru(II) reduction potentials (versus a Ag/AgCl reference) decrease in the order **1** (1.97V) >**2** (1.92V)> **3** (1.87V), whereas the time constants increase in the order **1** (24fs) < **3** (30fs) < **2** (49fs). In the complexes with methylene spacers, the reduction potentials decrease in the order **3C** (2.08V) > **2C** (2.07V) > **1C** (2.03V), and time constants increase in the order **2C** (0.10ps) < **1C** (0.15ps) < **3C** (0.17ps). Although there are trends in the data between τ_1 and the reduction potentials, the differences are small and comparable to the experimental error.[19] *A significant conclusion to be*

drawn from these data is that the injection from the [1]MLCT state slows by at least a factor of 2 when a methylene spacer is introduced between the chromophore and the semiconductor surface.

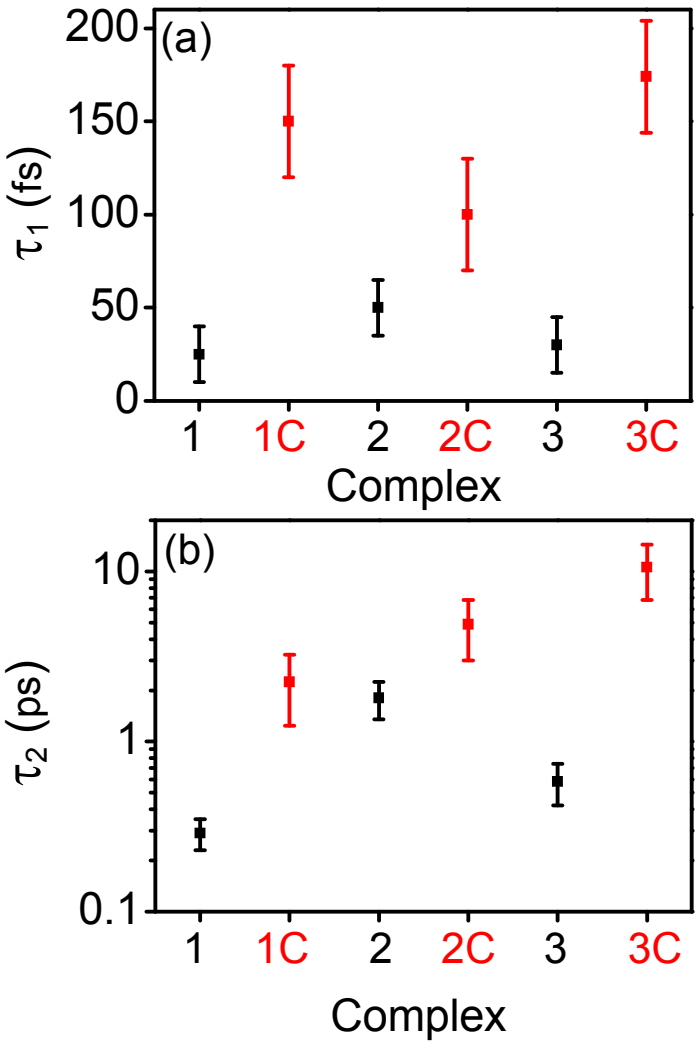

Figure 4.10: Transient absorption time constants obtained for ruthenium complexes on TiO_2. (a) The component, τ_1, represents electron injection into TiO_2 from the photoexcited ^{1}MLCT state. (b) The component, τ_2, corresponds to electron injection from the "hot" ^{3}MLCT states. These data show that the presence of a methylene linker reduces the injection rates for all three pairs of systems (**1** and **1C**, **2** and **2C**, **3** and **3C**). Contributions from interfering ESA resonances and intramolecular relaxation processes complicate the interpretation of the τ_2 time constants.

The time constants, τ_2, are assigned to injection of the "hot" ^{3}MLCT state because the dynamics are slower than intersystem crossing but faster than nuclear relaxation.[13,22] Small decreases in τ_2 are found for injection through methylene linkers (e.g., **1** versus **1C**). However, the complex kinetics derived from the visible wavelength range precludes detailed analysis. Vibrational cooling, MLCT interconversion, and molecule-to-TiO_2 electron transfer from the ^{3}MLCT state all occur on similar time scales. Our own experiments conducted on these molecules in solution confirm the presence of picosecond intramolecular relaxation processes (cf., Figure 4.8 and Figure A.22 in Appendix A). Deconvolution of such time coincident dynamics will be better achieved with TA experiments in which the bipyridine radical is probed in the near UV.[23,24]

Table 4.3. TA fitting Parameters for ruthenium complexes on TiO_2

[(a)]Parameter	1	2	3	1C	2C	3C
A_0	0.0038±0.001	0.0055±0.001	0.0039±0.001	0.0041±0.001	0.0049±0.001	0.0064±0.001
A_1	0.14±0.01	0.08±0.01	0.15±0.01	0.42±0.03	0.29±0.04	0.35±0.02
τ_1 (ps)	0.025±0.01	0.05±0.01	0.03±0.01	0.15±0.03	0.10±0.03	0.17±0.03
A_2	0.45±0.24	0.27±0.15	0.29±0.10	0.24±0.10	0.15±0.04	0.17±0.10
τ_2 (ps)	0.29±0.06	1.80±0.45	0.58±0.16	2.24±1.0	4.9±1.9	10.6±3.8
A_3	0.41±0.21	0.65±0.22	0.56±0.23	0.33±0.14	0.56±0.05	0.48±0.16
τ_3 (ps)	270±40	376±40	680±80	382±70	513±110	850±160

[(a)]Equation (4.21).

An alternate approach to data analysis focuses on the wavelength at which the TA signal changes sign in the visible spectral range. The "zero crossing wavenumber" (ZCW) is fairly insensitive to noise in the pump-probe delay time, which possesses contributions from fluctuations in the laser intensity and motion of the sample (i.e., the sample is oscillated to suppress photodamage). We determine the ZCW by fitting the TA spectra to fifth order polynomials then solving for the point at which ΔA equals zero. The ZCW's are plotted with respect to the pulse delay, T, and fit with the following phenomenological function,

$$\Omega_{ZCW}(T) = \lambda_0 + \sum_{n=1}^{3} \exp\left(-\frac{T}{\tau_n}\right) . \qquad \textbf{(0.23)}$$

The $\Omega_{ZCW}(T)$ for all for dye-sensitized systems are shown in Figure 4.11. For molecules **1-3**, a 2000-3000cm^{-1} shift in $\Omega_{ZCW}(T)$ occurs in less than 200fs, whereas the $\Omega_{ZCW}(T)$ of **1C-3C** are relatively insensitive to the delay time. We attribute the large spectral shift observed in **1-3** to electron injection from the ^{1}MLCT state(s). The sub-100cm^{-1} spectral shifts in $\Omega_{ZCW}(T)$ observed for **1-3** in solution are consistent with this interpretation. Relatively small shifts in $\Omega_{ZCW}(T)$ are observed for **1C-3C** on TiO_2, where intramolecular relaxation processes dominate the sub-ps timescale because weak molecule-TiO_2 couplings suppress electron transfer. Overall, the $\Omega_{ZCW}(T)$ lend further support to the interpretation (reached in the discussion of Figures 9-10) that molecule-to-TiO_2 electron transfer from the ^{1}MLCT states dominate the sub-200fs time scale in **1-3**.

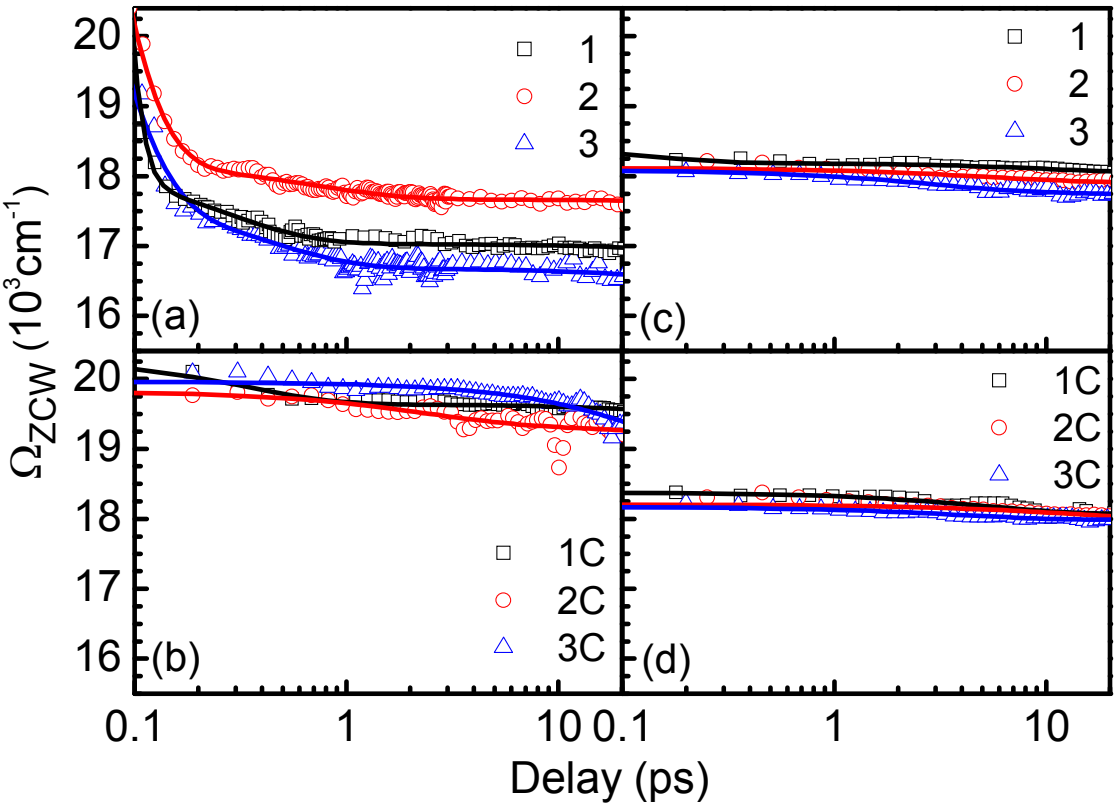

Figure 4.11: Zero crossing wavenumbers, $\Omega_{ZCW}(T)$, obtained for TA signals of all complexes on TiO_2 films (left) and in aqueous solution (right). (a) The large spectral shifts observed for **1-3** on TiO_2 are assigned to electron injection processes initiating in the ^{1}MLCT states of the molecules. (b) Relatively small spectral shifts are observed for **1C-3C** on TiO_2 because (intramolecular) intersystem crossing outcompetes electron injection from the ^{1}MLCT states. Fitting parameters are given in Appendix A.

The information provided by the present TA experiments is summarized in Figure 4.12. In systems **1-3**, photoinduced electron transfer transitions proceeds directly from the ^{1}MLCT state because of relatively large molecule-TiO_2 couplings. Intersystem crossing is slower than singlet injection, k_{ET}^{S}, but occurs on the sub-picosecond time scale, whereas vibrational cooling, k_{VC}, takes 10ps or more. Therefore, the second viable electron transfer channel necessarily

involves vibrationally "hot" ^{3}MLCT states, k_{ET}^{T} .[13,22] Electron injection from ^{1}MLCT into TiO_2 is naturally faster than processes initiating in ^{3}MLCT because the non-adiabatic electron transfer rate scales linearly with the density of states in TiO_2.[13] Electron injection from ^{3}MLCT into TiO_2 is most efficient in **1C-3C** because the molecule-TiO_2 coupling, which governs electron transfer, is not large enough to outcompete (intramolecular) intersystem crossing, k_{ISC} .

Implicit in this relaxation scheme is the assumption that the ^{1}MLCT electronic resonance involves orbitals that are localized on the molecule (i.e., the resonances possess little molecule-TiO_2 charge transfer character). This appears to be a good approximation based on the Raman results presented above. Still, while non-adiabatic rate formulas provide a useful framework, the breakdown of fundamental approximations should be recognized. Non-adiabatic rate constants imply that the time scale of nuclear motion surrounding the molecule-TiO_2 system is fast compared to the electron transfer transition (i.e., the process is assumed to be Markovian).[28] This separation in time scales is undoubtedly a poor approximation for the sub-200fs singlet injection dynamics in **1-3**. Future work will investigate the impact such non-Markovian effects and the closely related issue of orbital delocalization at the molecule-TiO_2 interface.

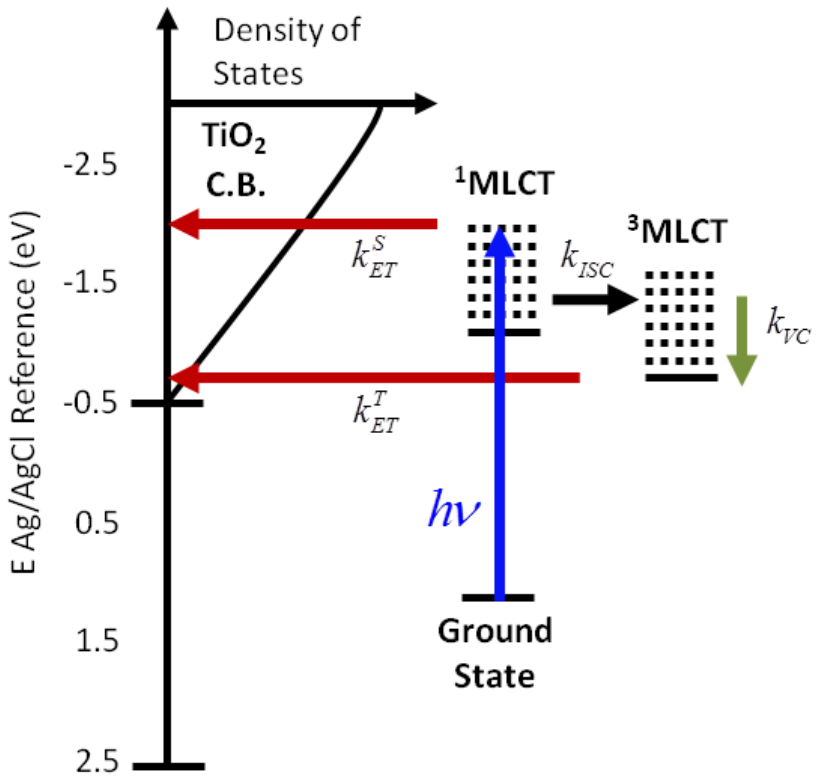

Figure 4.12: Relaxation scheme diagram. Relaxation scheme used to interpret transient absorption experiments. k_{ET}^{S} and k_{ET}^{T} correspond to injection from the singlet and triplet states localized on the ruthenium complex. Intersystem crossing and vibrational cooling in the triplet state correspond to k_{ISC} and k_{VC}, respectively. The manifold of energy levels associated with ^{1}MLCT and ^{3}MLCT represent vibrational states (i.e., the dashed black lines).

4.5. Conclusions

In summary, several physical insights into molecule-TiO_2 interfaces have been uncovered by applying optical spectroscopies to the family of ruthenium complexes shown in Figure 4.1. The physics under investigation includes: (i) the nature of thermal fluctuations in the molecular adsorbates; (ii) the electronic structure at the molecule-TiO_2 interface; (iii) the molecular binding

motifs; (iv) the mechanism of photoinduced electron transfer. Contributions in each of these areas are described below.

Section 4.2 draws connections between the Brownian oscillator coordinates in a (stochastic) spectroscopic model and the geometric picture of solvation proven to be effective in $[Ru^{II}(bpy)_3]^{2+}$ and $[Os^{II}(bpy)_3]^{2+}$.[23,24] It is shown that the established two-dimensional representation of the solvent coordinates translates into correlated ground and excited state energy level fluctuations in the stochastic model. We suggest that this (thermal noise suppressing) effect may originate in spatially correlated fluctuation statistics among the ligands. Such spatial correlations will also hold important implications for photoinduced ILET and MLCT interconversion processes (cf., Equations (14) and (19)), which should impact the overall electron injection efficiency.

To address points (ii) and (iii), we fit linear absorbance and resonance Raman cross sections simultaneously to obtain a set of parameters that includes solvent reorganization energies, intramolecular mode-specific reorganization energies, and the electronic resonance frequencies. Our discussion of these data focuses on the subset of parameters relevant to molecule-TiO_2 interactions. The finding of small reorganization energies on the phosphonate linkers suggests that the electronic resonances of these systems possess little molecule-to-TiO_2 charge transfer character. Thus, the photophysics are well-described in terms of sequential light absorption and electron injection events. The Raman spectra also indicate that binding generally does not involve only a single phosphonate groups. The vibrational spectra suggest that molecules **1** and **1C** likely bind using both of their phosphonate groups (cf., Figure 4.7c). However, the data do not rule out either of the two motifs shown in Figures 7b and 7c for the other four molecules.

Finally, TA measurements show that electron injection primarily initiates in the ^{1}MLCT states for molecules **1**, **2**, and **3**. These processes, which are denoted by k_{ET}^{S} in Figure 4.12, dominate the sub-200fs time scale. Transitions involving the "hot" ^{3}MLCT states are observed at later delay times in these systems. In contrast, the smaller molecule-TiO_2 couplings afforded by the methylene spacers allow intersystem crossing to outcompete electron transfer from ^{1}MLCT in **1C**, **2C**, and **3C**. In these three systems, electron transfer predominantly involves "hot" ^{3}MLCT states. The time constants presented in Figure 4.10 indicates that the methylene spacer has fairly minor effect on the molecule-TiO_2 coupling strength because electron transfer slows down by less than a factor of 10. The present findings complement an earlier study of nanosecond processes in these same molecules, where the dynamics of the vibrationally relaxed systems was investigated.[19] We find that the non-Markovian nature of the sub-picosecond dynamics examined here makes the electron transfer less sensitive to the (equilibrium) free energy gaps that govern electron transfer events on slower time scales.

Future work will address several issues not accessible with the present experimental methods. For example, it will be important to understand what happens to ^{3}MLCT states that don't inject but thermalize. Such relaxed states may give rise to slower injection dynamics or even transfer their excitations onto neighboring molecules. Time-resolved emission and/or nanosecond transient absorption experiments are better equipped to address these dynamics.[19,59] We would also like to explore the influence of MLCT interconversion transitions where the excitation is transferred from an ancillary ligand to the "bound" ligand, which is presumably the location from which most the electron injection takes place. These dynamics will be uncovered with transient absorption experiments utilizing probe pulses resonant with the bipyridine radical

near 380nm. Connections between signal strengths and injection yields can then be clearly established because the bipyridine radical dominates the optical response in this spectral range.

4.6 REFERENCES

(1) O'Regan, B.; Grätzel, M. *Nature* **1991**, *353*, 737.

(2) Grätzel, M. *Nature* **2001**, *414*, 338.

(3) Hagfeldt, A.; Boschloo, G.; Sun, L.; Kloo, L.; Pettersson, H. *Chem. Rev.* **2010**, *110*, 6595.

(4) Gregg, B. A. *J. Phys. Chem. B* **2003**, *107*, 4688.

(5) Zou, Z.; Ye, J.; Sayama, K.; Arakawa, H. *Nature* **2001**, *414*, 625.

(6) Asbury, J. B.; Hao, E.; Wang, Y.; Ghosh, H. N.; Lian, T. *J. Phys. Chem. B* **2001**, *105*, 4545.

(7) Concepcion, J. J.; Jurss, J.; Brennaman, M. K.; Hoertz, P. G.; Patrocinio, A. O. T.; Iha, N. Y. M.; Templeton, J. L.; Meyer, T. J. *Acc. Chem. Res.* **2009**, *42*, 1954.

(8) Kamat, P. V. *J. Phys. Chem. C* **2007**, *111*, 2834.

(9) Mallouk, T. E. *J. Phys. Chem. Lett.* **2010**, *1*, 2738.

(10) Duncan, W. R.; Prezhdo, O. V. *Annu. Rev. Phys. Chem.* **2007**, *58*, 143.

(11) Jakubikova, E.; Snoeberger III, R. C.; Batista, V. S.; Batista, E. R. *J. Phys. Chem. A* **2009**, *113*, 12532.

(12) Durrant, J. R.; Haque, S. A.; Palomares, E. *Coord. Chem. Rev.* **2004**, *248*, 1247.

(13) Anderson, N. A.; Lian, T. *Annu. Rev. Phys. Chem.* **2005**, *56*, 491.

(14) Tisdale, W. A.; Williams, K. J.; Timp, B. A.; Norris, D. J.; Aydil, E. S.; Zhu, X.-Y. *Science* **2010**, *328*, 1543.

(15) Morris-Cohen, A. J.; Frederick, M. T.; Cass, L. C.; Weiss, E. A. *J. Am. Chem. Soc.* **2011**, *133*, 10146.

(16) Pandey, A.; Guyot-Sionnest, P. *J. Phys. Chem. Lett.* **2010**, *1*, 45.

(17) Nozik, A. J. *Annu. Rev. Phys. Chem.* **2001**, *52*, 193.

(18) Ardo, S.; Meyer, G. J. *Chem. Soc. Rev.* **2009**, *38*, 115.

(19) Hanson, K.; Brennaman, M. K.; Akitaka, I.; Hanlin, L.; Song, W.; Parker, K. A.; Ghosh, R.; Norris, M. R.; Glasson, C. R. K.; Concepcion, J. J.; Lopez, R.; Meyer, T. J. *J. Phys. Chem. C.* **2012**, *116*, (14837.

(20) Kelley, A. M. *J. Phys. Chem. A* **1999**, *103*, 6891.

(21) Dattlebaum, D. M.; Kober, E. M.; Papanikolas, J. M.; Meyer, T. J. *Chem. Phys.* **2006**, *326*, 71.

(22) Asbury, J. B.; Anderson, N. E.; Hao, E.; Ai, X.; Lian, T. *J. Phys. Chem. B.* **2003**, *107*, 7376.

(23) Shaw, G. B.; Styers-Barnett, D. J.; Gannon, E. Z.; Granger, J. C.; Papanikolas, J. M. *J. Phys. Chem. A* **2004**, *108*, 4998.

(24) Shaw, G. B.; Brown, C. L.; Papanikolas, J. M. *J. Phys. Chem. A* **2002**, *106*, 1483.

(25) Myers, A. B.; Mathies, R. A. Resonance Raman intensities: a probe of excited state structures and dynamics. In *Biological Applications of Raman Spectroscopy*; Spiro, T. G., Ed.; Wiley: New York, 1987; Vol. 2; pp 1.

(26) Mukamel, S. *Principles of Nonlinear Optical Spectroscopy*; Oxford University Press: New York, 1995.

(27) Heller, E. J. *Acc. Chem. Res.* **1981**, *14*, 368.

(28) Nitzan, A. *Chemical Dynamics in Condensed Phases*; Oxford University Press: Oxford, 2006.

(29) Venkatramani, R.; Mukamel, S. *J. Chem. Phys.* **2002**, *117*, 11089.

(30) Nazir, A. *Phys. Rev. Lett.* **2009**, *103*, 146404:1.

(31) Hennebicq, E.; Beljonne, D.; Curutchet, C.; Scholes, G. D.; Silbey, R. J. *J. Chem. Phys.* **2009**, *130*, 214505/1.

(32) West, B. A.; Womick, J. M.; McNeil, L. E.; Tan, K. J.; Moran, A. M. *J. Phys. Chem. C* **2010**, *114*, 10580.

(33) Capek, V.; Silinish, E. *Organic Molecular Crystals: Interaction, Localization, and Transport Phenomena*; AIP: New York, 1994.

(34) van Amerongen, H.; Valkunas, L.; van Grondelle, R. *Photosynthetic Excitons*; World Scientific: Singapore, 2000.

(35) Mukamel, S.; Abramavicius, D. *Chem. Rev.* **2004**, *104*, 2073.

(36) Zhang, J. M.; Shiu, Y. J.; Hayashi, M.; Liang, K. K.; Chang, C. H.; Gulbinas, V.; Yang, C. M.; Yang, T.-S.; Wang, H. Z.; Chen, Y.-T.; Lin, S. H. *J. Phys. Chem. A* **2001**, *105*, 8878.

(37) Mebel, A. M.; Hayashi, M.; Liang, K. K.; Lin, S. H. *J. Phys. Chem. A* **1999**, *103*, 10674.

(38) Barbara, P. F.; Meyer, T. J.; Ratner, M. A. *J. Phys. Chem.* **1996**, *100*, 13148.

(39) Lee, S.-H. A.; Abrams, N. M.; Hoertz, P. G.; Barber, G. D.; Halaoui, L. I.; Mallouk, T. E. *J. Phys. Chem. B.* **2008**, *112*, 14415.

(40) Shriver, D. F.; Dunn, J. B. R. *Appl. Spectrosc.* **1974**, *28*, 319.

(41) Juris, A.; Balzani, V.; Barigelletti, F.; Campagna, S.; Belser, P.; von Zelewsky, A. *Coord. Chem. Rev.* **1988**, *84*, 85.

(42) Daasch, L. W.; Smith, D. C. *Anal. Chem.* **1951**, *23*, 853.

(43) Demas, J. N.; Crosby, G. A. *J. Amer. Chem. Soc.* **1971**, *93*, 2841.

(44) Lumpkin, R. S.; Kober, E. M.; Worl, L. A.; Murtaza, Z.; Meyer, T. J. *J. Phys. Chem.* **1990**, *94*, 239.

(45) Alexander, B. D.; Dines, T. J.; Longhurst, R. W. *Chem. Phys.* **2008**, *352*, 19.

(46) Mallick, P. K.; Danzer, G. D.; Strommen, D. P.; Kincaid, J. R. *J. Phys. Chem.* **1988**, *92*, 5628.

(47) Strommen, D. P.; Mallick, P. K.; Danzer, G. D.; Lumpkin, R. S.; Kincaid, J. R. *J. Phys. Chem.* **1990**, *94*, 1357.

(48) Thompson, D. G.; Schoonover, J. R.; Timpson, C. J.; Meyer, T. J. *J. Phys. Chem. A* **2003**, *107*, 10250.

(49) Shoute, L. C. T.; Loppnow, G. R. *J. Amer. Chem. Soc.* **2003**, *125*, 15636.

(50) Shoute, L. C. T.; Loppnow, G. R. *J. Chem. Phys.* **2002**, *117*, 842.

(51) Miller, S. A.; West, B. A.; Curtis, A. C.; Papanikolas, J. M.; Moran, A. M. *J. Chem. Phys.* **2011**, *135*, 081101/1.

(52) Tušek-Božić, L. *Vib. Spec.* **2002**, *28*, 235.

(53) Brennaman, M. K.; Patrocinio, A. O. T.; Song, W.; Jurss, J. W.; Concepcion, J. J.; Hoertz, P. G.; Traub, M. C.; Iha, N. Y. M.; Meyer, T. J. *Chem. Sus. Chem.* **2011**, *4*, 216.

(54) Kelly, C. A.; Farzad, F.; Thompson, D. W.; Stipkala, J. M.; Meyer, G. J. *Langmuir* **1999**, *15*, 7047.

(55) Bai, Y.; Zhang, J.; Wang, Y.; Zhang, M.; Wang, P. *Langmuir* **2011**, *27*, 4749.

(56) Koops, S. E.; O'Reagan, B. C.; Barnes, P. R. F.; Durrant, J. R. *J. Am. Chem. Soc.* **2008**, *131*, 4808.

(57) Heimer, T. A.; Meyer, G. J. *J. Luminescence* **1996**, *70*, 468.

(58) Haque, S. A.; Palomares, E.; Cho, B. M.; Green, A. N. M.; Hirata, N.; Klug, D. R.; Durrant, J. R. *J. Am. Chem. Soc.* **2005**, *127*, 3456.

(59) McNeil, I. J.; Ashford, D. L.; Luo, H.; Fecko, C. J. *J. Phys. Chem. C* **2012**, *116*, 15888.

(60) Kuciauskas, D.; Monat, J. E.; Villahermosa, R.; Gray, H. B.; Lewis, N. S.; McCusker, J. K. *J. Phys. Chem. B.* **2002**, *106*, 9347.

(61) Wallin, S.; Davidsson, J.; Modin, J.; Hammerström, L. *J. Phys. Chem. A.* **2005**, *109*, 4697.

(62) Kalyanasundaram, K. *Coord. Chem. Rev.* **1982**, *46*, 159.

(63) Damrauer, N. H.; Cerrullo, G.; Yeh, A.; Boussie, T. R.; Shank, C. V.; McCusker, J. K. *Science* **1997**, *275*, 54.

(64) Damrauer, N. H.; McCusker, J. K. *J. Phys. Chem. A.* **1999**, *103*, 8440.

(65) Yeh, A.; Shank, C. V.; McCusker, J. K. *Science* **2000**, *289*, 935.

(66) Moser, J. E.; Grätzel, M. *Chimia* **1998**, *52*, 160.

CHAPTER 5: MOLECULE-SEMICONDUCTOR INTERFACIAL GEOMETRY WITH RAMAN SPECTROSCOPY

5.1. Introduction

Dye-sensitized photoelectrosynthesis cells (DSPECs) are devices of great interest for solar energy conversion. Central to many of these devices is a chromophore covalently bound to a semiconductor substrate, which harvests visible photons and transfers them into the conduction band of the electrode.[1-9] Depending on the intent of the device, the injected electrons may then be utilized directly or converted to chemical energy by reactions including the oxidation of water to oxygen and hydrogen or the reduction of CO_2 to methane or other carbon species. Electron transfer between the excited chromophore to the semiconductor is one of the key physical processes impacting the efficiency of such devices. In addition to the electrode identity[10], the chromophore's structure, particularly at the molecular interface with the semiconductor has a significant impact on the electronic coupling of the donor-acceptor system.[11-13] Thus, insight into this interfacial structure is crucial to the design of improved DSPECs.

This work follows a study of the electron injection dynamics and resonance Raman excitation profiles of a series of six phosphonate-derivatized $[Ru(bpy)_3]^{2+}$ complexes on TiO_2.[14] However, the Raman measurements were dominated by heterogeneity of the molecules at the nanocrystalline surface, which prevented clear modelling of the molecular binding geometries. Transient absorption measurements also performed in the above study revealed varying kinetics across the chromophore series which varied only in the anchoring group to the semiconductor.

This conclusion, in concert with previous work of others[10,15-17] highlighted the importance of chromophore attachment to electron transfer kinetics.

In this work, polarized resonance Raman measurements of a subset of these chromophores are used to further elucidate their binding to the semiconductor surface. The chomophores, shown in Figure 5.1, and referred to in this work as **RuP**, **Ru2P**, and **RuCP**, were selected from the original set because they each possess a defined difference with respect to the anchoring group. Compared to the simplest chromophore, **RuP**, which only has anchoring phosphonate groups on one of the bipyridine ligands, **Ru2P** possesses a second functionalized ligand, allowing for more potential binding configurations. Whereas in **1** the phosphonate groups are directly bound to the bipyridine rings, in **1C**, the two moieties are separated by a methylene group, which provides additional flexibility between the chromophore and the binding group.

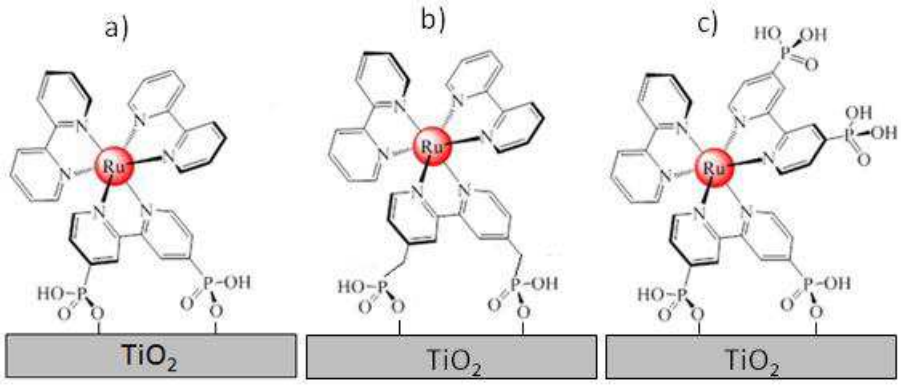

Figure 5.1: Chromophore molecular structures for (a) RuP, (b) RuCP, which contains a methylene spacer between the bipyridine ligand and the phosphorus and (c) Ru2P, a derivative of RuP with a second phosphonated ligand.

Rutile phase single crystal wafers of TiO_2 are used instead of nanocrystalline films in order to directly investigate the geometry of the chromophores themselves. Rutile is the most common of three main polymorphs of TiO_2, and is comparatively more stable than anatase, since anatase is a metastable state. As a result, while nanocrystalline TiO_2 can easily be synthesized in the anatase state[18], thermal treatment of larger crystals often results in conversion to rutile, and most commercially available single crystal wafers are of the rutile phase. Both polymorphs have tetragonal unit cells with octahedral coordination about titanium atoms, though those atoms are slightly closer together in anatase than rutile. Therefore, while the chromophore is likely to bind similarly to both forms of TiO_2, differences may exist.

5.2. Background on Polarized Resonance Raman Spectroscopy

5.2.A Dipole Interaction Model

In order to extract orientational information from the depolarization ratios calculated in Table 5.1, a theoretical model is defined to calculate the Raman signal generated by the chromophores over a parameter space of specific molecular geometries. The model incorporates several assumptions, the first of which is that the molecular shape is minimally distorted by adsorption onto the semiconductor surface. That is, the symmetry of the bipyridine rings about the ruthenium center remains approximately D_3 as in $Ru(bpy)_3^{2+}$, which is expected given the octahedral arrangement of bidentate Ru-N bonds. Secondly, since the measurements are performed at room temperature, there is certainly a degree of fluctuation about any preferred orientation- these fluctuations, being statistical in nature, are assumed to result in a Gaussian distribution of geometries. Thirdly, that the MLCT transition dipole can be represented as a

vector from the midpoint of a given ligand to the ruthenium metal (collinear with the C_3 rotation axis,) and that the Raman pump interacts with each transition dipole of the chromophore according to the projection of that dipole on the polarization vector of the beam.

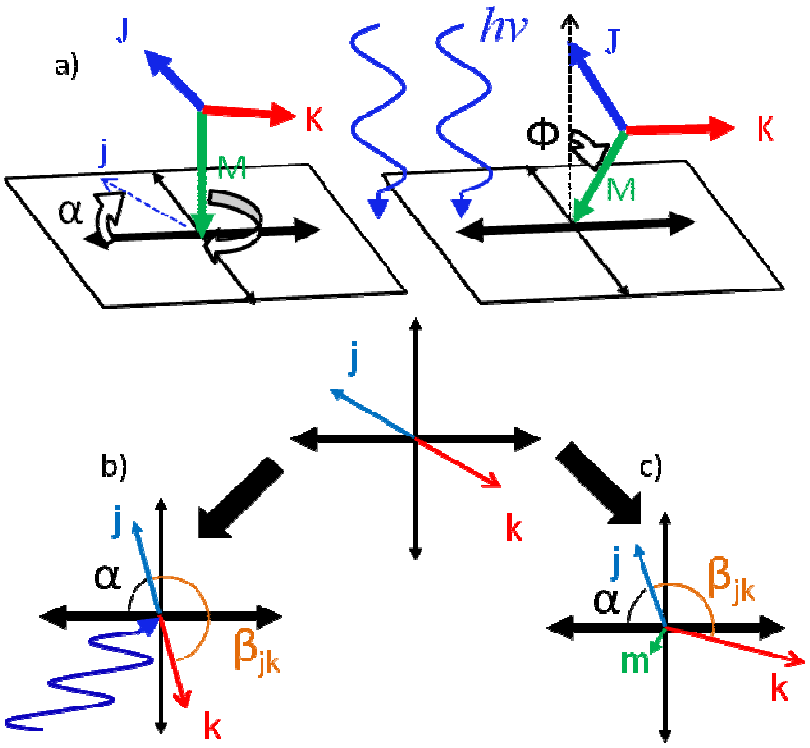

Figure 5.2: Dipole projection diagram. (a) The mean rotation angle refers to a rotation of the dipole J's projection, j from the axis of incident polarization in the XY laboratory frame. The tilt angle, on the other hand, refers to the angle that the bound ligand is tilted away from the axis of incident light propagation, the Z axis. (b) The effect on the projections resulting from a sample rotation from the above projections is shown to affect α only. (c) The effect of tilting on the above dipole projections is shown. Unlike the rotation angle, the tilting angle affects the angle between projections, β, as well as their relative magnitudes.

With these requirements in mind, equations are developed[19] which simulate the Raman signal expected when the measured polarization is parallel or perpendicular to the incident beam.

$$S_{XX} = \sum_{j=1}^{3}\sum_{k\geq j}^{3} \mu_j^2 \mu_k^2 \int_0^{2\pi} G(\varphi)\cdot\cos^2(\varphi+\beta_{jk})\cdot\cos^2(\varphi)d\varphi \ . \qquad \textbf{(5.1)}$$

$$S_{XY} = \sum_{j=1}^{3}\sum_{k\geq j}^{3} \mu_j^2 \mu_k^2 \int_0^{2\pi} G(\varphi)\cdot\sin^2(\varphi+\beta_{jk})\cdot\cos^2(\varphi)d\varphi \ . \qquad \textbf{(5.2)}$$

In the above equations, σ is the polarized Raman signal, μ_j is the projection of dipole j on the polarization axis, α_j is the angle φ in the XY plane between the polarization axis and the projection of dipole j, and β_{jk} is the angle φ between dipoles j and k. Since φ is integrated from 0 to 2π but the experiment is only sensitive to angles $0 < \varphi < \pi$, G is a bimodal Gaussian distribution described by the equation

$$G(\varphi) = e^{\left(\frac{-(\varphi-\alpha_j)^2}{2w^2}\right)} + e^{\left(\frac{-(\varphi-\alpha_j-\pi)^2}{2w^2}\right)} \ . \qquad \textbf{(5.3)}$$

In the computational program, the chromophore is represented as a set of 3 vectors as described above. Initially, the dipoles are orienented such that the projections of the unbound ligands are both 0 degrees from the incident polarization axis. Since the assumption is made that the ligands are not distorted relative to each other, α_j for each dipole j is related to the projected rotation angle of another dipole k by β_{jk}, which exclusively depends on ϕ. Therefore, a single mean rotation angle, α can be defined for the entire chromophore with respect to a single, arbitrary ligand. Using this property, σ_{XX}, σ_{XY}, σ_{YX}, and σ_{YY} are calculated at each rotation angle (to simulate average binding geometry of the chromophore) in the interval $0 \leq \alpha \leq \pi/2$, while *w* is simultaneously varied over the interval $0 \leq w \leq 2\pi$. Additionally, the bound chromophore is

rotated stepwise away from the Z axis (keeping the relative dipole positions constant) to simulate tilt in the chromophore toward the TiO_2 surface in the interval $0 \leq \phi \leq \pi/4$. At each of the points in this parameter space, ratios are calculated between corresponding polarization experiments, such that

$$R_X(\alpha,\phi,w) = \frac{S_{XX}(\alpha,\phi,w)}{S_{XY}(\alpha,\phi,w)}, R_Y(\alpha,\phi,w) = \frac{S_{YY}(\alpha,\phi,w)}{S_{YX}(\alpha,\phi,w)} \text{ , } \quad \textbf{(5.4)}$$

where R_X and R_Y are defined as the inverse depolarization ratios expected when the polarization axis of the incoming beam is aligned along the X and Y axes of the laboratory frame, respectively. Due to experimental symmetry, $R_X(\alpha,\phi,w) = R_Y([\pi-\alpha],\phi,w)$. For small values of w, R is strongly dependant on α- however as w increases and G(α,w) approaches a constant value and R approaches the value measured in solution, as intended.

5.3. Experimental Methods

5.3.A Sample Preparation

Ruthenium complexes are prepared according to previously published procedures.[20] The rutile wafers are purchased from MTI Corp, measuring 5x5x1mm. Wafers cut along the 100, 101, and 110 faces of rutile are purchased. TiO_2 wafers are cleaned using an aqueous solution of 20% ammonia and 20% hydrogen peroxide at room temperature for 30 minutes. The substrates are then loaded with dye by soaking in 100 μM chromophore in aqueous 0.1 M $HClO_4$ for approximately 24 hours followed by thorough rinsing with aqueous 0.1 M $HClO_4$ to remove excess non-adsorbed dye.

5.3.B Resonance Raman Measurements

Raman spectra were collected with a Renishaw inVia- Leica DM2500 M microscope setup using the 21,840 cm^{-1} laser line of an argon ion laser (Spectra Physics Stabilite 2017). For film Raman measurements, 30 μW laser beams are focused onto the sample with a Leica N PLAN EPI 50x/0.75 objective lens, which is also used to collect the scattered Raman signal through a 180º backscattering geometry.

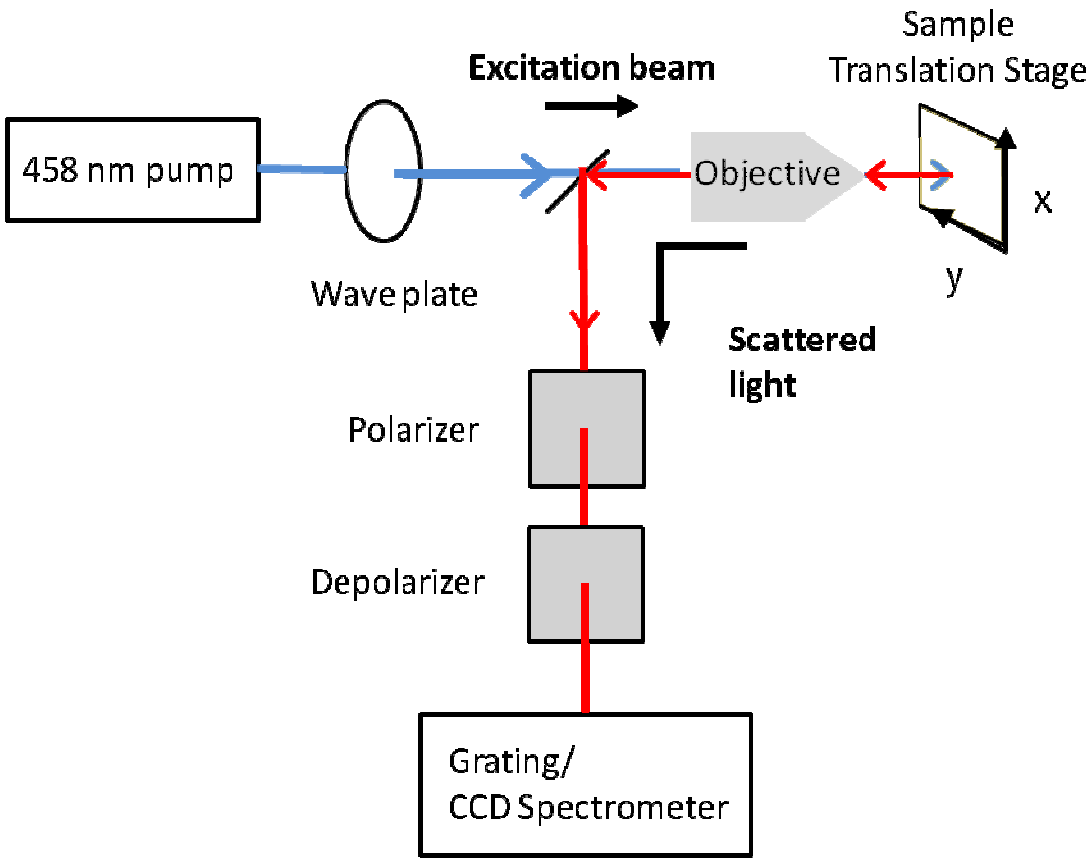

Figure 5.3: Diagram of the polarized Raman experimental setup. The beam generated in an Ar^{+} laser is directed through a $\lambda/2$ wave plate and the microscope objective to the sample stage. The scattered signal is collected through the same objective and reflected through a polarizer and a scrambler, and finally dispersed by a grating onto the detector.

For Raman measurements of solutions, dye loading solutions are contained in a 2 mm thick cuvettes (Starna Cells, Inc. #21-G-2). Approximately 0.6 mW laser beams are focused into the solutions and Raman scatter is collected using a Leica N PLAN EPI 20x/0.12 objective lens, also in a 180º backscattering geometry. The laboratory frame is defined by the input and measured polarizations, with the input photon propagating along the Z axis in the negative direction, and scattered light collected in the positive Z direction. Employing the notation of Porto[21] and others, the experiments performed are: –Z(XX)Z, -Z(XY)Z, -Z(YX)Z, -Z(YY)Z. Excitation beam polarization control is established by installation of a half wave plate prior to the sample. A wire grid polarizer is placed in the path of the scattered light to select measured polarization. All measurements utilize a depolarizer after the polarizer. Using a translation stage, data is collected at a series of sample locations in a grid pattern with points separated by 10 μm in the X and Y dimensions on the substrate in order to prevent photobleaching during data collection. At each location, signal is integrated for 60 seconds.

5.4. Results and Discussion

Resonance Raman spectra for complexes **RuP, RuCP,** and **Ru2P** on TiO_2 are shown in Figure 5.1. In contrast to resonance Raman spectra on nanocrystalline TiO_2, the signal intensities for all chromophore vibrations are significantly smaller due to the greatly reduced surface area of the single crystal substrate. All spectra exhibit four peaks between 1450 cm^{-1} and 1650 cm^{-1}, which have been assigned to bypyridine stretching modes in the chromophore ligands.[22-25] These modes are strongly coupled to the MLCT transition excited by the Raman pump, and are

therefore expected to have the largest intensities. For this reason, the bypyridine stretching peaks serve as ideal candidates for probing the geometry of the chromophore.

The spectral region between 100 cm^{-1} and 700 cm^{-1} consists of peaks corresponding to the TiO_2 substrate. The Raman spectrum of rutile TiO_2 is well known.[26-28] Useful for this study, the 450 cm^{-1} and 610 cm^{-1} peaks are highly polarization dependent. Specifically, since the vibration to which the 610 cm^{-1} peak corresponds is in-plane with the 001 face of the rutile unit cell it makes an excellent indicator of crystal orientation. By leveraging this peak's intensity as a function of polarization angle in combination with the fact that the substrate is a single crystal, direct conversion between the coordinate axes of the semiconductor interface and the laboratory frame is achieved. In addition to the vibrational modes of rutile already mentioned, there is an additional broad spectral feature centered near 1600 cm^{-1}.

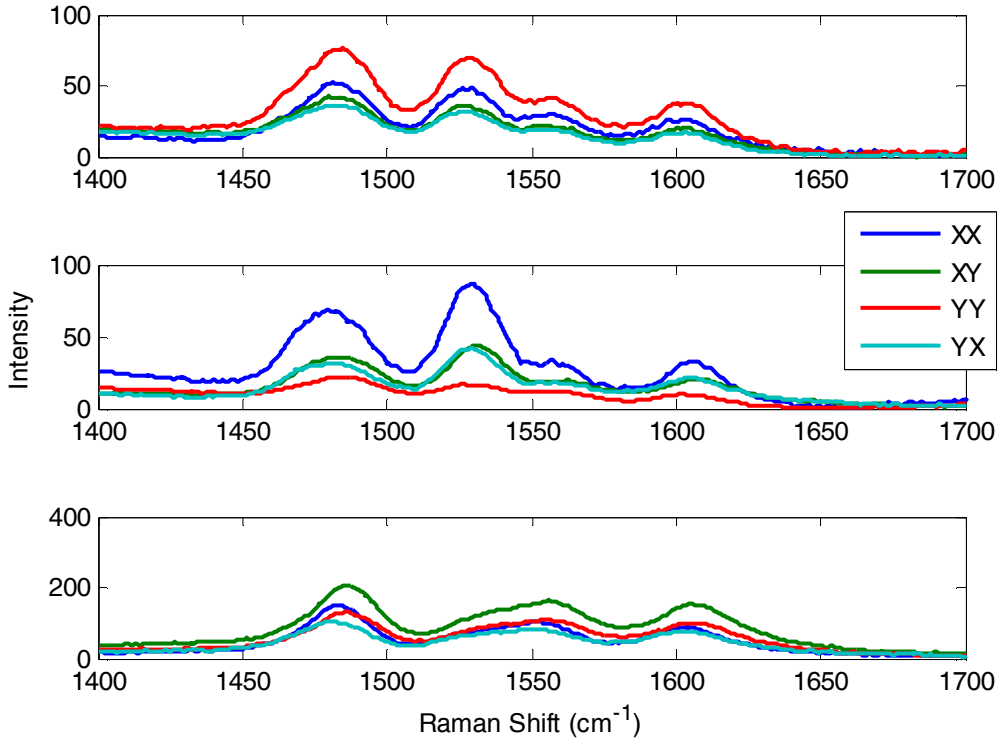

Figure 5.4: Polarized Resonance Raman spectra for (a) RuP on TiO_2, (b) Ru2P on TiO_2, and (c) RuCP on TiO_2 at the four combinations of polarization condition measured in the laboratory frame.

Raman spectra of bare rutile wafers are collected at each of the polarization conditions, in addition to sensitized wafer spectra. These spectra serve two main purposes- to provide adequate background spectra in order to isolate Raman scattering from the chromophore, and to eliminate erroneous spectra. As stated previously, the peaks at 450 cm^{-1} and 610 cm^{-1} peaks are dependent on the relationship between the polarization of the incident laser and the exposed crystal face. Namely, for a given set of polarization conditions, these two peaks will have fixed relative areas. Alterations in the crystal surface result in a deviation from this relation. Though the TiO_2 wafers are single crystals, they have a root mean square roughness of 945 nm. Since the data is collected

by scanning the microscope objective across the surface of the wafer, the possibility exists for some data points to correspond to rough locations on the crystal. However, these data points are easily identifiable by observable changes to the rutile peaks of the spectrum.

Peaks in the Raman spectra were fit using a Pseudo-Voigt profile

$$V(x) = \kappa L(x) + (1-\kappa)G(x), \tag{5.5}$$

where L(x) is a Lorentzian distribution such that

$$L(x) = \frac{a}{\pi\sigma\left(\frac{(x-x_0)^2}{\sigma^2}+1\right)}, \tag{5.6}$$

and G(x) is a Gaussian distribution such that

$$G(x) = \frac{a}{\sigma}\sqrt{\frac{\ln(2)}{\pi}}\cdot e^{\left(-\ln(2)\cdot\frac{(x-x_0)^2}{\sigma^2}\right)}. \tag{5.7}$$

Here, $0 < \kappa < 1$, a is the height, x_0 is the central Raman shift, and σ is the width of the peak. Each peak in a spectrum is fit using this function and integrated numerically to obtain the peak area. For each sample location in a data set, the area of the 610 cm^{-1} peak is divided by that of the 450 cm^{-1} peak. The ratio in the area of these to peaks is then compared against the ratio obtained on a polished rutile wafer, which is significantly more smooth, with a root mean square roughness of 1.68 nm. Data points for which the ratio deviates from the polished wafer are excluded when determining the average spectrum of each chromophore, ensuring that the averaged spectrum represents chromophore bound to a planar surface.

Table 5.1: Polarization ratios (R_x, R_y) for the chromophores on the crystal faces of TiO_2 measured. Uncertainty, δ, is obtained by propagating the standard deviation intensities in each polarization component measurement.

Chromophore	Surface	R_x	δ_x	R_y	δ_y
RuP	100	0.77665	0.39097	0.82355	0.56516
RuP	101	1.0142	0.95793	1.9842	1.8482
RuP	110	3.4255	2.8086	0.7047	1.2313
Ru2P	100	0.70883	1.2275	3.739	2.178
Ru2P	101	1.0105	1.9539	2.642	0.47625
Ru2P	110	2.7056	2.2096	4.0618	2.3879
RuCP	100	0.75835	0.37826	0.82085	0.6144
RuCP	101	0.54549	0.41147	0.99784	0.72186
RuCP	110	0.758	0.29639	0.8768	0.61313

Bipyridine stretching peaks are also fit to Pseudo-Voight lineshapes after subtraction of rutile background. For a given polarization experiment, the average intensity of the Raman signal is calculated by numerically integrating the four bipyridine peaks. The standard deviation in the intensity is calculated using only data points which contribute to the average. Therefore, for each chromophore, average and standard deviation intensities for the bipyridine stretching region are measured for four polarization conditions. These values are compiled in Table 5.1.

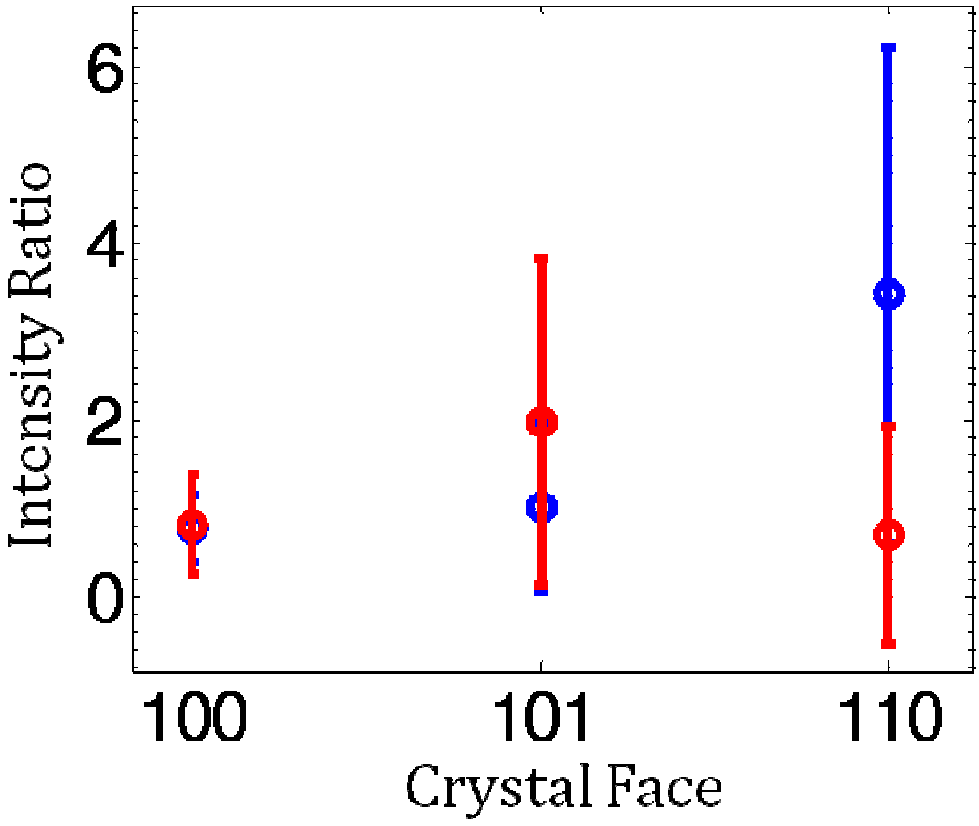

Figure 5.5: Average polarization ratios for **RuP** measured on each crystal face. XX, XY configurations give R_X (blue) and YY,YX configurations give R_Y (red). Error bars represent the ratio uncertainty calculated from standard deviation in the intensity of individual spectra for each configuration.

The experimental areas compiled in Table 5.1 are used to constrain the R_X and R_Y expected by the model to a limited region of molecular geometry subspace. That is, experimentally measured R_x and R_y are compared to calculated Raman signal ratios for a given chromophore, and a limited range of coordinates (α,ϕ,w) are determined which represent the molecular orientation of that chromophore on the TiO_2.

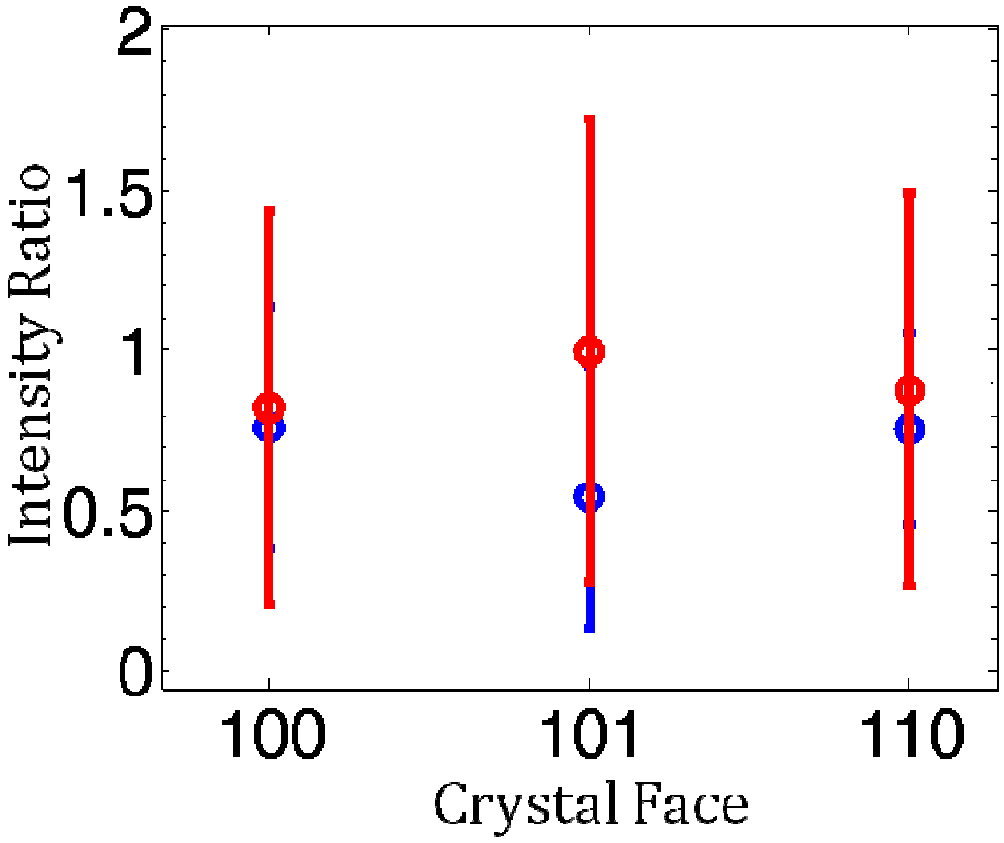

Figure 5.6: Average polarization ratios for **RuCP** measured on each crystal face. XX, XY configurations give R_X (blue) and YY,YX configurations give R_Y (red). Error bars represent the ratio uncertainty calculated from standard deviation in the intensity of individual spectra for each configuration.

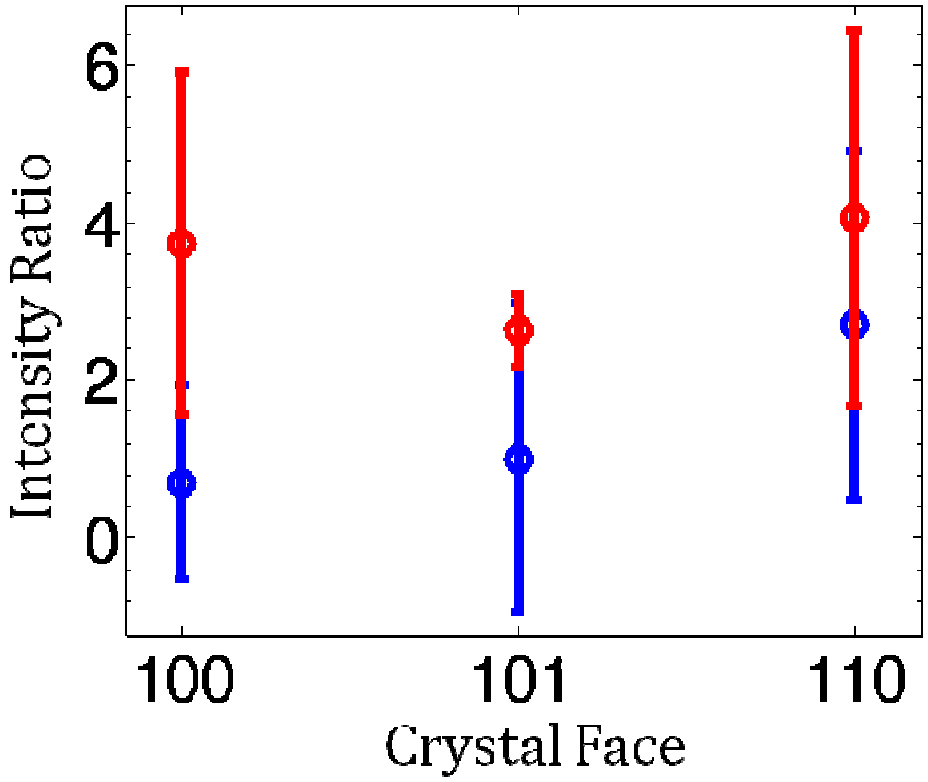

Figure 5.7: Average Average polarization ratios for **Ru2P** measured on each crystal face. XX, XY configurations give R_X (blue) and YY,YX configurations give R_Y (red). Error bars represent the ratio uncertainty calculated from standard deviation in the intensity of individual spectra for each configuration.

For all chromophores, little experimental dependence in polarization ratio on crystal surface is observed. RuP is limited to a tighter region of α and ϕ on 100 than the other surfaces, though its full width at half-maximum distribution coordinate is still greater than 60°. Additionally, the distribution angles calculated for the Ru2P chromophore range to the upper limit calculated, 200°, a distribution mildly dependant on α. The distributions for the RuCP

chromophore, however, only reach as high as 80° full width at half-maximum. While both represent heterogeneous binding geometries, the Ru2P appears to be so to a further degree.

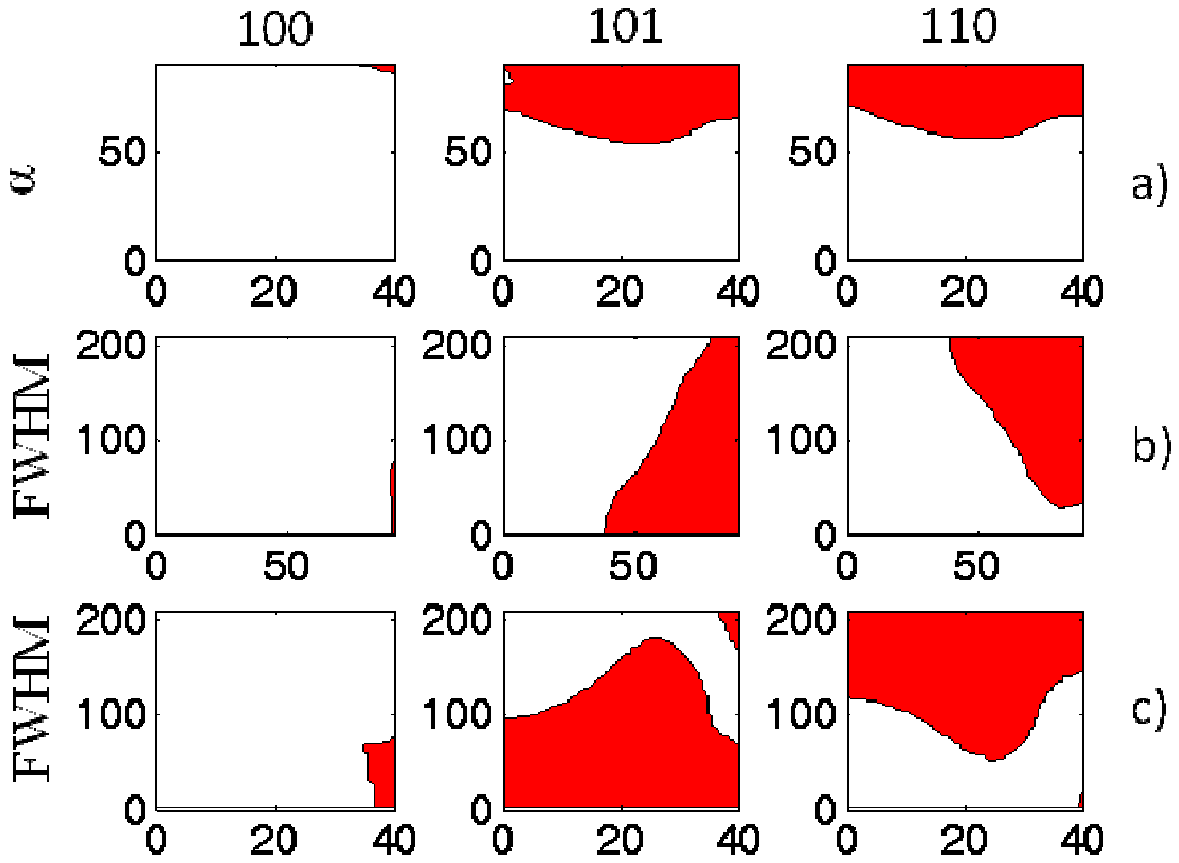

Figure 5.8: Geometry map for **RuP.** Each row of plots is a different two-dimensional projection of the three dimensional surface calculated for **RuP**, as follows: (a) Rotation angle, α, as a function of tilting angle, ϕ. (b) Full width at half-maximum distribution about the rotation angle, w, as a function of rotation angle, α. (c) Full width at half-maximum distribution about the rotation angle, w, as a function of tilting angle, ϕ. For all plots, the shaded regions indicate points at which experimental measurements suggest the molecule may exist. That is, the shaded region is the subspace of (α,ϕ,w) where the calculated intensity ratios agree with the measured intensity ratios.

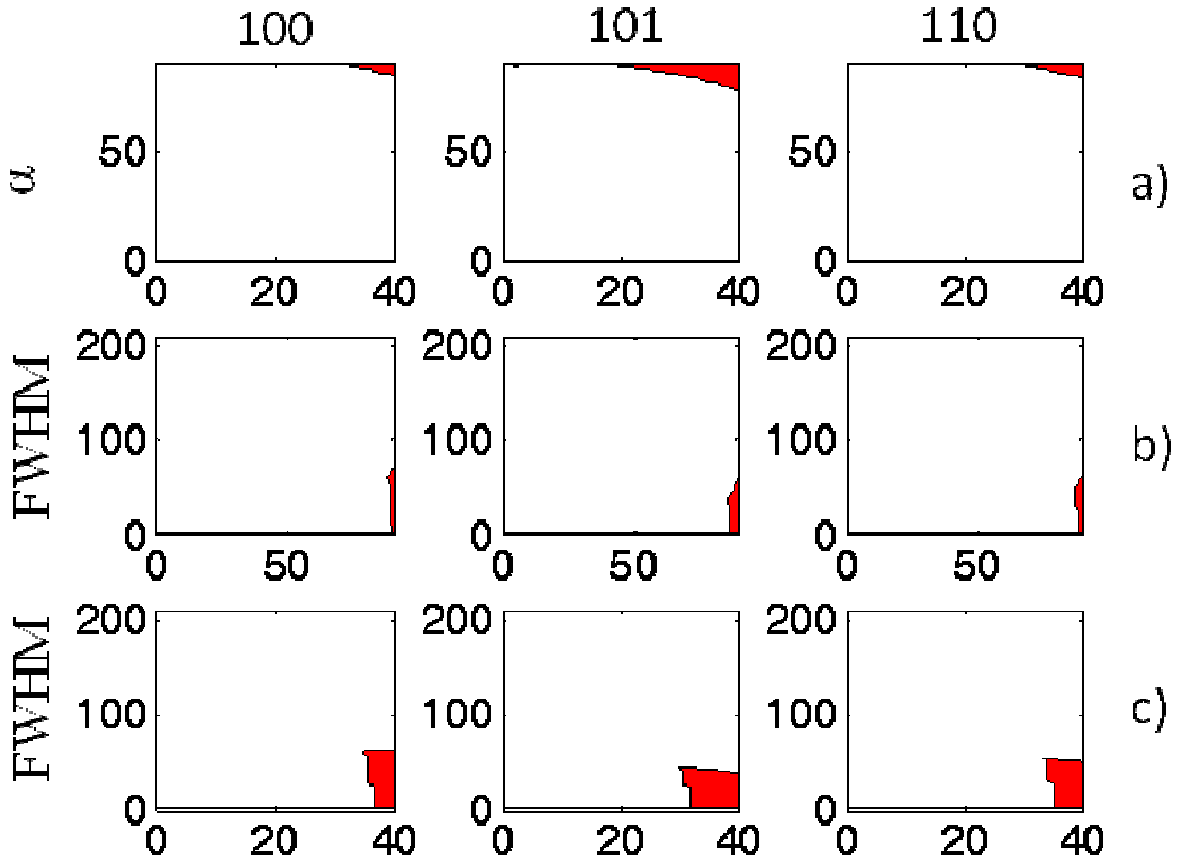

Figure 5.9: Geometry map for **RuCP.** Each row of plots is a different two-dimensional projection of the three dimensional surface calculated for **RuCP**, as follows: (a) Rotation angle, α, as a function of tilting angle, ϕ. (b) Full width at half-maximum distribution about the rotation angle, w, as a function of rotation angle, α. (c) Full width at half-maximum distribution about the rotation angle, w, as a function of tilting angle, ϕ. For all plots, the shaded regions indicate points at which experimental measurements suggest the molecule may exist. That is, the shaded region is the subspace of (α,ϕ,w) where the calculated intensity ratios agree with the measured intensity ratios.

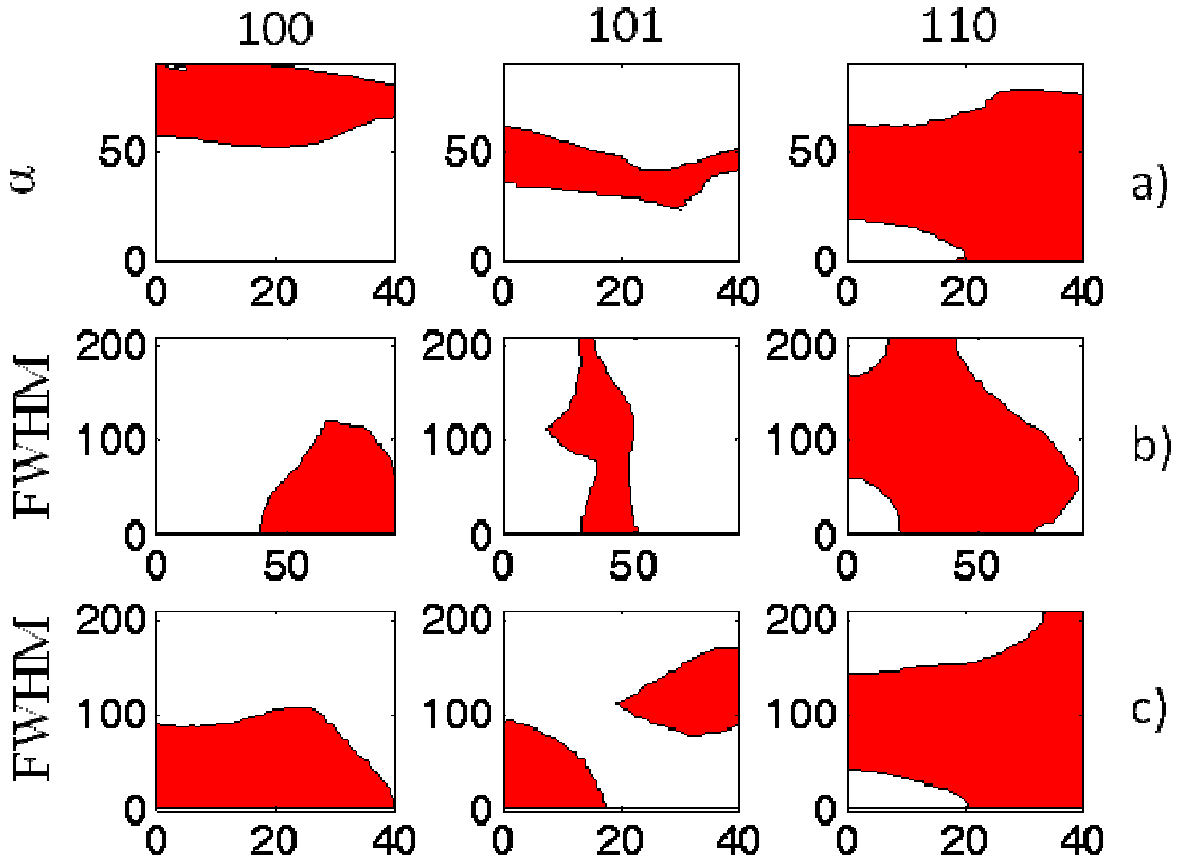

Figure 5.10: Geometry map for **Ru2P.** Each row of plots is a different two-dimensional projection of the three dimensional surface calculated for **Ru2P**, as follows: (a) Rotation angle, α, as a function of tilting angle, ϕ. (b) Full width at half-maximum distribution about the rotation angle, w, as a function of rotation angle, α. (c) Full width at half-maximum distribution about the rotation angle, w, as a function of tilting angle, ϕ. For all plots, the shaded regions indicate points at which experimental measurements suggest the molecule may exist. That is, the shaded region is the subspace of (α,ϕ,w) where the calculated intensity ratios agree with the measured intensity ratios.

Chromophores displayed a wide range of possible α values, and exhibited tilting angles ranging from normal to the surface to 40° away from normal. Further tilting would result in

deformation of the ligand orientations, and is therefore not included in this study. Combining this information with the wide distributions about those mean values provides a picture of the interface which is highly heterogeneous in nature with respect to this parameter. This compliments previous measurements of dye-sensitized TiO_2[29] which indicated various sub-ensembles of molecule geometries. The heterogeneity observed in those measurements has been shown to be a result of chromophore binding independent of surface irregularity.

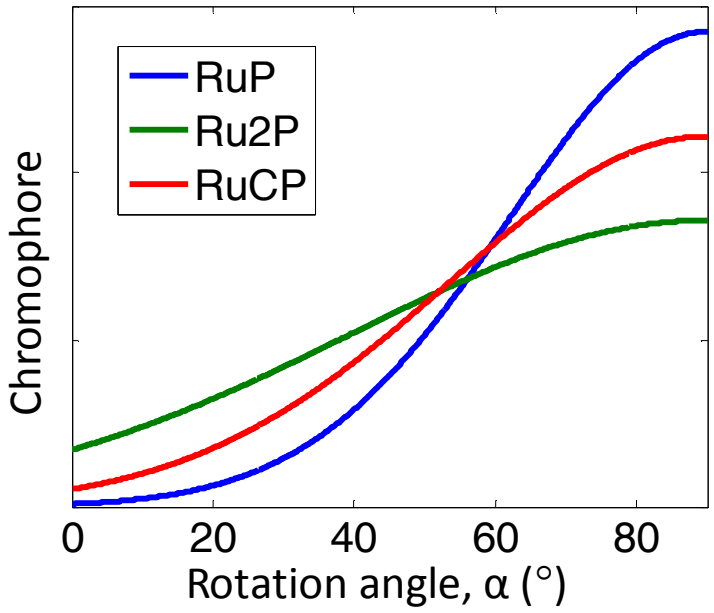

Figure 5.11: Chromophore geometry distributions. By combining the information from Figures 5.8-5.10, an ensemble distribution of each chromophore on the TiO_2 surface can be generated. From this representation, it is apparent that RuP has the most rigid binding of the three, and that all chromophores studied exhibit a moderately preferential binding orientation along the C axis of the unit cell.

5.5. Conclusions

Polarized resonance Raman measurements have shown the binding geometries of ruthenium chromophores RuP, RuCP, and Ru2P to be not well ordered on single crystal TiO_2, though a preferential orientation of the molecule toward the C axis of the tetragonal unit cell is observed. This result is found to be general with respect to the exposed crystal face of the semiconductor substrate- that is, across three different crystal faces of rutile TiO_2, the molecule has a consistent preference for the unit cell's C axis. This finding supports a model of variable chromophore-semiconductor couplings, which can help explain diverse electron transfer kinetics commonly measured in these systems.

The variation of chromophore orientations for each of the molecules measured also have implications for the binding preference of the phosphonate anchor groups. Specifically, the chromophore with multiple phosphonated ligands (Ru2P) shows a broader distribution in molecular orientation than either the RuP or RuCP chromophores. While the broadened distribution of the RuCP compared to the RuP can be explained by increased flexibility granted by the methylene spacer, Ru2P does not possess this structural feature. Therefore, the broad distribution is here attributed to multiple combinations of phosphate attachments. That is, in addition to attachment via both phosphonates of a single ligand, we conclude that this chromophore also binds to the TiO_2 surface via one phosphonate group on each of the functionalized bipyridine ligands. Such diversity in binding geometry has implications for chromophore-catalyst assemblies which may be constructed at the semiconductor interface.

5.6.REFERENCES

(1) Asbury, J. B.; Hao, E.; Wang, Y.; Ghosh, H. N.; Lian, T. J. *J. Phys. Chem. B* **2001**, *105*.

(2) Concepcion, J. J.; Jurss, J.; Brennaman, M. K.; Hoertz, P. G.; Patrocinio, A. O.; Iha, N. Y. M.; Templeton, J. L.; Meyer, T. J. *J. Acc. Chem. Res.* **2009**, *42*.

(3) Gratzel, M. *Nature* **2001**, *414*.

(4) Gregg, B. A. *J. Phys. Chem. B* **2003**, *107*.

(5) Hagfeldt, A.; Boschloo, G.; Sun, L.; Kloo, L.; Pettersson, H. *Chem Rev* **2010**, *110*.

(6) Kamat, P. V. *J. Phys. Chem. C* **2007**, *111*.

(7) Mallouk, T. E. *J. Phys. Chem. Lett.* **2010**, *1*.

(8) O'Regan, B.; Gratzel, M. *Nature* **1991**, *353*.

(9) Zou, Z.; Ye, J.; Sayama, K.; Arakawa, H. *Nature* **2001**, *414*.

(10) Xin, A.; Anderson, N. A.; Guo, J.; Lian, T. J. *J. Phys. Chem. B* **2005**, *109*.

(11) Ardo, S.; Meyer, G. J. *J. Chem. Soc. Rev* **2009**, *38*.

(12) Nozik, A. *J. Annu. Rev. Phys. Chem.* **2001**, *52*.

(13) Lu, H. P.; Xie, X. S. *J. Phys. Chem. B* **1997**, *101*.

(14) Giokas, P. G.; Miller, S. A.; Hanson, K.; Norris, M. R.; Glasson, C. R. K.; Concepcion, J. J.; Bettis, S. E.; Meyer, T. J.; Moran, A. M. *J. Phys. Chem. C* **2013**, *117*.

(15) Finnie, K. S.; Bartlett, J. R.; Woolfrey, J. L. *Langmuir* **1998**, *14*.

(16) Rensmo, H.; Westermark, K.; Sodergren, S.; Kohle, O.; Persson, P.; Lunnel, S.; Siegbahn, H. *J. Chem. Phys.* **1999**, *111*.

(17) Tachibana, Y.; Nazeeruddin, M. K.; Gratzel, M.; Klug, D. R.; Durrant, J. R. *Chem Phys* **2002**, *285*, 127.

(18) Reyes-Coronado, D.; Rodriguez-Gattorno, G.; Espinosa-Pesqueira, M. E.; C, C.; de Coss, R.; Oskham, G. *Nanotechnology* **2008**, *19*.

(19) Long, D. A. *The Raman Effect: A Unified Treatment of the Theory of Raman Scattering by Molecules*; Wiley: Chinchester, England, 2002.

(20) Hanson, K.; Brennaman, M. K.; Akitaka, I.; Hanlin, L.; Song, W.; Parker, K. A.; Ghosh, R.; Norris, M. R.; Glasson, C. R. K.; Concepcion, J. J. *J. Phys. Chem. C* **2012**, *116*.

(21) Damen, T. C.; Porto, S. P. S.; Tell, B. *Phys. Rev.* **1966**, *142*.

(22) Alexander, B. D.; Dines, T. J.; Longhurst, R. W. *Chem. Phys.* **2008**, *352*.

(23) Mallick, P. K.; Danzer, G. D.; Strommen, D. P.; Kincaid, J. R. *J. Phys. Chem.* **1988**, *92*.

(24) Strommen, D. P.; Mallick, P. K.; Danzer, G. D.; Lumpkin, R. S.; Kincaid, J. R. *J. Phys. Chem.* **1990**, *94*.

(25) Thompson, D. G.; Schoonover, J. R.; Timpson, C. j.; Meyer, T. J. *J. Phys. Chem. A* **2003**, *107*.

(26) Bersani, D.; Lottici, P. P.; Ding, X. Z. *Appl. Phys. Lett* **1998**, *72*.

(27) Narayanan, P. S. *Proc.of the Indian Acad. of Sci. - Sect A* **1953**, *37*.

(28) Toshiaki, O.; Fujio, I.; Yoshinori, F. *J. Raman Spectrosc.* **1978**, *7*.

(29) Miller, S. A.; West, B. A.; Curtis, A. C.; Papanikolas, J. M.; Moran, A. M. *J. Chem. Phys.* **2011**, *135*.

CHAPTER 6: MODELING TIME-COINCIDENT ULTRAFAST ELECTRON TRANSFER AND SOLVATION PROCESSES AT MOLECULE-SEMICONDUCTOR INTERFACES[1]

6.1. Introduction

Investigations of ultrafast electron transfer mechanisms at molecule-semiconductor interfaces are largely motivated by the development of photochemical cells.[1-18] Pioneering experimental work in this research area established 100 fs timescales for photoinduced electron injection in several dye-sensitized TiO_2 systems.[6,19] The observed dynamics conform to a sequential physical picture in which photoexcitation of the molecular sensitizer precedes electron injection into the semiconductor's conduction band.[20,21] Kinetic models based on Fermi's Golden Rule are a natural starting point for describing such non-radiative relaxation processes.[22-24] At this level of theory, the rate is determined primarily by the donor-acceptor coupling and the density of states (DOS) of the semiconductor at the energy of the excited molecular donor. Implicit in traditional second-order perturbative descriptions is the assumption that the time interval between light absorption and electron transfer is long compared to the time scale of nuclear relaxation. This approximation is generally not appropriate in systems with 100-fs electron injection time scales. Sophisticated theories for electron transfer have been developed to incorporate nonequilibrium effects related to photoinduced nuclear motions.[25-34] However, while elegant and powerful, these models are not easily adapted to fit and/or interpret experimental data. Researchers in this interdisciplinary field would benefit from an intuitive model with

[1] This article previously appeared as an article in the Journal of Chemical Physics. The original citation is as follows: Li, L., Giokas, P.G., Kanai, Y., Hanson, Moran, A.M. *J. Chem. Phys*. **2014**, *140*, 234109.

physically meaningful parameters, which can be obtained from standard spectroscopic measurements and/or first-principles electronic structure calculations.

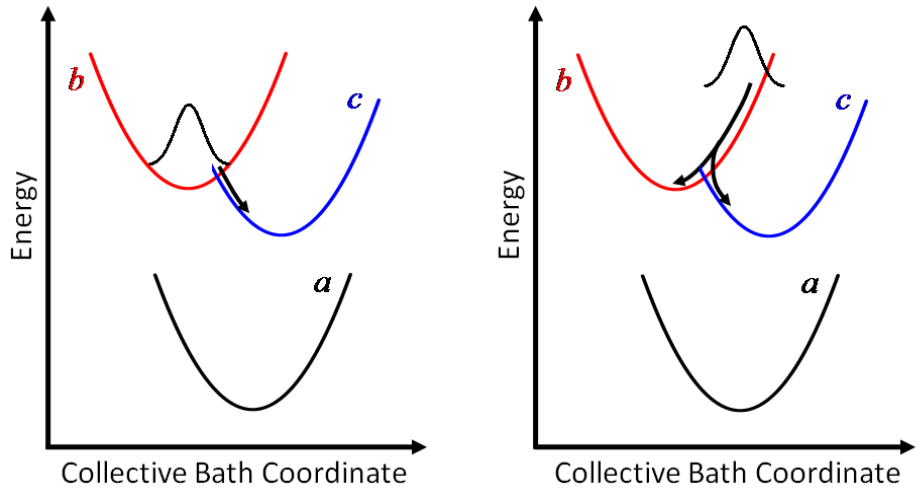

Figure 6.1: Wavepacket relaxation diagram. In the process of interest state b is first photoexcited, then transfers population to state c by way of an electron transfer transition. Second-order rate theories describe the scenario on the left, where thermalization of the wavepacket occurs before electron transfer to state c. The understanding of ultrafast electron transfer processes is complicated by the time-coincident electron transfer and nuclear relaxation dynamics, which are indicated on the right.

Inadequacies of second-order descriptions for ultrafast electron transfer dynamics can be understood by considering the three-level system depicted in Figure 6.1. Here, state a is the electronic ground state, whereas states b and c are electron-donating and electron-accepting states, respectively. The surfaces are plotted with respect to a collective bath coordinate, which reflects energy level fluctuations induced by the solvent and all low-frequency intramolecular modes.[35,36] In the process of interest, photoexcitation of state b precedes electron transfer to state c. Concepts such as activation energy barriers are applicable if an equilibrium distribution in state b governs the kinetics.[37] However, non-equilibrium wavepacket motions must be taken into

account in electron transfer processes that are fast compared to the time scale of nuclear relaxation. In this regime, the dynamic transition probability depends on the displacement of the wavepacket from the point where the diabatic surfaces of states b and c intersect; the likelihood of a transition increases with the footprint of the wavepacket at this point of intersection. The challenge is to translate this basic idea into a quantitative model with well-defined approximations.

Here, we develop a kinetic model at fourth-order in perturbation theory, which captures the interplay between time-coincident electron transfer and nuclear relaxation dynamics. A "short time approximation" is used to obtain analytical formulas for which most of the parameters can be derived from basic spectroscopic measurements (e.g., linear absorbance, fluorescence).[35,38] Although the model corresponds to fourth-order in perturbation theory, it conveniently converges to the classic second-order rate formula developed by Marcus at times that are long compared to nuclear relaxation (i.e., in the equilibrated system).[39] Model calculations are used to investigate dynamics for molecular systems coupled to (i) a single acceptor state and (ii) a continuum of levels in a semiconductor. The second and fourth-order descriptions are first compared for various electron transfer regimes (e.g., normal, activationless, inverted) in a three-level system. We then combine our perturbative model with a DOS for TiO_2 computed with a high-level, first-principles electronic structure model.

6.2. Modeling Ultrafast Electron Transfer Kinetics

This section presents models that can be used to calculate electron transfer dynamics at both second and fourth-order in perturbation theory. We begin by partitioning the Hamiltonian into system and bath components, then use time correlation functions to generate rate

formulas.[35,36,38] The traditional second-order rate formula can be applied when the nuclear coordinates relax on a time scale that is fast compared to electron transfer, whereas effects related to (photoinduced) nuclear motions are incorporated only at fourth-order. Key assumptions that are particular to the present model are summarized at the end of the section.

6.2.A. Hamiltonian

The three components of the Hamiltonian, $H = H_{sys} + H_{bath} + H_{sys-bath}$, are given by

$$H_{sys} = |a\rangle E_a \langle a| + |b\rangle E_b \langle b| + |c\rangle E_c \langle c| \ , \tag{6.1}$$

$$H_{bath} = \frac{1}{2}\sum_i \left[\frac{p_i^2}{m_i} + m_i \omega_i^2 q_i^2 \right] \left[|a\rangle\langle a| + |b\rangle\langle b| + |c\rangle\langle c| \right] \ , \tag{6.2}$$

and

$$H_{sys-bath} = |a\rangle Q_a \langle a| + |b\rangle Q_b \langle b| + |c\rangle Q_c \langle c| \ . \tag{6.3}$$

The basis set consists of three electronic energy levels: state a is the ground state; b represents an optically active, electron-donating state; state c represents an optically inactive, electron-accepting state. The bath consists of displaced harmonic oscillators for which the associated variables are written in lower case (m_i , ω_i , and q_i). Parameters of the bath are not treated explicitly in this reduced description. Instead, stochastic fluctuations in the energy levels of the system are introduced using a time-correlation function approach.[35,36,38]

(collective) Brownian oscillator coordinates in $H_{sys-bath}$ are related to the displaced harmonic modes in H_{bath} by $Q_b = \sum_i m_i \omega_i^2 d_{bi} q_i$, where d_{bi} is the displacement of mode i with

respect to the equilibrium position in the ground state (i.e., the coupling strength). It is instructive to consider that the Brownian oscillator coordinates satisfy the Langevin equation.[35,36,38] From this perspective, the overdamped limit considered here suggests that the amount of friction imposed by the secondary coordinates of the bath, q_i, is much larger than the frequencies of the primary oscillators ($\gamma_b >> \Omega_b$), which couple linearly to the system's energy levels. This approximation is generally appropriate for systems with absorbance spectra that do not exhibit vibronic structure (e.g., Gaussian line shapes). Ultimately, time correlation functions between the collective Brownian oscillator coordinates, $\langle Q_b(t) Q_b(0) \rangle$, will be evaluated. As discussed in detail elsewhere,[35] these correlation functions are related to the second term in a cumulant expansion by

$$g_b(t) = \frac{1}{\hbar^2} \int_0^t d\tau_2 \int_0^{\tau_2} d\tau_1 \langle Q_b(\tau_1) Q_b(0) \rangle \ . \tag{6.4}$$

Evaluation of Equation (6.4) in the high-temperature limit yields[35]

$$g_b(t) = \left(\frac{2\lambda_b k_B T}{\hbar^2 \Lambda_b^2} - i \frac{\lambda_b}{\hbar \Lambda_b} \right) \left[\exp(-\Lambda_b t) + \Lambda_b t - 1 \right] , \tag{6.5}$$

where Λ_b^{-1} is the time scale of nuclear relaxation in state b and λ_b is the reorganization energy.

6.2.B. Fourth-Order Rate Formula

In the process of interest, two laser-matter interactions occur before the donor-acceptor coupling induces population flow between excited states. Correlation functions involving three

time intervals must be evaluated at fourth-order to describe this sequential process. As in our related work on internal conversion processes,[40] the fourth-order rate constant for photoinduced electron transfer can be written as

$$K^{(4)} = \frac{2}{\hbar^4}\mathrm{Re}\int_0^\infty dt_1\int_0^\infty dt_2\int_0^\infty dt_3 \left\langle \hat{H}_{rad-mat}(t_1)\hat{V}(t_1+t_2)\hat{V}(t_1+t_2+t_3)\hat{H}_{rad-mat}(0)\right\rangle + \left\langle \hat{H}_{rad-mat}(0)\hat{V}(t_1+t_2)\hat{V}(t_1+t_2+t_3)\hat{H}_{rad-mat}(t_1)\right\rangle , \quad (6.6)$$

where $\hat{H}_{rad-mat}$ represents a field-matter interaction, $\hat{V}$ is the donor-acceptor coupling for electron transfer, and t_j are time intervals between interactions with the perturbations. Below, rate kernels will first be obtained by integrating only over t_1 and t_2, thereby retaining the waveform of the coherence (in t_3) between the two states involved in the non-radiative transition, b and c. Physical insights will be drawn by examining connections between this temporal coherence and the motion of a nuclear wavepacket.

Figure 6.2 presents fourth-order, double-sided Feynman diagrams for photoinduced electron transfer in the notation outlined in the previous section. The Feynman diagrams indicate that state b is populated after two interactions with the laser field; t_1 is the time interval in which the system absorbs light. Following photoexcitation, the system evolves in t_2 in an electronic population in state b. The final two interactions with the donor-acceptor coupling transfer population from state b to state c. The waveform of the coherence between states b and c in t_3 encodes key aspects of the electron transfer transition. For example, the magnitude of the rate kernel, which is discussed in more detail below, generally increases as the oscillation frequency in t_3 decreases. It will be shown below that this oscillation frequency can be translated into the

proximity of a wavepacket to the point of intersection between the diabatic potential energy surfaces of states b and c (see Figure 6.1).

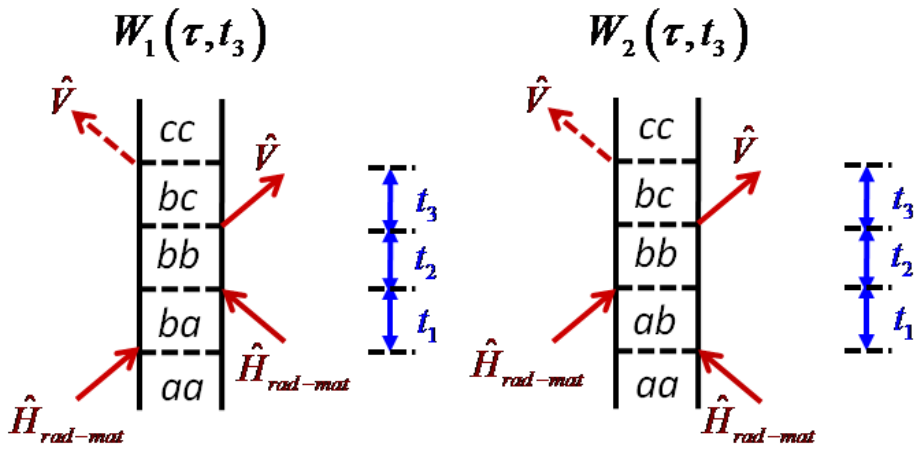

Figure 6.2: Double-sided Feynman diagrams corresponding to the two rate kernels. The time intervals, t_i, separate perturbative interactions with an external electric field, $\hat{H}_{rad-mat}$, and the donor-acceptor coupling, $\hat{V}$. In $W_1(\tau,t_3)$ and $W_2(\tau,t_3)$, the interval between the peak of the laser pulse and the first interaction with $\hat{V}$, τ, is closely related to t_2; $\tau = t_2$ for a delta-function laser pulse.

Attainment of the rate kernels associated with the two Feynman diagrams shown in Figure 6.2 basically involves substituting the donor-acceptor coupling, V_{bc}, for the final two field-matter interactions in four-wave mixing response functions.[35] The two rate kernels are

$$W_1(\tau,t_3) = 2\frac{|\mu_{ba}|^2 |V_{bc}|^2}{\hbar^4} \mathrm{Re}\left\{\int_0^\infty dt_1 \int_0^\infty dt_2 \exp^{\left[-i(\omega_{ba}t_1+\omega_{bc}t_3)-f_1(t_1,t_2,t_3)\right]} E(\tau-t_2-t_1)E^*(\tau-t_2)\right\}, \quad (6.7)$$

and

$$W_2(\tau,t_3)=2\frac{|\mu_{ba}|^2|V_{bc}|^2}{\hbar^4}\mathrm{Re}\left\{\int_0^\infty dt_1\int_0^\infty dt_2\exp^{\left[-i(\omega_{ab}t_1+\omega_{bc}t_3)-f_2(t_1,t_2,t_3)\right]}E^*(\tau-t_2-t_1)E(\tau-t_2)\right\}, \quad (6.8)$$

where μ_{ab} is a transition dipole and $f_j(t_1,t_2,t_3)$ are line shape functions. The electric field is given by

$$E(t)=\xi_L\exp\left[-i\omega_L t-w_L^2t^2/2\hbar^2\right], \quad (6.9)$$

where ω_L is the carrier frequency, ξ_L is the field amplitude, and w_L is the spectral width. In the short-time approximation, the line shape functions can be written as[35,41]

$$\begin{aligned}f_1(t_1,t_2,t_3)&=\frac{1}{2\hbar^2}\Delta_b^2\left(t_1^2+t_3^2\right)+\frac{1}{2\hbar^2}\Delta_c^2t_3^2+i\frac{2\lambda_b}{\hbar}\left[\exp\left(-\Lambda_b t_2\right)-1\right]t_3\\&+\frac{\Delta_b^2}{\hbar^2}\exp\left(-\Lambda_b t_2\right)t_1t_3\end{aligned} \quad (6.10)$$

and

$$\begin{aligned}f_2(t_1,t_2,t_3)&=\frac{1}{2\hbar^2}\Delta_b^2\left(t_1^2+t_3^2\right)+\frac{1}{2\hbar^2}\Delta_c^2t_3^2+i\frac{2\lambda_b}{\hbar^2}\left[\exp\left(-\Lambda_b t_2\right)-1\right]t_3\\&-\frac{\Delta_b^2}{\hbar^2}\exp\left(-\Lambda_b t_2\right)t_1t_3\end{aligned} \quad (6.11)$$

Here, Λ_b^{-1} is the time scale of nuclear relaxation in state b and Δ_b^2 (Δ_c^2) is the variance in thermal fluctuations of the energy level b(c). The variance is related to the reorganization energy by $\lambda_b=\Delta_b^2/2k_BT$.[35]

Ultimately, compact analytical expressions for the population dynamics are desired, because these will yield the clearest physical insights. The short-time approximation for the line shape functions employed in Equations (10) and (11) is an important step in this direction, but it does not solve the problem of handling finite laser bandwidths. Therefore, we adapt an approach

that has been used in nonlinear spectroscopies, where effects related to the laser bandwidth are incorporated by introducing the integration variable, $t' = \tau - t_2$.[35,41] This approximation is justified when the temporal width of the laser pulse is short compared to the time scale of the nuclear dynamics.[35,42] The rate kernels are then given by

$$W_1(\tau, t_3) = 2\frac{|\mu_{ba}|^2 |V_{bc}|^2}{\hbar^4} \mathrm{Re}\left\{\int_0^\infty dt_1 \int_0^\infty dt' \exp\left[-i(\omega_{ba}t_1 + \omega_{bc}t_3) - f_1(t_1, \tau, t_3)\right] E(t' - t_1) E^*(t')\right\} \quad (6.12)$$

and

$$W_2(\tau, t_3) = 2\frac{|\mu_{ba}|^2 |V_{bc}|^2}{\hbar^4} \mathrm{Re}\left\{\int_0^\infty dt_1 \int_0^\infty dt' \exp\left[-i(\omega_{ab}t_1 + \omega_{bc}t_3) - f_2(t_1, \tau, t_3)\right] E^*(t' - t_1) E(t')\right\}. \quad (6.13)$$

It is next useful to consider how the rate kernels influence the excited state population dynamics. To this end, we write the following set of integro-differential equations for states b and c,

$$\frac{d}{d\tau} P_b^{(4)}(\tau) = -\int_0^\tau dt' W_{cb}(\tau, \tau - t') P_b^{(4)}(t') + \int_0^\tau dt' W_{bc}(\tau, \tau - t') P_c^{(4)}(t'), \quad (6.14)$$

and

$$\frac{d}{d\tau} P_c^{(4)}(\tau) = \int_0^\tau dt' W_{cb}(\tau, \tau - t') P_b^{(4)}(t') - \int_0^\tau dt' W_{bc}(\tau, \tau - t') P_c^{(4)}(t'), \quad (6.15)$$

where

$$W_{cb}(\tau, t_3) = W_1(\tau, t_3) + W_2(\tau, t_3) \quad (6.16)$$

In Section 6.5, it is shown that the radiative transition rate between states a and b can be neglected in these kinetic equations by defining a normalized excitation probability. A set of ordinary differential equations can replace Equations (14) and (15) when dynamics in the

populations are slow compared to the time scale of dephasing (typically 10-20 fs for systems in solution at ambient temperatures). In this Markovian approximation, the upper limit of integration becomes infinite and the populations can be removed from the integrands in Equations (14) and (15).[36] We then have

$$\frac{d}{d\tau}P_b^{(4)}(\tau) \approx -P_b^{(4)}(\tau)K_{cb}^{(4)}(\tau) + P_c^{(4)}(\tau)K_{bc}^{(4)}(\tau)\,, \tag{6.17}$$

and

$$\frac{d}{d\tau}P_c^{(4)}(\tau) \approx P_b^{(4)}(\tau)K_{cb}^{(4)}(\tau) - P_c^{(4)}(\tau)K_{bc}^{(4)}(\tau)\,, \tag{6.18}$$

where

$$K_{cb}^{(4)}(\tau) = \mathrm{Re}\int_0^\infty dt_3 W_{cb}(\tau, t_3)\,. \tag{6.19}$$

The τ-dependence of $K_{cb}^{(4)}(\tau)$ and $K_{bc}^{(4)}(\tau)$ continuously "updates" the dynamic transition probability to account for the time-evolving geometry of the photoexcited system.

An analytical expression can be obtained for the fourth-order rate function, $K_{cb}^{(4)}(\tau)$, under the present approximations. The above equations are combined to obtain

$$\boxed{K_{cb}^{(4)}(\tau) = \frac{\pi^{3/2}\left|\xi_L\right|^2\left|\mu_{ba}\right|^2\left|V_{bc}\right|^2}{\hbar\left[w_L^2\left(\Delta_b^2 + w^2\right)\alpha^2(\tau)\right]^{1/2}}\exp\left[-\frac{\left(\hbar\omega_L - \hbar\omega_{ba}^0 - \lambda_b\right)^2}{2\left(\Delta_b^2 + w^2\right)}\right]\exp\left[-\frac{1}{2}\frac{\Omega^2(\tau)}{\alpha^2(\tau)}\right]}, \tag{6.20}$$

where

$$\Omega(\tau) = \hbar\omega_{bc}^0 - \lambda_b - \lambda_c + 2\lambda_b\exp(-\Lambda_b\tau) + \exp(-\Lambda_b\tau)\left[\frac{\Delta_b^2}{\Delta_b^2 + w_L^2}\left(\hbar\omega_L - \hbar\omega_{ba}^0 - \lambda_b\right)\right], \tag{6.21}$$

and

$$\alpha^2(\tau) = \left[\Delta_b^2 + \Delta_c^2 - \frac{\Delta_b^4}{\Delta_b^2 + w_L^2} \exp(-2\Lambda_b \tau) \right]. \quad (6.22)$$

In $K_{cb}^{(4)}(\tau)$, we have made use of purely electronic transition frequencies, ω_{ba}^0 and ω_{bc}^0, which correspond to free energy differences between the respective electronic states. These parameters are convenient to work with when considering electron transfer kinetics, because free energy differences are typically utilized in the electron transfer literature.[37] It should be emphasized that is constrained by the normalized excitation probability defined in Equation (6.28), which removes dependence on the rate of light absorption. We show in Section 6.5 that this normalization condition is justified by agreement between the second and fourth-order rate formulas in the equilibrated system (i.e., at $\tau >> \Lambda_b^{-1}$).

With a convenient formula for the fourth-order rate function in hand, the model can now be generalized to an arbitrary number of acceptor states to approximate conditions at a molecule-semiconductor interface. The total rate for electron transfer from the excited molecule (state b) to a continuum of acceptor states (state c) in a semiconductor is obtained by convoluting $K_{cb}^{(4)}(\tau)$ with the DOS, $\rho(E)$,

$$K_{total}^{(4)}(\tau) = \int_{-\infty}^{\infty} dE_c K_{cb}^{(4)}(\tau; E_c) \rho(E_c) . \quad (6.23)$$

6.2.C. Assumptions and Limitations of Model

This section further discusses key assumptions that are particular to the present fourth-order description. Approximations that are inherent in the correlation function approach employed here have been discussed in detail elsewhere.[35,36,38]

The Feynman diagrams presented in Figure 6.2 assume a sequential process in which light absorption precedes the non-radiative transition between excited states. That is, perturbative interactions with the donor-acceptor coupling are taken to occur after perturbative interactions with the external electric field. This assumption is valid when the duration of the laser pulse is short compared to the time scale of the electron transfer transition. Models for conventional transient absorption spectroscopies invoke similar approximations in the regime of well-separated pump and probe pulses (e.g., doorway-window model).[35] This approximation is also justified for systems with negligible rates of electron transfer in the molecular ground state. Sequences of interactions in which electron transfer processes precede light absorption can then be neglected even if the laser pulse duration is not short compared to the time scale of photoinduced electron transfer.

The primary goal of the model is to describe the interplay between time-coincident nuclear relaxation and electron transfer dynamics that occur after the system has absorbed light. The dynamics, rather than the absolute number of excitations, is of interest. Therefore, we have introduced a normalized excitation probability, which is motivated by correspondence between second and fourth-order descriptions at long times, to remove the dependence of the population dynamics on the laser intensity (see Section 6.5). Correspondence between these two orders of perturbation theory is based on three key assumptions. First, it is assumed that the laser is tuned near the peak of the electronic absorbance spectrum ($\hbar\omega_L \approx \hbar\omega_{ba}^0 + \lambda_b$). Second, the slow modulation regime of line broadening, $\sqrt{2\lambda_b k_B T} >> \hbar\Lambda_b$, must be satisfied (i.e., Gaussian line shapes).[35] Third, the electron transfer transition rate must be slower than the time scale of dephasing between states b and c. Similar assumptions were used to motivate a normalized excitation probability in our treatment of internal conversion dynamics.[40]

While the present model is fourth-order overall, it is only second-order with respect to both the field-matter interaction, $\hat{H}_{rad-mat}$, and the donor-acceptor coupling, $\hat{V}$. Thus, with respect to each operator, truncation of the perturbative expansion is justified by essentially the same assumptions that support traditional second-order rate theories. That is, it may be necessary to expand either (or both) of these perturbative couplings to higher-order if their magnitudes become large compared to the fluctuation amplitudes in the relevant energy gaps. We suggest that the present fourth-order model is sufficient if the following two conditions are satisfied: $\xi_L \mu_{ba} << \lambda_b$ and $V_{bc} << \lambda_b + \lambda_c$. The first condition compares the radiative coupling to the fluctuation amplitude in the molecular energy gap between levels a and b, whereas the second condition compares the donor-acceptor coupling to the fluctuation amplitude between levels b and c.

6.3. Second and Fourth-Order Dynamics in a Three-Level System

An attractive aspect of the present model is that many parameters can be obtained from steady state spectroscopic measurements and/or from theoretical calculations. Under the approximations outlined above, absorption and fluorescence line shapes are given by[35]

$$\sigma_A(\omega) = \frac{|\mu_{ba}|^2}{\sqrt{4\pi\lambda_b k_B T}} \exp\left[-\frac{\left(\hbar\omega - \hbar\omega_{ba}^0 - \lambda_b\right)^2}{4\lambda_b k_B T} \right], \tag{6.24}$$

and

$$\sigma_F(\omega) = \frac{|\mu_{ba}|^2}{\sqrt{4\pi\lambda_b k_B T}} \exp\left[-\frac{\left(\hbar\omega - \hbar\omega_{ba}^0 + \lambda_b\right)^2}{4\lambda_b k_B T} \right]. \tag{6.25}$$

The reorganization energy, λ_b, can be estimated using either the measured line widths or the Stokes shift between the absorbance and fluorescence spectra. The line width of the absorbance spectrum will be accessible even for weakly emissive molecules and/or systems that possess complicated intramolecular photophysics (e.g., ruthenium complexes).[43] Figure 6.3 displays these steady state spectroscopic line shapes overlaid with the laser spectrum employed in simulations of the dynamics below.

Physical insight into time-coincident electron transfer and nuclear relaxation processes is greatly facilitated by a wavepacket representation of the dynamics. In Section 6.6, we outline an approach, originally applied to pump-probe spectroscopies,[35] in which the position of the wavepacket is translated onto the energy gap between a pair of electronic states. To begin, we consider a three-level system with a single acceptor state, c. Physical intuition suggests that the transition probability should maximize when the wavepacket passes over the point of intersection between the diabatic surfaces as indicated in Figure 6.1. The formula for $K_{cb}^{(4)}(\tau)$ given in Section 4.2.B captures this behavior; $K_{cb}^{(4)}(\tau)$ maximizes when the peak of the wavepacket is located over the crossing point because $\Omega(\tau)$=0. More generally, it should be understood that the fourth-order rate kernel, $W_{cb}(\tau, t_3)$, loses oscillatory character (in t_3) at the point of intersection even if the Markovian approximation is not invoked (see Equations (17)-(19)). As a general "rule of thumb", the peak of the wavepacket will encounter the point of intersection if

$\lambda_c - \lambda_b \leq \hbar\omega_{bc}^0 \leq \lambda_c + \lambda_b$ when the laser is tuned into resonance with the peak of the absorbance spectrum ($\hbar\omega_L = \hbar\omega_{ba}^0 + \lambda_b$).

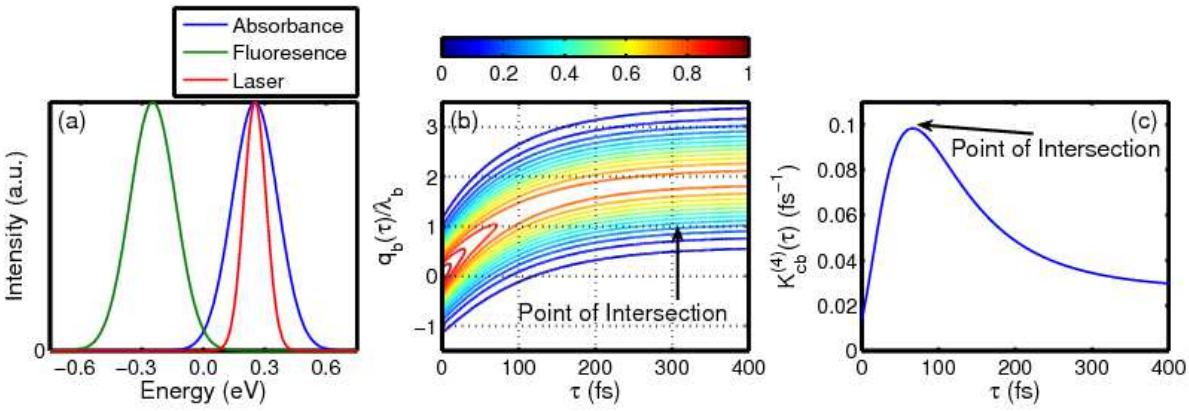

Figure 6.3: Wavepacket calculation plots. (a) Steady-state spectra, $\sigma_A(\omega)$ and $\sigma_F(\omega)$, overlaid with spectrum of laser. (b) Wavepacket computed using Equation (6.35). (c) The model predicts an enhancement in $K_{cb}^{(4)}(\tau)$ when the wavepacket passes over the point where the diabatic surfaces for states b and c intersect, $q_b(\tau)/\lambda_b$=1. Parameters are given in Table 6.1.

Insights derived from the wavepacket representation are illustrated in Figure 6.3. In addition to motion of its peak, the wavepacket expands as the system relaxes, because the laser spectrum is narrower than the absorbance line width. The calculations are carried out with $\hbar\omega_{bc}^0 = \lambda_c$, so the wavepacket passes over the point of intersection at $q_b(\tau)/\lambda_b$=1. The contour plot in Figure 6.3b shows that the wavepacket possesses significant amplitude at $q_b(\tau)/\lambda_b$=1 throughout the relaxation process because of its substantial width. Nonetheless, it is found that $K_{cb}^{(4)}(\tau)$ still exhibits a clear maximum when $q_b(\tau)/\lambda_b$=1, where its magnitude is roughly 5

times greater than the magnitudes computed at the equilibrium geometries of states b and c (i.e., at τ=0 and $\tau >> \Lambda_b^{-1}$).

In Figure 6.4, population dynamics are simulated under the assumption of an irreversible process, where population transfers from state b to state c but not vice-versa. The population of state b at nth-order is then given by

$$P_b^{(n)}(\tau) = P_b^{(n)}(0)\exp\left[-\int_0^\tau dt K_{cb}^{(n)}(t)\right] \tag{6.26}$$

where n is equal to either 2 or 4. Predictions of the second and fourth-order rate theories are compared in the normal, activationless, and inverted regimes of electron transfer. Notably, these regimes are defined with respect to the (thermalized) system at $\tau >> \Lambda_b^{-1}$. Calculations carried out in the normal regime show that the fourth-order population dynamics are several orders of magnitude faster than those computed at second-order. This discrepancy originates in the ability of the wavepacket to traverse the point of intersection between diabatic surfaces at fourth-order (see Figure 6.4a). In the activationless regime, the second-order population of state b decays roughly 10 times faster than that at fourth-order. The key issue is that equilibrium distribution is centered directly on top of the point of intersection between states b and c, whereas the photoinduced wavepacket reaches this location after the delay, Λ_b^{-1}. Finally, fairly similar population dynamics are computed in the inverted regime at both second and fourth-orders, because the same activation energy barrier to electron transfer must be overcome at both levels of theory.

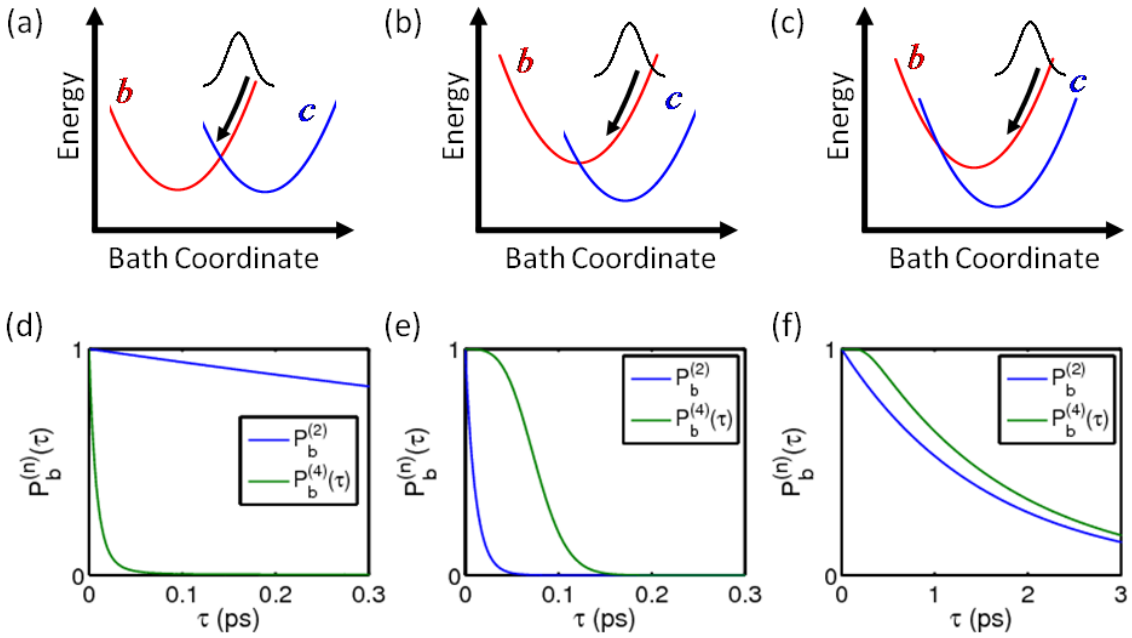

Figure 6.4: Second and fourth-order dynamics are simulated for a three-level system in the: (a),(d) normal regime with $\hbar\omega_{bc}^{0}$=0; (b),(e) activationless regime with $\hbar\omega_{bc}^{0}=\lambda_b+\lambda_c$;(c),(f) inverted regime with $\hbar\omega_{bc}^{0}=2\lambda_b+2\lambda_c$. The kinetics reveal sensitivity to the dynamic "footprint" of the wavepacket on the point of intersection between the diabatic surfaces b and c. $P_b^{(n)}$ represents the population of state b obtained at nth-order in perturbation theory.

The wavepacket dynamics simulated in the present model should not be mistaken for adiabatic relaxation processes.[44,45] Perturbative treatment of the donor-acceptor coupling is justified when V_{bc} is small compared to fluctuation amplitudes in the energy levels, b and c. In condensed phases at ambient temperatures, it is often not useful to consider wavefunction delocalization even if the average energies of states b and c are degenerate because the energy distributions (i.e., wavepackets) possess such broad widths. One litmus test for deciding on the most appropriate basis set compares V_{bc} and Δ_b; the dynamics are safely treated in the

perturbative regime when $\Delta_b / V_{bc} >> 1$ even when $\omega_{bc}^0 = 0$ ($\Delta_b / V_{bc} \approx 18$ in the present calculations). For example, if states b and c are degenerate at the geometry corresponding to the peak of the wavepacket, then the energy gaps between states b and c at the half-maxima of the wavepacket are still roughly 20 times larger than the coupling strength; this calculation assumes that V_{bc} (6 meV) and $\lambda_b + \lambda_c$ =0.25 eV.

6.4. Combining Fourth-Order Model with a First-Principles DOS for TiO_2

One strength of the present model is that most of the parameters can be obtained through basic spectroscopic measurements. For example, transition frequencies and reorganization energies can be derived from linear absorbance spectra. Nonetheless, complexity of molecule-semiconductor interfaces challenges the parameterization of the DOS in Equation (6.23). We demonstrate one way to combine the above model with advanced first-principles calculations in this section. The goal of this work is to explore basic physics of electron transfer processes at molecule-semiconductor interfaces. We are primarily interested in insights that will generalize to a wide variety of sensitizers and semiconductors. In the present simulation, we examine a TiO_2 surface because it is a commonly employed semiconductor in photochemical cells.

6.4.A. Theoretical Methods

The reorganization energy of the semiconductor , λ_c, can be obtained from the variance, Δ_c^2, in the thermal fluctuations of relevant energy levels via $\lambda_c = \Delta_c^2 / 2k_B T$. We employ First Principles Molecular Dynamics (FPMD) for this purpose.[46,47] An integration time step of 0.5 fs is used to generate a canonical ensemble at 300 K for approximately 20 picoseconds. We employ

a 2x2x2 super cell (768 valence electrons) with periodic boundary conditions at the Γ point in Brollouin Zone integration. Density Functional Theory (DFT) calculations with Perdew-Burke-Ernzerhof (PBE) [48] exchange-correlation functional was used to obtain the atomic forces in FPMD, together with ultrasoft pseudo-potentials[49] for describing core-valence electron interactions. Plane-waves are used to expand both Kohn-Sham (KS) wavefunctions and the electron density with the kinetic energy cutoff of 35 Ryd, a smooth charge density cutoff of 140 Ryd, and an augmented charge density cutoff of 200 Ryd.

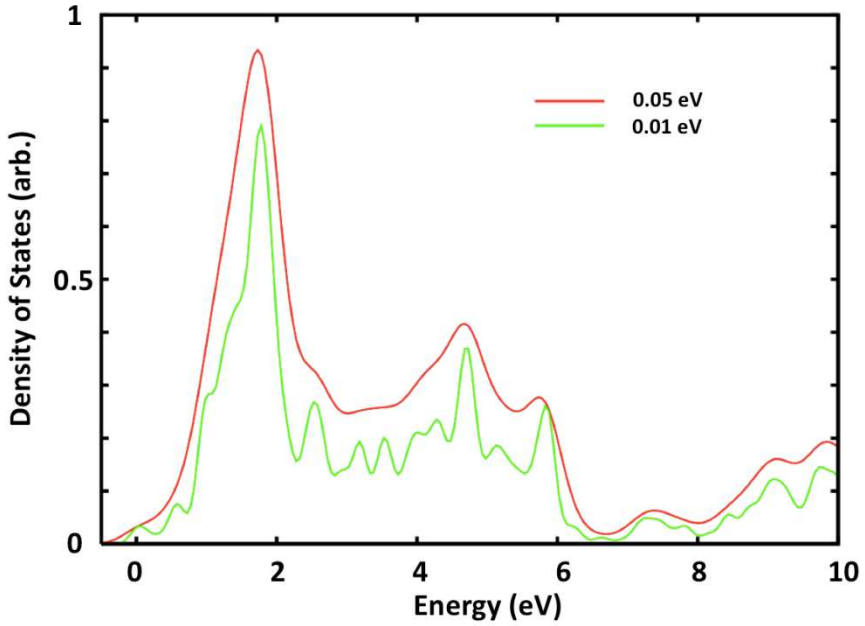

Figure 6.5: Conduction Band DOS of TiO_2 computed using a first-principles method based on GW approach described in section IVA. The DOS is plotted with Gaussian broadening of 0.01 eV and 0.05 eV.

We employ many-body perturbation theory based on Hedin's equation with the GW approximation[50 51] to obtain the DOS for anatase TiO_2. With the G_0W_0 level of the approximation, quasi-particle energies are obtained by computing the many-body correction to KS energies[52]. Brillouin Zone integration was performed with 6x6x6 Monkhorst-Pack k-points[53].

A kinetic energy cutoff of 50 Ryd was used for a plane-wave expansion of the wavefunction, and norm-conserving pseudo-potentials[54] with semi-core electrons are employed in the calculation.

6.4.B. Model Calculations

The first-principles DOS shown in Figure 6.5 is combined with our fourth-order perturbative model in this section using Equations (23) and (26). The FPMD simulations for anatase TiO_2 suggest that the reorganization energy, λ_c, ranges from 0.02-0.07 eV for the conduction band states. We present calculations carried out with λ_c=0.00 and 0.25 eV in the top and bottom rows of Figure 6.6 to illustrate the sensitivity of the dynamics to this parameter. The alignment of the molecular excited state with the DOS of the conduction band is of primary interest. Therefore, we examine general trends by calculating the population transfer dynamics as a function of the molecular excited state energy, E_b. In Figure 6.6a, the initial and final molecular energy distributions are overlaid on the DOS of the conduction band with E_b=2.5 eV at τ=0 and $\tau=\infty$. Evaluation of the fourth-order rate function in Figure 6.6b shows that the rate of population relaxation maximizes near E_b=1.7 eV. This behavior is understood by considering that the (dynamic) transition probability is greatest when the molecular energy distribution coincides with the maximum in the DOS (see Figure 6.7). With E_b=1.70 eV, the peaks of the distributions, $D_b(0)$ and $D_b(\infty)$, are located near 1.95 eV and 1.45 eV, respectively. *The simulation indicates that the optimal molecule-semiconductor energy level alignment corresponds to a structure that is intermediate between the equilibrium geometries for the ground and excited states.* Increasing the value of λ_c in the bottom row of Figure 6.6 imposes a linear shift in the molecule-semiconductor alignment as illustrated in Figure 6.7.

The difference, $P_b^{(4)}(\tau) - P_b^{(2)}$, displayed in Figure 6.6c shows that the second-order model overestimates the rate at E_b >1.7 eV. The discrepancy between $P_b^{(4)}(\tau)$ and $P_b^{(2)}$ is greatest near E_b >2.0 eV, where the system possesses near-perfect alignment between the peak in the DOS near 1.7 eV and the equilibrium molecular energy distribution $D_b(\infty)$, which is downshifted from E_b by $\lambda_b + \lambda_c$ (see Figure 6.7). The second-order model overestimates the rate in this regime because it does not account for the amount of time required for the molecule to reach favorable energy level alignment with TiO_2 ($\tau > \Lambda_b^{-1}$). The differences between second and fourth-order behaviors in the range E_b =1.9-2.4 eV parallel the activationless and/or slightly inverted regimes for a three-level system discussed in Figure 6.4. Notably, the difference, $P_b^{(4)}(\tau) - P_b^{(2)}$, decreases in magnitude as E_b approaches 3.0 eV because the dynamics become insensitive to the 1.7-eV feature in the DOS. Improved agreement between second and fourth-order theories above E_b =2.4 eV is reminiscent of the inverted regime for a three-level system.

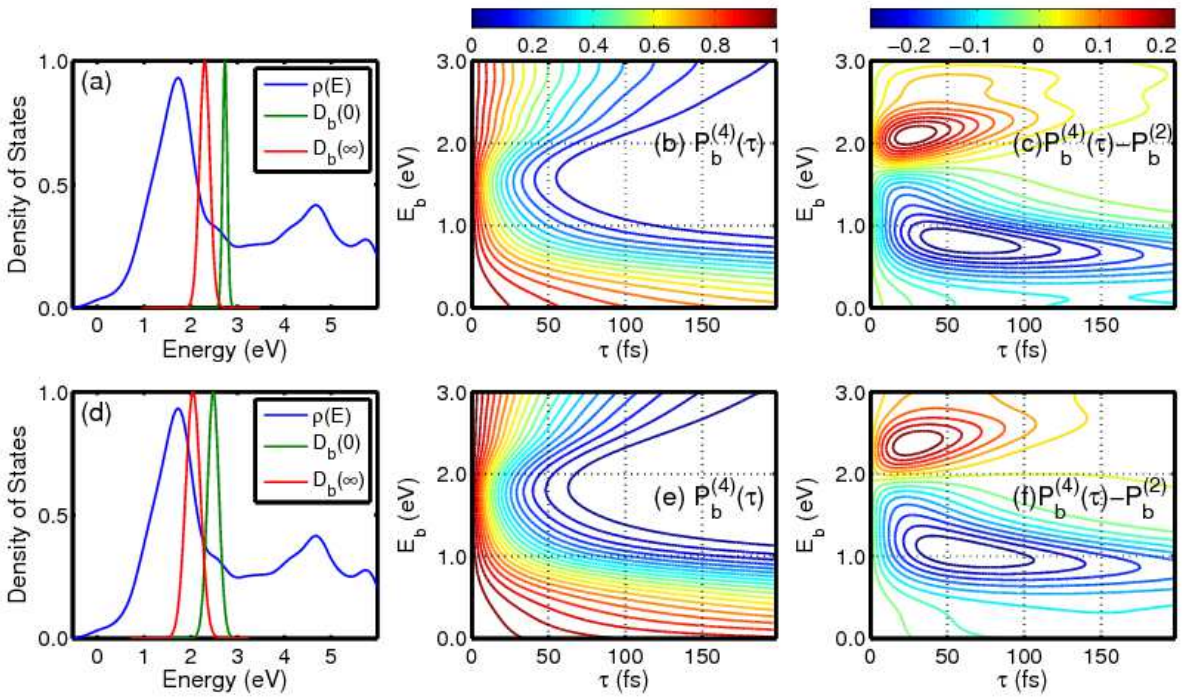

Figure 6.6: Electron transfer dynamics are computed with the first-principles DOS shown in Figure 6.5. Calculations in the top and bottom row differ in that λ_c=0.00 eV and λ_c=0.25 eV, respectively. (a),(d) The DOS of TiO_2, $\rho(E)$, is overlaid with molecular energy distributions at τ=0 and $\tau=\infty$ at E_b=2.5 eV. (b),(e) Fourth-order populations are calculated for state b using the parameters in Table 6.1. Electron transfer dynamics are most rapid when E_b is near the peak in the DOS at 1.7 eV. (c),(f) The negative sign of the difference, $P_b^{(4)}(\tau) - P_b^{(2)}$, below E_b=1.7 eV demonstrates that the fourth-order dynamics account for electron transfer transitions that take place during the nuclear relaxation process (i.e., transient molecule-semiconductor energy level alignment).

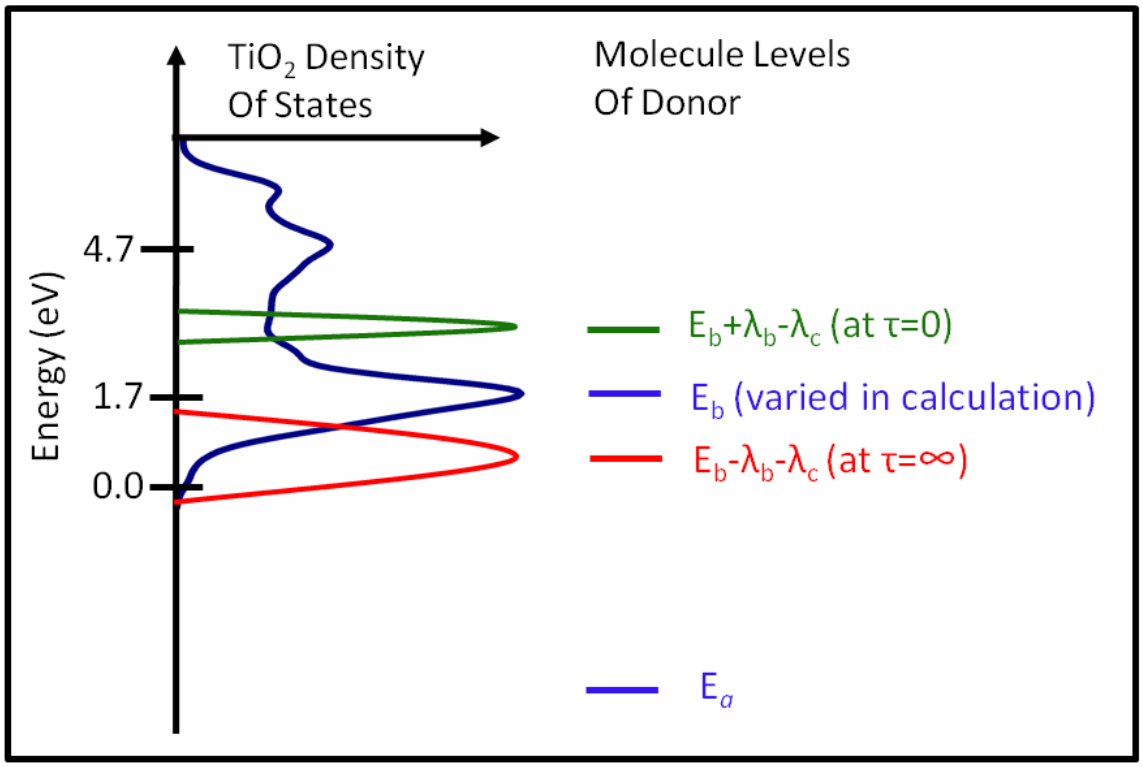

Figure 6.7: Energy Distribution Diagram. The dynamics calculated in Figure 6.6 are understood by comparing the molecular energy distributions, $D_b(0)$ and $D_b(\infty)$, to the DOS of the semiconductor. The fourth-order rate maximizes when E_b is slightly larger than 1.7 eV because optimal molecule-semiconductor energy level alignment is achieved near $\tau = \Lambda_b^{-1}$. Fourth-order dynamics are faster than those at second-order when E_b <1.7 eV because electron transfer processes that take place during the relaxation process are properly accounted for.

The equilibrium molecular energy distribution that enters the second-order model is in poor alignment with the peak in the DOS when E_b <1.7 eV (i.e., it is downshifted by $\lambda_b + \lambda_c$). The fourth-order model exhibits faster dynamics in this energy range because it accounts for electron transfer transitions that take place during the nuclear relaxation process. That is, the

negative sign of $P_b^{(4)}(\tau) - P_b^{(2)}$ at E_b <1.7 eV illustrates that the fourth-order model captures transient (favorable) energy level alignment between the molecule and TiO_2 at $\tau < \Lambda_b^{-1}$. Such dynamics resemble those found in the normal regime for a three-level system, where the fourth-order kinetics are influenced by the transient footprint of the wavepacket at the point of intersection between diabatic surfaces (see Figure 6.4). Such behavior should generalize to other molecule-semiconductor systems in which the energy of the equilibrium excited state is slightly below the conduction band edge.

6.5. Correspondence Between Second and Fourth-Order Rate Formulas

In this section, a normalized photoexcitation probability is defined to ensure that the second and fourth-order rate formulas converge in the thermalized system ($\tau >> \Lambda_b^{-1}$). In a transient absorption experiment, the laser intensity affects the overall signal amplitude but not the shape of the decay provided that the field-matter interactions with the pump pulse are in the perturbative regime. Therefore, the overall rate of light absorption is generally not of interest. The long time limit of $K_{cb}^{(4)}(\tau)$ is

$$K_{cb}^{(4)}(\tau \to \infty) = \frac{\pi^{3/2} |\xi_L|^2 |\mu_{ba}|^2 |V_{bc}|^2}{\hbar \left[w_L^2 \left(\Delta_b^2 + w_L^2 \right) \left(\Delta_b^2 + \Delta_c^2 \right) \right]^{1/2}} \exp\left[-\frac{\left(\hbar\omega_L - \hbar\omega_{ba}^0 - \lambda_b \right)^2}{2\left(\Delta_b^2 + w_L^2 \right)} \right] \times \exp\left[-\frac{1}{2} \frac{\left(\hbar\omega_{bc}^0 - \lambda_b - \lambda_c \right)^2}{\left(\Delta_b^2 + \Delta_c^2 \right)} \right] . \quad (6.27)$$

Next we define a normalization factor as

$$\frac{\left|\xi_L\right|^2\left|\mu_{ba}\right|^2\pi}{\left[w_L^2\left(\Delta_b^2+w_L^2\right)\right]^{1/2}}=1 \tag{6.28}$$

to eliminate the dependence of $K_{cb}^{(4)}(\tau)$ on the incident light intensity. The normalization factor is motivated by recovery of the second-order rate formula at $\tau >> \Lambda_{bb}^{-1}$. To show this, the fourth-order rate function is first rewritten as

$$K_{cb}^{(4)}(\tau\to\infty)=\frac{\left|V_{bc}\right|^2\sqrt{\pi}}{\hbar\left(\Delta_b^2+\Delta_c^2\right)^{1/2}}\exp\left[-\frac{\left(\hbar\omega_L-\hbar\omega_{ba}^0-\lambda_b\right)^2}{2\left(\Delta_b^2+w_L^2\right)}\right]\exp\left[-\frac{1}{2}\frac{\left(\hbar\omega_{bc}^0-\lambda_b-\lambda_c\right)^2}{\left(\Delta_b^2+\Delta_c^2\right)}\right], \tag{6.29}$$

by combining Equations (24) and (25). On resonance ($\hbar\omega_L=\hbar\omega_{ba}^0+\lambda_b$), $K_{cb}^{(4)}(\tau\to\infty)$ becomes

$$K_{cb}^{(4)}(\tau\to\infty)=\frac{\left|V_{bc}\right|^2\sqrt{\pi}}{\hbar\left(\Delta_b^2+\Delta_c^2\right)^{1/2}}\exp\left[-\frac{\left(\hbar\omega_{bc}^0-\lambda_b-\lambda_c\right)^2}{4k_BT\left(\lambda_b+\lambda_c\right)}\right]. \tag{6.30}$$

The next step is to show that $K_{cb}^{(2)}=K_{cb}^{(4)}(\tau\to\infty)$ under the same assumptions. Cumulant expansion approaches to second-order electron transfer rate constants have been described elsewhere, so we focus only on aspects of the derivation particular to the present model here.[27,44,45,55] As in the fourth-order description, the second-order rate constant is obtained using a time correlation function in the donor acceptor coupling,

$$K^{(2)}=\frac{1}{\hbar^2}\int_{-\infty}^{\infty}dt\left\langle\hat{V}(0)\hat{V}(t)\right\rangle. \tag{6.31}$$

Application of a cumulant expansion to the time correlation function yields

$$K_{cb}^{(2)}=\frac{\left|V_{bc}\right|^2}{\hbar^2}\int_{-\infty}^{\infty}dt\exp\left[-i\left(\omega_{bc}^0-\lambda_b-\lambda_c\right)t-g_b^*(t)-g_c^*(t)\right], \tag{6.32}$$

where the reorganization energies, λ_b and λ_c, correspond to the first-order terms in the cumulant expansion. State a is regarded as a reference state, so the reorganization energies and line shape functions corresponding to both states, b and c, contribute. Explicit treatment of the fluctuation parameters associated with one of the states involved in the non-radiative transition is usually avoided at second-order by regarding it as a reference. This convention is not employed here because parameters of $K_{cb}^{(2)}$ and $K_{cb}^{(4)}\left(\tau\to\infty\right)$ would then carry different meanings. In the short-time approximation, $K_{cb}^{(2)}$ can be rewritten as

$$K_{cb}^{(2)}=\frac{\left|V_{bc}\right|^2\sqrt{\pi}}{\hbar\left(\Delta_b^2+\Delta_c^2\right)^{1/2}}\exp\left[-\frac{\left(\hbar\omega_{bc}-\lambda_b-\lambda_c\right)^2}{2\left(\Delta_b^2+\Delta_c^2\right)}\right], \tag{6.33}$$

which is equivalent to Equation (6.30). Notably, by setting $\lambda=\lambda_b+\lambda_c$, we recover Marcus's classic equation for electron transfer,

$$K_{cb}^{(2)}=\frac{2\pi\left|V_{bc}\right|^2}{\hbar\sqrt{4\pi\lambda k_BT}}\exp\left[-\frac{\left(\hbar\omega_{bc}^0-\lambda\right)^2}{4\lambda k_BT}\right]. \tag{6.34}$$

6.6. Wavepacket Representation of Relaxation Processes

A photoinduced wavepacket that relaxes on the surface of state b can be written as[35]

$$D_b\left(t\right)=\frac{1}{\sqrt{2\pi\alpha^2\left(\tau\right)}}\exp\left\{-\frac{\left[q-q_b\left(t\right)\right]^2}{2\alpha^2\left(\tau\right)}\right\}, \tag{6.35}$$

where the position of the wavepacket is given by

$$q_b\left(\tau\right)=2\lambda_b\exp\left(-\Lambda_b\tau\right)+\exp\left(-\Lambda_b\tau\right)\left[\frac{\Delta_b^2}{\Delta_b^2+w_L^2}\left(\hbar\omega_L-\hbar\omega_{ba}^0-\lambda_b\right)\right]. \tag{6.36}$$

The variance, $\alpha^2(\tau)$, is defined in Equation (6.22). Equation (6.36) translates the wavepacket's position into the energy gap between states b and c for convenience (the energy gap is the quantity most relevant to both radiative and non-radiative transition rates). The energy gap is linear in the position of the wavepacket if the fluctuations have Gaussian statistics.

Generalization of this model to a system with a continuum of acceptor states is straightforward if it is assumed that each state, c, possesses the same reorganization energy, λ_c. Figure 6.7 explains how the parameters of the model can be viewed in terms of the overlap of molecular energy distributions with the DOS in the semiconductor. An amount of energy, $E_b + \lambda_b - \lambda_c$, is simply added to $q_b(\tau)$ in order to overlay the molecular energy distributions with the DOS's in Figure 6.7.

Table 6.1. Parameters used in Model Calculations

[(a)]**Parameter**	**Value**
$\left\|\xi_L\right\|^2 \left\|\mu_{ba}\right\|^2 \pi / \left[w_L^2 \left(\Delta_b^2 + w_L^2 \right) \right]^{1/2}$	1
λ_b	0.25 eV
Λ_b^{-1}	100 fs
ρ_0	0.01
$\hbar\omega_L - \hbar\omega_{ba}^0$	λ_b
w_L	0.05 eV

[(a)]Values for all other parameters are given in discussion of particular figures.

6.7. Concluding Remarks

In summary, we have developed a fourth-order perturbative model for ultrafast photoinduced electron transfer processes that can be applied to a molecular donor coupled to an arbitrary number of acceptor states. A principal result of this work is the laser intensity-independent, fourth-order rate function

$$K_{cb}^{(4)}(\tau) = \frac{\pi^{1/2}\left|V_{bc}\right|^2}{\hbar\alpha(\tau)} \exp\left[-\frac{\left(\hbar\omega_L - \hbar\omega_{ba}^0 - \lambda_b\right)^2}{2\left(\Delta_b^2 + w_L^2\right)}\right] \exp\left[-\frac{1}{2}\frac{\Omega^2(\tau)}{\alpha^2(\tau)}\right], \tag{6.37}$$

which is obtained by combining Equations (20) and (28). This phenomenological rate function is convenient for interpreting ultrafast nonlinear optical measurements, because many of the model parameters can be derived from conventional spectroscopies.

Basic insights provided by the model are illustrated in Figure 6.4 for a three-level system in various electron transfer regimes. The model calculations suggest that the main issue governing the electron transfer dynamics is whether or not the photoexcited wavepacket traverses the point of intersection between diabatic excited states. Motion of the wavepacket through this region of coordinate space enhances the fourth-order electron transfer dynamics (compared to a traditional second-order description) in the normal regime. By contrast, the second-order rate constant greatly overestimates the electron transfer time scale in the activationless regime, because a finite amount of time, Λ_b^{-1}, is required for the photoexcited wavepacket to reach the geometry of the energy degeneracy. Finally, calculations based on second-order and fourth-order treatments agree fairly well in the inverted regime, because the photoinitiated wavepacket largely equilibrates before electron transfer.

Under the assumption of uniform thermal fluctuation amplitudes for all acceptor levels, the molecular wavepackets examined in a three-level system can be translated into energy distributions and compared to the DOS in a semiconductor (see Figure 6.7). Electron transfer efficiency can then be interpreted in a manner similar to electronic energy transfer, where the overlap between donor emission and acceptor absorbance spectra is a useful and intuitive quantity. As expected, we find that agreement between the second and fourth-order models is sensitive to the alignment of the molecular energy distribution with the narrow feature in the first-principles DOS computed for TiO_2 (at 1.7 eV in Figure 6.5). Our analysis also quantifies the extent to which traditional second-order models underestimate electron transfer efficiency when the energy of the molecular excited state is below the conduction band edge and/or maxima in the DOS of the semiconductor. This insight underscores the potential power of combining state-of-the-art first-principles methods and phenomenological models.

6.8. REFERENCES

(1) O'Regan, B.; Grätzel, M. *Nature* **1991**, *353*, 737.

(2) Grätzel, M. *Nature* **2001**, *414*, 338.

(3) Hagfeldt, A.; Boschloo, G.; Sun, L.; Kloo, L.; Pettersson, H. *Chem. Rev.* **2010**, *110*, 6595.

(4) Gregg, B. A. *J. Phys. Chem. B* **2003**, *107*, 4688.

(5) Zou, Z.; Ye, J.; Sayama, K.; Arakawa, H. *Nature* **2001**, *414*, 625.

(6) Asbury, J. B.; Hao, E.; Wang, Y.; Ghosh, H. N.; Lian, T. *J. Phys. Chem. B* **2001**, *105*, 4545.

(7) Concepcion, J. J.; Jurss, J.; Brennaman, M. K.; Hoertz, P. G.; Patrocinio, A. O. T.; Iha, N. Y. M.; Templeton, J. L.; Meyer, T. J. *Acc. Chem. Res.* **2009**, *42*, 1954.

(8) Kamat, P. V. *J. Phys. Chem. C* **2007**, *111*, 2834.

(9) Mallouk, T. E. *J. Phys. Chem. Lett.* **2010**, *1*, 2738.

(10) Shoute, L. C. T.; Loppnow, G. R. *J. Amer. Chem. Soc.* **2003**, *125*, 15636.

(11) Smeigh, A. L.; Katz, J. E.; Brunschwig, B. S.; Lewis, N. S.; McCusker, J. K. *J. Phys. Chem. C* **2008**, *112*, 12065.

(12) Morandeira, A.; Boschloo, G.; Hagfeldt, A.; Hammarström, L. *J. Phys. Chem. C* **2008**, *112*, 9530.

(13) Xiong, W.; Laaser, J. E.; Paoprasert, P.; Franking, R. A.; Hamers, R. J.; Gopalan, P.; Zanni, M. T. *J. Am. Chem. Soc.* **2009**, *131*, 18040.

(14) Ardo, S.; Meyer, G. J. *Chem. Soc. Rev.* **2009**, *38*, 115.

(15) Morris-Cohen, A. J.; Frederick, M. T.; Cass, L. C.; Weiss, E. A. *J. Am. Chem. Soc.* **2011**, *133*, 10146.

(16) Huss, A. S.; Rossini, J. E.; Ceckanowicz, D. J.; Bohnsack, J. N.; Mann, K. R.; Gladfelter, W. L.; Blank, D. A. *J. Phys. Chem. C* **2011**, *115*, 2.

(17) Tseng, H.-W.; Wilker, M. B.; Damraurer, N. H.; Dukovic, G. *J. Am. Chem. Soc.* **2013**, *135*, 3383.

(18) Sarkany, L.; Wasylenko, J. M.; Roy, S.; Higgins, D. A.; Elles, C. G.; Chikan, V. *J. Phys. Chem. C* **2013**, *117*, 18818.

(19) Anderson, N. A.; Lian, T. *Annu. Rev. Phys. Chem.* **2005**, *56*, 491.

(20) Duncan, W. R.; Prezhdo, O. V. *Annu. Rev. Phys. Chem.* **2007**, *58*, 143.

(21) Akimov, A. V.; Neukirch, A. J.; Prezhdo, O. V. *Chem. Rev.* **2013**, *113*, 4496.

(22) Marcus, R. A. *J. Chem. Phys.* **1965**, *43*, 679.

(23) Gerischer, H. *Surf. Sci.* **1969**, *18*, 97.

(24) Gerischer, H. *Photochem. Photobiol.* **1972**, *16*, 243.

(25) Coalson, R. D.; Evans, D. G.; Nitzan, A. *J. Chem. Phys.* **1994**, *101*, 436.

(26) Evans, D. G.; Coalson, R. D. *J. Chem. Phys.* **1995**, *102*, 5658.

(27) Golosov, A. A.; Reichman, D. R. *J. Chem. Phys.* **2001**, *115*, 9848.

(28) Golosov, A. A.; Reichman, D. R. *J. Chem. Phys.* **2001**, *115*, 9862.

(29) Egorova, D.; Thoss, M.; Domcke, W.; Wang, H. *J. Chem. Phys.* **2003**, *119*, 2761.

(30) Kondov, I.; Thoss, M. *J. Phys. Chem. A* **2006**, *110*, 1364.

(31) Liang, K.-K.; Lin, C.-K.; Chang, H.-C.; Hayashi, M.; Lin, S. H. *J. Chem. Phys.* **2006**, *125*, 154706.

(32) Welack, S.; Schreiber, M.; Kleinekathöfer, U. *J. Chem. Phys.* **2006**, *124*, 044712.

(33) Zhang, M.-L.; Ka, B. J.; Geva, E. *J. Chem. Phys.* **2006**, *125*, 044106.

(34) Jakubikova, E.; Snoeberger III, R. C.; Batista, V. S.; Batista, E. R. *J. Phys. Chem. A* **2009**, *113*, 12532.

(35) Mukamel, S. *Principles of Nonlinear Optical Spectroscopy*; Oxford University Press: New York, 1995.

(36) Nitzan, A. *Chemical Dynamics in Condensed Phases*; Oxford University Press: Oxford, 2006.

(37) Barbara, P. F.; Meyer, T. J.; Ratner, M. A. *J. Phys. Chem.* **1996**, *100*, 13148.

(38) Valkunas, L.; Abramavicius, D.; Mančal, T. *Molecular Excitation Dynamics and Relaxation: Quantum Theory and Spectroscopy* Wiley-VCH: Weinheim, 2013.

(39) Marcus, R. A. *Annu. Rev. Phys. Chem.* **1964**, *15*, 155.

(40) Molesky, B. P.; Moran, A. M. *J. Phys. Chem. A* **2013, In Press**.

(41) Kwac, K.; Cho, M. *J. Phys. Chem. A* **2003**, *107*, 5903.

(42) Kwac, K.; Cho, M. *J. Phys. Chem. A* **2003**, *107*, 5903.

(43) Giokas, P. G.; Miller, S. A.; Hanson, K.; Norris, M. R.; Glasson, C. R. K.; Concepcion, J. J.; Bettis, S. E.; Meyer, T. J.; Moran, A. M. *J. Phys. Chem. C* **2013**, *117*, 812.

(44) Yan, Y. J.; Sparpaglione, M.; Mukamel, S. *J. Phys. Chem.* **1988**, *92*, 4842.

(45) Sparpaglione, M.; Mukamel, S. *J. Chem. Phys.* **1988**, *88*, 3263.

(46) Marx, D.; Hutter, J. *Ab Initio Molecular Dynamics: Basic Theory and Advanced Methods*; Cambridge University Press: Cambridge, 2009.

(47) Paolo, G.; Stefano, B.; Nicola, B.; Matteo, C.; Roberto, C.; Carlo, C.; Davide, C.; Guido, L. C.; Matteo, C.; Ismaila, D.; Andrea Dal, C.; Stefano de, G.; Stefano, F.; Guido, F.; Ralph, G.; Uwe, G.; Christos, G.; Anton, K.; Michele, L.; Layla, M.-S.; Nicola, M.; Francesco, M.; Riccardo, M.; Stefano, P.; Alfredo, P.; Lorenzo, P.; Carlo, S.; Sandro, S.; Gabriele, S.; Ari, P. S.; Alexander, S.; Paolo, U.; Renata, M. W. *Journal of Physics: Condensed Matter* **2009**, *21*, 395502.

(48) Perdew, J. P.; Burke, K.; Ernzerhof, M. *Physical Review Letters* **1996**, *77*, 3865.

(49) Vanderbilt, D. *Physical Review B* **1990**, *41*, 7892.

(50) Hedin, L. *Physical Review* **1965**, *139*, A796.

(51) Hybertsen, M. S.; Louie, S. G. *Physical Review B* **1986**, *34*, 5390.

(52) Marini, A.; Hogan, C.; Grüning, M.; Varsano, D. *Computer Physics Communications* **2009**, *180*, 1392.

(53) Monkhorst, H. J.; Pack, J. D. *Physical Review B* **1976**, *13*, 5188.

(54) Troullier, N.; Martins, J. L. *Physical Review B* **1991**, *43*, 1993.

(55) Georgievskii, Y.; Hsu, C.-P.; Marcus, R. A. *J. Chem. Phys.* **1999**, *110*, 5307.

CHAPTER 7: NONEQUILIBRIUM CHARGE TRANSFER ON SEMICONDUCTING NANOPARTICLES

7.1. Introduction

Electron transfer processes play a critical role in developing technologies, including photoelectrochemical devices.[1-17] In order to increase the efficiency and better understand such devices, considerable interest has developed in molecule-semiconductor interfaces, as these systems exhibit a diverse range of electron transfer kinetics and mechanisms, such as direct injection, triplet state injection, power law kinetics, and proton-coupled electron transfer.[18-23] Electron transfer has been measured to occur within 100 fs for a variety of chromophores on nanocrystalline semiconductors including TiO_2.[3,22,24-29] Such timescales preclude nuclear equilibration before the onset of charge transfer (CT), which challenges key assumptions present in conventional models of electron transfer such as Marcus-Gerischer theory.[30-33] The challenges present in interpreting the dynamics of these ultrafast CT systems have been met by the development of electron transfer models capable of incorporating nonequilibrium contributions.[34-43] In the interest of intuitive application to experimental results, however, a model has been developed[23] which utilizes parameters which can be measured via accessible spectroscopic techniques.

Here, the fourth-order theoretical model is applied to a molecule-semiconductor interface exhibiting ultrafast electron transfer. In order to demonstrate the effectiveness of the approach, catechol-sensitized TiO_2 nanoparticles are chosen for initial investigation. Catechol is a well-

studied system which is known to undergo ultrafast electron transfer to TiO_2.[8,26,28,29,44-51] Furthermore, the nuclear structure of catechol has been characterized with regard to ground-state vibrational motion as well as attachment to TiO_2, making it nearly ideal for study.[42,52-57] The known spectroscopic signatures of the interfacial system[28,29,46] are utilized together with a kinetic model to gain deeper insight into the mechanisms by which the catechol-TiO_2 CT complex relaxes after photoexcitation.

7.2. Background

7.2.A. Modeling Catechol Back Electron Transfer

In addition to influencing the rate of electron injection, non-equilibrium dynamics must also be accounted for when considering back electron transfer (BET) kinetics. The same strong coupling which allows for fast electron injection gives rise to ultrafast BET. In the case of the catechol-TiO_2 system where electron injection is non-sequential[48], the relaxation can be modeled with the assumption that the entire population of excited systems is initially in a vibrationally and electronically excited state, as depicted in Figure 7.1a. The electronic excitation includes the injection of an electron in the conjugated ring of the catechol into the TiO_2 conduction band.

To keep the model depicted in Figure 7.1 reasonable to apply to experimental data, several assumptions have been applied to the relaxation model. Most notably, only one vibrationally hot state is considered each for the ground and excited states, rather than considering an arbitrary distribution of vibrational energies. This assumption allows for simplicity in the interpretation of the vibrationally hot state as single species which converts to an equilibrated state as time progresses. The second assumption employed here is that the rate

constants are both first order and independent of time. In reality, these are likely rate functions[23] rather than rate constants, however considering them to be time-independent greatly simplifies the derivation of the population expressions. Specifically, the expressions for the slope of the m^{th} level of the excited state and n^{th} level of the ground state can be written as the following system of differential equations, which can be solved to determine the population of each state as a function of time after absorption,

$$\frac{dP_{e_m}}{dt} = -(k_1 + k_2)P_{e_m}(t) \ , \tag{1.1}$$

$$\frac{dP_{e_0}}{dt} = k_1 P_{e_m}(t) - k_3 P_{e_0}(t) \ , \tag{1.2}$$

$$\frac{dP_{g_n}}{dt} = k_2 P_{e_m}(t) + k_3 P_{e_0}(t) - k_4 P_{g_n}(t) \ , \tag{1.3}$$

and

$$\frac{dP_{g_0}}{dt} = k_4 P_{g_n}(t) \ . \tag{1.4}$$

In Equations (7.1)-(7.4), P_{e_m} and P_{g_n} represent the vibrationally hot excited and ground states, respectively, with P_{e_0} and P_{g_0} denoting their equilibrated counterparts. The rate constants listed correspond to the processes depicted in Figure 7.1. Solving these equations yields expressions for each of the four states of interest as a function of delay time, which are listed below in Equations (7.5)-(7.7). Though an equation for $P_{g_0}(t)$ is easily obtained from Equation (7.7), it is unnecessary, as $P_{e_m}(t) + P_{e_0}(t) + P_{g_n}(t) + P_{g_0}(t) = 1$ for all delay times, t. Additionally, in deriving

the below equations, it is assumed $P_{e_m}(0)=1$, and therefore $P_{e_0}(0)=P_{g_n}(0)=P_{g_0}(0)=0$. These equations are applied later in the chapter.

$$P_{e_m}(t)=P_{e_m}(0)\,\mathrm{e}^{-(k_1+k_2)t} \tag{1.5}$$

$$P_{e_0}(t)=\gamma\left(\mathrm{e}^{-(k_1+k_2)t}-\mathrm{e}^{-k_3 t}\right)\ ,\ \gamma=\frac{P_{e_m}(0)k_1}{\left(k_3-k_1-k_2\right)} \tag{1.6}$$

$$P_{g_n}(t)=\frac{\left(k_3\gamma+k_2P_{e_m}(0)\right)\mathrm{e}^{-(k_1-k_2)t}}{(k_4-k_1-k_2)}-\frac{k_3\gamma\,\mathrm{e}^{-k_3 t}}{(k_4-k_3)}-\left[\frac{k_3\gamma\,\mathrm{e}^{-k_3 t}}{(k_4-k_3)}+\frac{\left(k_3\gamma+k_2P_{e_m}(0)\right)}{(k_4-k_1-k_2)}\right]\mathrm{e}^{-k_4 t} \tag{1.7}$$

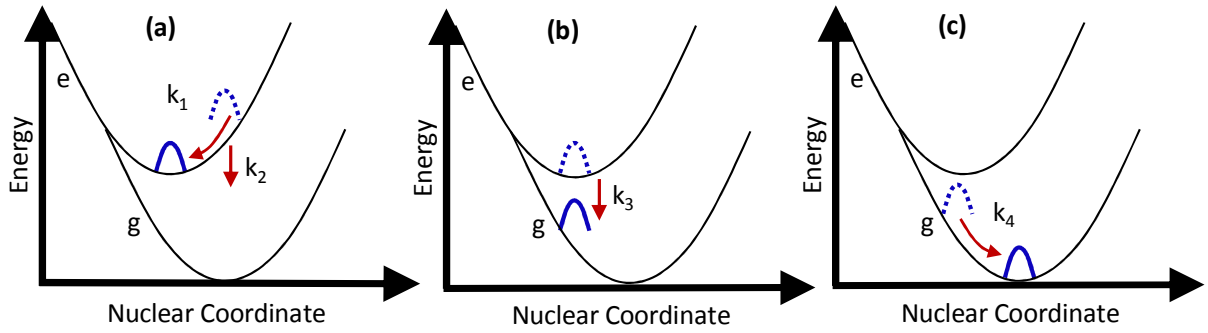

Figure 7.1: Catechol-TiO_2 proposed relaxation diagram. Light absorption results in a LMCT transition. The ground state well represents the states where the electron has returned to the catechol molecule. a) The excited wave packet vibrationally relaxes to the minimum of the charge-separated well $\left(e_m \rightarrow e_0\right)$ with rate constant k_1, while remaining on the excited energy surface. Nonequilibrium "fast channel" BET $\left(e_m \rightarrow g_n\right)$ occurs with rate constant k_2 in competition with this process. b) Population which has equilibrated in the excited state undergoes "slow channel" BET $\left(e_0 \rightarrow g_n\right)$ with rate constant k_3. d) Once BET has occurred, the system undergoes vibrational cooling $\left(g_n \rightarrow g_0\right)$ with rate constant k_4 in the ground state.

7.3. Experimental Methods

7.3.A. TiO_2 Nanoparticle Synthesis

Preparation of TiO_2 nanoparticles was performed via a hydrolytic synthesis modified from Reddy et al.[58] $TiCl_4$ was dissolved in concentrated HCl and the resulting solution was diluted with nanopure H_2O to 3M $TiCl_4$ after dissolution. Concentrated NH_3OH was added dropwise until a pH of 7-8 was reached. The solution was stirred for 24 hours at room temperature. The precipitate was separated from the solvent via vacuum filtration, and then washed with an excess of nanopure H_2O, after which the precipitate was dried in an oven at approximately 120 °C. The nanoparticles were then ground to a fine powder and suspended in nanopure H_2O.

Nanoparticle solutions of catechol loaded TiO_2 are prepared by adding 0.5g catechol to 50 mL of the aqueous nanoparticle solution and allowed to sensitize for 2 hours. The solution is then centrifuged at 6000 rpm for 10 minutes, and the supernatant is decanted for use. The precipitate is discarded.

7.3.B. Spontaneous Raman Measurements

Raman spectra were collected with a Renishaw inVia- Leica DM2500 M microscope setup using the 21,840 cm^{-1} laser line of an argon ion laser (Spectra Physics Stabilite 2017). For film Raman measurements, 30 μW laser beams are focused onto the sample with a Leica N PLAN EPI 50x/0.75 objective lens, which is also used to collect the scattered Raman signal through a 180º backscattering geometry (see Figure 7.2).

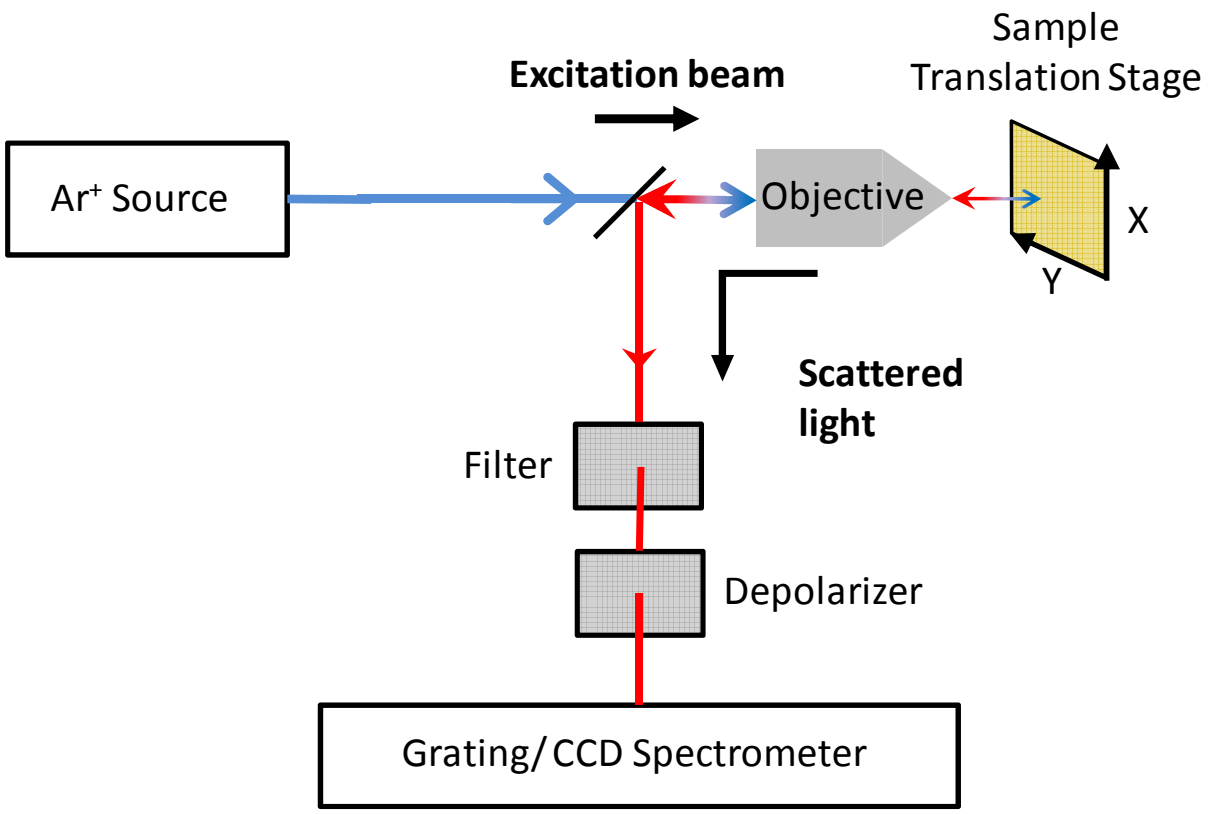

Figure 7.2: Diagram of the spontaneous Raman experimental setup. The incident beam is focused through an objective onto the sample, which sits on a translation stage. The Raman signal is backscattered through the same objective and dispersed onto the CCD via a grating.

For Raman measurements of solutions, dye loading solutions are contained in 1 mm thick cuvettes (Starna Cells, Inc. #21-G-1). Approximately 0.6 mW laser beams are focused into the solutions and Raman scatter is collected using a Leica N PLAN EPI 20x/0.12 objective lens, also in a 180º backscattering geometry.

7.3.C. Transient Absorption Spectroscopy Measurements

The probe pulse utilized in the experiments is a white light continuum ranging from 350nm - 750nm and generated in a CaF_2 window. The 800 nm Ti:Sapphire kHz pulse used to generate the continuum is obtained by splitting 2% of the beam power using a beam splitter. The window is translated in a circular pattern by a motorized arm with a period of 0.3 sec to maintain consistent spectral generation. The pump pulse is the second harmonic generated in a BBO crystal from the rest of the 800 nm pulse, and is delay controlled using a Newport GTS150 computerized translation stage. After passing through a chopper wheel, the pump and probe are overlapped at a small (5°) crossing angle at the sample position (see Figure 7.3, below.) Probe light is collected through an optical fiber with an Ultrafast spectrometer synchronized to the chopper wheel in the path of the pump. 200 difference spectra are collected at each delay point in the scan, and 20 scans are averaged to during each measurement.

Absorbance spectra are measured before and after data collection with an Hewlett−Packard 8453 UV− vis−NIR spectrometer to rule out signal contributions from sample degradation. Solutions of nanoparticles (see section III.A) are contained in a 500 μm path length quartz cuvette purchased from StarnaCells and moved continuously during the experiments using a rotary motor attached to the sample holder, resulting in elliptical rotation to prevent photobleaching.

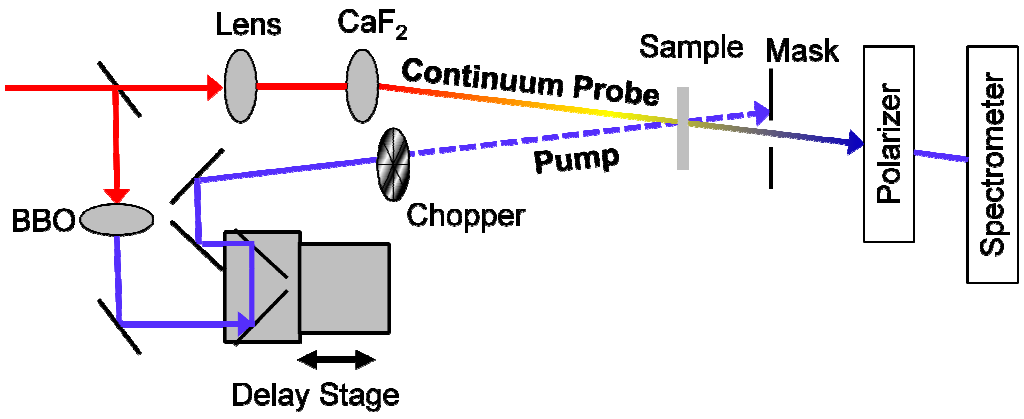

Figure 7.3: Experimental diagram for the transient absorption measurements. The 800 nm pulse is split into two paths. The first travels through a translating CaF_2 window to become a white light continuum probe, while the other is frequency doubled in a BBO crystal and passed through a chopper to serve as the pump. The position of the delay stage is used to control the time delay between the two pulses. After the sample position the relatively strong pump is blocked, and residual scatter is attenuated with a polarizer. The probe signal is finally detected by a spectrometer. Probe spectra collected from shots with chopped and unchopped pump pulses are differenced to calculate the transient signal.

7.3.D. Transient Grating Raman Spectroscopy Measurements

Solutions of catechol loaded nanoparticles are contained in a homemade sample jet described elsewhere[59] to simultaneously prevent photodegradation and minimize pulse duration. The sample jet eliminates the need for a cuvette and therefore helps to minimize third order dispersion introduced by second order dispersion correction. All pulses in the experiment are second harmonics of the 800 nm Ti:Sapphire fundamental which have been generated in a BBO crystal. After second harmonic generation the beam passes through a 50% beam splitter, allowing one path to be directed onto a Newport GTS150 delay stage while the other traverses an equal path length until both are reflected off of a 20 cm focal length concave silver mirror. The

beams focus on a diffractive optic, where they are divided into the four beams shown in Figure 7.4a, below. The beams travel another 20 cm to a second 20 cm focal length concave mirror (Figure 7.4b,) which focuses them on the sample position.

Transient grating Raman measurements consist of three incident beams in a boxcar geometry. In the case of the work presented here, these 3 beams are all split from the same pulse, and so have nearly identical frequencies. Two of the beams are termed as "pump" pulses, which are used to excite the sample out of the ground state. The interference of these pulses within the sample medium generates the "transient grating" for which the technique is named.[60,61] The remaining "probe" pulse scatters off of the grating produced by the pump pulses in such a way that carries information about the system. The system radiates the third-order signal in the direction given by

$$k_s = -k_1 + k_2 + k_3 \qquad \textbf{(1.8)}$$

where k_1 and k_2 are the pump pulses, k_3 is the probe, and k_s is the signal. A fourth incident pulse is delayed in time and interferes with the signal to produce a frequency resolved measurement on the CCD as a function of delay between the pumps and the probe. This signal is Fourier transformed - using a Gaussian apodization function to prevent ringing - to give a time domain response.[62]

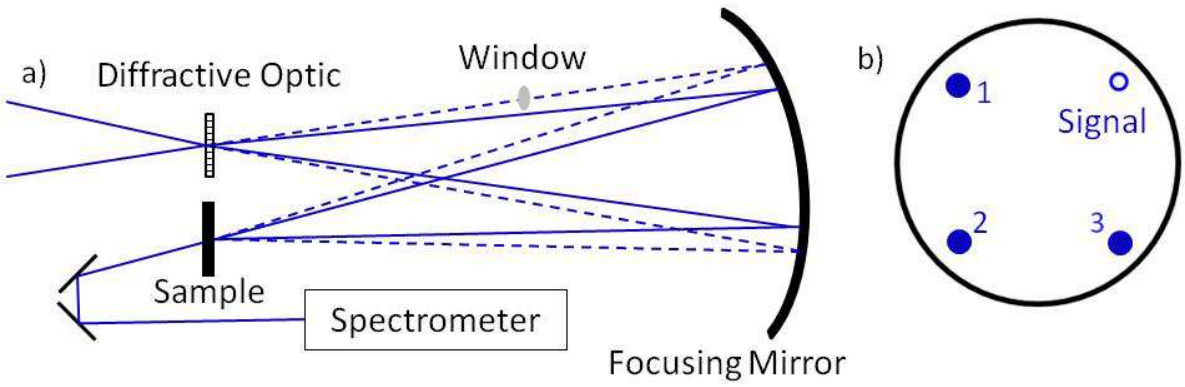

Figure 7.4: a) Experimental diagram for the transient grating Raman experiment. Four beams of interest are generated at a diffractive optic and incident on the concave mirror, which are subsequently focused on the sample. The beam geometry on the focusing mirror is shown in (b). Unlike other pump-probe spectroscopies, this transient grating experiment results in the signal propagating noncolinearly with the probe which eliminates the need for spectral differencing. Additionally, the separation of the pump pulses allows for polarization tuning of each pump beam independently.

The resulting data contains amplitude decay for each pixel of the probe. Convoluted with the exponential decay are oscillations which are the time-domain equivalent of the stimulated Raman spectrum of the system.

7.3.E. Six-Wave Mixing FSRS

FSRS measurements are performed using a six-wave mixing beam geometry based on the work of Berg and coworkers[63] and explained in previous work.[64,65] As shown in Figure 7.5, all beams are focused onto the diffractive optic with a 50 cm focal length spherical mirror and subsequently onto an off-axis imaging mirror of the same focal length, which focuses the beams at the sample. The transparent fused silica window delays pulse 3 by 290 fs with respect to pulse

4. Notably, this undesired signal (near $\tau_1 = 0$) does not possess narrow vibrational resonances due to the 250 cm^{-1} spectral width of the actinic pump pulse. In the five-beam geometry (see Figure 7.5), beams 1 and 2 are displaced by 2.4 cm and 3.5 cm from the center of the mirror, respectively.

Unlike conventional FSRS techniques, the experiment utilized in this work takes advantage of the direction of propagation of the nonlinear signal to collect the Raman spectrum in background-free geometry. Specifically, the desired signal is radiated with the wave vector

$$k_s = k_1 - k_2 + k_3 - k_4 + k_5 \quad \textbf{(1.9)}$$

using the same notation as Figure 7.5 (below.) With this knowledge, the signals measured have markedly higher[65] intensity with respect to noise than those obtained by conventional background subtraction. In conventional methods, the third and fifth order responses would be spatially overlapped, and must be differentiated[66,67]. The actinic pump is scanned in time with respect to the Raman pumps and Raman probe, which provides the stimulated Raman spectrum of the sample's excited state after a series of time intervals. The signals collected therefore provide dynamics of the evolution of the vibrations of the excited state as a function of pulse delay. These dynamics are fit with single exponential functions (see Equation 7.4).

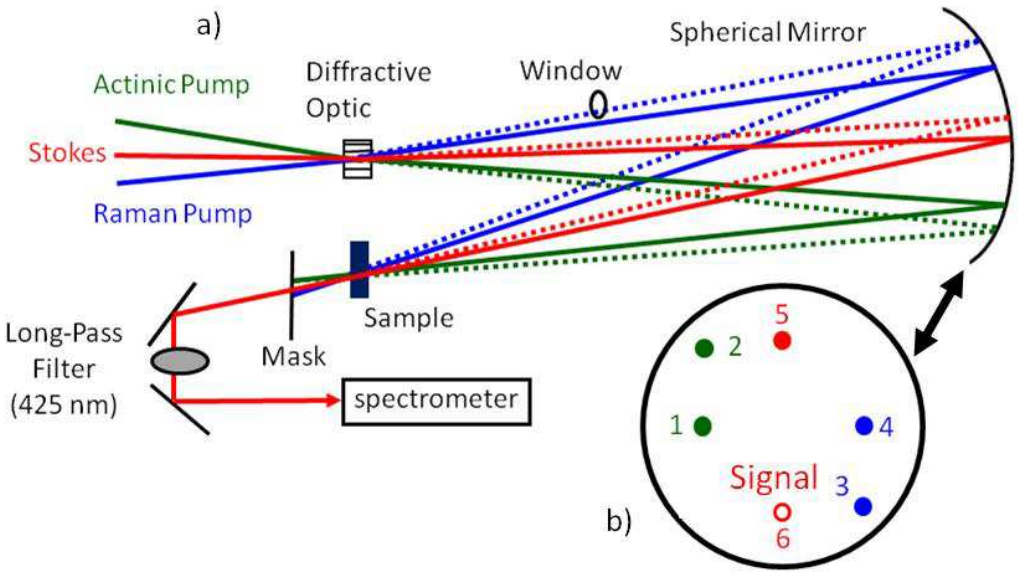

Figure 7.5: a) Experimental diagram for the six-wave mixing FSRS experiment. Six beams of interest are generated at a diffractive optic and incident on the concave mirror, which are subsequently focused on the sample. The beam geometry on the focusing mirror is shown in (b). This geometry ensures that the fifth order signal of interest propagates in a background free direction and thus allows for isolation of that signal during data collection.

In all experiments, signals are detected using a CCD array (Princeton Instruments PIXIS 100B) mounted on a 0.3 m spectrograph with a 1200 g/mm grating. The signal beam is focused to a spot size of 100 μm at the entrance to the spectrograph to obtain hardware-limited spectral resolution, approximately 10 cm^{-1}. The resolution of the measurement is limited by the 50 cm^{-1} spectral width of the Raman pump beam. The FWHM spot sizes of all laser beams are approximately 200 μm at the sample position.

The pulse energies of the actinic and Raman pump pulses are 150 nJ and 200 nJ, respectively. The Stokes beam has a pulse energy of 50 nJ. The 0.2 mM sample of catechol sensitized nanoparticles is drained through a 220 μm thick wire-guided jet. The sample is recycled continuously through a reservoir with a total sample volume of 50 mL. Absorbance spectra are measured before and after experiments to confirm the absence of sample degradation.

7.4. Results and Discussion

7.4.A. Spontaneous Raman Spectroscopy

Table 7.1: Raman peak assignments.

Raman Shift (cm^{-1})	Assignment
1042	in plane CH-bend
1169	in plane CH-bend
1279	C-O stretch
1321	O-C-C-O, ring stretching
1483	C_1-C_2 stretch

Solutions of catechol sensitized nanoparticles revealed multiple Raman peaks in the 600 cm^{-1} to 1500 cm^{-1} region (see Figure 7.6.) These peaks have previously been assigned using techniques including nonresonant Raman, resonance Raman, and surface enhanced Raman spectroscopies;[46,52-57,68-70] the current spectra agree with previous measurements. Of greatest relevance to the stimulated Raman work also presented here are the peaks in the region of 1100 cm^{-1} to 1500 cm^{-1}. The relatively weak band located at 1169 cm^{-1} corresponds to a C-H bend. The peaks at 1279 cm^{-1} and 1321 cm^{-1} are assigned as phenolate C-O stretch and ring stretching vibrations, respectively. The large peak at 1483 cm^{-1} is attributed to a stretch of C_1 and C_2 (which

are connected to the oxygens). The assignments are also consistent with the known charge transfer nature of the system. That is, since the electronic resonance is known to be a LMCT band, it is expected that vibrational motions which are coupled to the transition will receive the greatest enhancement, and be visible in the resonance Raman spectrum.[71]

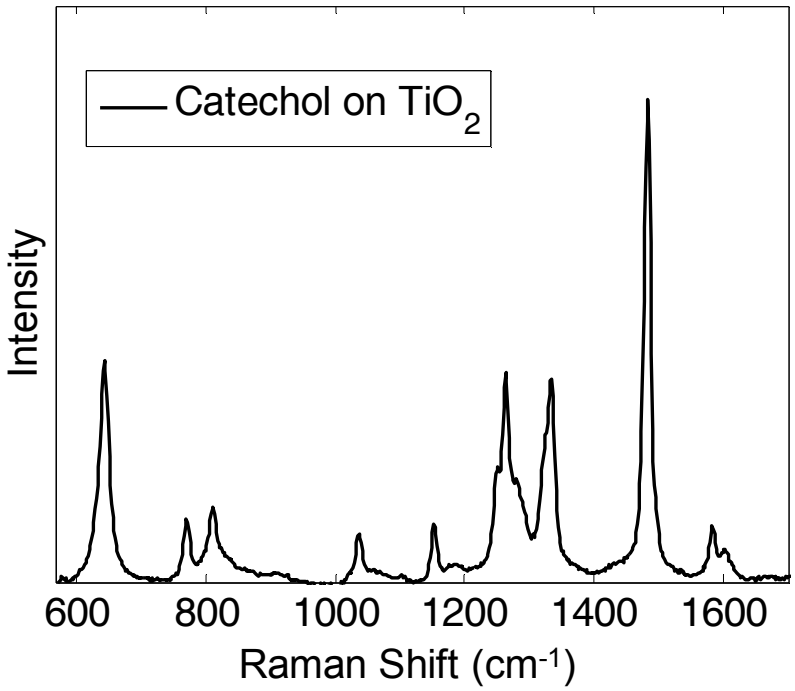

Figure 7.6: Resonance Raman measurement of dye- sensitized nanoparticles in aqueous solution. Excitation was accomplished through the 457.9 nm line of an argon ion laser. The peaks shown are characteristic of those measured and assigned by others for the charge transfer complex.

7.4.B. Transient Absorption Spectroscopy

Figure 7.7 shows the chirp corrected transient absorption spectra for the catechol on TiO_2 nanoparticles in aqueous solution. The spectra show three main features of interest; firstly, a

prominent feature centered at 443 nm is observed, which is assigned to a ground state bleach. The second and third features have a positive sign, and are assigned to a hot ground state absorption and an excited state absorption arising from injected electrons in the TiO_2. The nature of these features is explained in more detail below and in Figures 7.7, 7.8, and 7.9.

Individual features of the transient signal are isolated by line shape fitting. The pump scatter measured at negative delay is first subtracted from each subsequent delay point, as its contribution to the signal is effectively constant throughout the experiment. The remaining spectrum is then fit to a summation of three Gaussian peaks at each delay point in the experiment (see Figure 7.8). The individual Gaussian peaks are defined as

$$G(\lambda) = a \cdot \exp\left[\frac{-1}{2}\left(\frac{(\lambda - \lambda_0)}{\sigma}\right)^2\right], \qquad \textbf{(1.10)}$$

where a is the amplitude of the Gaussian, σ is the width of the Gaussian, and λ_0 is the center of the Gaussian in nm. These parameters are determined for each of the spectral features and every time delay in the experiment. The resulting components are shown in Figure 7.8. The advantages of utilizing the Gaussian lineshape to fit the signals are twofold. Firstly, the spectral peaks are well fit by Gaussian peaks, resulting in a fit that is able to reproduce the experimental data with minimal deviation (see Figure 7.7.) Second and most importantly, Gaussians have intuitive parameters which give insight into the behavior of the individual spectral features, despite their significant overlap on the wavelength axis. Isolation of these parameters is key to interpretation of the transient signals explained below (see Figure 7.9).

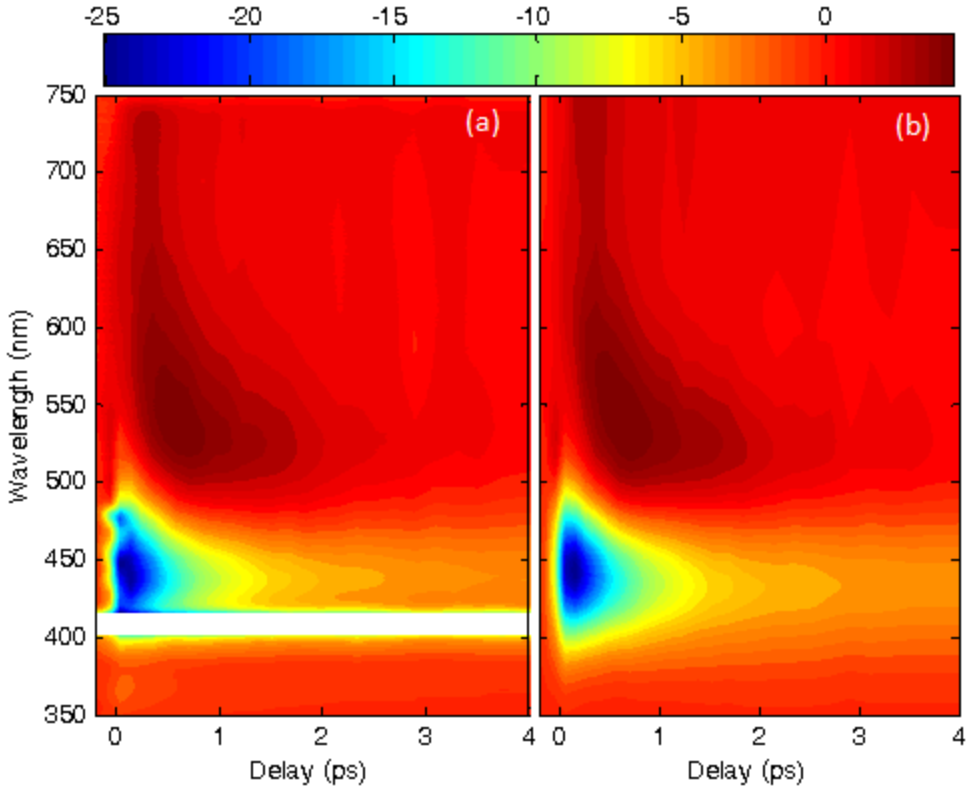

Figure 7.7: a) Transient absorption spectrogram for the chirp corrected signal from catechol loaded TiO_2 nanoparticle solution. The pump pulse scatter intensity at 410 nm has been removed to preserve color scale. The spectrum shows a 25 mOD spectral feature at 440 nm, a quickly blue-shifting feature of opposite sign near 550 nm, and a positive feature at the long wavelength edge of the probe. b) Gaussian peaks are used to successfully fit the experimental signals, allowing decoupling of the individual spectral components (see Figure 7.8). This spectrogram shows the signals reproduced by the Gaussian fitting algorithm.

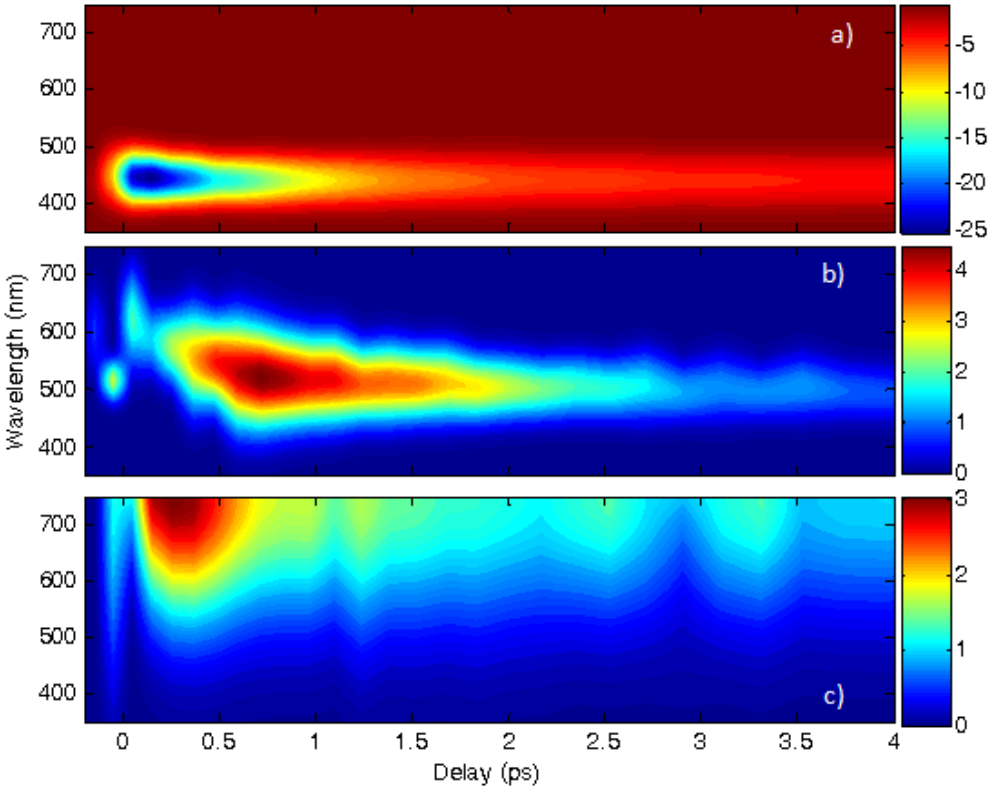

Figure 7.8: Transient absorption spectroscopy component spectrograms All plots shown are for catechol loaded TiO_2 nanoparticles in aqueous solution. a) The fitted ground state bleach portion of the spectrum, which decays by nearly half of its amplitude within the first 500 fs after light absorption, displaying ultrafast charge recombination. b) Only the positive (ESA) part of the chirp corrected transient absorption signal. c) The broad feature centered above 700 nm fit to a Gaussian lineshape decays concurrently with the ground state bleach, which is consistent with the assignment of this feature to electrons in the TiO_2 semiconductor.

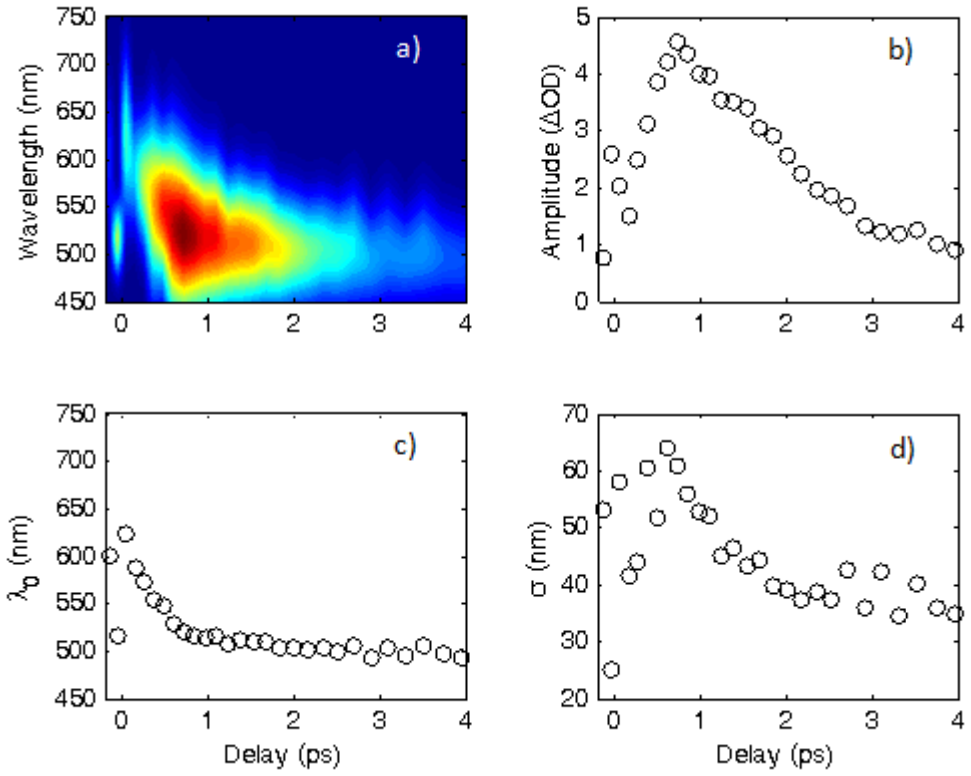

Figure 7.9: Detailed fitting of the hot ground state band over the first 4 ps. Plot a) shows the spectrogram of the spectral feature which decays rises and subsequently decays in the first few picoseconds. Plots b), c), and d) show the amplitude, center wavelength, and width of the Gaussian fit, respectively. From the amplitude, it is clear that the feature primarily grows in over the first 700 fs, which indicates a growing population of thermally excited catechol molecules; the amplitude is nonzero even at response limited delay times, however, which indicates that some charge recombination is occurring within the instrument response of the measurement. The large blue-shift of the central wavelength of the band is used to assign the feature to the hot ground state, since over the first picoseconds the energy gap decreases while the system relaxes within the ground state potential energy surface. The peak also appears to narrow significantly as the amplitude decreases, which is consistent with the model. As the system relaxes vibrationally in the well, the energy distribution will converge to the most stable vibrational state, resulting in a more homogeneous energy gap in the ensemble.

The peak feature centered at 443 nm (Figure 7.8a) loses more than half of its area within the first 500 fs, and its decay is mirrored by the broad feature above 700 nm. The overlap of the 443 nm peak with the catechol TiO_2 charge transfer band suggests an assignment of ground state bleach (GSB.)[8,28,50] The matching absorptive feature above 700 nm can be assigned as an excited state absorption (ESA) band possibly arising from electrons in the conduction band of TiO_2.[2,28,72,73] The kinetics of its decay mirror those of the GSB, which further supports the assignment. The absorptive feature located between the GSB and ESA bands exhibits a greater than 100 nm blue-shift within the first picosecond, with a time constant of 2.0 ps. The blue shift is indicative of a hot ground state (HGS) absorption, since as vibrational relaxation occurs, the average energy gap between system and the excited state increases.[74]

The decay of the bleach, on the other hand, occurs with a time constant of approximately 500 fs. This rate is likely too fast for vibrational cooling. It is known[8,75,76] that the electron transfer from catechol to TiO_2 is strongly coupled and occurs immediately upon light absorption. It is also previously reported that the fast decay of the bleach of the charge transfer band corresponds to back-electron transfer (BET) to the oxidized catechol.[8,28,50] The strong coupling of the system implies that BET will also be a fast process as observed here. The concurrent decline in the GSB and hot ground state signals further support this observation. Sub-picosecond BET dynamics provide motivation to measure the vibrational spectra of these nanoparticles at early times in order to provide insight into the mechnism of this process.

7.4.C. Transient Grating Raman Spectroscopy

Measured transient grating signals exhibit exponential decay on the order of picoseconds underneath coherent oscillations across the spectrum of the probe pulse. In order to properly obtain the vibrational frequencies from these signals, the decaying and oscillating portions of the signal must be separated. To accomplish this, the signal at each individual pixel is fit to a single exponential decay (see Equation 7.4 above.) Subtraction of this exponential decay followed by a Fourier transform of the residual oscillations yields vibrational peaks in the traditional frequency domain representation. Since this transform is performed for each pixel, the resulting data is a map of intensity as a function of both probe wavelength and Raman shift (see Figure 7.11).

Transient grating measurements exhibit multiple modes up to over 1400 cm^{-1}; the observation of these modes verifies the impressive time resolution of the experiment. By comparing the stimulated Raman spectrum to conventionally measured spontaneous Raman spectra of the sample (see Figure 7.6), peaks which are unique to the stimulated spectrum can be identified. Though a direct comparison of the stimulated signal obtained by the transient grating to the spontaneous Raman signal reveals a significant overlap in the observed peaks, there exists a notable exception of two peaks located at 870 cm^{-1} and 970 cm^{-1}, respectively.

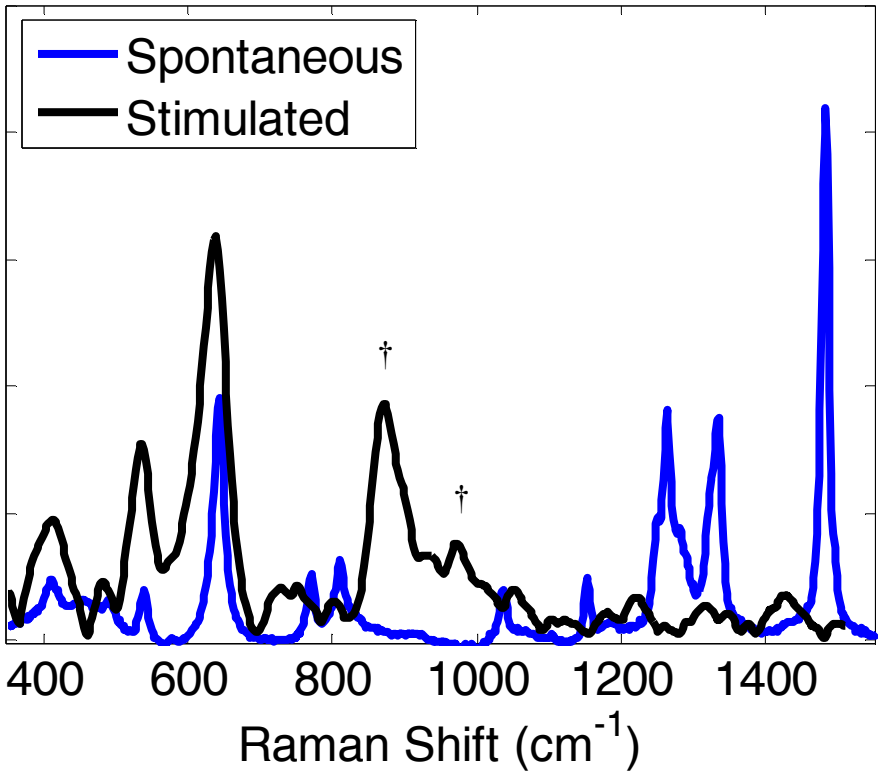

Figure 7.10: Raman spectra for the spontaneous (blue) and stimulated (black) Raman experiments from catechol loaded TiO_2 nanoparticle solution. While most of the peaks observed in the stimulated spectrum match to peaks in the spontaneous spectrum within error, the pronounced peaks at 870 cm^{-1} and 970 cm^{-1} (marked with daggers) have no spontaneous analogue. Therefore, these spectra are assigned to vibrational modes in the excited state of the catechol-TiO_2 complex.

The comparison of these spectra is shown in Figure 7.10. Catechol is reported[46,77] to convert to an o-benzosemiquinone radical upon oxidation. The 970cm^{-1} mode has been assigned[78,79] to a C-H bend in p-benzosemiquinone radical, and the structural similarity of these species allows the mode assignment to be applied here as well.

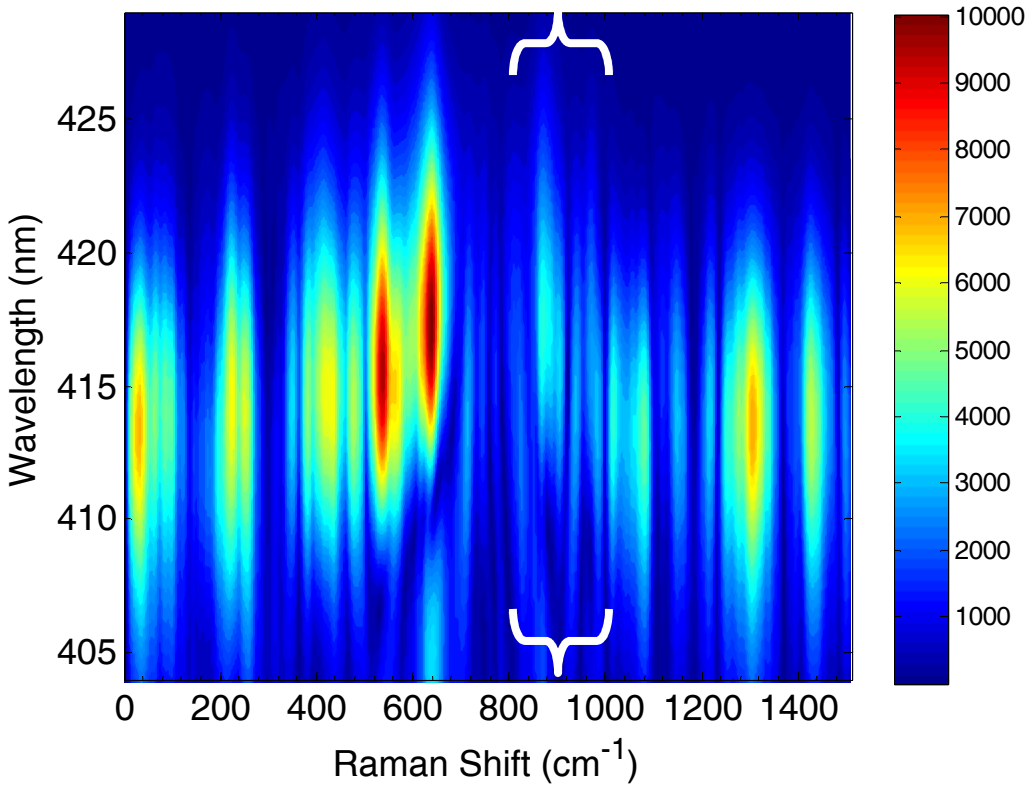

Figure 7.11: Stimulated Raman spectrogram from catechol loaded TiO_2 nanoparticle solution. The TG spectroscopy signal is Fourier transformed to reveal vibrational Raman peaks. The wavelength axis corresponds to the detected wavelength on the CCD, since the probe pulse is broadband, centered at 412 nm. The excited state vibrations between 870 cm^{-1} and 970 cm^{-1} have the strongest intensity between 413 nm and 420 nm, whereas the strength of many of the ground state modes correspond directly to the intensity of the probe, centered at 412-413 nm.

The 870 cm^{-1} mode which appears prominently in the stimulated spectrum (see Figures 7.10 and 7.11) has not been assigned in the studies referenced above. While the spontaneous resonance Raman signal is only sensitive to vibrational modes of the ground state,[71,80,81] the stimulated Raman can contain information about vibrations in the electronically excited state.[82]

A weak 830 cm^{-1} band has been observed[78] in p-benzosemiquinone as a C-C-C deformation, though the differing oxygen attachment to the ring in the oxidized catechol radical makes this assignment tentative. Additionally, the role of the TiO_2 surface should not be ignored when considering this mode. Since the LMCT transition being excited arises[46] from the chelated catechol, the ligand forms a 5-membered ring with the titanium atom. Vibrations of this ring are not well documented, and a breathing or deformation of this ring could also be the source of the 870 cm^{-1} peak.

7.4.D. Background-Free FSRS Measurements

Femtosecond stimulated Raman measurements are carried out on TiO_2 nanoparticles sensitized with catechol. The signal matches the expected vibrational signature of catechol measured via the other Raman techniques, though the peaks are significantly broader in Raman shift due to the fine time resolution of the pump. Five modes are clearly distinguishable from the spectrum: 800 cm^{-1}, 1169 cm^{-1}, 1269 cm^{-1}, 1321 cm^{-1}, and 1484 cm^{-1}; see Table 8.1 for peak assignments.

Table 7.2: Raman peak exponential fitting constants. Modes appear to exhibit similar relaxation kinetics based on peak assignment.

Raman Shift (cm^{-1})	**Amplitude (counts)**	**τ (ps)**	**Offset (counts)**
800 ± 2	187 ± 16	1.03 ± 0.15	54 ± 4
1169 ± 5	1352 ± 79	1.06 ± 0.10	271 ± 18
1269	1760 ± 50	1.74 ± 0.10	365 ± 17
1321	1323 ± 39	1.75 ± 0.09	301 ± 13
1478	1034 ± 24	1.91 ± 0.08	180 ± 9

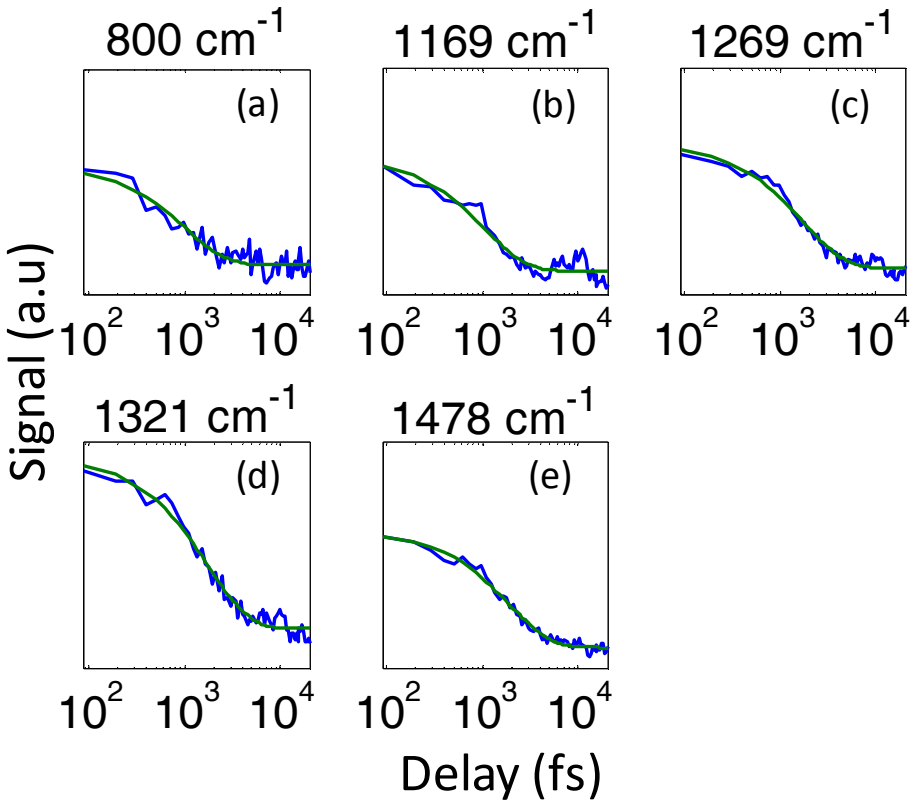

Figure 7.12: Femtosecond Stimulated Raman peak amplitudes for the catechol loaded TiO_2 nanoparticle solution overlaid with single exponential fits. The five modes observed experiment show varying decay constants, as follows: 800 cm^{-1} (a) and 1169 cm^{-1} (b): 1.0 ps. 1269 cm^{-1} (c) and 1321 cm^{-1} (d): 1.7 ps. 1478 cm^{-1} (e): 1.9 ps.

Vibrational modes reveal distinct relaxation rates as the delay between the actinic pump and probe is scanned. The five modes exhibit three individual decay rates, suggesting multiple vibrational relaxation channels. Interestingly, the decay rates observed are dependent on the assignment of the modes involved. The 800 cm^{-1} and 1169 cm^{-1} modes, both having been assigned to CH bending, display similar decay rates. Likewise, the 1269 cm^{-1} and 1321 cm^{-1}

modes share a CO stretching assignment and a longer decay constant. The longest decay is observed in the 1478 cm^{-1} mode, which corresponds to a C-C stretch, as mentioned previously.

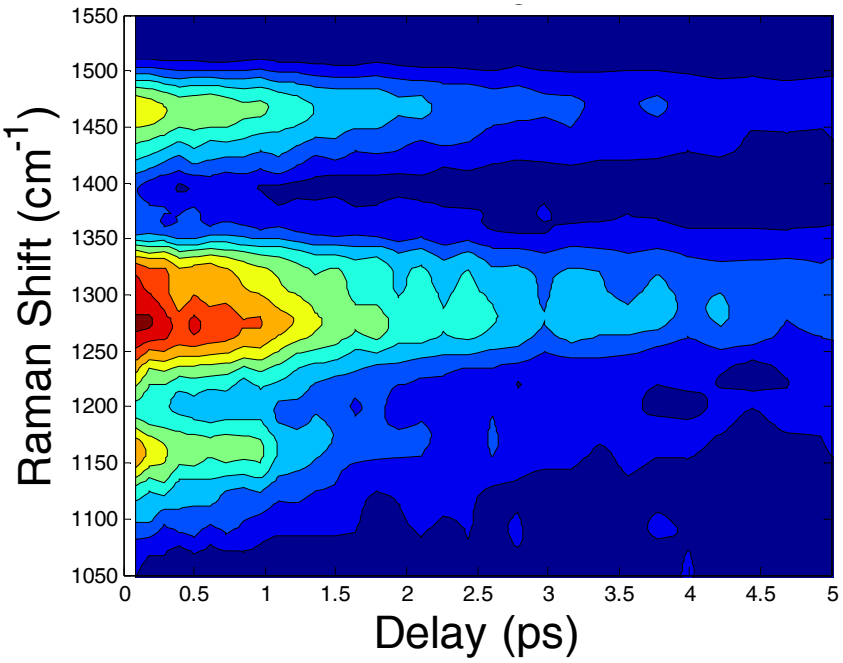

Figure 7.13: FSRS spectrogram for the catechol loaded TiO_2 nanoparticle solution. The four modes observed in the four-wave experiment show varying decay rates between 1 and 2 ps, indicating different relaxation mechanisms. Specifically, the vibrationally excited catechol relaxes via hydrogen bonding with the solvent through the CH bending and CO stretching modes allowing for faster relaxation, while the C-C stretching mode at 1478 cm^{-1} decays more slowly.

CH bending modes and CO stretching modes decay with time constants similar to those observed in the hot ground state transient absorption signals at wavelengths above 500 nm. These structural features (carbon-hydrogen bonds and carbon-oxygen bonds) are expected to be present in both the ground and transient species. Furthermore, both possess atoms capable of

hydrogen bonding interactions with the aqueous solvent. Based on the timescale, as well as the transient absorption signals reported here and elsewhere[28], it is reasonable to assume that the vibrationally excited catechol relaxes via hydrogen bonding with the solvent through the CH bending and CO stretching modes. Residual relaxation occurs via the longer lived C-C stretching mode at 1478 cm^{-1}.

7.5. Conclusions

Multiple electronic and Raman techniques have been used to characterize the nuclear relaxation of catechol-sensitized TiO_2 nanoparticles during BET. Transient absorption studies have measured the dynamics of the BET process. Additionally, stimulated Raman measurements including TG spectroscopy and a six-wave background free FSRS geometry have been used to identify the vibrational motions involved in the charge transfer and characterize the dynamics of nuclear relaxation. The information gained from the various spectroscopic techniques are utilized to propose a kinetic model for the BET dynamics consisting of multiple channels of electronic relaxation. The rate constants corresponding to the model (Equations (7.1)-(7.4)) are determined such that $k_1 = 0.33$ ps^{-1}, $k_2 = 1.32$ ps^{-1}, $k_3 = 0.03$ ps^{-1}, and $k_4 = 1.42$ ps^{-1}. These rate constants clearly show that BET occurs while the system is in a nonequilibrium nuclear geometry.

The Raman measurements heavily allude to the involvement of hydrogen bonding interactions in vibrational relaxation via heat transfer to the solvent. Specifically, CH bending modes and CO stretching modes appear to have a large role in the fast thermal relaxation of these chromophore modified nanoparticle interfaces, allowing for vibrational cooling with time constants on the order of 1 ps. Several of these modes are significantly enhanced by excitation

resonant with the charge transfer band, indicating their coupling to the charge transfer process, especially the 643cm^{-1}, 1159cm^{-1}, and 1269cm^{-1} modes.

The electronic and vibrational spectroscopies employed here have identified multiple ultrafast relaxation channels for resonantly an excited catechol-TiO_2 nanoparticle system. The dynamics are being further studied using a rate model presented previously.[23] Future studies will apply the same powerful experimental techniques to a related molecular system[18] which may provide a clearer picture of the charge transfer process. The molecular system will allow differentiation of the dynamics associated with the charge transfer by isolating it from processes in the semiconductor such as charge migration and charge trapping and could lead to deeper insight into relaxation pathways in charge transfer systems immediately following light absorption. Knowledge of these relaxation pathways is important for understanding and controlling the dynamics of ultrafast electron transfer reactions.

7.6. REFERENCES

(1) Akimov, A.; Neukirch, A.; Prezhdo, O. *Chem. Rev.* **2013**, *113*.

(2) Ardo, S.; Meyer, G. J. *Chem. Soc. Rev.* **2009**, *38*, 115.

(3) Asbury, J. B.; Hao, E.; Wang, Y.; Ghosh, H. N.; Lian, T. *J. Phys. Chem. B* **2001**, *105*, 4545.

(4) Concepcion, J. J.; Jurss, J.; Brennaman, M. K.; Hoertz, P. G.; Patrocinio, A. O. T.; Iha, N. Y. M.; Templeton, J. L.; Meyer, T. J. *Acc. Chem. Res.* **2009**, *42*, 1954.

(5) Grätzel, M. *Nature* **2001**, *414*, 338.

(6) Gregg, B. A. *J. Phys. Chem. B* **2003**, *107*, 4688.

(7) Hagfeldt, A.; Boschloo, G.; Sun, L.; Kloo, L.; Pettersson, H. *Chem. Rev.* **2010**, *110*, 6595.

(8) Hao, E.; Anderson, N.; Asbury, J.; Lian, T. *J Phys Chem B* **2002**, *106*.

(9) Kamat, P. V. *J. Phys. Chem. C* **2007**, *111*, 2834.

(10) Morandeira, A.; Boschloo, G.; Hagfeldt, A.; Hammarström, L. *J. Phys. Chem. C* **2008**, *112*, 9530.

(11) Morris-Cohen, A. J.; Frederick, M. T.; Cass, L. C.; Weiss, E. A. *J. Am. Chem. Soc.* **2011**, *133*, 10146.

(12) O'Regan, B.; Gratzel, M. *Nature* **1991**, *353*.

(13) Sarkany, L.; Wasylenko, J. M.; Roy, S.; Higgins, D. A.; Elles, C. G.; Chikan, V. *J. Phys. Chem. C* **2013**, *117*, 18818.

(14) Smeigh, A. L.; Katz, J. E.; Brunschwig, B. S.; Lewis, N. S.; McCusker, J. K. *J. Phys. Chem. C* **2008**, *112*, 12065.

(15) Tseng, H.-W.; Wilker, M. B.; Damraurer, N. H.; Dukovic, G. *J. Am. Chem. Soc.* **2013**, *135*, 3383.

(16) Weng, Y.; Wang, Y.; Asbury, J.; Ghosh, H. N.; Lian, T. *J Phys Chem B* **2000**, *104*.

(17) Zou, Z.; Ye, J.; Sayama, K.; Arakawa, H. *Nature* **2001**, *414*, 625.

(18) Asbury, J.; Anderson, N.; Hao, E.; Ai, X.; Lian, T. *J Phys Chem B* **2003**, *107*.

(19) Weinberg, D. R.; Gagliardi, C. J.; Hull, J. F.; Murphy, C. F.; Kent, C. A.; Westlake, B.; Paul, A.; Ess, D. H.; McCafferty, D. G.; Meyer, T. J. *Chem. Rev.* **2007**, *107*, 5004.

(20) Ashford, D.; Glasson, C. R.; Norris, M.; Concepcion, J. J.; Keinan, S.; Brennama, K.; Templeton, J. *Inorg. Chem* **2014**, *53*, 5637.

(21) Chen, Z.; Grumstrup, E. M.; Gilligan, A. T.; Papanikolas, J. M.; Schanze, K. S. *J Phys Chem B* **2014**, *118*, 372.

(22) Giokas, P. G.; Miller, S. A.; Hanson, K.; Norris, M.; Glasson, C. R.; Concepcion, J. J.; Bettis, S. E.; Meyer, T. J.; Moran, A. M. *J. Phys. Chem. C* **2013**, *117*, 812.

(23) Li, L.; Giokas, P. G.; Kanai, Y.; Moran, A. M. *J. Chem. Phys* **2014**, *140*, 234109.

(24) Anderson, N. A.; Lian, T. *Annu. Rev. Phys. Chem.* **2005**, *56*, 491.

(25) Ghosh, H. N.; Asbury, J.; Weng, Y.; Lian, T. *J. Phys. Chem. B* **1998**, *102*, 10208.

(26) Gundlach, L.; Ernstorfer, R.; Willig, F. *Phys. Rev. B* **2006**, *74*, 035324.

(27) Shoute, L. C. T.; Loppnow, G. R. *J. Amer. Chem. Soc.* **2003**, *125*, 15636.

(28) Varaganti, S.; Ramakrishna, G. *J Phys Chem C* **2010**, *114*.

(29) Wang, Y.; Hang, K.; Anderson, N.; Lian, T. *J. Phys. Chem. B* **2003**, *107*, 9434.

(30) Gerischer, H. *Surf. Sci.* **1969**, *18*, 97.

(31) Gerischer, H. *Photochem. Photobiol.* **1972**, *16*, 243.

(32) Marcus, R. A. *Annu. Rev. Phys. Chem.* **1964**, *15*, 155.

(33) Marcus, R. A. *J. Chem. Phys.* **1965**, *43*, 679.

(34) Coalson, R. D.; Evans, D. G.; Nitzan, A. *J. Chem. Phys.* **1994**, *101*, 436.

(35) Egorova, D.; Thoss, M.; Domcke, W.; Wang, H. *J. Chem. Phys.* **2003**, *119*, 2761.

(36) Evans, D. G.; Coalson, R. D. *J. Chem. Phys.* **1995**, *102*, 5658.

(37) Golosov, A. A.; Reichman, D. R. *J. Chem. Phys.* **2001**, *115*, 9848.

(38) Golosov, A. A.; Reichman, D. R. *J. Chem. Phys.* **2001**, *115*, 9862.

(39) Jakubikova, E.; Snoeberger III, R. C.; Batista, V. S.; Batista, E. R. *J. Phys. Chem. A* **2009**, *113*, 12532.

(40) Kondov, I.; Thoss, M. *J. Phys. Chem. A* **2006**, *110*, 1364.

(41) Liang, K.-K.; Lin, C.-K.; Chang, H.-C.; Hayashi, M.; Lin, S. H. *J. Chem. Phys.* **2006**, *125*, 154706.

(42) Welack, S.; Schreiber, M.; Kleinekathöfer, U. *J. Chem. Phys.* **2006**, *124*, 044712.

(43) Zhang, M.-L.; Ka, B. J.; Geva, E. *J. Chem. Phys.* **2006**, *125*, 044106.

(44) Hupp, J. T.; Williams, R. D. *Acc. Chem. Res.* **2001**, *34*, 808.

(45) Kaniyankandy, S.; Rawalekar, S.; Sen, A.; Ganguly, B.; Ghosh, H. N. *J. Phys. Chem C* **2012**, *116*, 98.

(46) Lana-Villarreal, T.; Rodes, A.; Perez, J.; Gomez, R. *J. Am. Chem. Soc.* **2005**, *127*.

(47) Liu, Y.; Dadap, J. I.; Zimdars, D.; Eisenthal, K. *J. Phys. Chem. B* **1999**, *103*.

(48) Miller, S. A.; West, B. A.; Curtis, A. C.; Papanikolas, J. M.; Moran, A. M. *J. Chem. Phys* **2011**, *135*, 081101_1.

(49) Moser, J.; Punchihewa, S.; Infelta, P. P.; Gratzel, M. *Langmuir* **1991**, *7*, 3012.

(50) Ramakrishna, G.; Singh, A. K.; Palit, D. K.; Ghosh, H. N. *J Phys Chem B* **2004**, *108*.

(51) Redfern, P. C.; Zapol, P.; Curtiss, L. A.; Rajh, T.; Thurnauer, M. C. *J. Phys. Chem. B* **2003**, *107*, 11419.

(52) Greaves, S.; Griffith, W. *Spectrochimica Acta* **1991**, *47A*.

(53) Hurst, S. J.; Fry, C.; Gosztola, D. J.; Rajh, T. *J. Phys. Chem C* **2011**, *115*, 620.

(54) Lee, N.; Hsieh, Y.; Paisley, R. F.; Morris, M. D. *Anal. Chem* **1988**, *60*, 442.

(55) Ramirez, F. J.; Navarrete, J. T. *Vib. Spectr.* **1993**, *4*, 321.

(56) Rego, L.; Batista, V. *J. Am. Chem. Soc.* **2003**, *125*.

(57) Salama, S.; Strong, J. D.; Neilands, J. B.; Spiro, T. G. *Biochemistry* **1978**, *17*, 3781.

(58) Reddy, K. M.; Reddy, C. V. G.; Manorama, S. V. *Journal of Solid State Chemistry* **2001**, *158*.

(59) Tauber, M. J.; Mathies, R. A.; Chen, X.; Bradforth, S. E. *Rev. Sci. Instrum.* **2003**, *74*.

(60) Brown, E.; Zhang, Q.; Dantus, M. *J. Chem. Phys* **1999**, *110*.

(61) Knoester, J.; Mukamel, S. *Physics Reports* **1991**, *205*.

(62) Kubarych, K. J.; Joffre, M.; Moore, A.; Belabas, N.; Jonas, D. *Opt. Lett.* **2005**, *30*, 1228.

(63) Khurmi, C.; Berg, M. A. *J. Opt. Soc. Am. B* **2009**, *26*, 2357.

(64) Molesky, B. P.; Giokas, P. G.; Guo, Z.; Moran, A. M. *J. Chem. Phys* **2014**, *141*.

(65) Molesky, B. P.; Guo, Z.; Moran, A. M. *J. Chem. Phys.* **2015**, *142*.

(66) Grumstrup, E. M.; Chen, Z.; Vary, R. P.; Moran, A. M.; Schanze, K. S.; Papanikolas, J. M. *J Phys Chem B* **2013**, *117*, 8245.

(67) McCamant, D. W.; Kukura, P.; Yoon, S.; Mathies, R. A. *Rev. Sci. Instrum.* **2004**, *75*.

(68) Doorn, S. K.; Hupp, J. T. *J. Am. Chem. Soc.* **1989**, *111*, 4704.

(69) Lee, N.; Schuck, P. J.; Nico, P. S.; Gilbert, B. *J. Phys. Chem. Lett.* **2015**, *6*, 970.

(70) Gerhards, M.; Perl, W.; Schumm, S.; Heinrichs, U.; Jacoby, C.; Kleinemanns, K. *J. Chem. Phys* **1996**, *104*.

(71) Myers Kelley, A. *J. Phys. Chem. A* **1999**, *103*, 6891.

(72) Berger, T.; Anta, J.; Morales-Florez, V. *J Phys Chem C* **2012**, *116*, 11444.

(73) Yoshihara, T.; Katoh, R.; Furube, A.; Tamaki, Y.; Murai, M. *J Phys Chem B* **2004**, *108*, 3817.

(74) Fedunov, R. G.; Plotnikova, A. V.; Ionkin, V. N.; Ivanov, A. I. *J. Phys. Chem. A* **2015**, *119*, 1964.

(75) Creutz, C.; Chou, M. H. *Inorg. Chem* **2008**, *47*.

(76) Monllor-Satoca, D.; Gomez, R. *Electrochimica Acta* **2010**, *55*.

(77) Hoskins, R. *J. Chem. Phys* **1955**, *23*.

(78) Beck, S. M.; Brus, L. E. *J. Am. Chem. Soc.* **1982**, *104*.

(79) Tripathi, G. N. R.; Schuler, R. H. *J. Phys. Chem* **1987**, *91*, 5881.

(80) Long, D. A. *The Raman Effect: A Unified Treatment of the Theory of Raman Scattering by Molecules*; Wiley: Chinchester, England, 2002.

(81) Mukamel, S. *Principles of Nonlinear Optical Spectroscopy*; Oxford University Press: New York, 1995.

(82) Vöhringer, P.; Scherer, N. F. *J. Phys. Chem.* **1995**, *99*, 2684.

CHAPTER 8: ULTRAFAST SPECTROSCOPIC SIGNATURES OF COHERENT ELECTRON TRANSFER MECHANISM IN A TRANSITION METAL COMPLEX

8.1. Introduction

Knowledge of coherent chemical reaction mechanisms has motivated a large body of work in the past few decades.[1-8] Interest in the role of vibronic coherence on electron transfer processes can be traced back to the earliest experimental studies of femtosecond dynamics in the bacterial photosynthetic reaction center.[1,2] This study was followed by numerous observations of similar behaviors in other biological systems; examples include photo-induced isomerization of bacteriorhodopsin[3] and photo-dissociation in myoglobin.[5] Recent advances in femtosecond laser spectroscopies have enabled more detailed investigations of coherent electron transfer mechanisms in photosynthetic complexes,[9] polymer-fullerene blends,[10] and molecule-semiconductor interfaces.[11,12] A commonality in these systems is that electron transfer takes place on a time scale that is shorter than vibrational dephasing and/or solvation dynamics. Traditional second-order models should not be applied in this non-equilibrium regime.[13-16] Recurrences of the donor at the transition state may give rise to periodic bursts in the acceptor's population in some cases.[1,2,6,9,10,17] An understanding of such coherent reaction dynamics holds implications for hot electron transfer processes, which can boost solar energy conversion efficiency if properly harnessed.[18-21]

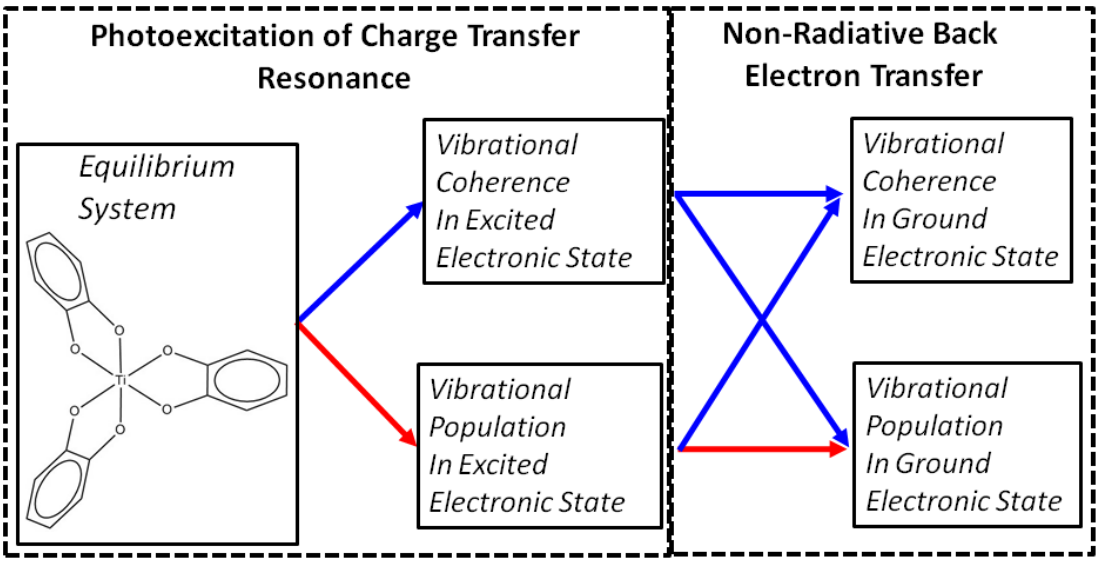

Figure 8.1: Four potential $[Ti(cat)_3]^{2-}$ photoexcitation pathways. Photoexcitation of $[Ti(cat)_3]^{2-}$ can be described with four potential pathways. The pathway connected by red arrows can be described with traditional models if a Boltzmann distribution of vibrational quanta is established before back-electron transfer; however, a non-equilibrium electron transfer model is required if this condition is not satisfied. The pathways involving vibrational coherences contribute if back-electron transfer is faster than vibrational dephasing.

In this paper, femtosecond transient absorption spectroscopy is used to investigate the influence of vibronic coherence on electron transfer in a transition metal complex in which a titanium atom is bonded to three catechol ligands, $[Ti(cat)_3]^{2-}$. Strong interactions between catechol and titanium give rise to a charge transfer electronic resonance near 400 nm.[22] Following light-induced electron transfer from catechol to titanium, the strong titanium-catechol interactions also promote a fast non-radiative back electron transfer (BET) from titanium to catechol.[23] The well-defined nature of this system is leveraged to understand how the BET process initiates coherent nuclear motion in the product state. The charge transfer nature of the electronic resonance is essential for this investigation, because it guarantees significant

projections of Franck-Condon active modes onto the reaction coordinate.[24,25] With inspiration from earlier work,[26,27] we use normal mode displacements determined with resonance Raman spectroscopy to parameterize a non-equilibrium model that incorporates coherent BET mechanisms.

Photoexcitation and BET are decomposed into four "pathways" in Figure 8.1. Traditional second-order kinetic models describe the pathway connected by red arrows for thermalized excited states. The other three possibilities involve coherent nuclear motion before and/or after the BET process. Coherent nuclear motion is directly initiated by light absorption in most of the experimental studies discussed above (i.e., a stimulated Raman process). Bursts of population flow into the product state may be observed in such cases, and the wavepacket can retain coherence in the product state (i.e., a vibronic coherence transfer transition).[1,2,6,9,10,17] It is also possible for vibrational coherence to be initiated in the product state if the reactant does not undergo coherent nuclear motion. Fleming and Jean emphasized this point in an earlier theoretical study based on a density matrix approach.[28] The two pathways in which BET initiates vibrational coherence in the product are of primary interest in this work (i.e., paths ending on top in Figure 8.1).

In previous work, we showed that a fourth-order perturbative model can be used to simulate time-coincident electron transfer and solvation dynamics under many of the same approximations made in Marcus' theory.[29] The non-equilibrium state of the system initiated by light absorption was modeled using experimentally accessible parameters such as the solvation time and absorbance line width. The fourth-order model revealed large discrepancies with Marcus' model in regimes where the photoinitiated wavepacket traverses the point of intersection between diabatic surfaces.[29] This earlier model is applicable to systems with weak vibronic

activity; however, we show in this work that the addition of quantized vibrational levels is relatively straightforward and will support a description of the coherent pathways in Figure 8.1.

8.2. Model for Spectroscopy and Dynamics

In this section, we develop a model for transient absorption spectroscopy that incorporates the four types of BET transitions defined in Figure 8.1. The model is developed under the assumption that the optical response and BET process depend on the same parameters because of the charge transfer nature of the electronic resonance.[27] The model will be parameterized using a spectral fitting approach for which key equations are summarized the end of this section.

8.2.A. Hamiltonian

We employ a reduced description in which the Hamiltonian is partitioned into three components: the system (H_{sys}), bath (H_{bath}), and system-bath interaction ($H_{sys-bath}$). The three operators may be written as

$$H_{sys} = |g\rangle\langle g|\sum_m |m\rangle\langle m|\left(E_g + E_m\right) + |e\rangle\langle e|\sum_n |n\rangle\langle n|\left(E_e + E_n\right) \ , \tag{8.1}$$

$$H_{bath} = \frac{1}{2}\sum_i \left[\frac{p_i^2}{\mu_i} + \mu_i\omega_i^2 q_i^2\right]\left[|g\rangle\langle g| + |e\rangle\langle e|\right] \ , \tag{8.2}$$

and

$$H_{sys-bath} = |g\rangle Q_{g,c}\langle g| + |e\rangle Q_{e,c}\langle e| \ . \tag{8.3}$$

The dynamics of interest in this work can be simulated by treating only the ground (g) and lowest energy excited (e) electronic states of the system if we assume that BET is fast compared to transitions between excited states. The summations in H_{sys} are carried out over dummy indices, m and n, that represent quantized vibrational levels of the system. Throughout this paper, the indices m, l, and u will be associated with the ground electronic state, whereas n, k, and v will correspond to the excited electronic state. In the harmonic approximation, the basis vectors are direct products, $|m\rangle = \prod_{\alpha} |N_{\alpha m}\rangle$, where $N_{\alpha m}$ is the number of vibrational quanta in normal mode α for basis vector m. The bath consists of displaced harmonic oscillators for which the associated variables are written in lower case (μ_i , ω_i , and q_i).[13-15] The collective primary oscillator coordinates in $H_{sys-bath}$ are related to the secondary harmonic modes in H_{bath} by $Q_{g,c} = \sum_i \mu_i \omega_i^2 d_{g,i} q_i$, where $d_{g,i}$ is the displacement of mode i for the ground electronic state; an analogous formula can be written for the excited electronic state.

Stochastic fluctuations in the energy levels of the system are handled using a time-correlation function formalism for the collective coordinates. The cumulant expansion approach may be employed, because the bath is taken to be harmonic. In the overdamped limit, time correlation functions between the collective Brownian oscillator coordinates are related to the second term in a cumulant expansion by[13]

$$\gamma(t) = \left(\frac{2\lambda k_B T}{\hbar^2 \Lambda^2} - i \frac{\lambda}{\hbar \Lambda} \right) \left[\exp(-\Lambda t) + \Lambda t - 1 \right] , \tag{8.4}$$

where Λ^{-1} is the time-scale of nuclear relaxation and λ is the reorganization energy. The reorganization energy of the bath is related to the variance of fluctuations in the energy gap between ground and excited states by

$$\lambda = \frac{\Delta^2}{2k_B T} \ . \tag{8.5}$$

The assumption of an overdamped primary oscillator coordinate is justified for systems in which vibronic structure in the absorbance spectrum is not resolved. Both electron transfer and light absorbance are governed by the same reorganization energy in systems that posses charge transfer resonances.[24,25]

8.2.B. Model for Transient Absorption Signals

The model presented in this section establishes transient absorption signatures of the non-equilibrium pathways in Figure 8.1. Both populations and coherences between vibrational states can be treated by extending the fourth-order perturbative model for electron transfer developed in earlier work.[29,30] The system undergoes BET between pump and probe events in the signal component of interest. Overall, the process can be described as a sequence of six perturbative interactions. The formulas can be greatly simplified by invoking a "doorway-window" picture in which the signal is written as a product of wavepackets associated with excitation and detection. Such models have been used extensively in descriptions of transient absorption experiments.[13]

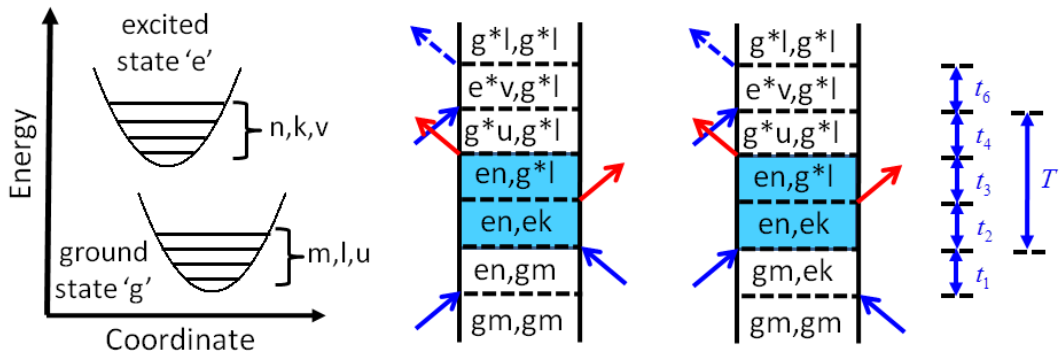

Figure 8.2: Nonlinearities associated with the hot ground state signal component can be obtained by incorporating two field-matter interactions after the back-electron transfer step. The time intervals, t_i, separate perturbative interactions with an external electric field, $\hat{H}_{rad-mat}$ (blue arrows), and the donor-acceptor coupling, $\hat{V}$ (red arrows). The indices g and e represent the ground and excited states of $[Ti(cat)_3]^{2-}$, whereas the vibrational levels are represented by dummy indices (m, n, k, l, u, v). The indices m , l, and u are associated with the ground electronic state, whereas n, k, and v correspond to the excited electronic state. The non-radiative transition from state e to state g is referred to as "back-electron transfer" (i.e., the events shaded in blue).

The doorway function incorporates dynamics that take place in the t_1, t_2, and t_3 time intervals shown in Figure 8.2. We must assume that the dynamics are uncorrelated with those in the t_4 and t_5 time intervals in this approach. The assumption is good in systems with fast solvation times such as aqueous solutions.[31] The two components of the doorway function can be written as

$$\phi_1(t_2) = 2\frac{|\mu_{eg}|^2|V_{eg}|^2}{\hbar^4}\sum_{mnklu} B_m \langle n|m\rangle\langle k|m\rangle\langle n|u\rangle\langle k|l\rangle \mathrm{Re}\left\{\int_0^\infty dt_1\int_0^\infty dt_2\int_0^\infty dt_3 \right.$$
$$\times\exp\left[-i\left(\omega_{eg}t_1+\omega_{nm}t_1+\omega_{nk}t_2-i\Gamma_{nk}t_2+\omega_{eg}t_3+\omega_{nl}t_3\right)\right. \quad , \qquad (8.6)$$
$$\left.\left.-\frac{1}{2}\Delta^2\left(t_1^2+t_3^2\right)-f\left(t_1,\tau,t_3\right)\right]E^*\left(t'-t_1\right)E\left(t'\right)\right\}$$

and

$$\phi_2(t_2) = 2\frac{|\mu_{eg}|^2|V_{eg}|^2}{\hbar^4}\sum_{mnklu} B_m \langle n|m\rangle\langle k|m\rangle\langle n|u\rangle\langle k|l\rangle \mathrm{Re}\left\{\int_0^\infty dt_1\int_0^\infty dt_2\int_0^\infty dt_3 \right.$$
$$\times\exp\left[-i\left(-\omega_{eg}t_1+\omega_{mk}t_1+\omega_{nk}t_2-i\Gamma_{nk}t_2+\omega_{eg}t_3+\omega_{nl}t_3\right)\right. \quad , \qquad (8.7)$$
$$\left.\left.-\frac{1}{2}\Delta^2\left(t_1^2+t_3^2\right)+f^*\left(t_1,\tau,t_3\right)\right]E^*\left(t'-t_1\right)E\left(t'\right)\right\}$$

where

$$f\left(t_1,t_2,t_3\right) = \gamma^*\left(t_2\right)-\gamma^*\left(t_2+t_3\right)-\gamma\left(t_1+t_2\right)+\gamma\left(t_1+t_2+t_3\right) . \qquad (8.8)$$

In Equations (8.6) and (8.7), we use the convention of Reference [32], where vibrational levels of the excited state are written in the bra of the inner products.

The five nested summations over vibrational levels will be computationally expensive to evaluate for a system with multiple vibrational modes. Analytic integration can be accomplished with inspiration from earlier descriptions of transient absorption spectroscopies.[13,33] To begin, the effect of finite laser bandwidth is incorporated by introducing the integration variable, $t' = \tau - t_2$. This approximation is justified when the temporal width of the laser pulse is short compared to the time scale of the nuclear dynamics. In addition we make the "short-time approximation" for the linear combination of line broadening functions, $\gamma(t)$, in ϕ_1 and ϕ_2.

Similar approaches have been used to described electron transfer and internal conversion in earlier work.[29,30] The two functions are then written as

$$\phi_1(\tau) = 2\frac{\left|\mu_{eg}\right|^2\left|V_{eg}\right|^2}{\hbar^4}\sum_{mnklu} B_m \langle n|m\rangle\langle k|m\rangle\langle n|u\rangle\langle k|l\rangle \mathrm{Re}\Big\{\int_0^\infty dt_1\int_{-\infty}^\infty dt'\int_0^\infty dt_3 \\ \times\exp\Big[-i\left(\omega_{eg}t_1+\omega_{nm}t_1+\omega_{nk}\tau-i\Gamma_{nk}\tau+\omega_{eg}t_3+\omega_{nl}t_3\right) \\ -\frac{1}{2}\Delta^2\left(t_1^2+t_3^2\right)-f\left(t_1,\tau,t_3\right)\Big]E^*\left(t'-t_1\right)E\left(t'\right)\Big\} \quad , \tag{8.9}$$

and

$$\phi_2(\tau) = 2\frac{\left|\mu_{eg}\right|^2\left|V_{eg}\right|^2}{\hbar^4}\sum_{mnklu} B_m \langle k|m\rangle\langle n|m\rangle\langle n|u\rangle\langle k|l\rangle \mathrm{Re}\Big\{\int_0^\infty dt_1\int_{-\infty}^\infty dt'\int_0^\infty dt_3 \\ \times\exp\Big[-\left(-\omega_{eg}t_1+\omega_{mk}t_1+\omega_{nk}t_2-i\Gamma_{nk}t_2+\omega_{eg}t_3+\omega_{nl}t_3\right) \\ -\frac{1}{2}\Delta^2\left(t_1^2+t_3^2\right)+f^*\left(t_1,\tau,t_3\right)\Big]E^*\left(t'-t_1\right)E\left(t'\right)\Big\} \quad , \tag{8.10}$$

where

$$f\left(t_1,t_2,t_3\right) = i\frac{2\lambda}{\hbar}\left[\exp\left(-\Lambda t_2\right)-1\right]t_3+\frac{\Delta^2}{\hbar^2}\exp\left(-\Lambda t_2\right)t_1t_3 \ . \tag{8.11}$$

In addition, a Gaussian laser spectrum will be assumed for convenience,

$$E\left(t\right) = \xi_L\exp\left(-i\omega_L t - w_L^2t^2/2\hbar^2\right) \ . \tag{8.12}$$

Equations (8.9)-(8.10) set up the description in a way that parallels an earlier formulation of transient absorption signals.[13,33] The key difference in the present case is that quantized vibrational levels have been incorporated into the system. The present formulas assume the same mathematical form as the earlier model if vibrational levels are removed from the first time interval between field-matter interactions, $\omega_{ge}t_1+\omega_{mn}t_1 \approx \omega_{ge}t_1$. This is a good approximation

provided that the absorbance spectrum has a broad Gaussian shape (i.e., vibronic progression is unresolved). The sum of Equations (8.9) and (8.10) then yields

$$D(\tau) = \sum_{mnklu} D_{nk\to lu}(\tau) \ , \tag{8.13}$$

where

$$\begin{aligned} D_{nk\to ul}(\tau) = & \frac{\pi^{3/2}\left|\xi_L \mu_{eg}\right|^2 \left|V_{eg}\right|^2}{\hbar w_L^2 \sqrt{\left(\Delta^2 + w_L^2\right)\alpha^2(\tau)}} B_m \langle n|m\rangle\langle k|m\rangle\langle n|u\rangle\langle k|l\rangle \\ & \times \exp\left[-\frac{\hbar^2\left(\omega_L - \omega_{eg}\right)^2}{4\lambda k_B T}\right] \exp\left[-\frac{\Omega^2(\tau)}{2\alpha(\tau)^2}\right] \cos(\omega_{nk}\tau) \exp\left(-\Gamma_{nk}\tau\right) \end{aligned} \ , \tag{8.14}$$

$$\Omega(\tau) = \Delta G_{eg}^0 + \lambda - \hbar\omega_{nl} + \exp(-\Lambda\tau)\left[-\hbar\omega_L - \Delta G_{eg}^0 - \lambda + \hbar\omega_{nl}\right] \ , \tag{8.15}$$

and

$$\alpha^2(\tau) = \Delta^2\left[1 - \frac{\Delta^2}{\Delta^2 + w_L^2}\exp(-2\Lambda\tau)\right] \ . \tag{8.16}$$

The laser spectrum is assumed to be narrower than the absorbance line width in $\Omega(\tau)$, because this approximation is appropriate for the experiments described in section 8.4. The magnitude of the free energy gap, ΔG_{eg}^0, is equal to the difference between the peak of the absorbance spectrum, ω_{eg}, and the solvent reorganization energy, λ (i.e., ΔG_{eg}^0 corresponds to the "electronic origin").

We resort to an empirical approach in writing the line shape of the window function. The signal associated with the "hot ground state" induced by BET undergoes a vibrational cooling

process following BET, which greatly reduces the electronic resonance frequency. An explicit treatment of such vibrational cooling mechanisms is beyond the scope of this paper. Therefore, we take the hot ground state into account with an empiircal function, $\omega_{eg}^{*}(\tau)$, that will be extracted from experimental data. The window function may then be written as

$$W_{luv}(\tau,\omega_{det}) = \frac{\langle v|u\rangle\langle v|l\rangle}{\sqrt{4\pi\lambda k_B T}} \exp\left\{-\frac{\left[\omega_{det}-\omega_{eg}^{*}(\tau)\right]^2}{4\lambda k_B T}\right\} \cos(\omega_{ul}\tau)\exp(-\Gamma_{ul}\tau) \ , \qquad (8.17)$$

where ω_{det} is the peak detection frequency extracted from a transient absorption experiment. Finally, the transient absorption signal associated with the signal component of interest is then obtained by summing over the product of $D_{nk\to ul}(\tau)$ and $W_{luv}(\tau,\omega_{det})$,

$$S(\tau,\omega_{det}) = \sum_{mnkluv} D_{nk\to ul}(\tau) W_{luv}(\tau,\omega_{det}) \ . \qquad (8.18)$$

8.2.C. Spectral Fitting of Absorbance and Resonance Raman Cross Sections

Iterative fitting of both the linear absorbance spectrum and the resonance Raman cross sections imposes constraints on the displacement of each intramolecular mode, the electronic origin of the transition, the solvent reorganization energy, and the relative contributions of homogeneous and inhomogeneous line broadening mechanisms.[32,34] Many of these same parameters also control non-radiative BET in systems that possess charge transfer resonances.[27] We summarize essential aspects of the model in this section. Additional background on the approach can be found elsewhere.[34,35]

In a basis set of delocalized excited states, $[Ti(cat)_3]^{2-}$ possesses two allowed LMCT transitions and one (higher energy) forbidden LMCT transition; these transitions correspond to the E and A irreducible representations of the C_3 point group, respectively. This aspect of the

electronic structure is taken into account in the expressions for the absorption and resonance Raman cross sections given in this section. The best choice of a basis set in a transition metal complex is not necessarily obvious and can even be dynamic in some cases.[36-39] Energy level fluctuations induced by solute-solvent interactions tend to localize the excited states in transition metal complexes, whereas electronic coupling between ligands promotes delocalization.[36-38] Therefore, charge transfer states should be treated as localized if the inter-ligand electronic couplings are much smaller than the energy level fluctuations. Such general rules of thumb have been applied extensively to distinguish localized electronic excitations from Frenkel excitons in molecular aggregates, molecular crystals, and photosynthetic complexes.[15,40-42,43] The Frenkel exciton model has been adapted to transition metal complexes in recent work.[44,45] We opt for a delocalized basis set in $[Ti(cat)_3]^{2-}$ for the following reasons. As will be shown in sections 8.4.A and 8.4.C, the three-fold symmetric Ti-catechol bond stretching mode possesses a large potential energy surface displacement and also exhibits oscillations with large amplitudes in the isotropic component of the transient absorption signal. In contrast, photoexcitation of local ligand-to-metal charge transfer transition would induce asymmetric vibrational motions. In addition, estimates of the local (inter-ligand) electronic couplings obtained with density functional theory are not consistent with the local basis set (see Appendix C). We emphasize that the main conclusions drawn in this work are independent of the basis set of the system.

The linear absorbance line shape of $[Ti(cat)_3]^{2-}$ is given by

$$\sigma_A(\omega) = \frac{8\pi\omega\mu_{eg}^2}{3\hbar c}\sum_{m=1} B_m \,\mathrm{Re}\int_{-\infty}^{\infty} d\delta G(\delta)\int_0^{\infty} dt \left\langle m\middle| m(t)\right\rangle \exp\left[i(\omega-\omega_0-\delta+\omega_m)t-\gamma(t)\right], \quad (8.19)$$

where m is an index for a nuclear mode, B_m is the Boltzmann population of the initial state, μ_{eg} is the electronic transition dipole, ω_m is the frequency associated with vibrational state m, ω_0 is

the purely electronic transition frequency (i.e., electronic origin), and $\langle m|m(t)\rangle$ is a dynamic overlap integral between nuclear wavefunctions (the Fourier transform of $\langle m|m(t)\rangle$ is a Franck-Condon progression). The dynamic overlap integral, $\langle m|m(t)\rangle$, is controlled by the mode frequencies and dimensionless potential energy surface displacements. Fluctuations in the electronic resonance frequency induced by thermal motion in the solvent are partitioned into fast (homogeneous) and slow (inhomogeneous) components. Inhomogeneous line broadening is incorporated by integrating over the static Gaussian distribution, $G(\delta)$, whereas the homogeneous line shape is captured by the line broadening function, $\gamma(t)$ (see Equation (8.4)).

The differential resonance Raman cross section is written as

$$\sigma_{R,ml}(\omega) = \frac{8\omega_S^3\omega_L}{15c^4}\sum_{mn} P_m \int d\omega_S \int_{-\infty}^{\infty} d\delta G(\delta) L_{ml}(\omega_L - \omega_S)\left|\alpha_{ml}(\omega_L,\delta)\right|^2 , \tag{8.20}$$

where m (l) is an index for the initial (final) vibrational state, ω_L (ω_S) is the incident (scattered) light frequency, and $L_{ml}(\omega_L - \omega_S)$ is the normalized line shape of the $m \rightarrow l$ ground state vibrational transition. The integral with respect to the scattered frequency, ω_S, extends over the full Raman emission band. The Raman polarizability of $[Ti(cat)_3]^{2-}$ is given by

$$\alpha_{ml}(\omega_L,\delta) = \frac{2\mu_{eg}^2}{\hbar}\int_0^{\infty} dt \langle l|m(t)\rangle \exp\left[i(\omega_L - \omega_0 - \delta + \omega_m)t - \gamma(t)\right] . \tag{8.21}$$

Dependence of the optical response and electron transfer rate on the same parameters has been leveraged for physical insight in earlier work.[27] The short-time approximation was taken in section 8.2.B to obtain Gaussian functions, whereas the more general form of $\gamma(t)$ appears in

$\sigma_A(\omega)$ and $\alpha_{ml}(\omega_L,\delta)$. The ratio, Λ/Δ (referred to here as κ)[13] is generally much less than 1 for electronic transitions in polar solvents at room temperature;[46,47] significant motional narrowing is generally not observed judging by Gaussian line shapes and Stokes shifts. The classical reorganization energy associated with electron transfer, $\lambda = D^2/2k_BT$, can be computed with

$$D = \Gamma\left[\frac{1+0.85\kappa+0.88\kappa^2}{2.355+1.76\kappa}\right], \tag{8.22}$$

where the homogeneous line width is given by $\Gamma = \lambda k_B T/\hbar\Lambda$. We note that $D \approx \Delta$ when $\kappa << 1$ (see Equation (8.5)).

8.3. Experimental Methods

8.3.A. Sample Preparation

Synthesis of is carried out using the procedure described in Reference [22]. The aqueous solutions are flowed through a wire-guided jet with a thickness of 300 μm, where the volume of the reservoir is 50 mL. The absorbance of the solution is equal to 0.5 at 400 nm in 300-μm path length. Absorbance spectra are acquired before and after experiments to confirm the absence of sample degradation.

8.3.B. Raman Spectroscopy

Resonance Raman spectra are collected with a Renishaw Via- Leica DM2500 M microscope. Excitation is accomplished using the 458, 488, and 515 nm laser lines of an argon

ion laser (Spectra Physics Stabilite 2017). The 2-mW laser beams are focused into 1-mm thick cuvettes with a Leica N PLAN EPI 20x/0.4 objective lens, which is also used to collect the scattered Raman emission in a confocal geometry. A polarization scrambler is placed between the sample and detector during measurements.[34] Reabsorption of the Raman emission is corrected using an established procedure.[48] The signals are averaged for 10-20 minutes with integration times of 30 seconds. All cosmic spikes are removed using software provided by Renishaw. The solutions contain a mixture of $[Ti(cat)_3]^{2-}$ (6 mmol/L) and sulfate (850 mmol/L), which is used as an internal standard.[49] All experiments are repeated 3 times with fresh solutions to establish reproducibility of the Raman cross sections.

8.3.C. Transient Absorption Experiments

Transient absorption experiments are carried out with a 1-kHz, 1-mJ Ti:Sapphire laser system. Pump pulses are produced by doubling the frequency of the fundamental laser beam in a 0.25-mm thick BBO crystal. The resulting 90-μJ, 410-nm second harmonic beam is then focused with a 30-cm focal length lens into a 75-cm long, 100-μm inner diameter hollow core fiber. The fiber is housed in a stainless steel cell filled with 1.0 atm of argon gas. Pulse compression to 25 fs is achieved with a fused silica prism compressor with a 50-cm prism separation. Probe laser pulses are generated using either CaF_2 or sapphire windows with 3-mm thicknesses. The CaF_2 window is used to acquire signals from 350-700 nm with the magic angle polarization condition. Isotropic and anisotropic vibrational motions are detected with probe pulses generated in sapphire. Slightly better signal-to-noise (roughly a factor of 5-10) is achieved with sapphire because the window is stationary, whereas the CaF_2 window must be continuously moved to avoid damage.

The 400-nm pump pulsed is focused onto the sample jet with a 30-cm focal length spherical mirror, whereas the continuum is relayed from the sapphire plate onto the sample using a single 5-cm focal length mirror (the continuum focuses 35 cm from the spherical mirror). The FWHM spot sizes of the 400-nm pump beam is 600 μm, whereas that of the continuum is 400 μm. The pulse energy of the pump is 200 nJ at the sample position. The angle between the two beams is 5°. Signal detection is accomplished with a CMOS array detector that is synchronized to the 1-kHz repetition rate of the laser system. The pump beam pass through a chopper wheel operated at 500 Hz, thereby enabling the acquisition of absorption spectra with and without the pump pulse on a shot-to-shot basis. The signals are averaged over 30-40 scans of the delay line if the magic angle polarization condition is employed. Isotropic and anisotropic vibrational motions are compared by interleaving 100 scans of the delay with parallel and perpendicular pump and probe polarizations. In all cases, a calcite polarizer is placed between the sample and detector during data acquisition to ensure that the polarization condition is well-defined.

8.4. Results and Discussion

In this section, we present the results of a resonance Raman intensity analysis. Potential energy surface displacements are determined and mode assignments are summarized. Transient absorption signals are then discussed with emphasis on the vibrational coherences initiated by BET. The BET mechanism is then simulated using empirical parameters determined by spectral fitting.

8.4.A. Resonance Raman Intensity Analysis and Spectral Fitting

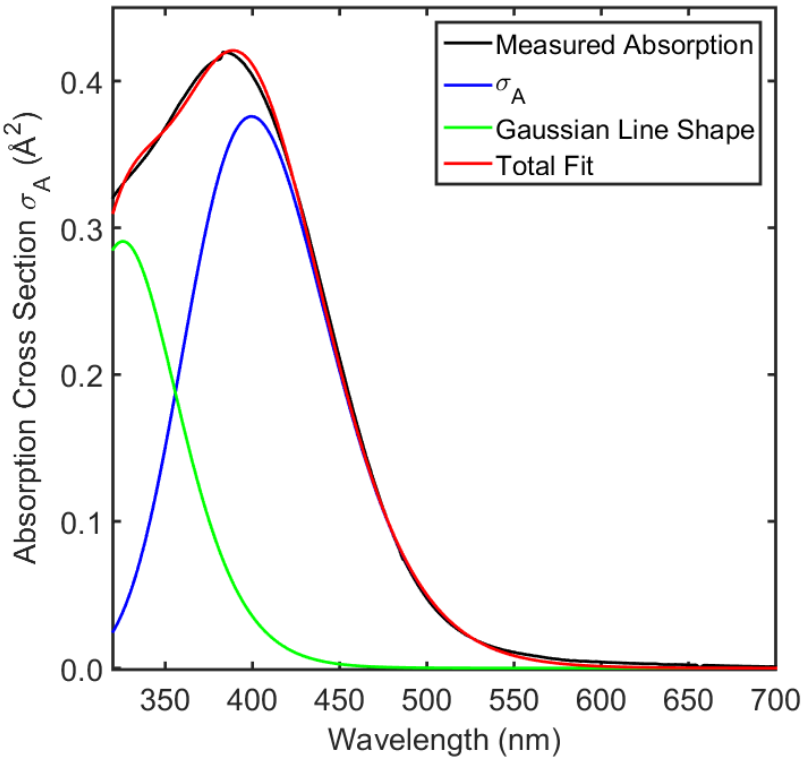

Figure 8.3: The measured absorption spectrum is fit with Equation (8.19) and the parameters in Table 8.1. The absorption cross section, σ_A, is used to fit the low-energy side of the line shape subject to the constraints imposed by the Raman cross sections. An additional Gaussian line shape (green) is used to estimate the contribution of the second-to-lowest energy transition to the total absorbance.

In Figure 8.3, the lower energy side of the absorption spectrum is fit using Equation (8.19) and the parameters in Table 8.1. The rise of the band at longer wavelengths imposes useful constraints, because the line shape is quite sensitive to the relative contributions of the intramolecular and solvent reorganization energies. Inflation of the homogeneous width increases the Lorentzian character of the line shape, whereas the inhomogeneous contribution is purely Gaussian. Example fits carried out with different distributions of homogeneous and

inhomogeneous widths are presented in Appendix C. An additional Gaussian line shape is added to the fit at shorter wavelengths in order to estimate the contribution of the second-to-lowest energy electronic transition to the total absorbance spectrum.

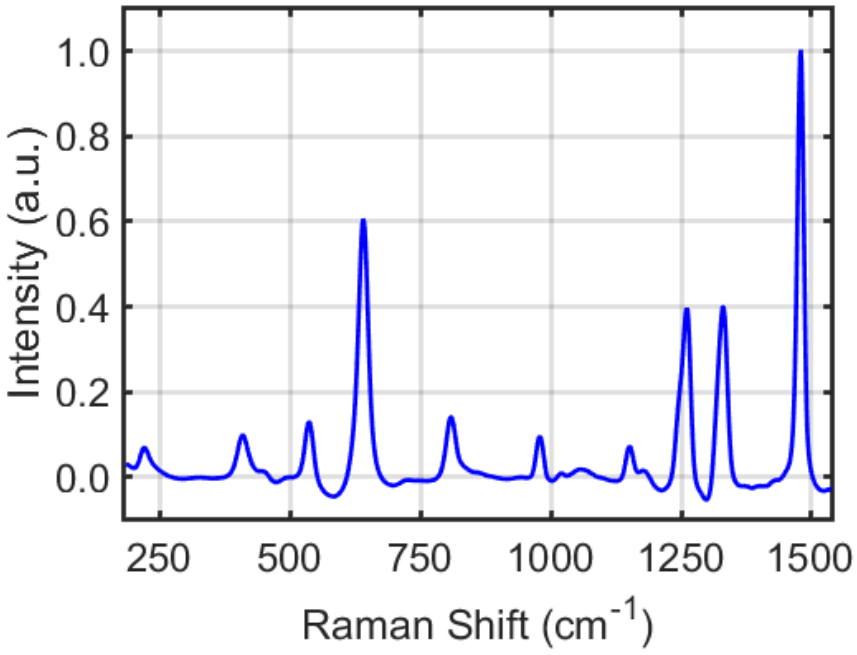

Figure 8.4: Resonance Raman spectrum of $[Ti(cat)_3]^{2-}$ acquired in aqueous solution with excitation at 488 nm.

The resonance Raman spectrum of $[Ti(cat)_3]^{2-}$ acquired with excitation at 488 nm is shown in Figure 8.4. We suggest tentative assignments of the normal modes using a calculation carried out at the B3LYP/6-311G(2d,3p) level of theory in Gaussian 2009.[50] The assignments in Table 8.1 are based on agreement between the experimental and calculated vibrational frequencies in addition to aspects of the nuclear motion. As in earlier work,[46] we assume that the most intense transitions involve modes with larger reduced masses (i.e., coordinates of the hydrogen atoms are weakly coupled to charge transfer). It is also assumed that the response is

dominated by in-plane motions of the catechol ligands, which preserve bond-conjugation in the aromatic rings. For most of these assignments, the motion described in Table 8.1 applies to a number of "candidate modes" with similar frequencies. Thus, most of the descriptions (e.g., Ti-cat stretch, C=C stretch) are likely to hold even if assignments to particular modes are later revised.

A full resonance Raman excitation profile cannot be generated because of available laser sources and contributions from higher energy electronic resonances to the charge transfer band at shorter wavelengths. Nonetheless, determination of the Raman cross sections on the lower energy side of the charge transfer resonance still imposes strong constraints on the line broadening parameters, because the resonance Raman cross sections increase as the inhomogeneous component of the absorbance line shape increases. Experimental and calculated Raman cross sections are compared in Figure 8.5.

Simultaneous fitting of absorbance and resonance Raman cross sections has been carried out in numerous earlier works.[27,34,46,47] It is not straightforward to produce error bars for this highly nonlinear model.[51] Therefore, we have explored fits in different regions of parameter space in Appendix C, where we show that the data are poorly fit if the homogeneous width is either increased or decreased by 500 cm^{-1}. For example, a decrease in the homogeneous line width is generally compensated for by increasing the electronic origin, increasing the inhomogeneous width, and decreasing the mode displacements. We find that the line widths and mode displacements can be changed by roughly 25% and 33% before large

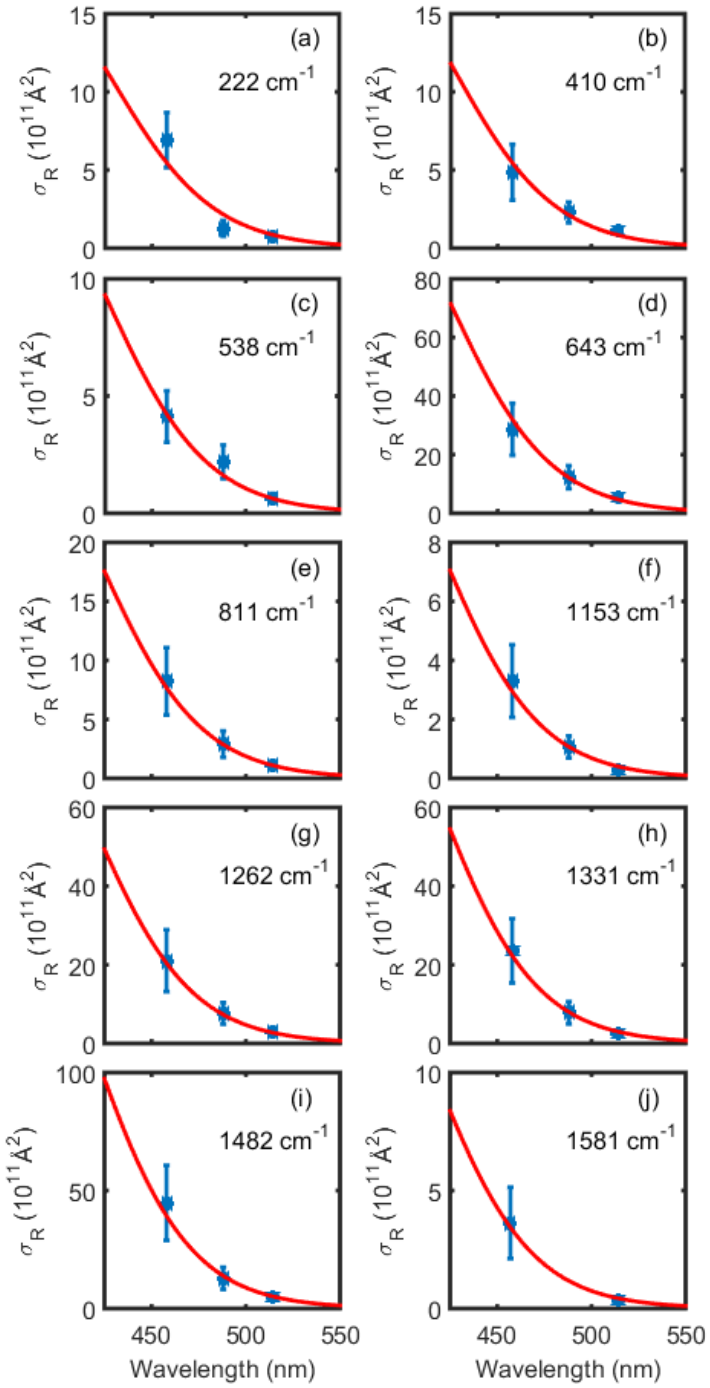

Figure 8.5: Experimental Raman cross sections are fit using Equation (8.20) and the parameters in Table 8.1.

discrepancies between the measurements and fits are produced. The error bars in Table 8.1 reflect these percentages.

Table 8.1. Resonance Raman Fitting Parameters

[a]Parameter	Value	
ω_0	21020 ± 3000 cm^{-1} (476 ± 68 nm)	
δ	2100 ± 500 cm^{-1} (48 ± 11 nm)	
Γ	2455 ± 600 cm^{-1} (55 ± 14 nm)	
$\kappa = \Delta / \Lambda$	0.01	
[b] λ	2720 ± 650 cm^{-1}	
μ_{eg}	4.1 ± 0.4 D	
Raman Shift (cm^{-1})	**Dimensionless Displacement**	**[c]Assignment**
222	1.09 ± 0.35	Symmetric Ti-cat stretch (214 cm^{-1})
410	0.61 ± 0.20	Ti-cat bend (413 cm^{-1})
538	0.42 ± 0.14	O-C-C-O bend & ring distortion (534 cm^{-1})
643	0.99 ± 0.33	O-C-C-O bend & ring distortion (641 cm^{-1})
811	0.40 ± 0.13	O-C-C-O bend and ring 'breathing' (814 cm^{-1})
1153	0.19 ± 0.06	C-H bending (1156 cm^{-1})
1262	0.47 ± 0.16	O-C-C-O stretch (1283 cm^{-1})
1330	0.48 ± 0.16	C=C stretch, C-O stretch, & Ti-O stretch (1305 cm^{-1})
1482	0.59 ± 0.19	C=C stretch & C-O stretch (1511 cm^{-1})
1580	0.17 ± 0.06	C=C stretch (1594 cm^{-1})

[a]Determination of the uncertainties in the parameters is discussed in Appendix C. Fits are carried out in the frequency domain.

[b] Computed with $\lambda = D^2 / 2k_B T$, where D is found with Equation (8.22).

[c] Assignments for vibrational modes computed at the B3LYP/6-311G(2d,3p) level in Gaussian 2009.[50] Frequencies of the calculated modes are given in parentheses.

The model yields the best fit for homogeneous and inhomogeneous line widths of 2100 and 2455 cm^{-1}, respectively. The homogeneous line width can be converted into a classical solvent reorganization energy of 2720 cm^{-1} using the Padé approximant.[13,46,47] This is a modest amount of reorganization energy for an electron transfer transition in aqueous solution. However, it was noted in earlier work that the Padé approximant may underestimate solvent reorganization energies in hydrogen bonding solvents.[46,47] In such cases, the inhomogeneous line width may account for a portion of the "slower" solvent reorganization. The dominant low-frequency modes at 222 and 643 cm^{-1} involve motions on the linkers between titanium and the ligands. Intense transition above 1000 cm^{-1} mostly correspond to bond-stretching motions on the aromatic rings.

8.4.B. Decomposition of Transient Absorption Signal Components

Photoexcitation of the charge transfer resonance at 400 nm induces electron transfer from the catechol ligands to the titanium atom. In Figure 8.6, the decrease in absorbance near 420 nm represents depopulation of the ground electronic state. This nonlinearity is denoted as the ground state bleach (GSB). BET from titanium to catechol is evidenced by growth of an absorptive response near 520 nm on the 100-fs time scale. This signal component is referred to as the "hot ground state" (HGS). The HGS resonance is observed at longer wavelengths, because BET leaves the molecule in a highly non-equilibrium state which subsequently relaxes through vibrational energy transfer to the solvent. The HGS response blue-shifts with increasing delay because of vibrational energy transfer to the solvent.

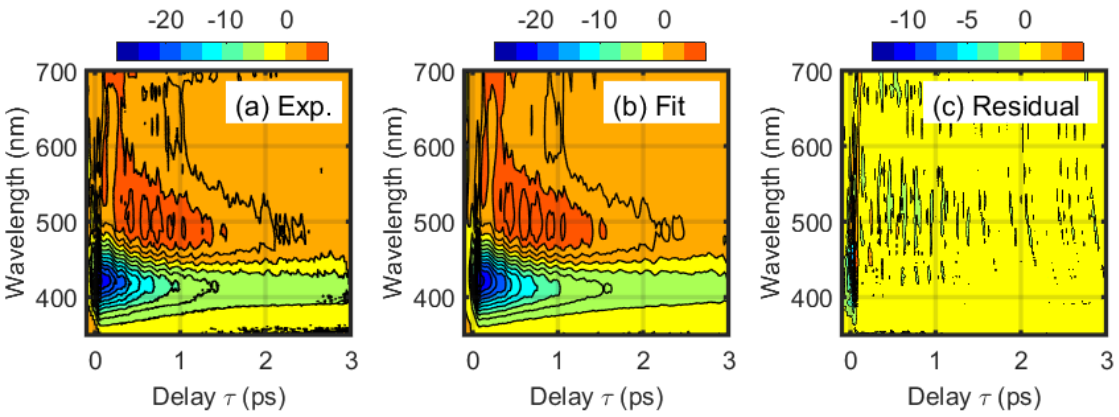

Figure 8.6: The (a) experimental transient absorption signal is (b) fit using Equation (8.23). The residual shows that agreement between the experiment in fit is best at delay times greater than 20 fs (i.e., outside the region of pulse overlap).

The transient absorption signal shown in Figure 8.6 is fit with the following function,

$$F(\tau,\lambda) = A_{GSB}(\tau)\exp\left\{-4\ln(2)\frac{\left[\lambda-\lambda_{GSB}(\tau)\right]^2}{\Delta^2_{GSB}(\tau)}\right\} + A_{HGS}(\tau)\left\{-4\ln(2)\frac{\left[\lambda-\lambda_{HGS}(\tau)\right]^2}{\Delta^2_{HGS}(\tau)}\right\} + A_{BB}(\tau)\left\{-4\ln(2)\frac{\left[\lambda-\lambda_{BB}(\tau)\right]^2}{\Delta^2_{BB}(\tau)}\right\} \quad (8.23)$$

In addition to the GSB and HGS signal components, we have included a broadband Gaussian function that contributes at longer wavelengths. Parameters associated with the GSB and HGS signal resonances, which are displayed in Figure 8.7, are of primary interest. The GSB response rises instantaneously and decays because of vibrational energy transfer to the solvent. In contrast, the magnitude of the HGS response rises for 500 fs before vibrational cooling induces decay. Large-amplitude oscillations in the HGS signal magnitude are observed at a wavenumber of 222cm^{-1} in the first picosecond (three-fold symmetric Ti-cat stretching motions); however, vibrational coherences are not detected in the GSB. The peak of the HGS response blue-shifts as

vibrational energy is transferred into the surrounding solvent, whereas the peak of the GSB response is essentially delay-independent. The line width of the HGS also decreases on the picosecond time scale, whereas the line width of the GSB is insensitive to the delay time. The blue-shift and line-narrowing exhibited by the HGS response are common indicators of vibrational cooling following ultrafast ground state recovery. Systems such as nucleobases and p-nitroaniline behave in a similar way.[52,53]

A broadband signal component is required at both short and long delay times, because a residual response in excess of 50% of the total signal strength is found without this term in Equation (8.23). At sub-picosecond delay times, we observe a broad response without a peak at longer wavelengths. It is likely that the resonance frequency for the broadband signal component is red-shifted beyond the limit of our detection range at 700 nm. The picosecond rate of decay suggests that this resonance relaxes on the time scale of vibrational cooling; however, relatively weak transient absorption persists in the near-infrared for delay times of 100's of picoseconds. Lian and co-workers, who conducted earlier experiments on $[Ti(cat)_3]^{2-}$, suggested that one of the bonds between catechol and the titanium atom may detach following excitation then reattach after 100's of ps.[23] We hypothesize that this species is also responsible for the broadband, red-shifted signal component in our experiments. Because the response appears to be red-shifted beyond our detection range, we have constrained both $\lambda_{BB}(\tau)$ and $\Delta_{BB}(\tau)$ (650 nm$<\lambda_{BB}(\tau)<$850 nm and 400 nm$<\Delta_{BB}(\tau)<$1000 nm). These constraints were required to eliminate discontinuities in the parameters of the GSB and HGS signal components, which were left unconstrained.

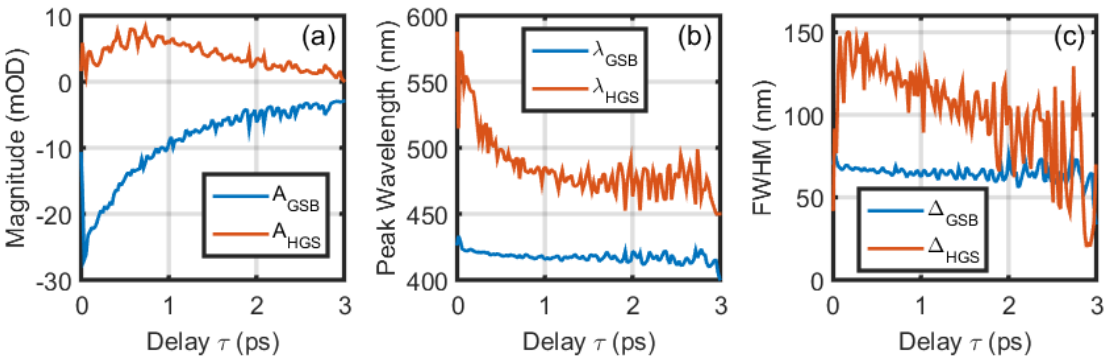

Figure 8.7: (a) The magnitude of the HGS signal component rises until a delay time of 0.5 ps before vibrational cooling causes the signal to decay. The GSB signal component rises instantaneously and decays on the time-scale of vibrational cooling. (b) The HGS signal component shifts to shorter wavelengths because of vibrational cooling, whereas the peak of the GSB resonance is insensitive to the delay time. (c) The FWHM of the HGS resonance decreases by 50% within the first 3 ps, whereas the line width of the GSB is insensitive to the delay time. The 100-fs time scale of the BET process is the key information provided by these data.

8.4.C. Initiation of Vibrational Coherence by Back-Electron Transfer

Transient absorption signals are Fourier Transformed in Figure 8.8 to reveal BET-induced vibrational motions. The vibrational coherences are quite prominent in the HGS signal component; the recurrences reach 25% of the total signal magnitude in the 450-560 nm range (see Appendix C). The relatively weak oscillations exhibited by the GSB nonlinearity in the 350-450 nm wavelength range underscores the distinction between BET-induced (HGS) and radiation-induced (GSB) vibrational coherences.[54] Isotropic and anisotropic signals at 500 nm are processed in Figure 8.8 to facilitate a better understanding of the HGS response. The isotropic signal component is produced by combining signals measured with both parallel and perpendicular pump and probe pulses, $S_{\parallel} + 2S_{\perp}$, whereas the anisotropic response is proportional

to the difference in the two tensor elements, $S_{\parallel} - S_{\perp}$.[55] These combinations of tensor elements are examined to determine whether or not the transition dipole orientations for the charge transfer resonance are affected by vibrational motions. Totally symmetric modes should not affect the transition dipole angles, because they preserve the C_3 symmetry of the system, whereas vibrational modes with lower symmetry may cause the transition dipoles to oscillate through a non-Condon effect.[56]

The Raman spectra in Figure 8.8 show that vibrational resonances associated with the isotropic signal component are 10 times more intense than those found in the anisotropic signal components. We observe resonances corresponding to the 222, 410, 538, and 643 cm^{-1} modes. The resonances are observed at 200, 400, 510, and 600 cm^{-1}, which indicates that the modes are highly populated following the back-electron transfer process (i.e., the lower frequencies reflect anharmonicity). Relative to the isotropic response, the largest anisotropic intensities are found in the two highest frequency modes at 505 and 610 cm^{-1}, which may reflect weak non-Condon activity.

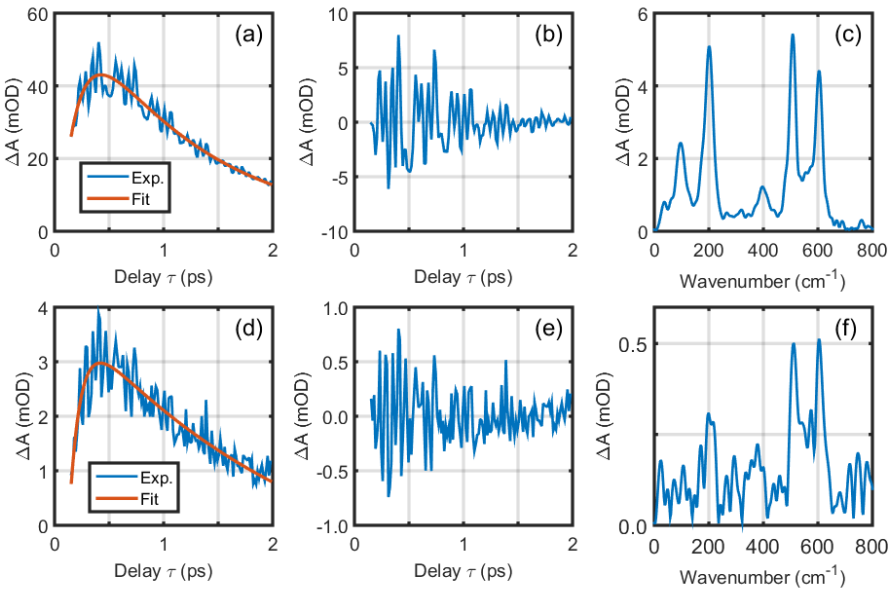

Figure 8.8: (a) An incoherent baseline is subtracted from the isotropic signal component at 500 nm to (b) isolate the coherent response. (c) Fourier transformation yields a coherent Raman spectrum for the isotropic HGS signal component. (d) An incoherent baseline is subtracted from the anisotropic signal component at 500 nm to (e) isolate the coherent response. (f) Fourier transformation yields a coherent Raman spectrum for the anisotropic HGS signal component. These data show that the back-electron transfer primarily initiates totally symmetric vibrational motion. All mode frequencies are slightly smaller than those observed with spontaneous Raman spectroscopy, which indicates that the modes are highly populated following back-electron transfer (i.e., the frequencies are lower because of anharmonicity).

Dominant isotropic BET-induced vibrational motion indicates that the charge transfer states are not localized on individual ligands. Asymmetric stretching of individual titanium-catechol bonds would be initiated following back electron transfer if the transitions were localized. Rather the Raman response observed for $[Ti(cat)_3]^{2-}$ is consistent with delocalization

of the charge transfer excitation among the three ligands. This interpretation is consistent with the 640-cm^{-1} inter-ligand electronic coupling estimated with density function theory (see Appendix C). A localized basis set is a good approximation only if the coupling is much smaller compared to the thermal fluctuation amplitude, which was determined to be 1040 cm^{-1} in section 8.4.A. The similar magnitudes of these two quantities suggest that delocalization of the electronic excitation should take hold.

8.4.D. Analysis of the Back-Electron Transfer Mechanism

The HGS signal component presented above demonstrate that vibrational coherences are initiated by the BET process. Such coherences can originate in either vibrational populations or coherences in the excited electronic state (i.e., the two paths ending in the upper right of Figure 8.1). The model developed in Section 8.2 can be used to explore the relative contributions of these pathways. All of the parameters with the exception of the solvation time, Λ^{-1}, can be extracted from the spectral fitting approach described above. We set Λ^{-1} equal to the 90 fs, which is reasonable for aqueous solution.[31] In addition, damping times for the ground (Γ_{ul}^{-1}) and excited (Γ_{nk}^{-1}) states are set equal to 1 ps and 200 fs, respectively. The damping time for the excited state are shorter because of BET. It is not necessary to parameterize the product of matrix elements, $\left|\xi_L \mu_{eg}\right|^2 \left|V_{eg}\right|^2$, in the doorway function, because normalized signal intensities are analyzed in this section.

We begin by depicting the physical picture associated with the model in Figure 8.9. Energy has been (linearly) mapped onto the collective coordinate for convenience.[13] Ground and excited state potential energy minima appear at $+\lambda$ and $-\lambda$ for a harmonic bath (and the Stokes

shift is 2λ). The point of intersection between free energy surfaces is located at $-\lambda-\left(\Delta G_{eg}+\lambda\right)^2/4\lambda$. The wavepacket initiated by the pump pulse can be written as[29]

$$Y(\tau,q)=\frac{1}{\alpha(\tau)\sqrt{2\pi}}\exp\left[-\frac{\left[q+\lambda+\exp(-\Lambda\tau)\left(-\hbar\omega_L-\Delta G_{eg}-\lambda\right)\right]^2}{2\alpha^2(\tau)}\right]. \tag{8.24}$$

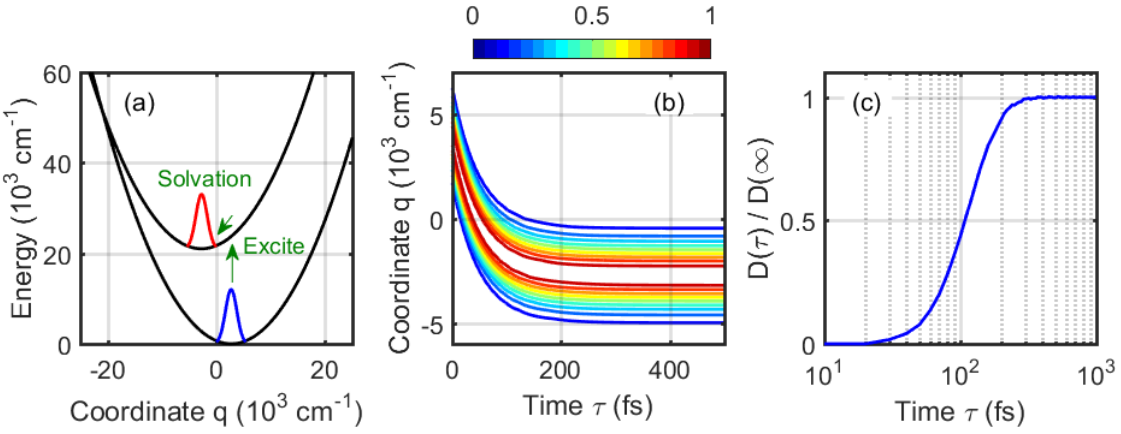

Figure 8.9: Physical picture suggested by theoretical model. (a) The pump pulse initiates a wavepacket in the collective 'solvent' coordinate, which approaches the point of intersection between potential energy surfaces as τ increases. Energy can be (linearly) mapped onto the collective coordinate for convenience. (b) Motion of the wavepacket, $Y(\tau,q)$, is simulated with Equation (8.24). (c) Growth in the magnitude of the doorway function with τ represents an increase in the probability of a back-electron transfer transition. Quantized vibrational modes must promote the transition deep within the inverted regime, because the excited state wavepacket possesses little overlap with the geometry of the transition state.

Ground state equilibrium and asymptotic ($Y(\tau\to\infty,q)$) probability distributions are overlaid on the potential energy surfaces in Figure 8.9a. The excited state wavepacket never possesses significant amplitude at the point of intersection at any time during the relaxation process in

Figure 8.9b, because $[Ti(cat)_3]^{2-}$ is deep within the inverted regime. Nonetheless, the transition probability can be large, because displaced intramolecular modes promote transitions across the 21020-cm^{-1} free energy gap. Motion of the wavepacket in the solvation coordinate is the key physical process responsible for the time-dependence of $D(\tau)$ (i.e., oscillations induced by the vibrational coherences are relatively weak).

The expression for the HGS signal component given in Equation (8.18) accounts for all four pathways in Figure 8.1. We begin by treating only the dominant 222-cm^{-1} mode explicitly to illustrate key points then present a more general multi-mode calculation. Doorway functions associated with the 6 lowest energy vibrational states are plotted in Figure 8.10 for three different population times, τ = 50, 200, and 2000 fs. The density matrix elements are shuffled to separate functions associated with different classes of transitions. Indices 1-6 correspond to populations with 0-5 vibrational quanta, where the number of quanta is the index minus 1. Indices 7-36 correspond to coherences. For the coherences, the indices are given by

$$i = s \cdot n + k - n + \beta, \quad \begin{cases} \beta = 0, & n < k \\ \beta = 1, & n > k \end{cases}, \tag{8.25}$$

and

$$i = s \cdot l + u - l + \beta, \quad \begin{cases} \beta = 0, & l < u \\ \beta = 1, & l > u \end{cases}, \tag{8.26}$$

where s is the number of states in the basis set (6 in Figure 8.10). With these rules, population-to-population transfer and coherence-to-coherence transitions appear in the lower left and upper right portions of the matrices in Figure 8.10 (white grid lines separate these classes of transitions). Population-to-coherence transitions appear in the lower right portion (and vice-versa

in the upper left). The pathways of interest in this work end in vibronic coherences, which are located on the right side of the vertical grid line.

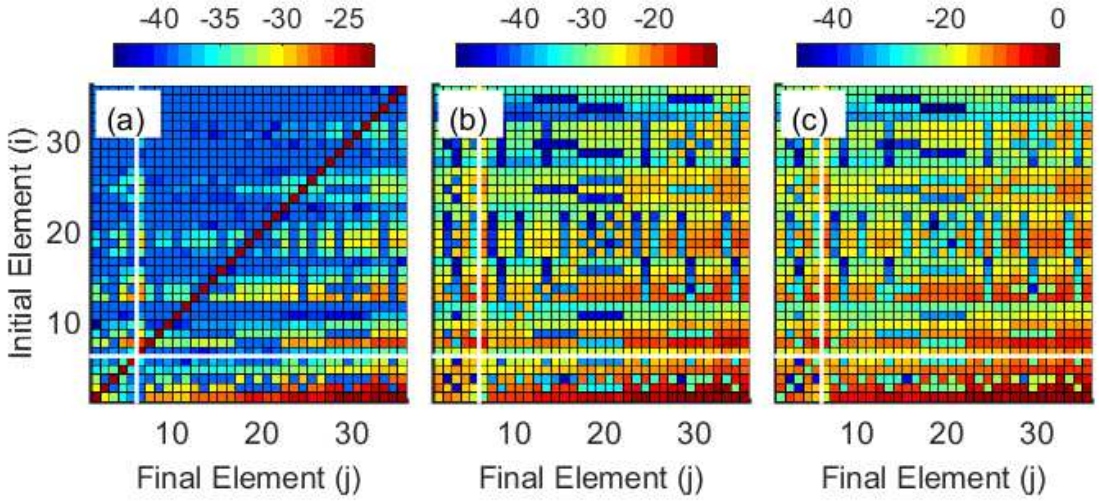

Figure 8.10: Doorway functions, $D_{i\to j}(\tau)$, are computed with Equation (8.20) and the parameters in Table 8.1. Only the 222-cm^{-1} mode is included in these calculations. The times, τ, are (a) 50 fs, (b) 200 fs, (c) 2000 fs. The calculations suggest that vibrational coherences are initiated in the ground electronic state following back-electron transfer if the system is initially in either a vibrational coherence (upper right) or population (lower right). Transitions become more favorable as the vibrational coherence frequency in t_3 approaches the free energy difference, ΔG_{eg} (see Figure 8.2). All plots are normalized to the maximum value of $D_{i\to j}(\tau)$ at 2 ps.

Magnitudes of the doorway functions $D_{i\to j}(\tau)$ are distributed in a fairly consistent way for all times in Figure 8.10. The calculations suggest that the population-to-coherence pathway is primarily responsible for the vibrational coherences in the HGS signal component (i.e., the largest magnitudes are found in the lower right portion of the plots). Moreover, the fastest population-to-coherence processes correspond to the lowest-energy vibrational population in the

excited state, i=1, and the largest value of the index, $j = 6$. For example, row i=1 (where $n = k$) corresponds to zero vibrational quanta, and column j=32-36 corresponds to a vibrational coherence in which state l represents the maximum of 5 vibrational quanta (see Figure 8.2). The fastest non-radiative transitions correspond to the lowest *overall* coherence frequencies in the t_3-interval between the two interactions with the donor-acceptor coupling in Figure 8.2. Such favorable overall coherence frequencies are found when the vibrational contribution, ω_{nl}, cancels the part associated with the free energy, ΔG_{eg}. The argument of the exponential in the doorway function is minimized when the coherence frequency is small, thereby increasing the overall probability of a transition (see $\Omega(\tau)$ in Equation (8.15)).

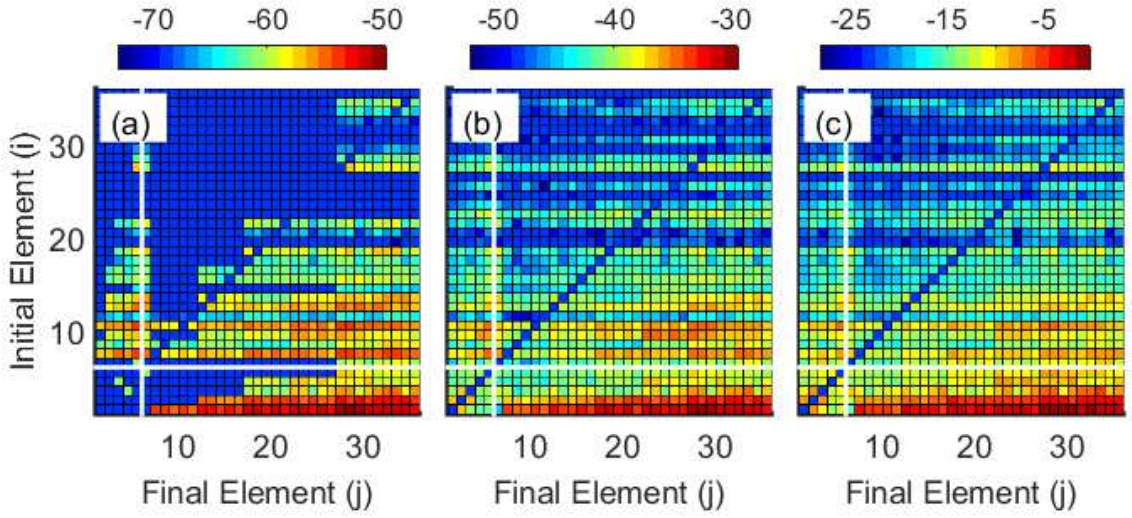

Figure 8.11: Doorway functions, $D_{i\to j}(\tau)$, are computed with Equation (8.20) and the parameters in Table 8.1. The 222, 538, 643, and 1481-cm^{-1} modes are included in these calculations. The times, τ , are (a) 50 fs, (b) 200 fs, and (c) 2000 fs. Indices associated with the multi-mode vibrational states are defined Table 8.2. The large magnitudes in the lower right portion of the plots suggest that vibrational coherences in the HGS transient absorption signal component primarily originate from the vibrational population-to-coherence pathway in Figure 8.1.

We next carry out calculations for a system with 4 vibrational modes to show that the insights derived from Figure 8.10 generalize to a multi-mode system. The 222, 538, 643, and 1481-cm^{-1} modes are included in the simulation. The three lower-frequency modes are required for comparisons to the transient absorption measurements (wavenumbers less than 1000 cm^{-1} can be detected with our time resolution). The 1481-cm^{-1} mode is included because of its impact on the overall transition probability (i.e., it is an effective promoting mode because of its higher frequency). Doorway functions for the 6 lowest energy basis states are plotted in Figure 8.11. The indices are assigned in order of increasing energy (see Table 8.2). As in Figure 8.10, indices 1-6 correspond to vibrational populations and indices 7-36 correspond to vibrational coherences.

The overall magnitudes of the doorway functions in Figure 8.11 increase with τ, which represents the approach of the wavepacket to the excited state equilibrium geometry (see Figure 8.9). At all times, the functions with the largest magnitudes are found in the lower right portions of the plots. A similar effect was demonstrated in Figure 8.10; however, the population-to-coherence pathway is even more prominent in the multi-mode system. The most probable transitions correspond to the lowest-energy populations ($n=k$ is small) and highest-frequency vibrational coherences, ω_{nl}. In other words, the rate of a population-to-coherence transition increases with the vibrational energy of the state with index, l; the rate also increases as the vibrational energy associated with the states represented by n and k decrease.

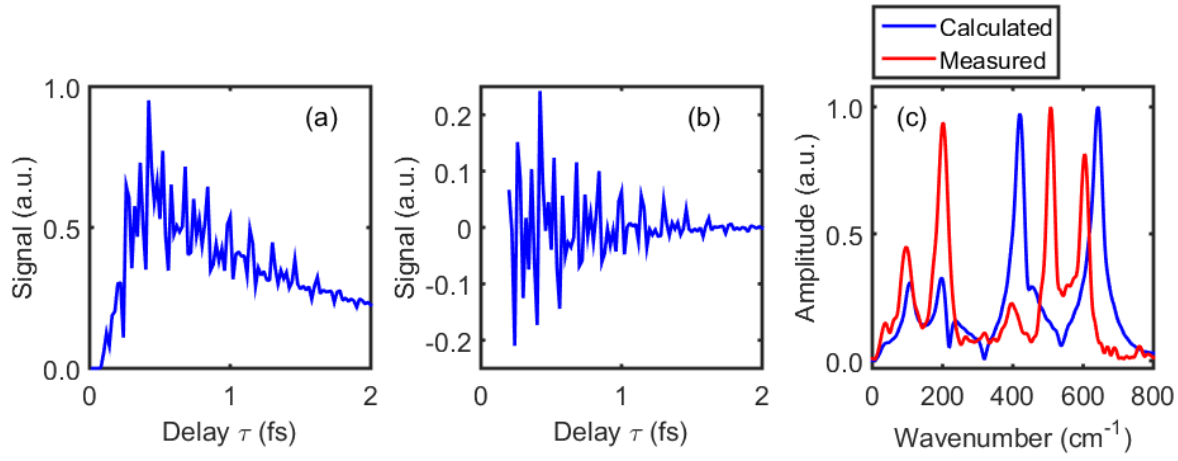

Figure 8.12: (a) Transient absorption signal calculated at 500 nm with Equation (8.18) and the parameters in Table 8.1. The calculations can be compared to the measurements in Figure 8.8. (b) The oscillatory part of the HGS signal component at 500 nm. (c) Fourier transformation of the signal in panel (b) yields the spectrum of vibrational coherences initiated by back-electron transfer. The calculated spectrum is overlaid with the measurement at 500 nm. Large differences in the calculated (505 and 610 cm^{-1}) and measured (538 and 643 cm^{-1}) resonance frequencies suggest that the two higher-frequency modes are highly populated following back-electron transfer. Discrepancies in the relative intensities of the higher frequency transitions may reflect an inability to extrapolate parameters determined with spontaneous resonance Raman spectroscopy to geometries outside of the Franck-Condon region of coordinate space.

The calculated transient absorption signal in Figure 8.12a possesses both coherent and incoherent components. The calculated signal can be compared to the measurement in Figure 8.8, where the detection wavelength is also 500 nm. The coherent part of the signal carries information about the BET mechanism, whereas the incoherent component represents vibrational cooling dynamics. The signal rises in the first 500 fs then decays due to the dynamic blue-shift in

the window function, $W_{luv}(\tau, \omega_{det})$, in Equation (8.17). The coherent response is separated from the total signal and Fourier transformed for comparison to the measured vibrational spectrum.

Relative intensities of the peaks calculated below 300 cm^{-1} agree fairly well with the measurement. The peak at 105 cm^{-1} corresponds to the difference between frequencies of the 538 and 643-cm^{-1} modes. The relative intensities of the calculated vibrational resonances deviate markedly from the measurement at higher frequencies. The resonance calculated near 400 cm^{-1} is significantly larger in the calculated spectrum. This peak has contributions from the 410-cm^{-1} mode, the overtone of the 222 cm^{-1} mode, and the difference frequency between the 643 and 222 cm^{-1} modes. It appears that the displacements of the 538 and 643-cm^{-1} modes determined by the resonance Raman analysis in section 8.4.A are respectively underestimated and overestimated with respect to the BET process. An inability to extrapolate parameters determined at the Franck-Condon geometry to other regions of coordinate space probably reflects anharmonicity, which is not included in the model. It should also be noted that the resonance Raman intensities primarily reflect the excited state potential energy gradient at the Franck-Condon geometry in room temperature solution, because the electronic dephasing time is shorter than the vibrational period.[35]

The vibrational frequencies carry the most readily interpreted information about the BET mechanisms. Significant deviation from the predictions of the harmonic model are found for modes above 300 cm^{-1}. Harmonic vibrational resonances are calculated at 538 and 643 cm^{-1}, whereas the transient absorption experiment yields peaks at 505 and 610 cm^{-1}. This discrepancy suggests that these two modes are highly excited following the BET process (i.e., anharmonicity is responsible for the frequency decrease). This behavior is consistent with the model calculations presented in Figures 8.10 and 8.11, where the fastest transitions are associated with

the maximum value of the index l (see Figure 8.2). Although its period cannot be resolved in our experimental setup, the 1481-cm^{-1} mode is also likely to promote the back-electron transfer process, because it is higher in frequency possesses a large displacement.

Table 8.2. Organization of Quantum Numbers for Multi-Mode Basis Set

State Index	222 cm^{-1}	538 cm^{-1}	643 cm^{-1}	1481 cm^{-1}
1	0	0	0	0
2	1	0	0	0
3	2	0	0	0
4	0	1	0	0
5	3	0	0	0
6	0	0	1	0

In summary, the calculations presented in this section have been used to investigate the two BET pathways that lead to vibrational coherences in the ground electronic state. The key conclusions drawn from these calculations are:

(i) The most dominant BET transitions involve high-frequency vibrational coherences, ω_{nl}, in the t_3-interval between perturbative interactions with the donor-acceptor coupling (see Figure 8.2).

(ii) The frequencies of promoting modes will generally deviate from the predictions of a harmonic model because they will be highly excited following BET.

(iii) A comparison of transient absorption experiments and model calculations suggests that the 538 and 643-cm^{-1} modes of $[Ti(cat)_3]^{2-}$ serve as promoting modes for BET.

(iv) For $[Ti(cat)_3]^{2-}$, model calculations based on empirical parameters suggest that the vibrational population-to-coherence pathway is more efficient than the vibrational coherence-to-coherence pathway.

8.5. Broader Implications for Electron Transfer Reactions

Coherent dynamics in which broadband laser pulses initiate vibrational coherences are not necessarily relevant to applications such as photoelectrochemical cells.[57,58] For example, the vibrational coherence-to-coherence pathway in Figure 8.1 requires impulsive excitation and is arguably irrelevant to processes initiated by sunlight. The vibrational population-to-coherence pathway differs from the vibrational coherence-to-coherence pathway in that impulsive excitation is not required. Moreover, according to the model presented in section 8.2, the population-to-coherence pathway may contribute even at times that are long compared to solvation and vibrational dephasing.

The potential implications of this work are more clearly seen if the doorway function is rewritten as a fourth-order rate function.[29,30,57] In fact, the derivation of the doorway function in section 8.2.B parallels the derivation of the fourth-order rate function for electron transfer presented in earlier work.[29] The fourth-order rate function can written as

$$K^{(4)}_{nk\to ul}(\tau)=\left(\frac{\hbar w_L^2\sqrt{2\left(\Delta^2+w_L^2\right)}}{\pi\left|\xi_L\mu_{eg}\right|^2}\right)\cdot D_{nk\to ul}(\tau)\ , \tag{8.27}$$

if the normalization condition of Reference [29] is applied. The normalization condition ensures convergence to Marcus' equation at times that are long compared to the solvation time for models with weak vibronic couplings. When τ becomes longer than solvation and vibrational dephasing, the fourth-order rate function becomes

$$K_{nn\to ul}^{(4)}\left(\tau\to\infty\right)=\frac{\pi^{1/2}\left|V_{eg}\right|^2}{\hbar\sqrt{\lambda k_B T}}B_m\left\langle n\middle|m\right\rangle\left\langle n\middle|m\right\rangle\left\langle n\middle|u\right\rangle\left\langle n\middle|l\right\rangle \times\exp\left[-\frac{\hbar^2\left(\omega_L-\omega_{eg}\right)^2}{4\lambda k_B T}\right]\exp\left[-\frac{\Delta G_{eg}^0+\lambda-\hbar\omega_{nl}}{4\lambda k_B T}\right], \tag{8.28}$$

where the only surviving terms are those in which $n=k$. In other words, the coherence-to-coherence pathway, $nk\to ul$, vanishes when τ is large but the population-to-coherence pathway, $nn\to ul$, survives.

This idea can be taken a step further if we let the system establish a Boltzmann distribution of vibrational populations in the excited state before BET. In our notation, the traditional second-order (population-to-population) expression for the BET process can written as[16]

$$K_{nn\to mm}^{(2)}=\frac{\pi^{1/2}\left|V_{eg}\right|^2}{\hbar\sqrt{\lambda k_B T}}\sum_{nm}B_m\left|\left\langle n\middle|m\right\rangle\right|^2\exp\left[\frac{-\left(\Delta G+\lambda-\hbar\omega_{nm}\right)^2}{4\lambda k_B T}\right], \tag{8.29}$$

Vibrational coherences are not initiated by BET at this level of theory, because the coherences do not survive the trace over all quantum states taken in the evaluation of the correlation function.[14] We question whether or not elimination of the population-to-coherence pathway is justified in Equation (8.29). Restoration of a Boltzmann distribution of vibrational quanta occurs rapidly following BET-induced vibrational coherence because of intramolecular vibrational cooling and solute-to-solvent vibrational energy transfer. These processes generally occur on a time scale comparable to picosecond vibrational dephasing in solution. Thus, the sequence of BET and vibrational cooling could be described as a higher-order perturbative process. For example, in a third-order description, the two donor-acceptor interactions associated with BET could be followed by one perturbative interaction with a component of the Hamiltonian associated with

solute-solvent interactions, thereby producing a population that survive the trace over quantum states (see Figure 8.13).

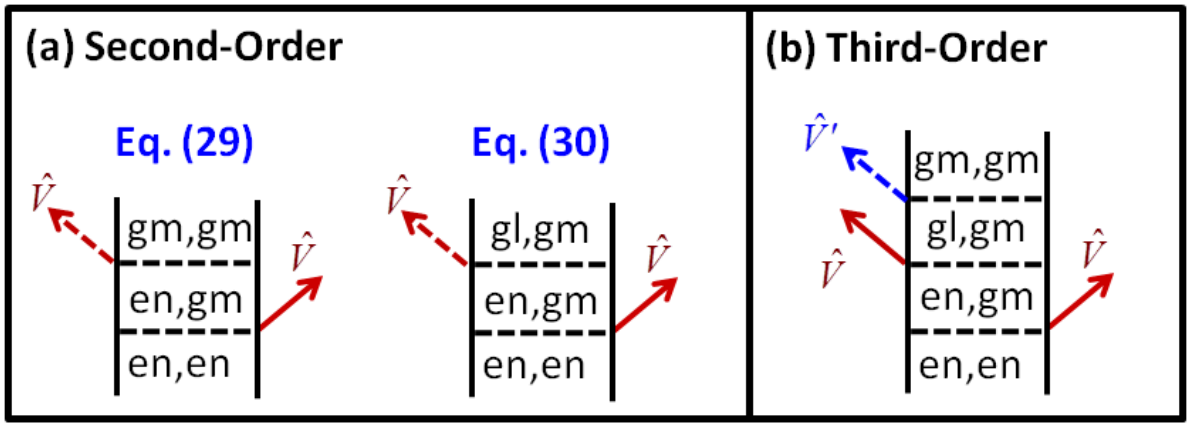

Figure 8.13: We consider whether or not population-to-coherence pathways are relevant in systems regardless of the electron transfer time-scale. (a) Only population-to-population transitions occur in the traditional second order rate formula, Equation (8.29). The population-to-coherence pathway survives if the trace is taken only over electronic states in Equation (8.30). (b) In a higher-order model, a trace over all quantum states can be carried out if subsequent vibrational cooling dynamics are accounted for. Vibrational population-to-coherence transitions may then contribute regardless of the electron transfer rate. The operators $\hat{V}$ and $\hat{V}'$ denote the donor-acceptor coupling and the solute-solvent interaction, respectively.

Because a detailed description of vibrational cooling dynamics is beyond the scope of this work, we suggest that it is instructive to simply take the trace over the electronic states in writing an *ad hoc* second-order rate formula for BET processes that begin with an equilibrium condition. Equation (8.29) can be rewritten as

$$K^{(2)}_{nn\to lm} = \frac{\pi^{1/2}\left|V_{eg}\right|^2}{\hbar\sqrt{\lambda k_B T}} \sum_{mnl} B_n \langle n|m\rangle\langle n|l\rangle \exp\left[\frac{-\left(\Delta G + \lambda - \hbar\omega_{nm}\right)^2}{4\lambda k_B T}\right], \tag{8.30}$$

if we let the transition terminate in a vibrational coherence. Feynman diagrams associated with Equations (8.29) and (8.30) are given in Figure 8.13a. The diagrams take only the interactions with the donor-acceptor coupling into account. The larger number of pathways found in $K^{(2)}_{nn\rightarrow lm}$ will generally enhance the overall rate. For example, the ratio, $K^{(2)}_{nn\rightarrow lm} / K^{(2)}_{nn\rightarrow mm}$, is equal to 25 for a system with the 4 modes accounted for in Figures 8.12-8.13 when the summation are taken over the 20 lowest energy states. This ratio will become even larger when additional intramolecular modes are taken into account. The problem of ending the $K^{(2)}_{nn\rightarrow lm}$ pathway in Figure 8.13a in vibrational coherence can be remedied by incorporating the perturbative part of the Hamiltonian that induces vibrational cooling (see Figure 8.13b). Only one additional interaction is required to convert the system from a coherence to a population. Thus, a third-order rate function can be developed to describe this type of process.

8.6. Concluding Remarks

In summary, optical spectroscopies and model calculations have been used to investigate contributions of non-equilibrium BET pathways in the transition metal complex, $[Ti(cat)_3]^{2-}$. Parameters obtained with a resonance Raman spectral fitting procedure were used to simulate transient absorption signals associated with BET. The model suggests that both vibrational population-to-coherence and vibrational coherence-to coherence pathways make significant contributions, although the population-to-coherence pathway is slightly more favorable. For both mechanisms, the most dominant BET transitions involve the highest frequency vibrational coherences, ω_{nl}, in the t_3-interval between interactions with the donor-acceptor coupling (see Figure 8.2). We conclude that the 538 and 643-cm^{-1} modes serve as promoting modes based on their highly populated states following BET. Higher-frequency modes may be even more

effective in promoting BET, because larger coherence frequencies, ω_{nl}, can be produced with smaller quantum numbers; however, mode frequencies above 1000 cm^{-1} cannot be resolved with our apparatus. For this reason, experiments carried out with shorter pulses could provide more details about the BET mechanism.

The broader implication of this work is that contributions from the coherent pathways in Figure 8.1 are generally not negligible if electron transfer is faster than solvation and vibrational dephasing. Such sub-picosecond electron transfer processes are fairly common at molecule-semiconductor interfaces in photoelectrochemical cells. [57,58] Therefore, a better understanding of these pathways will be useful for interpreting ultrafast spectroscopy measurements in these systems.[11,57,59-62] In this work, parameters derived from spontaneous Raman experiments were used to simulate transient absorption signals; however, this parameterization scheme may fail in systems that undergo large excited state geometry changes. The femtosecond stimulated Raman scattering method[63,64] or two-dimensional vibrational-electronic spectroscopy[65,66] may be used to obtain parameters associated with nonequilibrium geometries in such systems. It will also be helpful to integrate molecular dynamics simulations into the description.

We question whether or not the population-to-coherence pathway is relevant to electron transfer processes regardless of their time scales. Observations based on ultrafast spectroscopies are limited to BET dynamics that are faster than vibrational dephasing, because vibrational motions can only be detected if a macroscopic coherence is produced. However, it will be interesting to consider the relevance of vibrational coherences initiated from quasi-equilibrium initial conditions as suggested by Equation (8.30). These pathways do not survive the trace over electronic and vibrational quantum states at second-order in perturbation theory but can contribute in higher-order descriptions that take vibrational cooling processes into account.

8.7 REFERENCES

(1) Vos, M. H.; Lambry, J.-C.; Robles, S. J.; Youvan, D. C.; Breton, J.; Martin, J.-L. *Proc. Natl. Acad. Sci.* **1991**, *88*, 8885.

(2) Vos, M. H.; Rappaport, F.; Lambry, J.-C.; Breton, J.; Martin, J.-L. *Nature* **1993**, *363*, 320.

(3) Peteanu, L. A.; Schoenlein, R. W.; Wang, H.; Mathies, R. A.; Shank, C. V. *Proc. Natl. Acad. Sci.* **1993**, *90*, 11762.

(4) Banin, U.; Kosloff, R.; Ruhman, S. *Isr. J. Chem.* **1993**, *33*, 141.

(5) Zhu, L.; Sage, J. T.; Champion, P. M. *Science* **1994**, *266*, 629.

(6) Wynne, K.; Reid, G. D.; Hochstrasser, R. M. *J. Chem. Phys.* **1996**, *105*, 2287.

(7) Spörlein, S.; Zinth, W.; Wachtveitl, J. *J. Phys. Chem. B* **1998**, *102*, 7492.

(8) Arnett, D. C.; Moser, C. C.; Dutton, P. L.; Scherer, N. F. *J. Phys. Chem. B* **1999**, *103*, 2014.

(9) Fuller, F. D.; Pan, J.; Gelzinis, A.; Butkus, V.; Senlik, S. S.; Wilcox, D. E.; Yocum, C. F.; Valkunas, L.; Abramavicius, D.; Ogilvie, J. P. *Nat. Chem.* **2014**, *6*, 706.

(10) Song, Y.; Clafton, S. N.; Pensack, R. D.; Kee, T. W.; Scholes, G. D. *Nat. Commun.* **2014**, *5*, 4933.

(11) Tisdale, W. A.; Williams, K. J.; Timp, B. A.; Norris, D. J.; Aydil, E. S.; Zhu, X.-Y. *Science* **2010**, *328*, 1543.

(12) Huber, R.; Dworak, L.; Moser, J. E.; Grätzel, J.; Wachtveitl, J. *J. Phys. Chem. C* **2016**, DOI: 10.1021/acs.jpcc.6b02012.

(13) Mukamel, S. *Principles of Nonlinear Optical Spectroscopy*; Oxford University Press: New York, 1995.

(14) Nitzan, A. *Chemical Dynamics in Condensed Phases*; Oxford University Press: Oxford, 2006.

(15) Valkunas, L.; Abramavicius, D.; Mančal, T. *Molecular Excitation Dynamics and Relaxation: Quantum Theory and Spectroscopy* Wiley-VCH: Weinheim, 2013.

(16) Barbara, P. F.; Meyer, T. J.; Ratner, M. A. *J. Phys. Chem.* **1996**, *100*, 13148.

(17) Bixon, M.; Jortner, J. *J. Chem. Phys.* **1997**, *107*, 1470.

(18) Clarke, T. M.; Durrant, J. R. *Chem. Rev.* **2010**, *110*, 6736.

(19) Ross, R. T.; Nozik, A. J. *J. Appl. Phys.* **1982**, *53*, 3813.

(20) Jin, X.; Li, Y.; Chen, Z.; Wei, T.-H.; He, X.; Sun, W. *Sci. Rep.* **2014**, *4*, 5983.

(21) Li, L.; Kanai, Y. *J. Phys. Chem. Lett.* **2016**, *7*, 1495.

(22) Borgias, B. A.; Cooper, S. R.; Koh, Y. B.; Raymond, K. N. *Inorg. Chem.* **1984**, *23*, 1009.

(23) Wang, Y.; Hang, K.; Anderson, N. A.; Lian, T. *J. Phys. Chem. B* **2003**, *107*, 9434.

(24) Hush, N. S. *Electrochimica Acta.* **1968**, *13*, 1005.

(25) Yan, Y. J.; Sparpaglione, M.; Mukamel, S. *J. Phys. Chem.* **1988**, *92*, 4842.

(26) Britt, B. M.; McHale, J. L.; Friedrich, D. M. *J. Phys. Chem.* **1995**, *99*, 6347.

(27) Kelley, A. M. *J. Phys. Chem. A* **1999**, *103*, 6891.

(28) Jean, J. M.; Fleming, G. R. *J. Chem. Phys.* **1995**, *103*, 2092.

(29) Lesheng, L.; Giokas, P. G.; Kanai, Y.; Moran, A. M. *J. Chem. Phys.* **2014**, *140*, 234109.

(30) Molesky, B. P.; Moran, A. M. *J. Phys. Chem. A* **2013**, *117*, 13954.

(31) Horng, M. L.; Gardecki, J. A.; Papazyan, A.; Maroncelli, M. *J. Phys. Chem.* **1995**, *99*, 17311.

(32) Myers, A. B.; Mathies, R. A.; Tannor, D. J.; Heller, E. J. *J. Chem. Phys.* **1982**, *77*, 3857.

(33) Kwac, K.; Cho, M. *J. Phys. Chem. A* **2003**, *107*, 5903.

(34) Myers, A. B.; Mathies, R. A. Resonance Raman intensities: a probe of excited state structures and dynamics. In *Biological Applications of Raman Spectroscopy*; Spiro, T. G., Ed.; Wiley: New York, 1987; Vol. 2; pp 1.

(35) Myers, A. B. Excited Electronic State Properties From Ground-State Resonance Raman Intensities. In *Laser Techniques in Chemistry*; Myers, A. B., Rizzo, T. R., Eds.; John Wiley & Sons: New York, 1995; Vol. 23; pp 325.

(36) Damraurer, N. H.; Cerullo, G.; Yeh, A.; Boussie, T. R.; Shank, C. V.; McCusker, J. K. *Science* **1997**, *275*, 54.

(37) Yeh, A.; Shank, C. V.; McCusker, J. K. *Science* **2000**, *289*, 935.

(38) Shaw, G. B.; Brown, C. L.; Papanikolas, J. M. *J. Phys. Chem. A* **2002**, *106*, 1483.

(39) Stark, C. W.; Schreier, W. J.; Lucon, J.; Edwards, E.; Douglas, T.; Kohler, B. *J. Phys. Chem. A* **2015**, *119*, 4813.

(40) Davydov, A. *Theory of Molecular Excitons*; Plenum: New York, 1971.

(41) van Amerongen, H.; Valkunas, L.; van Grondelle, R. *Photosynthetic Excitons*; World Scientific: Singapore, 2000.

(42) Spano, F. C. *Annu. Rev. Phys. Chem.* **2006**, *57*, 217.

(43) Abramavicius, D.; Palmieri, B.; Voronine, D. V.; Sanda, F.; Mukamel, S. *Chem. Rev.* **2009**, *109*, 2350.

(44) Miller, S. A.; Moran, A. M. *J. Phys. Chem. A* **2010**, *114*, 2117.

(45) Albert, V. V.; Badaeva, E.; Kilina, S.; Sykora, M.; S., T. *J. Lumin.* **2011**, *131*, 1739.

(46) Moran, A. M.; Delbecque, C. *J. Phys. Chem. A* **2001**, *105*, 10208.

(47) Moran, A. M.; Kelley, A. M. *J. Chem. Phys.* **2001**, *115*, 912.

(48) Shriver, D. F.; Dunn, J. B. R. *Appl. Spectrosc.* **1974**, *28*, 319.

(49) Dudik, J. M.; Johnson, C. R.; Asher, S. A. *J. Chem. Phys.* **1985**, *82*, 1732.

(50) Frisch, M. J.; Trucks, G. W.; Schlegel, H. B.; Scuseria, G. E.; Robb, M. A.; Cheeseman, J. R.; Scalmani, G.; Barone, V.; Mennucci, B.; Petersson, G. A.; Nakatsuji, H.; Caricato, M.; Li, X.; Hratchian, H. P.; Izmaylov, A. F.; Bloino, J.; Zheng, G.; Sonnenberg, J. L.; Hada, M.; Ehara, M.; Toyota, K.; Fukuda, R.; Hasegawa, J.; Ishida, M.; Nakajima, T.; Honda, Y.; Kitao, O.; Nakai, H.; Vreven, T.; Montgomery, J. A., Jr.; Peralta, J. E.; Ogliaro, F.; Bearpark, M.; Heyd, J. J.; Brothers, E.; Kudin, K. N.; Staroverov, V. N.; Kobayashi, R.; Normand, J.; Raghavachari, K.; Rendell, A.; Burant, J. C.; Iyengar, S. S.; Tomasi, J.; Cossi, M.; Rega, N.; Millam, J. M.; Klene, M.; Knox, J. E.; Cross, J. B.; Bakken, V.; Adamo, C.; Jaramillo, J.; Gomperts, R.; Stratmann, R. E.; Yazyev, O.; Austin, A. J.; Cammi, R.; Pomelli, C.; Ochterski, J. W.; Martin, R. L.; Morokuma, K.; Zakrzewski, V. G.; Voth, G. A.; Salvador, P.; Dannenberg, J. J.; Dapprich, S.; Daniels, A. D.; Farkas, Ö.; Foresman, J. B.; Ortiz, J. V.; Cioslowski, J.; Fox, D. J. Gaussian 09 Wallingford,CT, 2009.

(51) Lilichenko, M.; Kelley, A. M. *J. Chem. Phys.* **2001**, *114*, 7094.

(52) Pecourt, J.-M.; Peon, J.; Kohler, B. *J. Am. Chem. Soc.* **2001**, *123*, 10370.

(53) Kovalenko, S. A.; Schanz, R.; Hennig, H.; Ernsting, N. P. *J. Chem. Phys.* **2001**, *115*, 3256.

(54) Champion, P. M.; Rosca, F.; Ionascu, D.; Cao, W.; Ye, X. *Faraday. Discuss.* **2004**, *127*, 123.

(55) Vöhringer, P.; Scherer, N. F. *J. Phys. Chem.* **1995**, *99*, 2684.

(56) Womick, J. M.; West, B. A.; Scherer, N. F.; Moran, A. M. *J. Phys. B.* **2012**, *45*, 154016.

(57) Ardo, S.; Meyer, G. J. *Chem. Soc. Rev.* **2009**, *38*, 115.

(58) Concepcion, J. J.; Jurss, J.; Brennaman, M. K.; Hoertz, P. G.; Patrocinio, A. O. T.; Iha, N. Y. M.; Templeton, J. L.; Meyer, T. J. *Acc. Chem. Res.* **2009**, *42*, 1954.

(59) Zimmerman, C.; Willig, F.; Ramakrishna, S.; Burnfeindt, B.; Pettinger, B.; Eichberger, R.; Storck, W. *J. Phys. Chem. B* **2001**, *105*, 9425.

(60) Asbury, J. B.; Hao, E.; Wang, Y.; Ghosh, H. N.; Lian, T. *J. Phys. Chem. B* **2001**, *105*, 4545.

(61) Anderson, N. A.; Lian, T. *Annu. Rev. Phys. Chem.* **2005**, *56*, 491.

(62) Duncan, W. R.; Prezhdo, O. V. *Annu. Rev. Phys. Chem.* **2007**, *58*, 143.

(63) McCamant, D. W.; Kukura, P.; Yoon, S.; Mathies, R. A. *Rev. Sci. Instrum.* **2004**, *75*, 4971.

(64) Kukura, P.; McCamant, D. W.; Mathies, R. A. *Annu. Rev. Phys. Chem.* **2007**, *58*, 461.

(65) Oliver, T. A. A.; Lewis, N. H. C.; Fleming, G. R. *Proc. Natl. Acad. Sci.* **2014**, *111*, 10061.

(66) Courtney, T. L.; Fox, Z. W.; Estergreen, L.; Khalil, M. *J. Phys. Chem. Lett.* **2015**, *6*, 1286.

CHAPTER 9: CONCLUDING REMARKS

The studies presented in this dissertation have explored the fundamental nature of electron transfer at molecule semiconductor interfaces using ultrafast laser spectroscopies. Specifically, the investigations are focused on uncovering the impact of molecular structure and nuclear geometry on relaxation rates in chromophore-nanoparticle systems. The insight gained into the dynamics at these interfaces is applicable to the design and of DSPEC devices. Chapter 2 introduced the scientific models which are needed to discuss the underlying physical and chemical processes in electron transfer systems. Chapter 3 described the ultrafast spectroscopic techniques used to investigate the interfacial dynamics in condensed phase systems. Together, these two chapters provide the framework and context necessary to appreciate the scientific impact of the research contained in the dissertation.

The first experimental study of the dissertation is found in Chapter 4. Several physical insights into molecule-TiO_2 interfaces were uncovered by applying TA and resonance Raman spectroscopies to films sensitized by a series of closely- related ruthenium chromophores. Connections were drawn between thermal fluctuations in the solvated systems and the occurrence of MLCT and ILET processes in the bipyridyl chromophores. Additionally, the Raman excitation profiles suggested a relatively small degree of charge transfer character in the complexes, which impacted the understanding of nuclear coherences measured in these systems. However, injection from a subset of the chromophores was demonstrated to be occurring on a timescale shorter than nuclear relaxation.

The above findings prompted further investigation into the geometry of the chromophore attachment to the semiconductor surface. Polarized resonance Raman spectroscopy measurements have showed the binding geometries of the ruthenium chromophores studied in Chapter 4 were not well-ordered on single crystal TiO_2, though there was an observed preferential orientation of the molecule. This finding supported modeling the interface as a distribution of molecule-semiconductor couplings which is supported by experiments measuring a distribution in electron transfer rates.

More recently, device design has led to protection of the phosphonate anchoring groups on TiO_2 by the deposition of several layers of alumina in order to prevent desorption at higher pH conditions. These additional layers of semiconductor would likely lead to a narrower distribution in the tilt angle of the chromophore, as sterics could force the chromophore to adopt a geometry more normal to the surface. The effects of such a constrained geometry on the electron transfer dynamics are unknown. Additionally, it would be important to determine if the decreased distance between the bipyridine ligand and the surface results in other changes, such as increased rate of BET. If such a change is observed, modifications to the linker such as the methylene spacers studied here might preserve acceptable BET timescales as well as increased stability of the chromophore attachment.

The sixth chapter details the development of a rate function used to model electron transfer processes in donor acceptor systems which experience electron transfer from nonequilibrium donor states. Such a model is important particularly for systems which undergo ultrafast electron transfer as is desirable in a high-efficiency DSPEC. The parameters of the rate function can be obtained from conventional spectroscopies, which makes it convenient for application to ultrafast nonlinear optical measurements. The extent to which traditional second-

order rate models underestimate electron transfer efficiency when the energy of the molecular excited state is below the conduction band edge of the semiconductor is also quantified by the analysis. This insight underscores the potential power of combining state-of-the-art first-principles methods and phenomenological models.

Demonstrating the need for a nonequilibrium electron transfer model is an investigation of catechol sensitized TiO_2 nanoparticles found in Chapter 7. A related study of a molecular charge transfer system, $[Ti(cat)_3]^{2-}$, is found in Chapter 8. The strongly coupled charge transfer systems exhibit BET to the donor ligand on the picosecond timescale, having undergone electron transfer well before nuclear relaxation. Multiple spectroscopic techniques were used to characterize the relaxation as a transfer of population between different states on the donor-acceptor surfaces. Additionally, transient grating spectroscopy measurements paired with six-wave background free FSRS geometry indicate energy transfer to solvent specific vibrational modes. The molecular catechol complex provides new insights into relaxation pathways of vibrational motion induced by light absorption.

The catechol sensitized TiO_2 nanoparticle system involves a degree of delocalized charge between the conjugated ring system on the ligand and the metal atom. It is likely that the Ti-O and O-C bonds between these moieties play a role in the electron transfer mechanism. Replacing the catechol molecule with 1,2 benzenedithiol would replace the oxygen atoms in these bonds with sulfur, which could prove useful in quantifying the involvement of these bonds by altering their vibrational frequencies as well as the charge distribution of the system. Alternately, TiS_2 nanoparticles synthesized in a similar fashion to the TiO_2 nanoparticles used here to alter the semiconductor state energies. A corresponding molecular complex would provide a useful point of comparison to such work.

In summary, the work presented here investigates several electronic and vibrational phenomena impacting ultrafast electron transfer dynamics in molecule-semiconductor systems. Properties explored include donor –acceptor coupling , molecular geometry, vibrational reorganization energy, thermal energy transfer to solvent, and semiconductor acceptor state overlap. The findings demonstrate that properties measured by conventional spectroscopic techniques are useful for interpreting complex ultrafast electron transfer dynamics. Additionally, traditional second-order electron transfer models such as Marcus theory are insufficient to accurately describe the behavior at interfaces in which electron transfer occurs from predominantly nonequilibrium nuclear geometries, including widely utilized transition metal chromophore systems.

APPENDIX A: SUPPLEMENT TO "SPECTROSCOPY AND DYNAMICS OF PHOSPHONATE-DERIVITIZED RUTHENIUM COMPLEXES ON TIO_2"

A.1. Spectral broadening of 400 nm laser pulses in a hollow-core fiber

In this Section, we describe an apparatus used to spectrally broaden 150fs, 400nm pulses derived from an amplified Ti:Sapphire laser system. The hollow-core fiber setup is shown in Figure A.1.

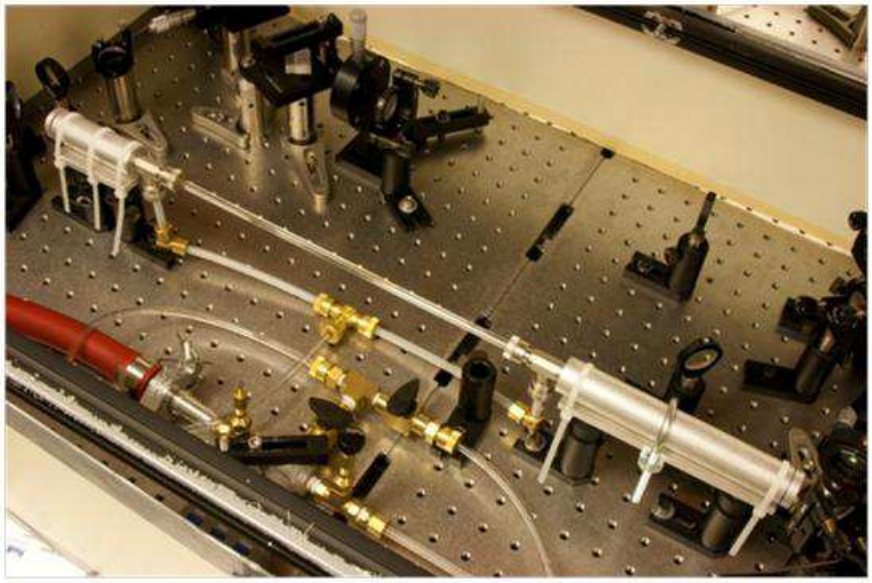

Figure A.1: Hollow core fiber setup used to generate 35-55fs, 400nm laser pulses used in the transient absorption experiments.

In this setup, 400nm pulses with 40μJ energies and FWHM bandwidths of 160cm^{-1} are focused into a 75μm diameter fiber filled with argon gas at a pressure of 1.7atm. Spectral broadening is induced by self-phase modulation in the argon medium. Figure S2 presents spectra measured at the entrance and exit of the hollow-core fiber. The pulses emerging from the fiber possess 10μJ energies and FWHM bandwidths of 800-1000cm^{-1}. A fused silica prism compressor with a tip-to-tip prism separation of 79cm compensates for dispersion accumulated

in transmissive optics between the hollow-core fiber and the sample. The compressed pulse durations range from 35-55fs.

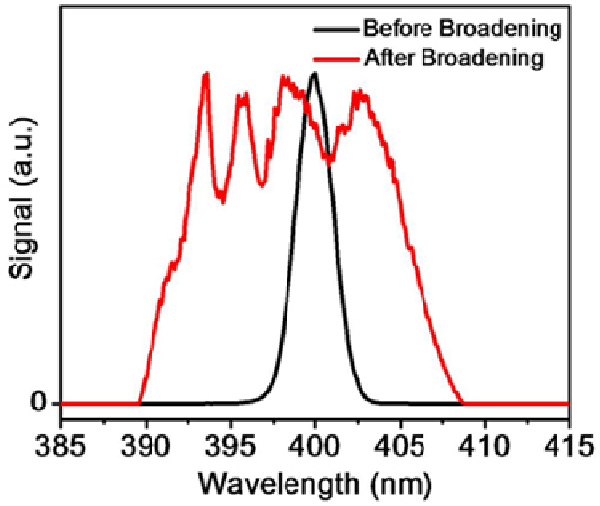

Figure A.2: Spectra of 400 nm pulses measured at the entrance (black) and exit (red) of the hollow-core fiber.

A.2. Sample holder for dye-sensitized TiO_2 films

TA experiments involving dye-sensitized films were conducted with the samples immersed in solutions. The presence of the solution enables the quenching of long lived photoexcitations (in the $[(Ru(bpy)_2(4,4'\text{-}(PO_3H_2)_2bpy)]^{2+}$ experiments) in addition to suppressing sample degradation by dissipating thermal energy from the film surface. In this Section, we describe a homemade cuvette used to immerse the samples in solutions during the TA experiments. As shown in Figure S3, two metallic washers (~1 mm thick) are sandwiched between two 3x1" (~1mm thick) borosilicate microscope slides. Both washers are situated at the ends of the glass slides in order to leave empty space for the sample between them. Initially, the slides are held together with binder clips. In order to create a water tight cavity for the sample,

the bottom and sides of the two microscope slides are bonded together with waterproof epoxy and left to set overnight. After the epoxy cures, the binder clips are removed and the sample holder is ready for use.

Figure A.3: Homemade cuvette used to contain dye-sensitized films during transient absorption experiments.

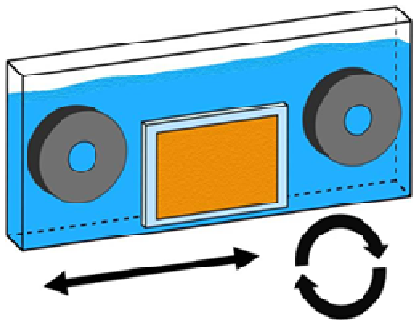

Figure A.4: Sample films are held in a homemade cuvette and oscillated in the plane of the film with a linear actuator to suppress sample degradation. A motor simultaneously translates the sample in a circular path.

When performing TA experiments, we insert the microscope slide covered with the dye sensitized TiO_2 film into the homemade cuvette; the cuvette is also filled with the appropriate solution. The thickness of the washers is such that the spacing between the two glass surfaces is just thick enough for the microscope slide to fit snugly. Throughout the experiment, the entire

sample container is oscillated with a linear actuator and a rotating motor. The result is a series of circular paths which are displaced linearly across the face of the sample, thereby minimizing the number of shots incident on any particular spot.

A.3. Solvent and pH dependence of Raman spectra

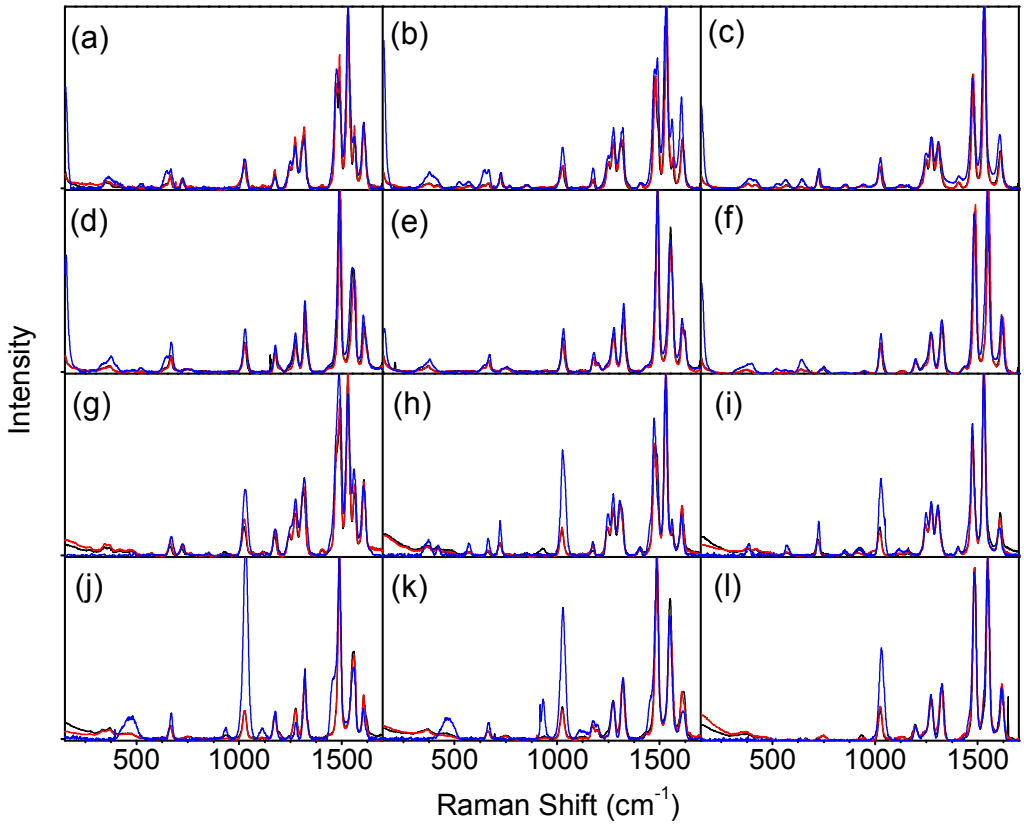

Figure A.5: (a)-(f):Raman Spectra of dye-sensitized films under methanol (blue,) water (red,) and 0.1M $HClO_4$ in water (black.) (g)-(l): Raman Spectra of samples in solutions (not films) of methanol (blue,) water (red,) and 0.1M $HClO_4$ in water (black.) Complex **1** is shown in (a),(g). Complex **2** is shown in (b),(h). Complex **3** is shown in (c),(i). Complex **1C** is shown in (d),(j). Complex **2C** is shown in (e),(k). Complex **3C** is shown in (f),(l). All spectra have been normalized to the most intense peak.

Figure A.5 shows that, in general, the Raman spectra of all six molecules are weakly sensitive to the solvent and pH. The 1030 cm^{-1} resonance is an exception. Some notable exceptions are discussed in Chapter 4. The spectra measured at pH 1 and pH 7 in aqueous solutions are nearly identical. However, sensitivity of the phosphonate moiety to pH may be anticipated based on its pK_a. We observe carbon-phosphorous stretching motions in the spectra, but see no evidence of the hydrogen-phosphorous or oxygen-phosphorous vibrations.

A.4. Fitting Linear Absorbance Spectra and Resonance Raman Cross Sections

Table A.1. Complete set of Resonance Raman fitting parameters for all complexes in methanol.

Sample	1	2	3	1C	2C	3C
Inhomog. width (cm^{-1})	1180	1200	1370	1220	1525	1600
Electronic origin (cm^{-1})	21800	21690	21400	20930	21790	21040
Homog. width (cm^{-1})	870	935	923	1000	940	970
Transition Length (Å)	1.02	1.4	1.43	1.3	1.43	1.35
Shift (cm^{-1})	Δ, λ(cm^{-1})	Δ, λ(cm^{-1})	Δ, λ(cm^{-1})	Δ, λ(cm^{-1})	Δ, λ(cm^{-1})	Δ, λ(cm^{-1})
377	--	0.14, 3.44	0.12, 2.71	--	--	--
421	--	0.07, 0.94	0.09, 1.57	--	0.20, 8.00	--
571	--	0.06, 1.10	0.11, 3.45	--	--	--
667	0.09, 2.41	0.06, 1.18	0.05, 0.77	0.16, 8.92	0.07, 1.54	--
724	0.06, 1.16	0.08, 2.26	0.07, 1.96	--	--	--
853	--	--	0.02, 0.14	--	--	--
929	--	--	0.06, 1.84	0.09, 4.00	0.11, 5.12	--
1030	0.06, 1.67	0.03, 0.53	0.05, 1.16	--	--	--
1119	--	--	0.13, 9.68	0.10, 5.16	0.07, 2.98	--
1172	0.08, 3.66	0.05, 1.19	0.13, 9.90	0.12, 8.72	0.06, 1.97	--
1198	--	--	0.16, 15.72	--	0.06, 2.35	0.09, 4.33
1248	0.08, 3.99	0.09, 4.99	0.06, 2.25	--	--	--
1274	0.12, 9.63	0.11, 7.05	0.17, 19.06	0.08, 3.99	0.10, 5.75	0.16, 16.10
1316	0.15, 15.71	0.13, 11.71	--	0.18, 20.62	0.12, 9.96	0.17, 18.80
1404	0.02, 0.2	0.04, 1.08	0.06, 2.53	--	--	--
1473	0.21, 32.16	0.07, 3.61	--	--	--	--
1485	--	0.15, 15.74	--	0.28, 59.86	0.12, 10.87	0.19, 26.53
1529	0.19, 26.17	0.18, 25.43	0.26, 51.68	--	--	--
1554	0.13, 13.44	0.09, 6.02	--	0.23, 40.75	0.19, 27.32	0.29, 65.35
1608	0.12, 11.56	0.09, 6.46	0.11, 10.45	0.12, 11.39	0.10, 7.88	0.17, 22.97

Table A.2. Complete set of Resonance Raman fitting parameters for all complexes on TiO_2 films

Sample	1	2	3	1C	2C	3C
Inhomog. width (cm^{-1})	2390	2070	2050	1700	1580	2150
Electronic origin (cm^{-1})	21800	22170	21835	22050	21850	21090
Homog. width (cm^{-1})	640	400	430	270	600	410
Transition Length (Å)	0.97	1.29	1.29	1.22	1.253	1.113
Shift (cm^{-1})	Δ, λ(cm^{-1})	Δ, λ(cm^{-1})	Δ, λ(cm^{-1})	Δ, λ(cm^{-1})	Δ, λ(cm^{-1})	Δ, λ(cm^{-1})
281	--	0.03, 0.15	--	--	--	--
340	--	--	--	--	--	0.07, 0.88
364	--	--	--	--	0.09, 1.57	--
382	--	--	0.11, 2.48	--	0.04, 0.37	0.1, 1.99
420	--	--	0.07, 1.03	--	--	--
453	--	--	--	0.03, 0.26	--	--
482	--	--	--	0.07, 1.02	--	--
523	--	0.05, 0.65	0.05, 0.61	0.05, 0.68	--	--
568	0.17, 8.31	0.06, 0.99	0.08, 1.93	--	--	--
646	--	--	--	0.11, 4.12	0.03, 0.22	--
669	0.11, 3.69	0.01, 0.01	--	0.12, 4.5	0.05, 0.68	--
726	0.08, 2.1	0.06, 1.3	0.09, 2.81	--	--	--
747	--	--	--	0.04, 0.68	0.04, 0.58	0.06, 1.23
765	--	--	0.03, 0.27	0.04, 0.76	--	--
854	--	0.04, 0.68	0.04, 0.86	--	--	--
947	--	--	0.04, 0.84	--	--	--
1028	0.12, 7.65	0.1, 5.56	0.11, 6.68	0.17, 14.33	0.08, 3.66	0.13, 8.82
1127	--		0.05, 1.33	--	--	--
1162	--	0.05, 1.63	0.04, 0.75	--	--	--
1177	0.08, 3.79	--	--	0.14, 10.96	0.06, 1.91	--
1198	--	--	--	--	0.04, 0.73	0.09, 4.53
1248	0.14, 11.37	0.09, 5.09	0.15, 13.97	--	0.05, 1.35	--
1274	0.15, 15.11	0.12, 8.87	0.14, 12.13	0.18, 19.89	0.1, 5.98	0.12, 9.72
1318	0.19, 23.79	0.14, 12.37	0.19, 22.56	0.22, 31.9	0.12, 9.81	0.18, 21.35
1350	--	0.04, 0.88	--	--	--	--
1410	--	0.03, 0.85	0.08, 4.4	--	--	--
1474	0.33, 80.76	0.16, 18.92	0.26, 51.38	--	--	--
1487	--	0.16, 18.2	--	0.35, 93.56	0.2, 30.63	0.3, 66.89
1530	0.32, 78.32	0.24, 42.96	0.33, 81.28	--	--	--
1554	0.18, 25.17	0.13, 12.93	--	0.35, 92.74	0.2, 31.7	0.33, 84.6
1609	0.21, 35.47	0.15, 17.15	0.19, 29.65	0.23, 42.55	0.13, 13.51	0.17, 23.94

A.5. Linear Absorbance Spectra

Linear absorbance spectra of the six molecules in solution are overlaid in Figure A.6. Fits are presented in Figure 4.3 of Chapter 4.

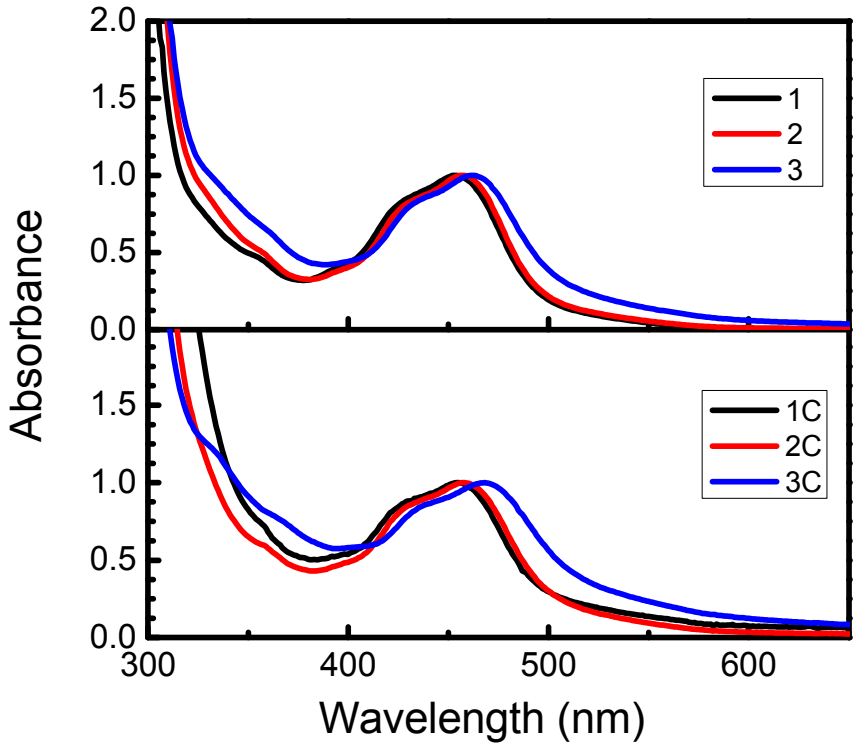

Figure A.6: The absorption spectra of the six Ru(bpy) complexes in methanol solution. The spectra have been normalized to the peak at 450 nm.

A.6. Fits to Raman Excitation Profiles

Fits for some of the Raman excitation profiles in molecule 2 are presented in Figure 4.5 of Chapter 4. Here we show excitation profiles for all modes in all systems.

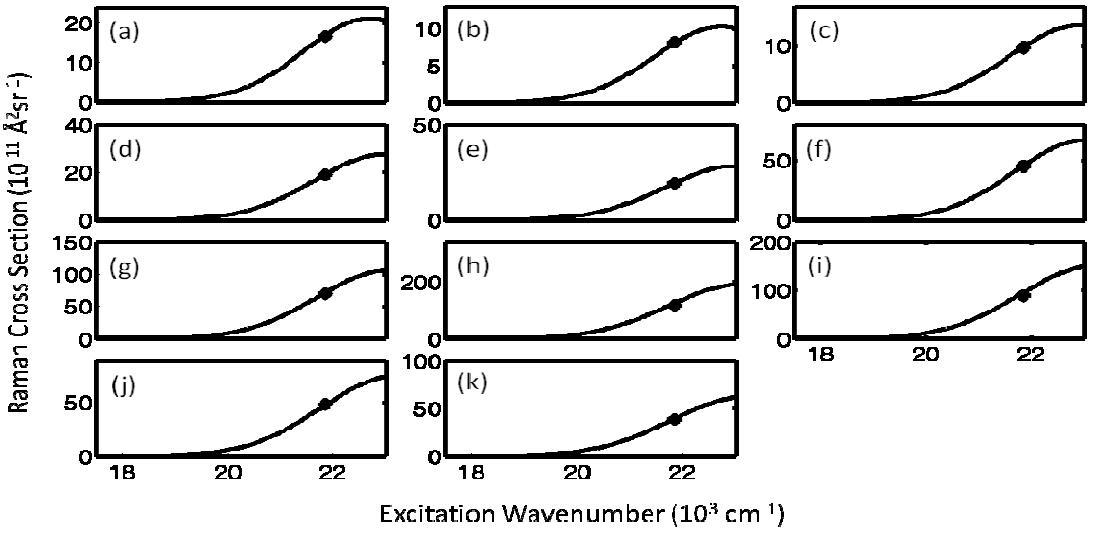

Figure A.7: The excitation profiles of **1** in methanol solution overlaid with fitting curve. The modes shown are (a)667 cm^{-1}, (b)724 cm^{-1}, (c)1030 cm^{-1}, (d)1171 cm^{-1}, (e)1248 cm^{-1}, (f)1274 cm^{-1}, (g)1316 cm^{-1}, (h)1483 cm^{-1}, (i)1529 cm^{-1}, (j)1560 cm^{-1}, and (k)1608 cm^{-1}.

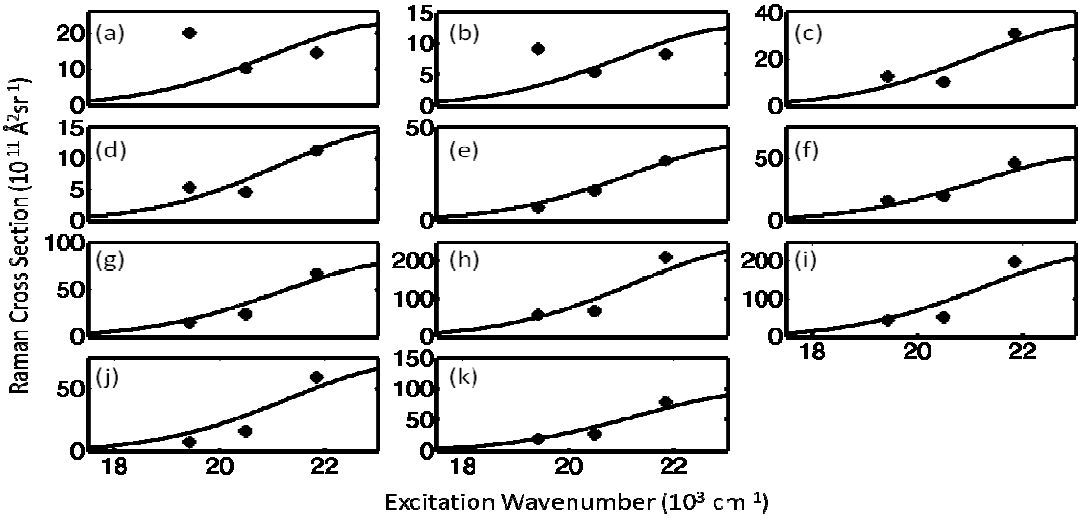

Figure A.8: The excitation profiles of **1** on TiO_2 wetted with methanol solution overlaid with fitting curve. The modes shown (a)669 cm^{-1}, (b)726 cm^{-1}, (c)1028 cm^{-1}, (d)1162 cm^{-1}, (e)1248 cm^{-1}, (f)1274 cm^{-1}, (g)1318 cm^{-1}, (h)1474 cm^{-1}, (i)1530 cm^{-1}, (j)1554 cm^{-1}, and (k)1609 cm^{-1}.

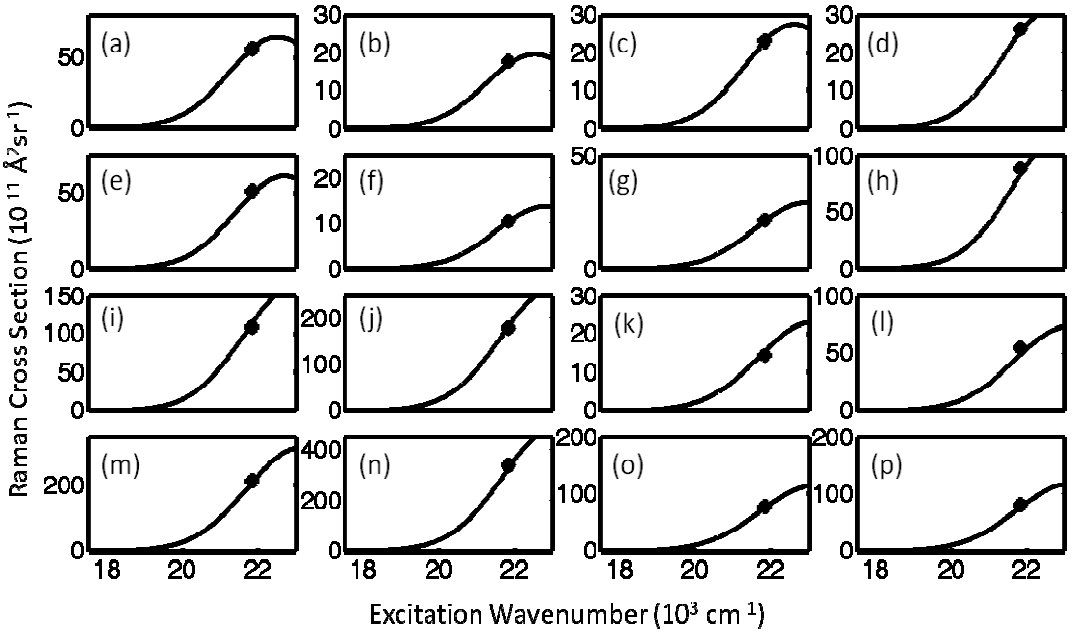

Figure A.9: The excitation profiles of **2** in methanol solution overlaid with fitting curve. The modes shown are (a)377 cm^{-1}, (b)421 cm^{-1}, (c)571cm^{-1}, (d)667 cm^{-1}, (e) 724 cm^{-1}, (f)1030 cm^{-1}, (g)1171 cm^{-1}, (h)1248 cm^{-1}, (i)1274 cm^{-1}, (j)1316 cm^{-1}, (j)1404 cm^{-1}, (j)1466 cm^{-1}, (m)1483 cm^{-1}, (n)1530 cm^{-1}, (o)1555 cm^{-1}, and (p)1606 cm^{-1}

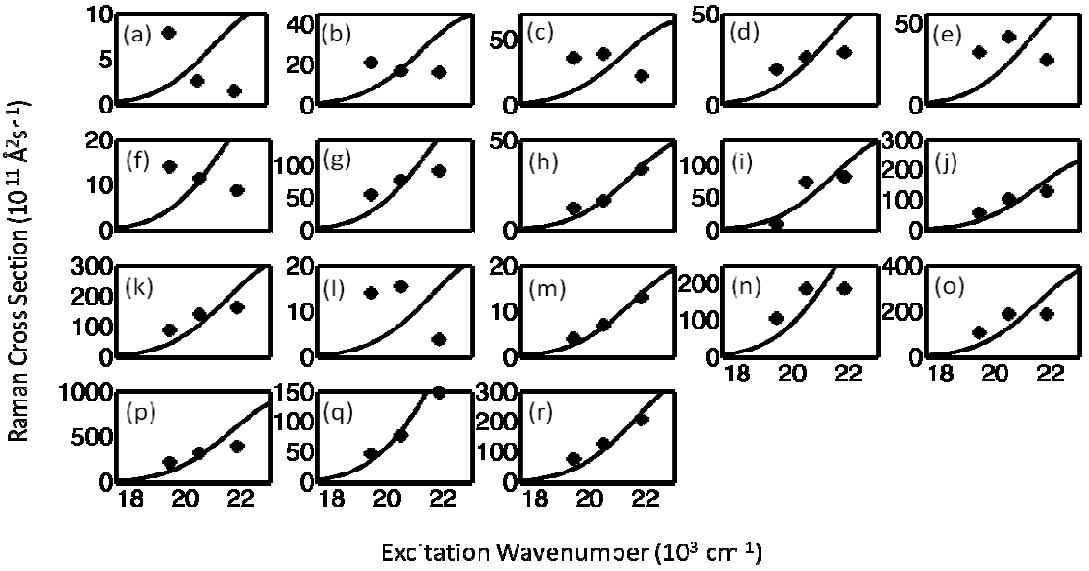

Figure A.10: The excitation profiles of **2** on TiO_2 wetted with methanol solution overlaid with fitting curve. The modes shown are (a)281 cm^{-1}, (b)523 cm^{-1}, (c)569 cm^{-1}, (d)669 cm^{-1}, (e)726 cm^{-1}, (f)854 cm^{-1}, (g)1028 cm^{-1}, (h)1162 cm^{-1}, (i)1248 cm^{-1}, (j)1274 cm^{-1}, (k)1318 cm^{-1}, (l)1350 cm^{-1}, (m)1410 cm^{-1}, (n)1474 cm^{-1}, (o)1487 cm^{-1}, (p)1530 cm^{-1}, (q)1554 cm^{-1}, and (r)1608 cm^{-1}.

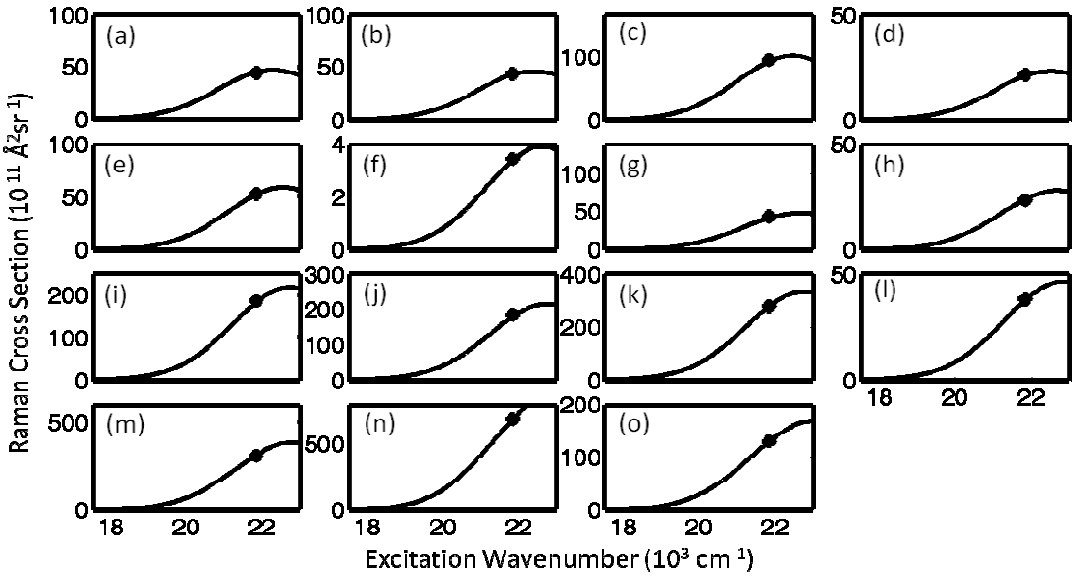

Figure A.11: The excitation profiles of **3** in methanol solution overlaid with fitting curve. The modes shown are (a)377 cm^{-1}, (b)571cm^{-1}, (c)724 cm^{-1}, (d) 854 cm^{-1}, (e)929 cm^{-1}, (f)1030 cm^{-1}, (g)1119 cm^{-1}, (h)1171 cm^{-1}, (i)1248 cm^{-1}, (j)1274 cm^{-1}, (k)1316 cm^{-1}, (l)1404 cm^{-1}, (m)1466 cm^{-1}, (n)1529 cm^{-1}, and (o)1606 cm^{-1}.

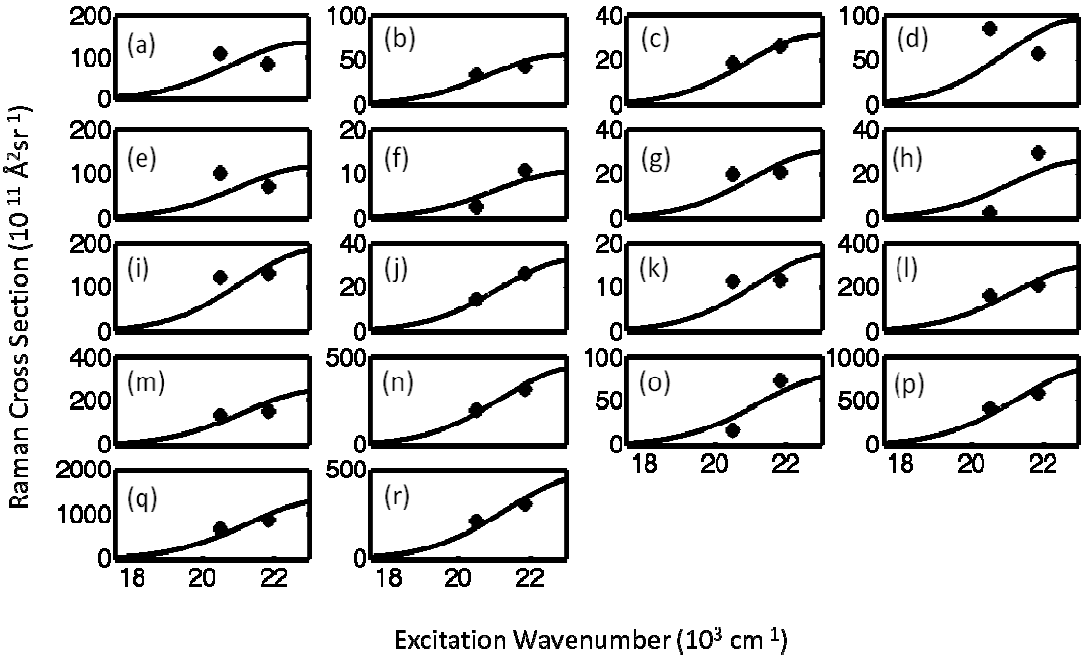

Figure A.12: The excitation profiles of **3** on TiO_2 wetted with methanol solution overlaid with fitting curve. The modes shown are (a)382 cm^{-1}, (b)420cm^{-1}, (c)523 cm^{-1}, (d)568 cm^{-1}, (e)726 cm^{-1}, (f)747 cm^{-1}, (g)854 cm^{-1}, (h)947 cm^{-1}, (i)1028 cm^{-1}, (j)1127 cm^{-1}, (k)1248 cm^{-1}, (l)1274 cm^{-1}, (m)1318 cm^{-1}, (n)1410 cm^{-1}, (o)1474 cm^{-1}, (p)1530 cm^{-1}, (q)1554 cm^{-1}, and (r)1608 cm^{-1}.

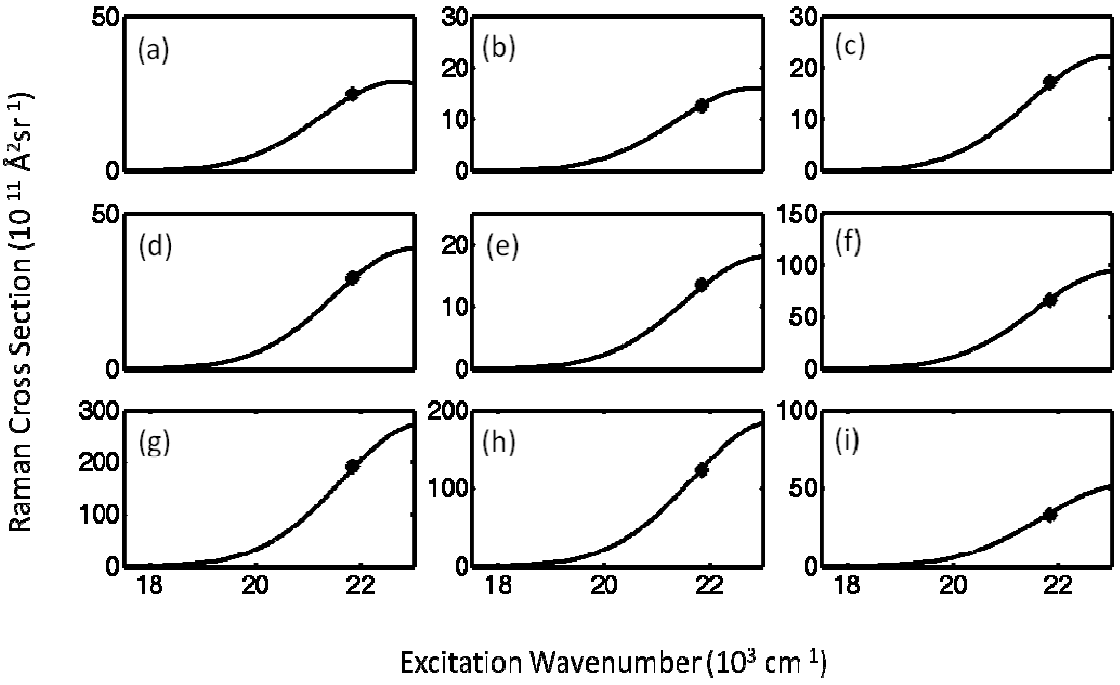

Figure A.13: The excitation profiles of **1C** in methanol solution overlaid with fitting curve. The modes shown are (a)667 cm^{-1}, (b)929 cm^{-1}, (c)1119 cm^{-1}, (d)1171 cm^{-1}, (e)1274 cm^{-1}, (f)1316 cm^{-1}, (g)1483 cm^{-1}, (h)1554 cm^{-1}, and (i)1606 cm^{-1}.

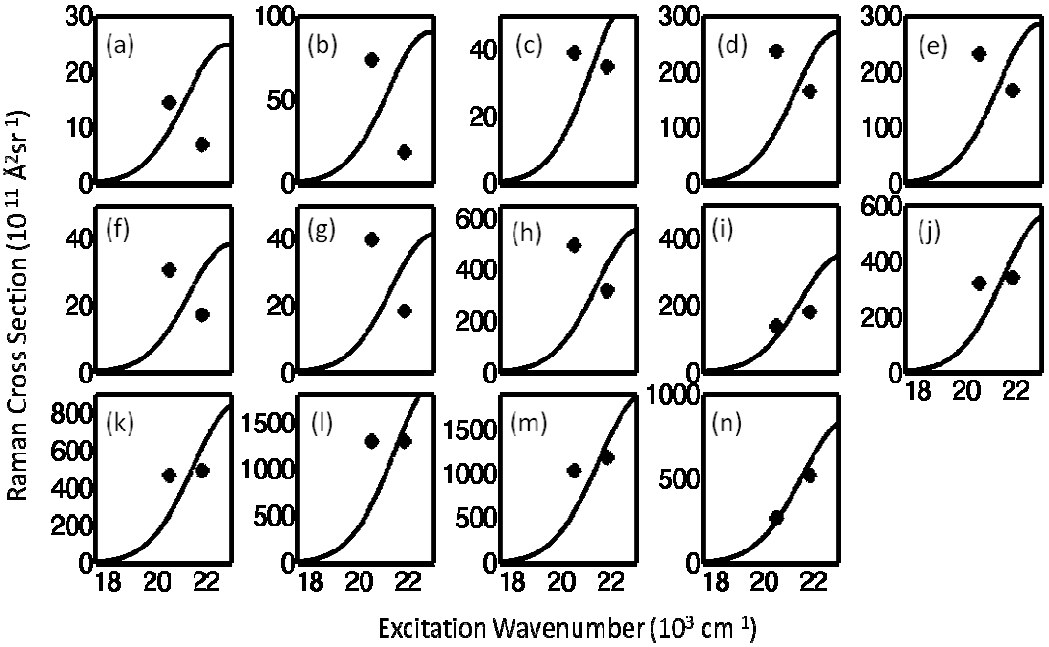

Figure A.14: The excitation profiles of **1C** on TiO_2 wetted with methanol solution overlaid with fitting curve. The modes shown are (a)453cm^{-1}, (b)482 cm^{-1}, (c)523 cm^{-1}, (d)646 cm^{-1}, (e)669 cm^{-1}, (f)747 cm^{-1}, (g)765 cm^{-1}, (h)1028 cm^{-1}, (i)1198 cm^{-1}, (j)1274 cm^{-1}, (k)1318 cm^{-1}, (l)1487 cm^{-1}, (m)1554 cm^{-1}, and (n)1608 cm^{-1}.

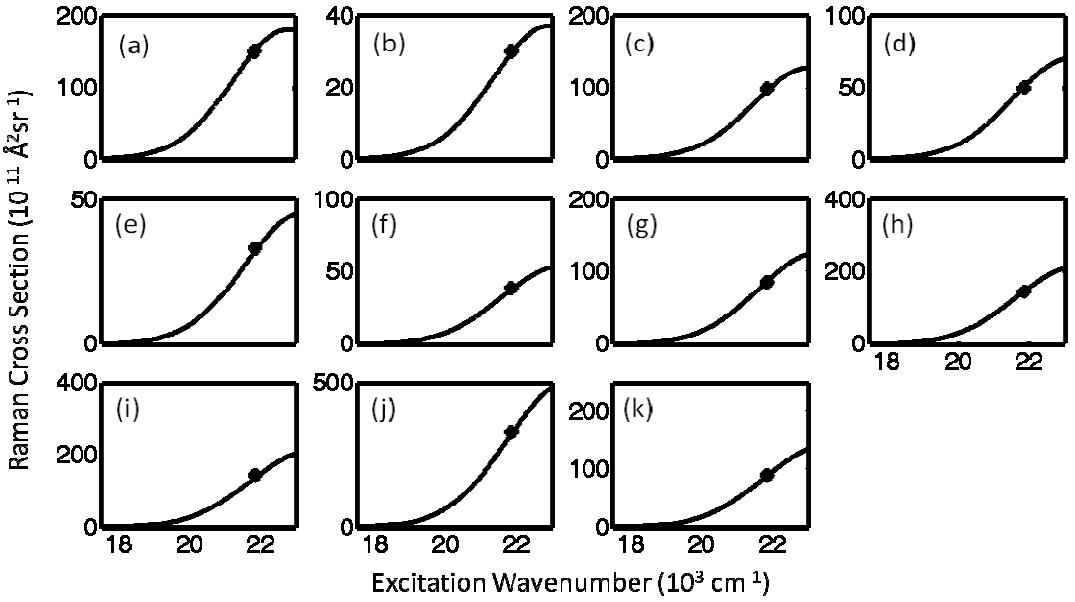

Figure A.15: The excitation profiles of **2C** in methanol solution overlaid with fitting curve. The modes shown are (a)421cm^{-1}, (b)667cm^{-1} (c)929 cm^{-1}, (d)1119 cm^{-1}, (e)1171 cm^{-1}, (f)1190 cm^{-1}, (g)1274 cm^{-1}, (h)1316 cm^{-1}, (i)1483 cm^{-1}, (j)1554 cm^{-1}, and (k)1606 cm^{-1}.

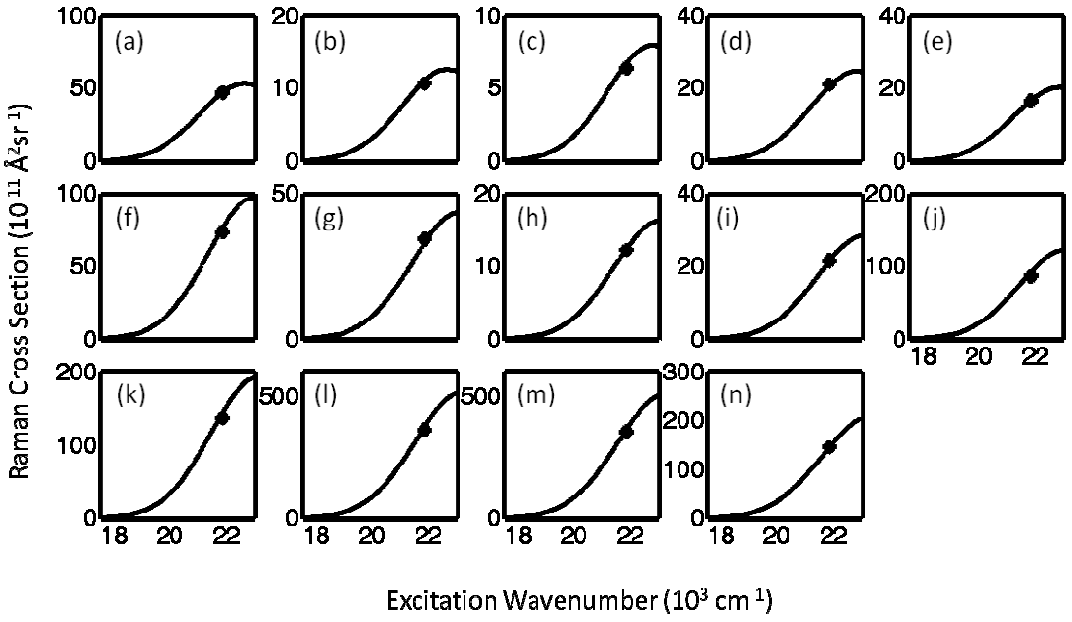

Figure A.16: The excitation profiles of **2C** on TiO_2 wetted with methanol solution overlaid with fitting curve. The modes shown are (a)364 cm^{-1}, (b)382 cm^{-1}, (c)646 cm^{-1}, (d)669 cm^{-1}, (e)747 cm^{-1}, (f)1028 cm^{-1}, (g)1177 cm^{-1}, (h)1198 cm^{-1}, (i)1248 cm^{-1}, (j)1274 cm^{-1}, (k)1318 cm^{-1}, (l)1487 cm^{-1}, (m)1554 cm^{-1}, and (n)1608 cm^{-1}.

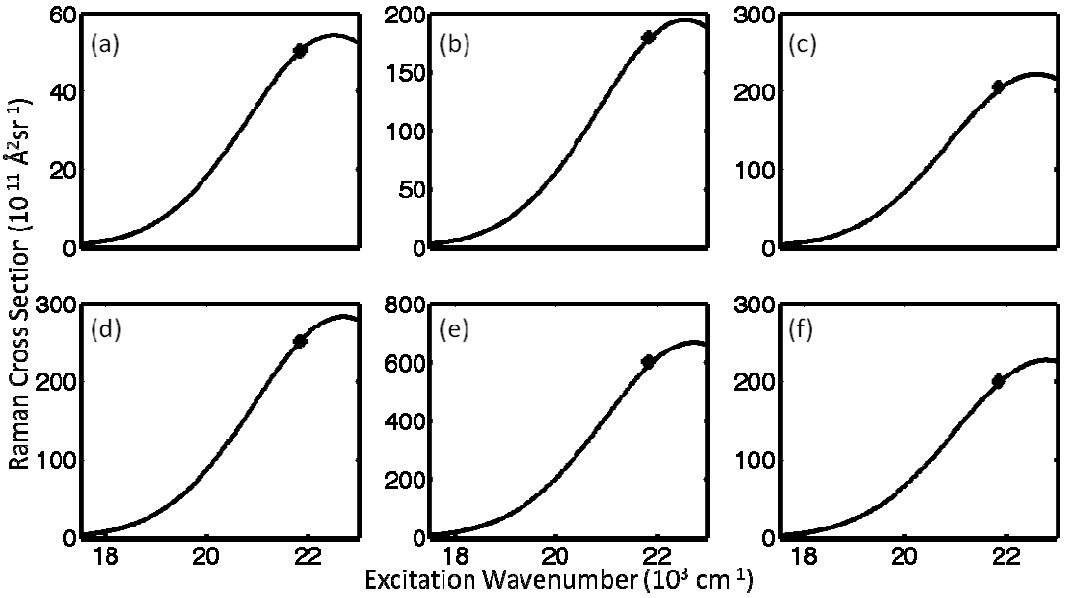

Figure A.17: The excitation profiles of **3C** in methanol solution overlaid with fitting curve. The modes shown are (a)1190 cm^{-1}, (b)1274 cm^{-1}, (c)1316 cm^{-1}, (d)1483 cm^{-1}, (e)1554 cm^{-1}, and (f)1606 cm^{-1}.

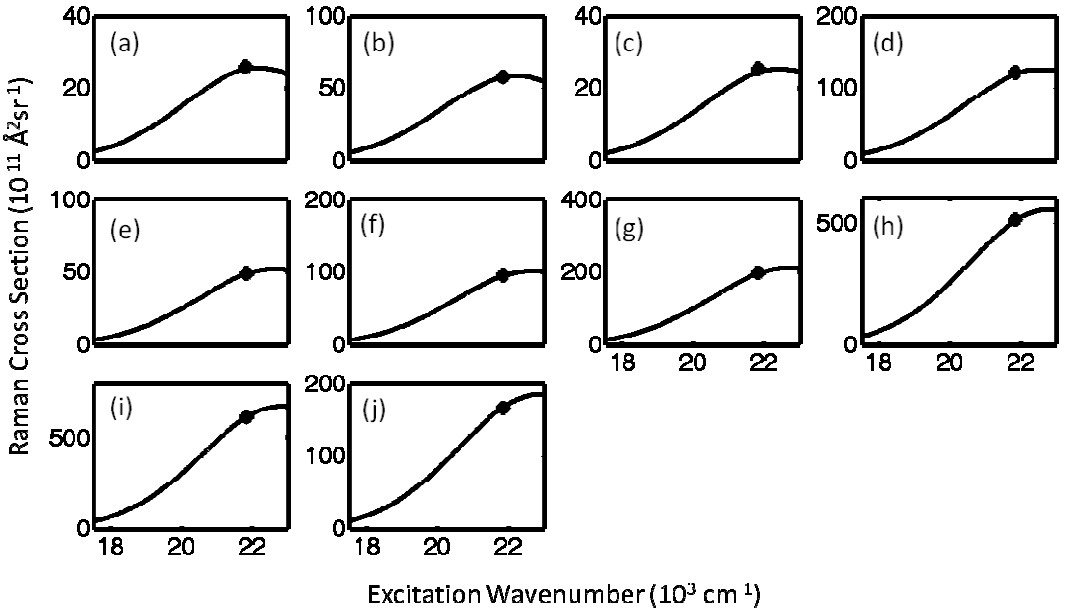

Figure A.18: The excitation profiles of **3C** on TiO_2 wetted with methanol solution overlaid with fitting curve. The modes shown are (a)340 cm^{-1}, (b)382 cm^{-1}, (c)747cm^{-1}, (d)1028 cm^{-1}, (e)1198 cm^{-1}, (f)1274 cm^{-1}, (g)1318 cm^{-1}, (h)1487 cm^{-1}, (i)1554 cm^{-1}, and (j)1609 cm^{-1}.

A.7. Fits to Linear Absorbance Spectra

Fits for the linear absorbance spectra are shown in Figure 4.3 of Chapter 4. Here we show the absorbance line shapes of the ^{1}MLCT transitions underlying the total simulated absorbance spectra. The total spectrum is obtained by adding a Gaussian function. We find that including these Gaussian functions is helpful for gauging the contribution of the higher frequency resonance to the blue side of the absorbance band.

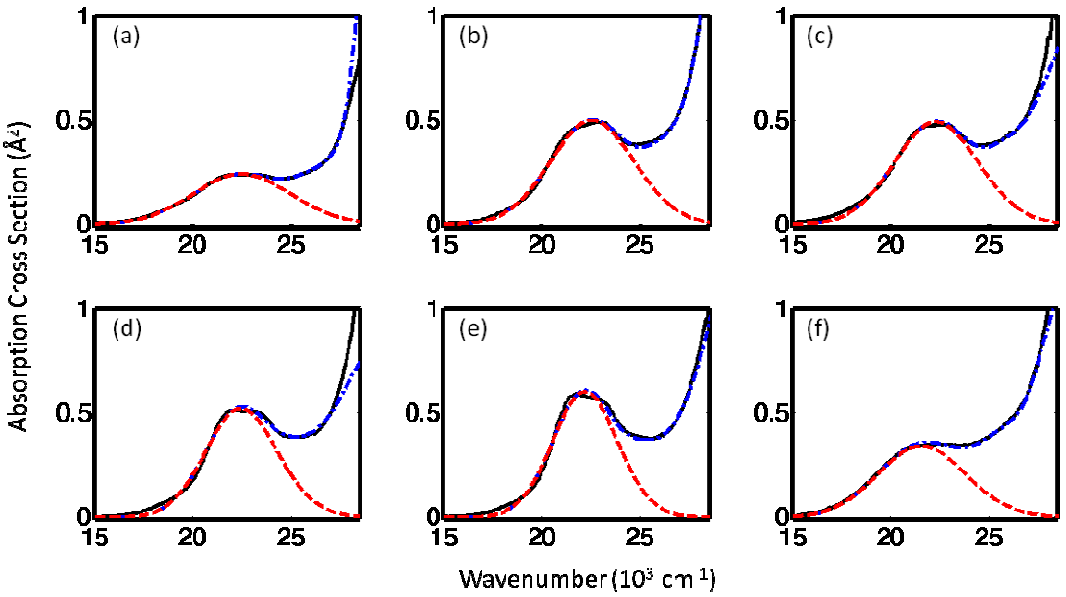

Figure A.19: Experimental absorption spectra (black, solid) overlaid with model fit (red, dashed) and combined with high-frequency sum of Gaussians (blue, dot-dashed.) Each subplot corresponds to a different sample on TiO_2, with (a) **1**, (b) **2**, (c) **3**, (d) **1C**, (e) **2C**, and (f) **3C**.

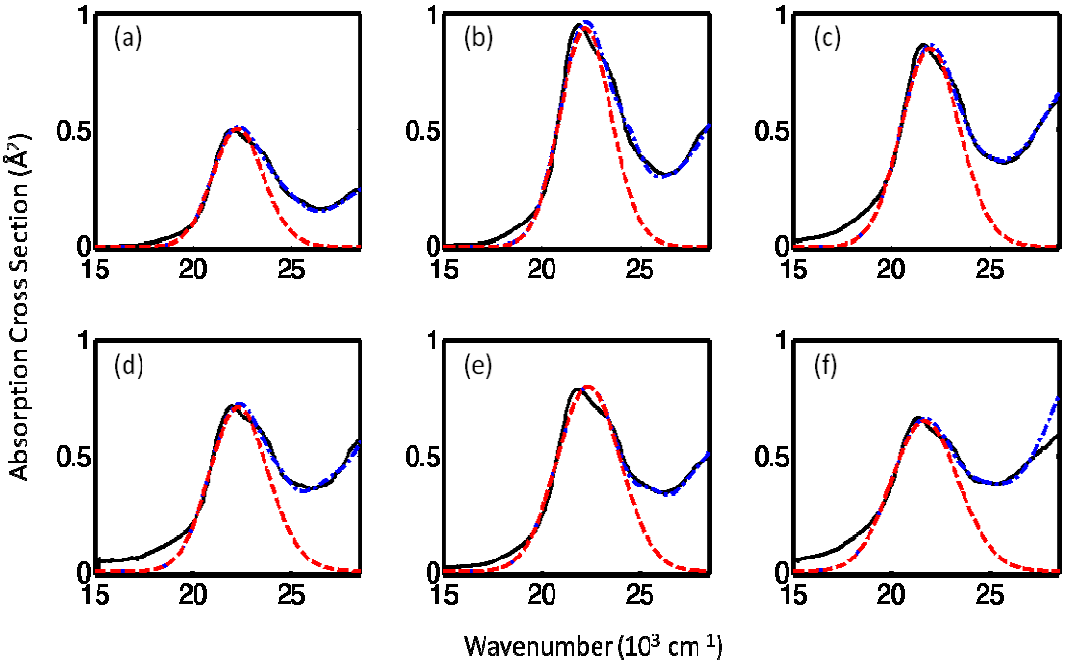

Figure A.20: Experimental absorption spectra (black, solid) overlaid with model fit (red, dashed) and combined with high-frequency sum of Gaussians (blue, dot-dashed.) Each subplot corresponds to a different sample in methanol, with (a) **1**, (b) **2**, (c) **3**, (d) **1C**, (e) **2C**,and (f) **3C**.

A.8. Effect of Fluence on TA Line Shapes

Our analysis of the transient absorption signals assumes that the fraction of excited molecules is low enough that interactions between excitations can be neglected. To test this assumption, transient absorption spectra were collected at a fixed delay of 2 ps over a range of pulse energies. These normalized spectra are shown below in Figure S21. While the spectra are experimentally indistinguishable from 550-920 nm, there are slight differences observed from 550 nm and into the ground state bleach region of the spectrum. There is a slight but distinguishable difference between the TA spectra measured below 1.5 μJ, and those with a pulse energy between 2.3 and 5.0 μJ. It is concluded that as the pulse energy increases above 1. 5 μJ,

excitation interactions become increasingly significant. We therefore do not exceed this fluence in our TA experiments.

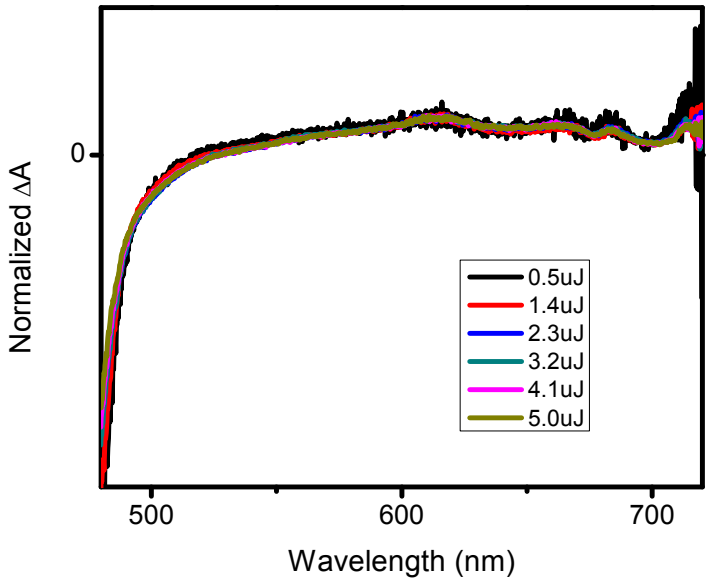

Figure A.21: Transient absorption spectra of **1C** on TiO_2. The spectra have been normalized to the peak at 650 nm.

A.9. Fitting Transient Absorption Signals

The zero crossing wavenumber is defined in Equation (4.18). The fitting parameters in Table A.3 correspond to the fits shown in Figure 4.11. Below are plots and fitting parameters on a semilog delay scale for samples in solution (see main paper for dye-sensitized films). The samples were excited with a 35-55 fs 400 nm pulse with an energy of 1.5 μJ. The signals are fit using the phenomenological equation $S(T) = A_0 G(T) + \theta(T) \sum_{i=1}^{4} A_i \int_{-\infty}^{\infty} dt G(t) \exp\left[\frac{-(t+T)}{\tau_i}\right]$, where $\theta(T)$ is a Heaviside step function, T is the pump-probe delay time, and $G(T)$ is the instrument response function.

Table A.3. Zero Crossing Fitting Parameters

Parameter	1	2	3	1C	2C	3C
A_0	623±1	574 ±1	596±1	558±1	548.1±2	519±1
A_1	-457 ±98	-753±109	-795±30	--	--	--
τ_1	0.04±0.01	0.04±0.01	0.04±0.01	--	--	--
A_2	-37.7±5.6	-16.9±1.2	-16.4±1.9	-19.7±7.5	-12.3±3.6	-17.4±1.7
τ_2	0.42±0.06	0.72±0.08	0.65±0.12	0.25±0.13	2.36±1.39	0.3±0.1
A_3	-23.5±1.0	-8.3±0.7	-8.0±0.8	-55.8±0.9	-31.3±2.0	-9.8±0.3
τ_3	148±20	265±64	123±36	78±4	260±49	92±7

[(a)]Parameters correspond to the equation $S(T) = A_0 + \sum_{i=1}^{3} A_i \exp\left(-T/\tau_i\right)$.

[(b)]Uncertainties correspond to the standard error.

Table A.4. Fitting Parameters for Figure A.22, (b),(d), and (f). Fitting parameters correspond to the samples in aqueous solution.

Sample	1	2	3	1C	2C	3C
A_0	0.013±0.001	0.013±0.001	0.026±0.001	0.011±0.001	0.007±0.001	0.01±0.001
A_1	0.24±0.03	0.36±0.06	0.36±0.08	0.11±0.07	0.1±0.06	0.28±0.06
τ_1 (ps)	0.40±0.24	0.60±0.34	0.56±0.25	0.26±0.11	1.75±1.00	0.45±0.30
A_2	0.13±0.08					
τ_2 (ps)	15±12.69					
A_3	0.78±0.10	0.73±0.08	0.74±0.11	0.88±0.32	0.89±0.59	0.78±0.13
τ_3 (ps)	1480±1000	1530±980	1530±1180	2370±2000	2300±890	1620±890

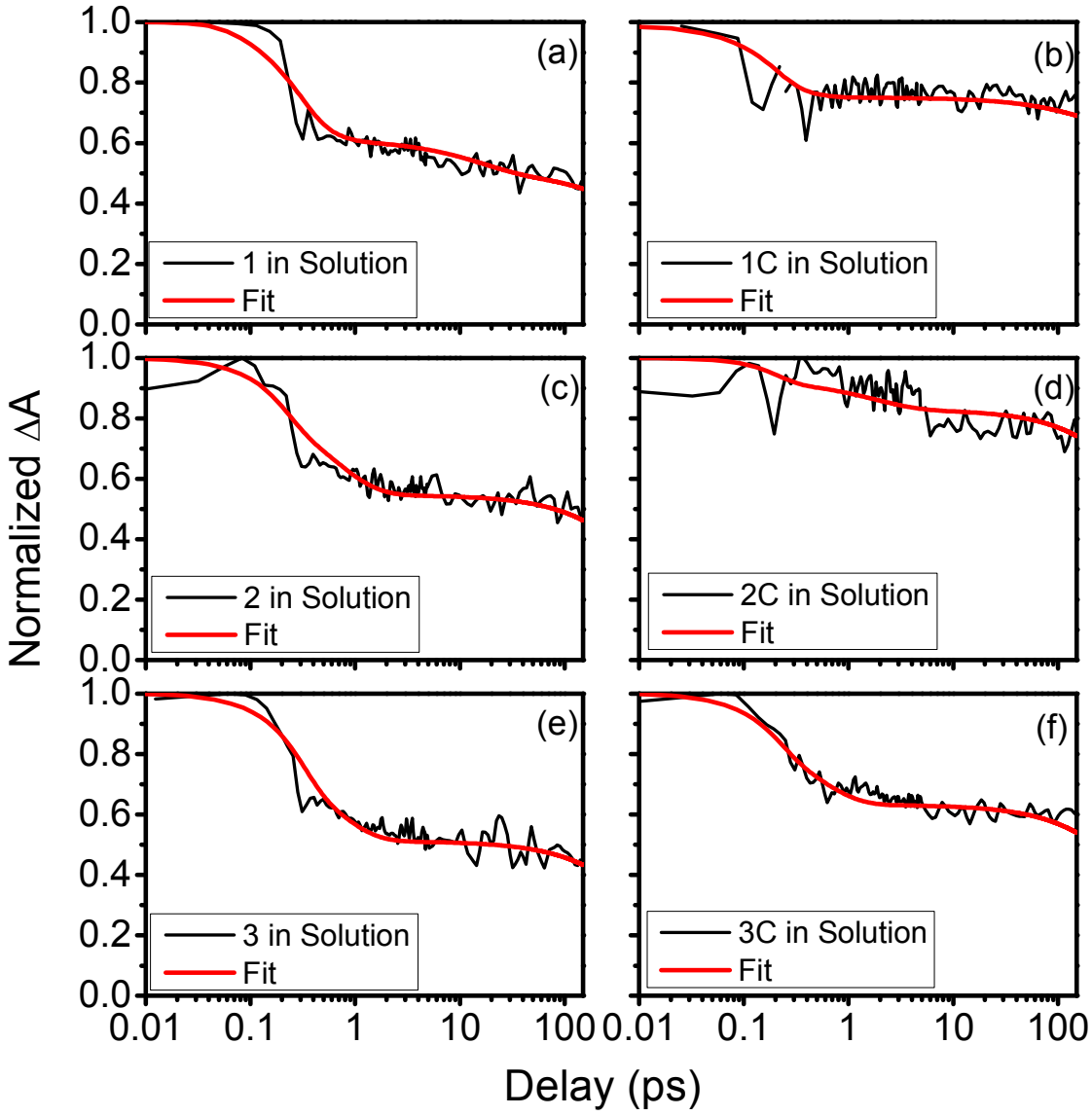

Figure A.22: Normalized TA signals and fits for all ruthenium complexes in solution. In all cases, the pump and probe wavelengths are 400nm and 655 nm, respectively.

A.10. Raman Fit Optimization

In this section, we describe the method used to optimize the Raman spectral fits. Initially, the displacements were obtained by manually adjusting their values until the curves reproduced the excitation profile for each mode as well as the absorption spectra. We then scaled the

displacements by constant factor and refit the absorbance spectrum. For each value of the scaling factor, the sum of squares error in the absorbance spectrum was computed. The parameters which best fit the absorption spectrum were obtained by fitting the sum of squares errors to a parabola and setting the displacements to the values corresponding to the minima of the parabola (i.e., the minimum error).

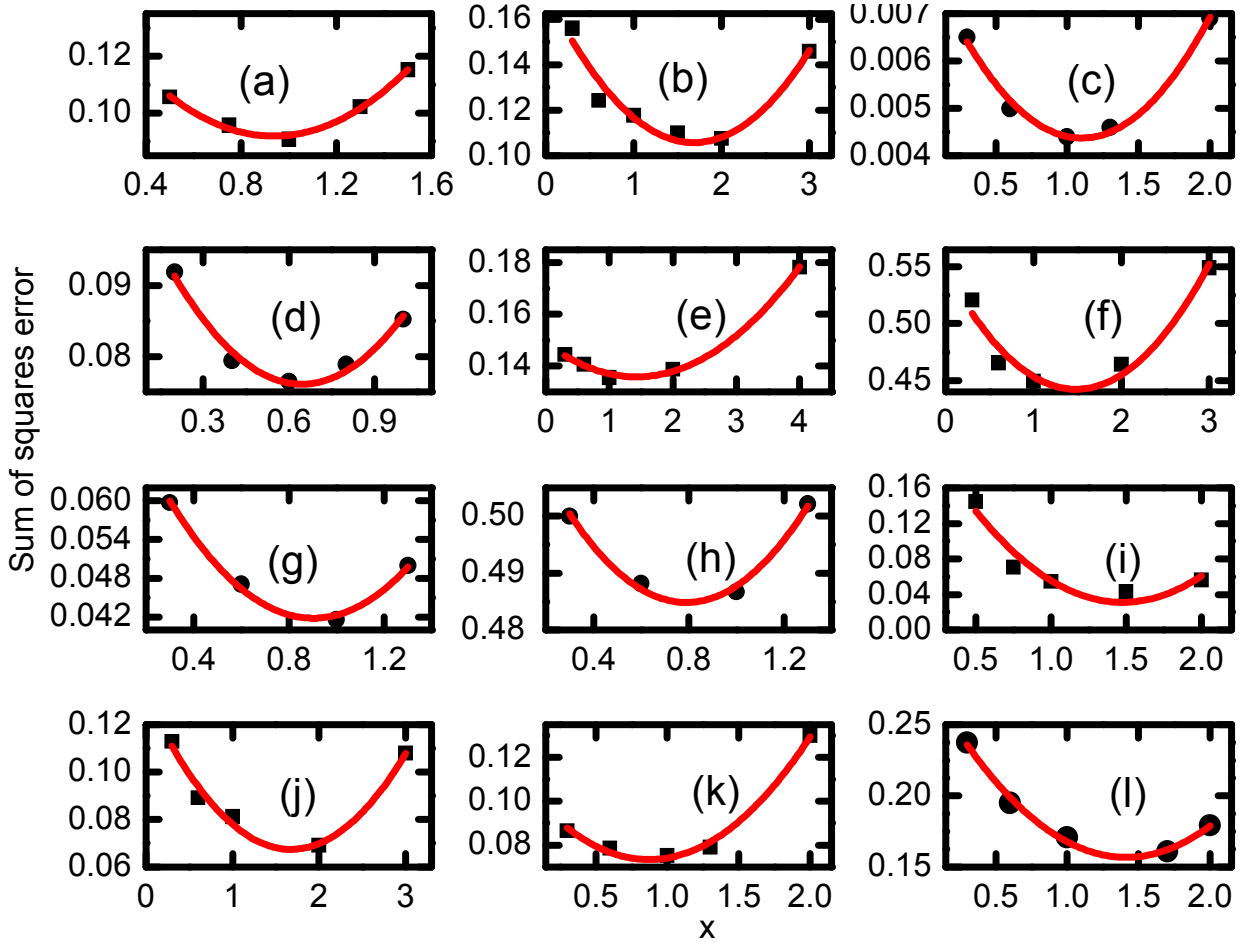

Figure A.23: Sum of squares error of the fit of the absorbance spectrum as a function of the multiplication factor, x. The points are fit to a quadratic polynomial (red curve.) Each subplot corresponds to a different sample, with (a) **1C** on TiO_2, (b) **1C** in methanol, (c) **1** on TiO_2, (d) **1** in methanol, (e) **2C** on TiO_2, (f) **2C** in methanol, (g) **2** on TiO_2, (h) **2** in methanol, (i) **3C** on TiO_2, (j) **3C** in methanol, (k) **3** on TiO_2, (l) **3** in methanol.

A.11. Oxidation Potentials

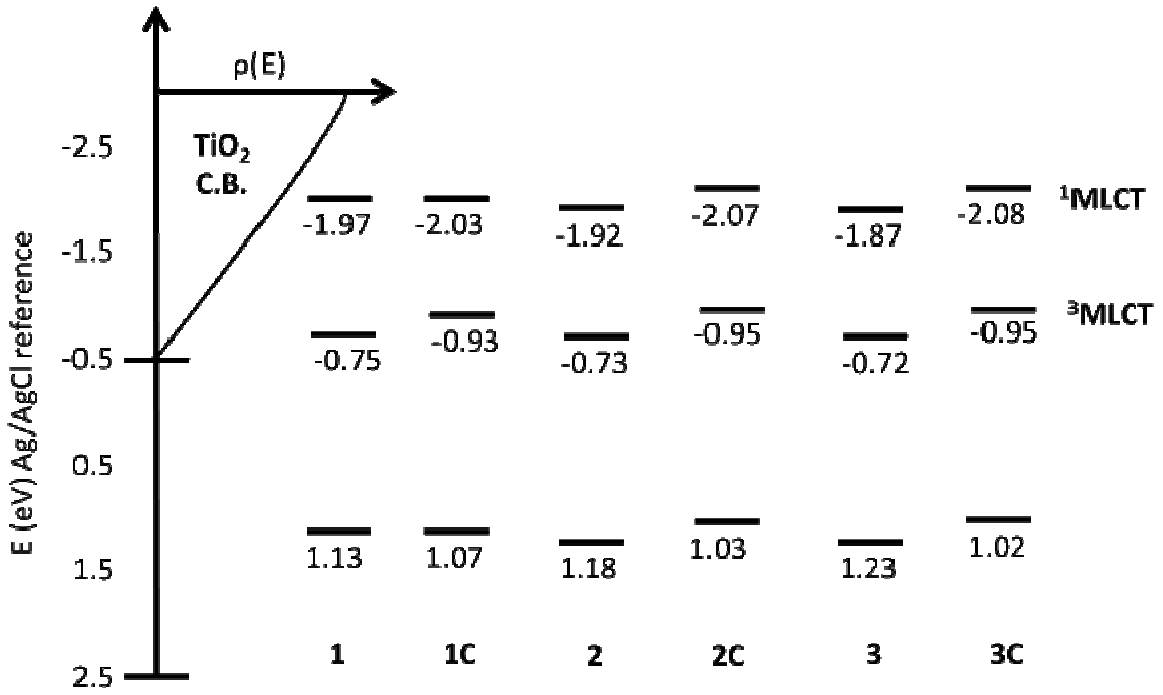

Figure A.24: Comparison of energy levels for each of the six ruthenium complexes and TiO_2. Energies of the "hot" singlet states energies are calculated by adding the energy of a 400nm photon to the ground state.

APPENDIX B: SUPPLEMENTS TO "NONEQUILIBRIUM CHARGE TRANSFER ON SEMICONDUCTING NANOPARTICLES"

B.1. Linear Absorption of Sensitized Nanoparticles

In this Section, we describe the process of measuring the charge transfer band of catechol on TiO_2. The spectrum is shown in Figure B.1.

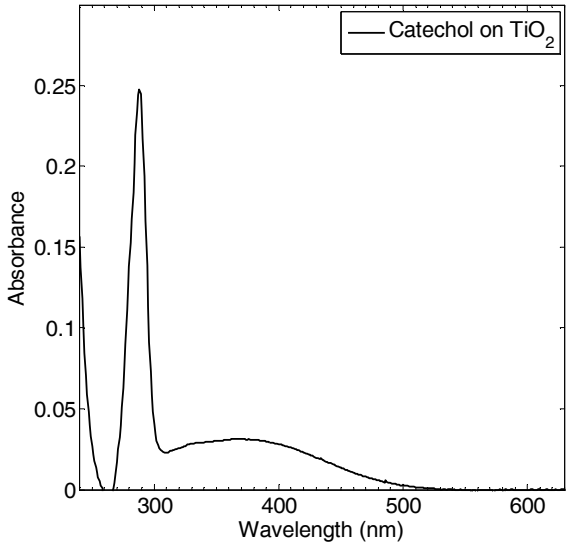

Figure B.1: Catechol-TiO_2 charge transfer absorption spectrum. The charge transfer band is calculated by differencing the absorbance of catechol on TiO_2 nanoparticles with that of catechol and TiO_2 separately.

Two flasks are filled with TiO_2 nanoparticles in aqueous solution, and another is filled with an equal volume of water. Catechol is added to the water and one of the solutions of nanoparticles such that the concentration based on mass of catechol added is 0.01M. The TiO_2 nanoparticles were estimated at synthesis to have a concentration of approximately 0.25M. The absorption spectrum of the aqueous TiO_2 and aqueous catechol solutions are combined to form a reference spectrum and differenced with that of the charge transfer complex. The resulting spectrum shows absorbance due to the newly formed CT band. The CT band is known (see Chapter 7) to be

approximately Gaussian in shape and centered around 400 nm. The sharp feature shown in Figure B.1 at 290 nm is attributed to other changes in the sample (for example, changes in the scattering intensity of the nanoparticles on catechol binding, or a shift in the absorbance of the catechol benzene ring), and is not considered part of the charge transfer resonance.

B.2. Resonance Raman Intensity Analysis

Resonance Raman Intensity analysis was performed using methods described previously in Chapter 4 and Appendix A. 458 nm, 488 nm, and 514 nm excitation beams were utilized in the resonance Raman measurements. The parameters resulting from the fit are shown in Table B.2.

Table B.1. Complete set of Resonance Raman fitting parameters for catechol on TiO_2.

Inhomogeneous width (cm^{-1})	2550
Electronic origin (cm^{-1})	22400
Homogenous width (cm^{-1})	1950
Transition Length (Å)	1.2
Raman Shift (cm^{-1})	Δ
769	0.33
810	0.21
1336	0.28
1153	0.18
1260	0.33
1284	0.19
1329	0.28
1481	0.34
1581	0.06
1601	0.21

APPENDIX C: SUPPLEMENT TO "ULTRAFAST SPECTROSCOPIC SIGNATURES OF COHERENT ELECTRON TRANSFER MECHANISMS IN A TRANSITION METAL COMPLEX"

C.1. Decomposition of Transient Absorption Signals

In this section, we present parameters associated with the broadband response observed in $[Ti(cat)_3]^{2-}$. The transient absorption data shown in Figure 6 of the main paper are fit using

$$F(\tau,\lambda) = A_{GSB}(\tau)\exp\left\{-4\ln(2)\frac{\left[\lambda-\lambda_{GSB}(\tau)\right]^2}{\Delta^2_{GSB}(\tau)}\right\} + A_{HGS}(\tau)\left\{-4\ln(2)\frac{\left[\lambda-\lambda_{HGS}(\tau)\right]^2}{\Delta^2_{HGS}(\tau)}\right\} + A_{BB}(\tau)\left\{-4\ln(2)\frac{\left[\lambda-\lambda_{BB}(\tau)\right]^2}{\Delta^2_{BB}(\tau)}\right\} \quad \text{(C.1)}$$

Because the broadband component of the response is red-shifted beyond our detection range, we have constrained both $\lambda_{BB}(\tau)$ and $\Delta_{BB}(\tau)$ (650 nm< $\lambda_{BB}(\tau)$ <850 nm and 400 nm< $\Delta_{BB}(\tau)$ <1000 nm). These constraints were required to suppress discontinuities in the parameters of the HGS signal component, which were left unconstrained. The residual can be further reduced by adding a constant offset to Equation (C.1) or replacing the broadband Gaussian function with a fifth order polynomial. We choose to use a Gaussian because it is the most physical choice in that it presumably approximates the line shape of an electronic resonance.

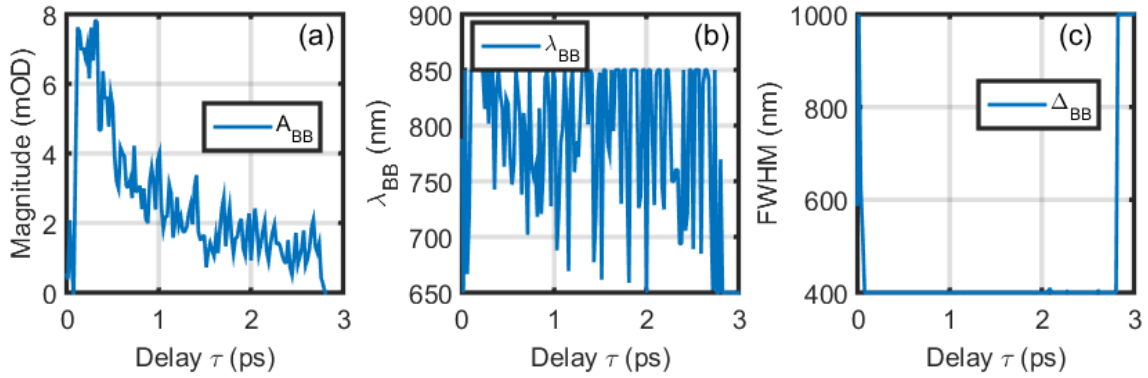

Figure C.1: Parameters of a broadband signal component determined in the decomposition of transient absorption signals. (a) Magnitude of the broadband signal component. (b) Peak wavelength computed for the broadband signal component. (c) FWHM line width for the broadband signal component. It is necessary to include a signal component at longer wavelengths because discontinuities in the parameters of the GSB and HGS resonances are found otherwise.

C.2. Analysis of Uncertainty in Spectral Fits

Determination of error bars in this highly nonlinear model is not straightforward.[1] We have carried out the fits in the traditional way. The parameters are adjusted manually over many iterations until the best agreement is achieved between the experimental data and model. Here, we provide example fits to show how the optimal region of parameter space was located. In the two fits shown below, we reduced and increased the homogeneous width by 500 cm^{-1} to show how the model diverges from the experimental line shape in each regime. The other parameters are adjusted to compensate for the fixed homogeneous width.

C.2.A. Fits Conducted with Homogeneous Width Fixed at 2150 cm^{-1}

Reduction of the homogeneous width causes a red shift in the absorbance spectrum, because the peak is displaced from the electronic origin by the sum of the intramolecular and solvent reorganization energies. The electronic origin must be increased to compensate for this effect, which also causes the Raman cross sections to increase (i.e., a second effect that must be compensated for). This is why the mode displacements given in Table C.1 are smaller than those

reported in the best fit. Poor agreement between the experimental and calculated absorbance line shapes at wavelengths longer than 400 nm is the primary reason that we consider this to be an unrealistic region of parameter space; the rising side of the absorbance line shape becomes too steep. The quality of the fits become worse if the homogeneous width is decreased further.

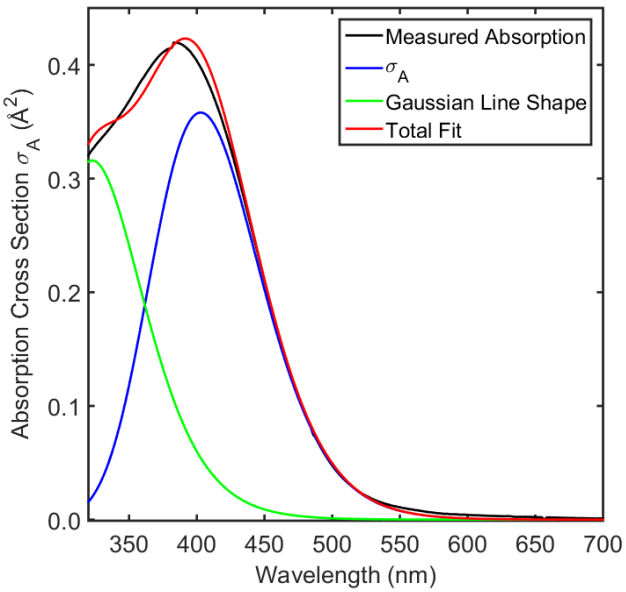

Figure C.2: Absorption spectrum fit with Equation (8.19) and the parameters in Table C.1. The absorption cross section, σ_A, is used to fit the low-energy side of the line shape subject to the constraints imposed by the Raman cross sections. A Gaussian line shape (green) is used to estimate the contribution of the second-to-lowest energy transition to the total absorbance.

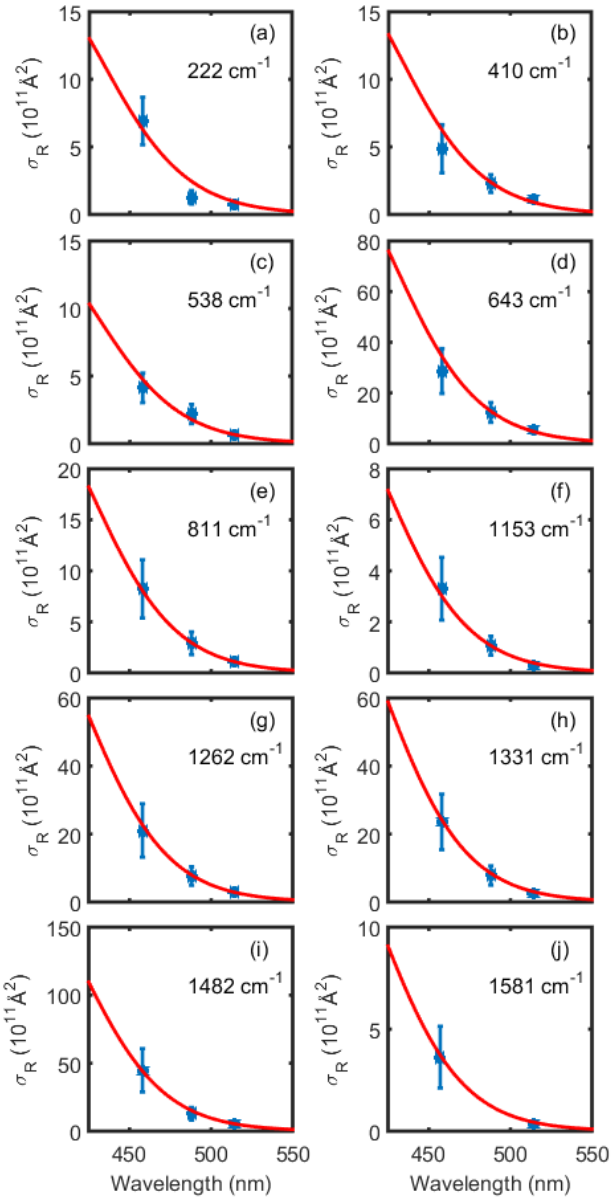

Figure C.3: Experimental Raman cross sections fit using Equation (8.20) and the parameters in Table C.1.

Table C.1. Resonance Raman Fitting Parameters for Homogeneous Width Fixed at 2150 cm^{-1}

[a]**Parameter**	**Value**	
ω_0	21600 cm^{-1} (463 nm)	
δ	2080 cm^{-1} (47 nm)	
Γ	2150 cm^{-1} (46 nm)	
$\kappa = \Delta / \Lambda$	0.01	
[b] λ	2088 cm^{-1}	
μ_{eg}	3.8 D	
Raman Shift (cm^{-1})	**Δ**	[c]**Assignment**
222	1.02	Symmetric Ti-cat stretch (214 cm^{-1})
410	0.57	Ti-cat bend (413 cm^{-1})
538	0.39	O-C-C-O bend & ring distortion (534 cm^{-1})
643	0.90	O-C-C-O bend & ring distortion (641 cm^{-1})
811	0.36	O-C-C-O bend and ring 'breathing' (814 cm^{-1})
1153	0.17	C-H bending (1156 cm^{-1})
1262	0.44	O-C-C-O stretch (1283 cm^{-1})
1330	0.44	C=C stretch, C-O stretch, Ti-O stretch (1305 cm^{-1})
1482	0.56	C=C stretch & C-O stretch (1511 cm^{-1})
1580	0.16	C=C stretch (1594 cm^{-1})

[a] Fits are carried out in the frequency domain (not wavelength).

[b] Computed with $\lambda = D^2 / 2k_B T$, where D is found with Equation (8.22).

[c] Assignments for vibrational modes computed at the B3LYP/6-311G(2d,3p) level in Gaussian 2009[2]. Frequencies of the calculated modes are given in parentheses.

C.2.B. Fits Conducted with Homogeneous Width Fixed at 3150 cm^{-1}

Increasing the homogeneous width causes a blue-shift in the absorbance spectrum, because the peak is displaced from the electronic origin by the sum of the intramolecular and solvent reorganization energies. The electronic origin is decreased to compensate for this effect, which causes the Raman cross sections to decrease (a second effect that must be compensated for). This is why the mode displacements given in Table C.2 are larger than those reported in the best fit. Poor agreement between the experimental and calculated absorbance line shapes at wavelengths longer than 400 nm is the one reason that we consider this to be an unrealistic region of parameter space; the rising side of the absorbance line shape is not sufficiently steep. We are also unable to produce an adequate fit to the Raman cross sections of the 222-cm^{-1} mode. Moreover, the parameters seem to become unphysical, because the 6838-cm^{-1} sum of the solvent and intramolecular reorganization energies is extremely large. For example, the electronic origin is at 709 nm when the homogeneous with is 3150 cm^{-1}, which is an extremely far displacement from the onset of light absorption. The quality of the fit becomes worse if the homogeneous width is increased further.

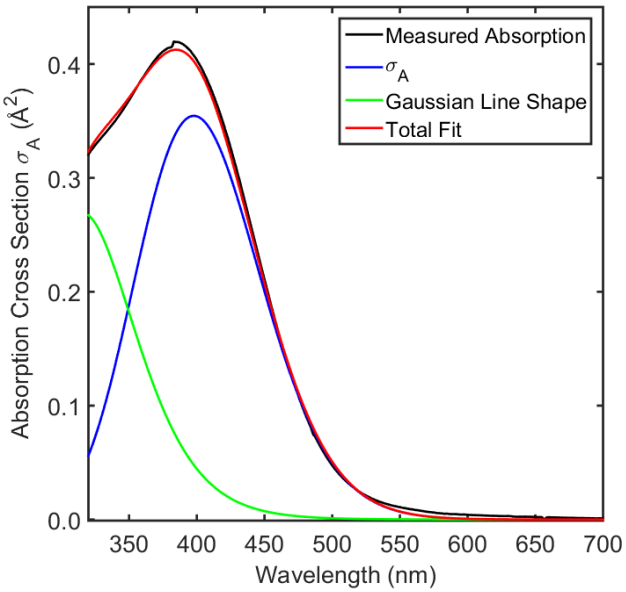

Figure C.4: Absorption spectrum fit with Equation (8.19) and the parameters in Table C.2. The absorption cross section, σ_A, is used to fit the low-energy side of the line shape subject to the constraints imposed by the Raman cross sections. A Gaussian line shape (green) is used to estimate the contribution of the second-to-lowest energy transition to the total absorbance.

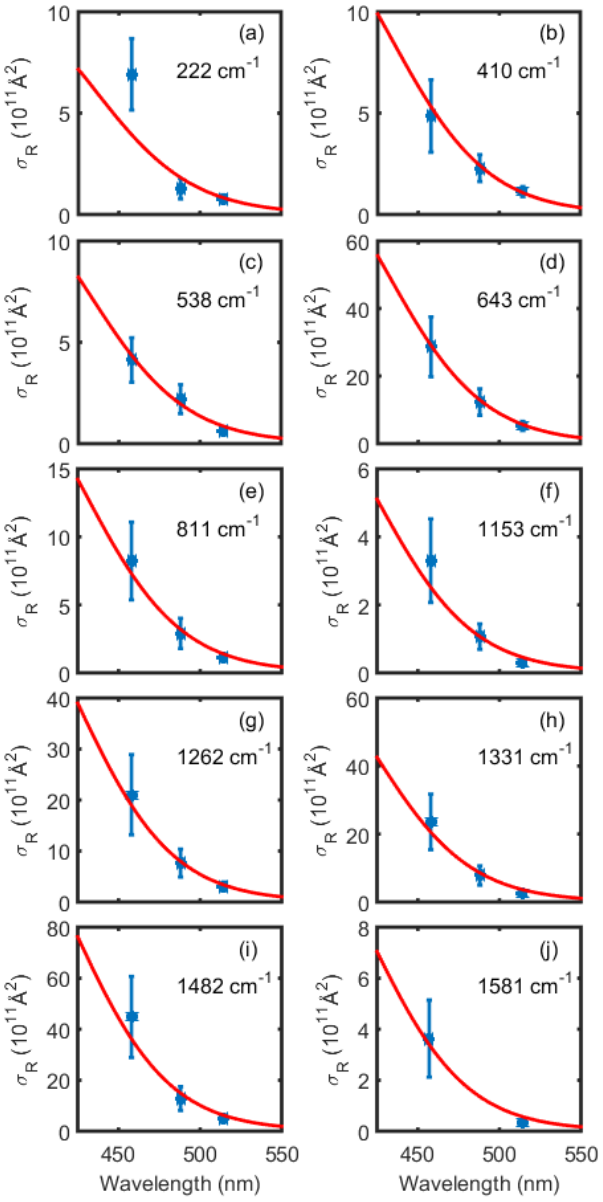

Figure C.5: Experimental Raman cross sections are fit using Equation (8.20) and the parameters in Table C.2.

Table C.2. Resonance Raman Fitting Parameters

[a]**Parameter**	**Value**	
ω_0	14100 cm^{-1} (709 nm)	
δ	300 cm^{-1} (15 nm)	
Γ	3150 cm^{-1} (160 nm)	
$\kappa = \Delta / \Lambda$	0.01	
[b] λ	4483 cm^{-1}	
μ_{eg}	4.0 D	
Raman Shift (cm^{-1})	**Δ**	[c]**Assignment**
222	2.4	Symmetric Ti-cat stretch (214 cm^{-1})
410	1.55	Ti-cat bend (413 cm^{-1})
538	1.09	O-C-C-O bend (534 cm^{-1})
643	2.4	O-C-C-O bend (641 cm^{-1})
811	0.98	O-C-C-O bend and ring 'breathing' (814 cm^{-1})
1153	0.43	C-H bending (1156 cm^{-1})
1262	1.10	O-C-C-O stretch (1283 cm^{-1})
1330	1.10	C=C stretch, C-O stretch, Ti-O stretch (1305 cm^{-1})
1482	1.35	C=C stretch & C-O stretch (1511 cm^{-1})
1580	0.39	C=C stretch (1594 cm^{-1})

[a] Fits are carried out in the frequency domain (not wavelength).

[b] Computed with $\lambda = D^2 / 2k_B T$, where D is found with Equation (8.22).

[c] Assignments for vibrational modes computed at the B3LYP/6-311G(2d,3p) level in Gaussian 2009.[2] Frequencies of the calculated modes are given in parentheses.

C.3. The Hot Ground State Signal Component Dominates the Coherent Raman Response of $[Ti(cat)_3]^{2-}$

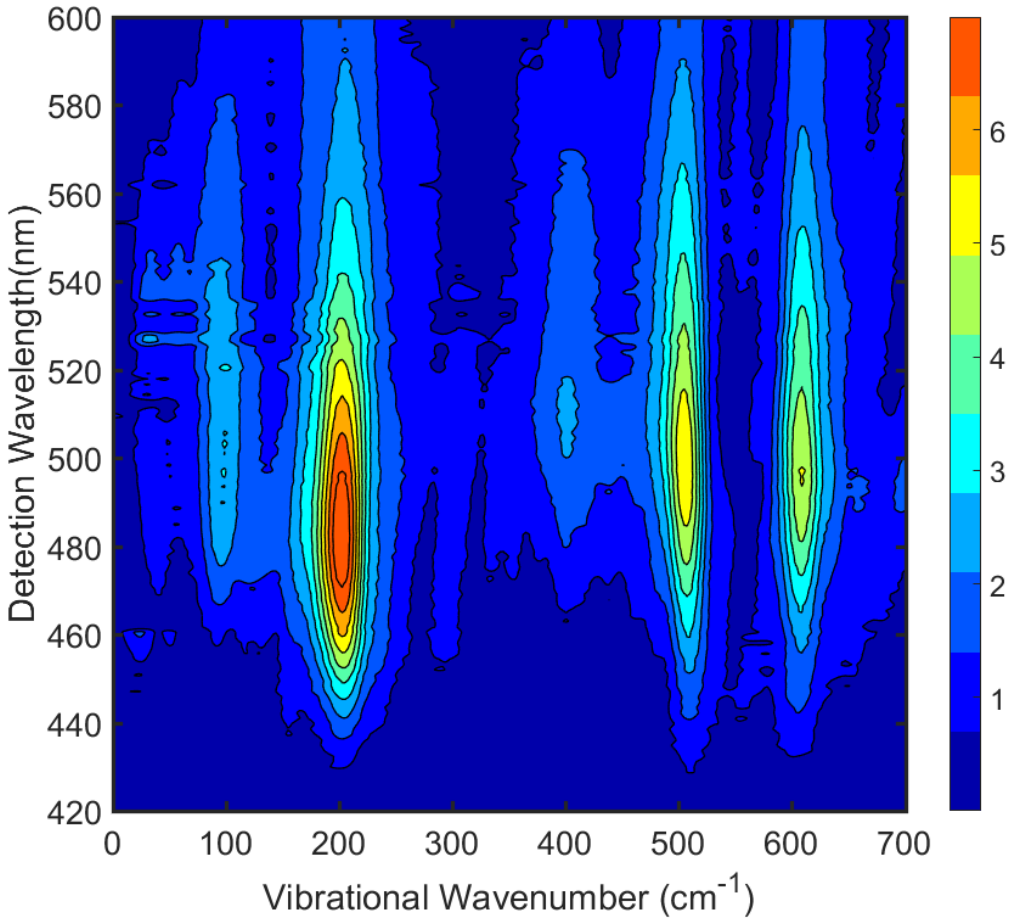

Figure C.6: The coherent response of the $[Ti(cat)_3]^{2-}$ is analyzed for a range of detection wavelengths. Coherent vibrational motion is detected at wavelengths that correspond to the HGS signal component in the 450-560-nm range. The stimulated Raman response for the GSB signal component is relatively weak. These data suggest that the back electron transfer process induces the vibrational motions detection in our transient absorption experiments.

C.4. Density Functional Theory Analysis of the Most Appropriate Basis Set

The LMCT transitions should be treated as localized if interactions between the local charge transfer states are small compared to the thermal fluctuation amplitudes in the energy levels. This general rule of thumb also governs Frenkel exciton delocalization in molecular aggregates and crystals.[3] The thermal fluctuation amplitude that we have determined experimentally is Δ=1040 cm^{-1} (see Table 1 in the main article). The coupling between LMCT states can be estimated with electronic structure calculations if we invoke a four-level basis set that consists of the ground state and the three local charge transfer states. The Hamiltonian matrix for a system with C_3 or D_3 symmetry can be written as

$$H = \begin{pmatrix} E_G & V_{G,CT} & V_{G,CT} & V_{G,CT} \\ V_{G,CT} & E_{CT} & V_{CT,CT} & V_{CT,CT} \\ V_{G,CT} & V_{CT,CT} & E_{CT} & V_{CT,CT} \\ V_{G,CT} & V_{CT,CT} & V_{CT,CT} & E_{CT} \end{pmatrix}, \tag{C.2}$$

where E_G is the energy of the ground state, E_{CT} is the energy of the charge transfer state, $V_{G,CT}$ is the coupling between the ground state and a charge transfer state, and $V_{CT,CT}$ is the coupling between charge transfer states. The approximation, $E_{CT} - E_G >> \left|V_{G,CT}\right|$, is likely to hold in $[Ti(cat)_3]^{2-}$, because of the large LMCT resonance frequency. In this limit, the 4x4 problem can be reduced to a 3x3 problem,

$$H = \begin{pmatrix} E_{CT} & V_{CT,CT} & V_{CT,CT} \\ V_{CT,CT} & E_{CT} & V_{CT,CT} \\ V_{CT,CT} & V_{CT,CT} & E_{CT} \end{pmatrix}, \tag{C.3}$$

where E_{CT} now represents the local LMCT absorption frequency. A similar approximation is made to obtain the Frenkel exciton Hamiltonian for molecular aggregates.

The LMCT resonance frequencies computed at the B3LYP/6-311G(2d,3p) level are 24321, 24321, and 26248 cm^{-1}. The two lower energy resonances correspond to charge transfer states with E symmetry, whereas the higher energy resonance is totally symmetric. The elements of the 3x3 Hamiltonian in Equation (S3) that yield these resonance frequencies are E_{CT} =24963 cm^{-1} and $V_{CT,CT}$ =642 cm^{-1}. The coupling, $V_{CT,CT}$, is not much smaller than the empirical thermal fluctuation magnitude (Δ=1040 cm^{-1}). This calculation give further support to our choice of a delocalized LMCT basis set in this work. These two quantities, $V_{CT,CT}$ and Δ, are similar in magnitude, so legitimate arguments could be made either way.

C.5. Comparison of GSB, HGS, and BB Signal Components to Catechol on TiO_2 in Aqueous Solution

In this section, we present transient absorption measurements conducted with catechol on TiO_2 in aqueous solution. Such a comparison was discussed by Lian in earlier work.[4] We present these signals here in the interest of completeness. To begin, we show in Figure S8 that the charge transfer resonances of the two systems have similar peak wavelengths and line widths. Lian and co-workers, who conducted earlier transient absorption experiments on $[Ti(cat)_3]^{2-}$, suggested that one of the bonds between catechol and the titanium atom may detach following excitation then reattach after 100's of ps[4]. We hypothesize that this species is also responsible for the long-lived, red-shifted signal component in our experiments. In support of this interpretation, we present transient absorption signals acquired for catechol on TiO_2 nanoparticles in Figure S9. The signal closely resembles that of $[Ti(cat)_3]^{2-}$ in that clear GSB and HGS components relax on the picosecond time-scale. In addition, we observe a broadband, red-shifted response that is most prominent at sub-picosecond delay times. Like $[Ti(cat)_3]^{2-}$, ground state recovery is not complete

within the first several picoseconds; a much longer-lived signal component is observed (the ground state population fully recovers in the millisecond between shots of our 1-kHz laser systems).

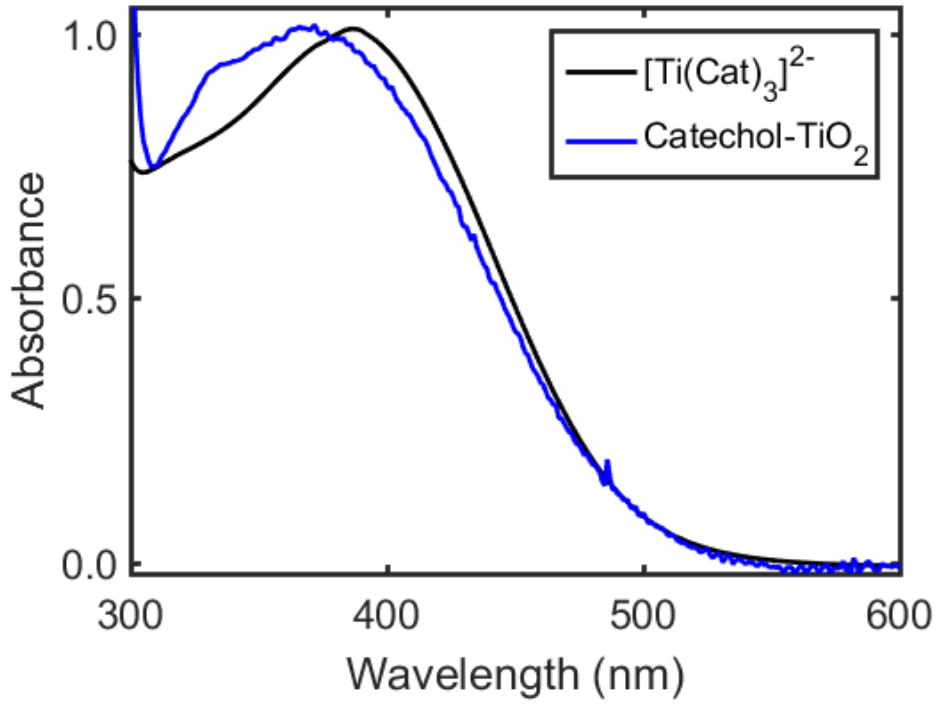

Figure C.7: Linear absorbance spectra of $[Ti(cat)_3]^{2-}$ and catechol on a TiO_2 nanocrystalline film. Both measurements are conducted in aqueous solution.

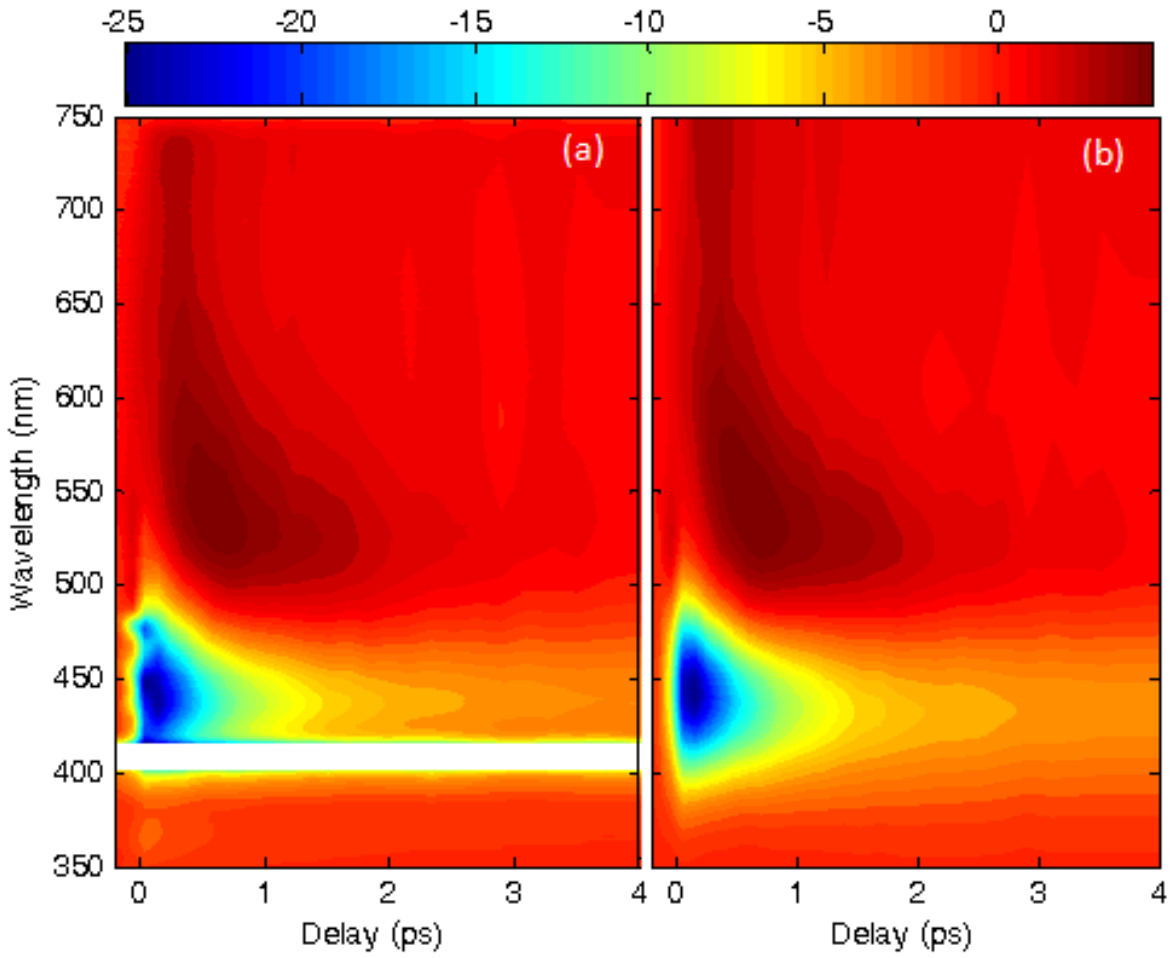

Figure C.8: (a) Transient absorption spectrogram for the chirp-corrected signal from catechol on TiO_2 . Scatter of the pump pulse at 410 nm has been removed to preserve the color scale. The spectrum shows a 25-mOD GSB repsonse at 440 nm, a blue-shifting HGS resonance near 550 nm, and an absorptive feature at longer wavelengths. (b) Gaussian functions are used to fit the experimental signals (see Figure C.9 for components).

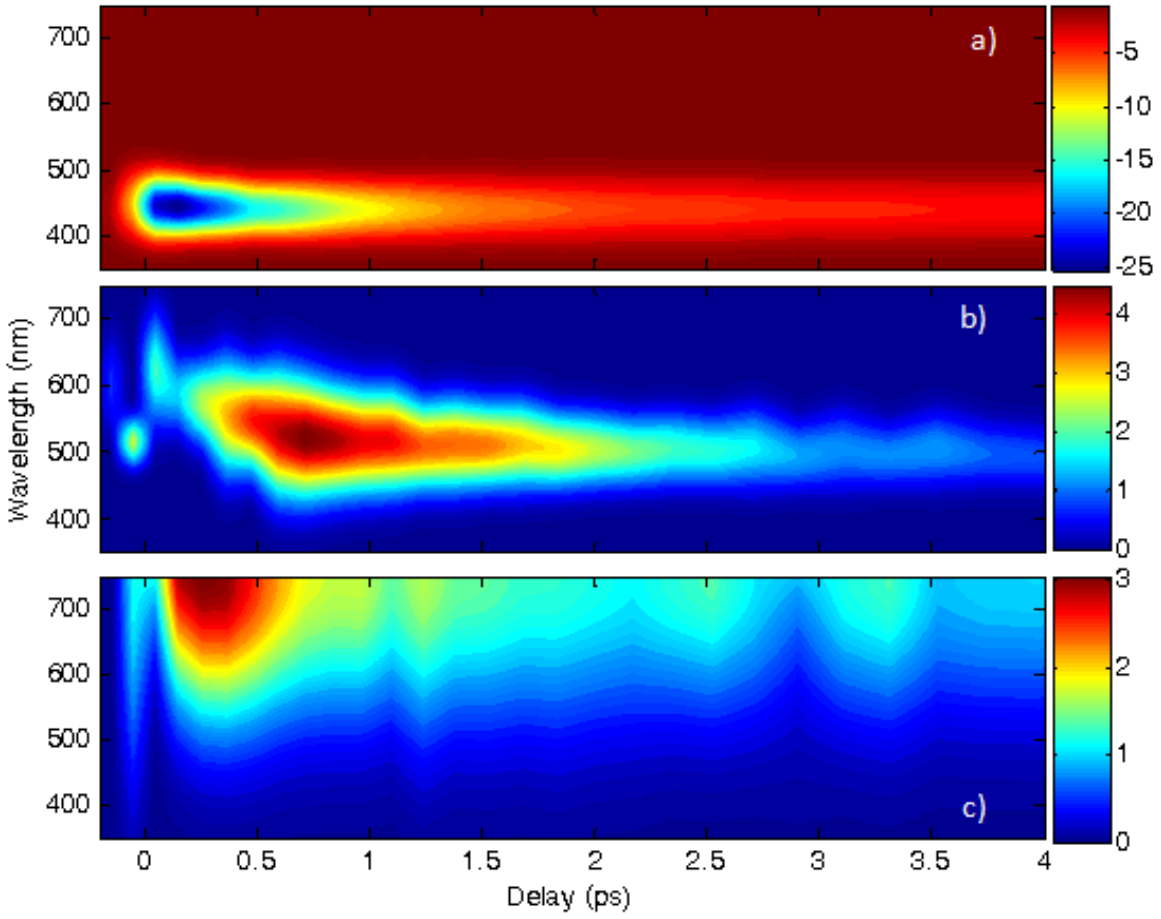

Figure C.9: Decomposition of GSB, HGS, and broadband signal components for catechol on TiO_2. (a) The peak wavelength of the GSB portion of the spectrum is insensitive to the delay time. (b) The HGS signal component blue-shifts and narrows as the delay increases. c) The long-lived feature centered above 700 nm is also fit to a Gaussian line shape.

C.6. REFERENCES

(1) Myers, A. B.; Mathies, R. A. Resonance Raman intensities: a probe of excited state structures and dynamics. In *Biological Applications of Raman Spectroscopy*; Spiro, T. G., Ed.; Wiley: New York, 1987; Vol. 2; pp 1.

(2) Frisch, M. J.; Trucks, G. W.; Schlegel, H. B.; Scuseria, G. E.; Robb, M. A.; Cheeseman, J. R.; Scalmani, G.; Barone, V.; Mennucci, B.; Petersson, G. A.; Nakatsuji, H.; Caricato, M.; Li, X.; Hratchian, H. P.; Izmaylov, A. F.; Bloino, J.; Zheng, G.; Sonnenberg, J. L.; Hada, M.; Ehara, M.; Toyota, K.; Fukuda, R.; Hasegawa, J.; Ishida, M.; Nakajima, T.; Honda, Y.; Kitao, O.; Nakai, H.; Vreven, T.; Montgomery, J. A., Jr.; Peralta, J. E.; Ogliaro, F.; Bearpark, M.; Heyd, J. J.; Brothers, E.; Kudin, K. N.; Staroverov, V. N.; Kobayashi, R.; Normand, J.; Raghavachari, K.; Rendell, A.; Burant, J. C.; Iyengar, S. S.; Tomasi, J.; Cossi, M.; Rega, N.; Millam, J. M.; Klene, M.; Knox, J. E.; Cross, J. B.; Bakken, V.; Adamo, C.; Jaramillo, J.; Gomperts, R.; Stratmann, R. E.; Yazyev, O.; Austin, A. J.; Cammi, R.; Pomelli, C.; Ochterski, J. W.; Martin, R. L.; Morokuma, K.; Zakrzewski, V. G.; Voth, G. A.; Salvador, P.; Dannenberg, J. J.; Dapprich, S.; Daniels, A. D.; Farkas, Ö.; Foresman, J. B.; Ortiz, J. V.; Cioslowski, J.; Fox, D. J. Gaussian 09 Wallingford,CT, 2009.

(3) Valkunas, L.; Abramavicius, D.; Mančal, T. *Molecular Excitation Dynamics and Relaxation: Quantum Theory and Spectroscopy* Wiley-VCH: Weinheim, 2013.

(4) Wang, Y.; Hang, K.; Anderson, N. A.; Lian, T. *J. Phys. Chem. B* **2003**, *107*, 9434.